

# Multi-Scalar Mixing in Turbulent Coaxial Jets

Alaïs Hewes

Doctor of Philosophy

Department of Mechanical Engineering

McGill University

Montréal, Québec

December 15, 2020

A thesis submitted to the Faculty of Graduate Studies and Research in partial fulfillment of the requirements for the degree of Doctor of Philosophy

©Alaïs Hewes, Montréal, Canada 2020



## ACKNOWLEDGEMENTS

First, I would like to express my sincere gratitude to my supervisor, Professor Mydlarski, for his guidance and support over the last four years, as well as his continuous optimism throughout the painstaking process required to develop the measurement techniques used herein.

I am also grateful to the National Science and Engineering Research Council of Canada (NSERC) for funding my research.

I would additionally like to thank all of my colleagues for their assistance, notably Vincent Tremblay-Dionne, Alexandre Cohen, and Abraham Gómez.

Finally, I would like to thank my family and friends, most particularly, my parents, for their encouragement and support throughout every step of my education, and Alexandre Imbeault, for keeping me sane through the last stretch of this work, written in the midst of a global pandemic.

## ABSTRACT

An experimental investigation of multi-scalar mixing in turbulent coaxial jets is presented herein. Although many flows of interest contain more than one scalar (e.g. combustion, atmospheric, and oceanic flows), there have been relatively few studies of turbulent multi-scalar mixing. Moreover, the vast majority of these studies (i) have not been capable of measuring multiple scalars simultaneously, and (ii) have focused only on the scalar field, despite the need for simultaneous velocity-scalar measurements to fully describe the mixing of scalars in turbulent flows. The objective of the present work is therefore to study the evolution of multiple scalars (helium concentration and temperature) *and* velocity in turbulent coaxial jets, with the aim of ultimately furthering our understanding of multi-scalar mixing, in addition to providing valuable experimental data for the testing of numerical simulations.

The first part of this work involves the development of a thermal-anemometry-based probe to simultaneously measure two scalars and velocity in turbulent flows. The work of Hewes (2016) on the simultaneous measurement of velocity and helium concentration is extended, and the necessary and optimal design parameters for thermal-anemometry-based probes capable of making such measurements are refined in the current work. An analysis of measurements from different interference probes reveals that, unlike what has previously been reported in the literature, hot-wires of differing diameters are not required for concurrent velocity and concentration measurements. Furthermore, both theoretical arguments and experiments in flows of varying helium concentration are used to demonstrate that the cold-wire thermometer is effectively insensitive to helium concentration. The temperature field can therefore be measured independently of the velocity or concentration fields. This has important implications for interference probes, since the cold-wire can be used

to compensate for temperature effects on these probes, allowing them to be used in non-isothermal flows. Consequently, it is shown that an interference probe can be combined with a cold-wire thermometer to form a novel 3-wire probe to simultaneously measure velocity, helium concentration, and temperature in a turbulent flow.

In the second part of this work, the novel 3-wire probe is used to study the evolution of multiple scalars in turbulent coaxial jets consisting of (i) a center jet containing a mixture of helium and air, (ii) an annular jet containing pure (unheated) air, and (iii) a coflow of (pure) heated air. The flow can be viewed as containing three scalars:  $\phi_1$ , normalized helium concentration,  $\phi_2$ , pure, unheated air in the annular jet (which is inferred from measurements of the other two scalars), and  $\phi_3$ , normalized temperature. Measurements are performed along axis of the jets for three different momentum ratios ( $M_2/M_1 = 0.77$ ,  $M_2/M_1 = 2.1$ , and  $M_2/M_1 = 4.2$ ). Mean and rms quantities, covariances, velocity-scalar triple moments, probability density functions (PDFs), joint probability density functions (JPDFs), and conditional expectations of the fluctuating velocity are measured. Three distinct regions are identified along the axis of the coaxial jets: (i) the potential core of the center jet, consisting primarily of  $\phi_1$ , (ii) the inner mixing region, dominated by large fluctuations of anti-correlated  $\phi_1$  and  $\phi_2$ , and (iii) the fully merged region, where the coaxial jets behave similarly to a single jet. In this final region, one can observe that  $\phi_1$  and  $\phi_3$ , and  $\phi_2$  and  $\phi_3$ , become progressively anti-correlated in the downstream direction, whereas  $\phi_1$  and  $\phi_2$  become progressively more correlated. Increasing the momentum ratio ( $M$ ) initially causes  $\phi_1$  and  $\phi_2$  to mix more quickly, however, examination of the JPDFs suggest that far downstream, these effects may be reversed. Furthermore, distinct differences are observed between coaxial jets in which  $M < 1$  and those in which  $M > 1$ , most likely resulting from the fact that the annular jet is entrained into center jet in the

former, whereas the center jet is entrained into annular jet in the latter. Finally, it worth pointing out that  $M$  may have a significant effect on the shapes and distributions of the scalar-scalar JPDFs, even where the correlation coefficients of different cases have converged to similar values. Thus, the need for simultaneous multi-scalar measurements when studying multi-scalar mixing is emphasized.

## RÉSUMÉ

La présente thèse propose une étude expérimentale du mélange de multiples scalaires dans des jets coaxiaux turbulents. Alors que plusieurs écoulements d'intérêt contiennent plus d'un scalaire (par ex. les écoulements combustibles, atmosphériques, et océaniques), il existe relativement peu d'études du mélange multi-scalaire turbulent. Par ailleurs, la grande majorité de ces études (i) ne sont pas parvenues à mesurer les scalaires simultanément, et (ii) n'ont pris pour objet que les scalaires. Il est pourtant impératif, si l'on souhaite décrire le plus adéquatement possible le mélange de scalaires dans un écoulement turbulent, de mesurer simultanément les scalaires et la vitesse. L'objectif de ce travail est donc d'étudier l'évolution de multiple scalaires (la concentration d'hélium et la température) *et* de la vitesse dans des jets coaxiaux turbulents, dans le but d'approfondir nos connaissances sur le mélange multi-scalaire, et aussi de fournir de précieuses données expérimentales pour la validation de simulations numériques.

La première partie de ce travail se porte sur la conception d'une sonde à base d'anémométrie thermique capable de simultanément mesurer deux scalaires, en plus de la vitesse, dans des écoulements turbulents. Les travaux de Hewes (2016) portant sur les mesures simultanées de vitesse et de concentration d'hélium sont approfondis, ainsi que l'identification des critères optimaux à la conception de sondes à base d'anémométrie thermique capable de réaliser telles mesures. La comparaison de plusieurs sondes d'interférence de conceptions variées démontre que, contrairement à ce qui apparaît dans la littérature scientifique, des fil-chauds de diamètres différents ne sont pas nécessaires pour effectuer des mesures de vitesse et de concentration simultanées. En outre, des arguments théoriques et des mesures expérimentales indiquent qu'un thermomètre à fil-froid est insensible à la concentration d'hélium de

l'écoulement. La température peut alors être mesurer indépendamment des champs de vitesse ou de concentration. Ceci a des implications importantes pour les sondes d'interférence, car le fil-froid peut compenser pour les variations de température ambiante, ce qui permet de les utiliser dans des écoulements non-isothermes. En conséquence, une sonde d'interférence peut être combinée avec un thermomètre à fil-froid pour former une nouvelle sonde à 3-fils et simultanément mesurer la vitesse, la concentration d'hélium, et la température dans un écoulement turbulent.

Dans la deuxième partie de ce travail, la sonde à 3-fils est utilisée pour étudier l'évolution de plusieurs scalaires dans des jets coaxiaux étant composés (i) d'un jet central d'un mélange d'air et d'hélium, (ii) un jet annulaire d'air pur (non-chauffé), et (iii) un co-courant d'air (pur) chauffé. Il est possible de représenter l'écoulement en fonction de trois scalaires:  $\phi_1$ , la concentration normalisée d'hélium,  $\phi_2$ , l'air pure, non-chauffé (deduit des deux autres scalaires), et  $\phi_3$ , la température normalisée. Des mesures sont effectuées le long de l'axe des jets pour trois rapports de quantité de mouvement différents ( $M_2/M_1 = 0.77$ ,  $M_2/M_1 = 2.1$ , et  $M_2/M_1 = 4.2$ ). Les moyennes et moyennes quadratiques, les covariances, les moments croisés de vitesse et de scalaires d'ordre trois, les fonctions de densité de probabilité (PDFs), les fonctions de densité de probabilité conjointes (JPDFs), et les moyennes conditionnelles de la vitesse fluctuante sont mesurés. Trois régions distinctes sont identifiées le long de l'axe des jets coaxiaux: (i) le cône potentiel du jet central, (ii) la région du mélange interne, et (iii) la région confluée. Dans cette dernière région,  $\phi_1$  et  $\phi_3$ , et  $\phi_2$  et  $\phi_3$ , deviennent de plus en plus négativement corrélés en aval, alors que  $\phi_1$  et  $\phi_2$  deviennent de plus en plus positivement corrélés. Dans un premier temps, l'augmentation de  $M$  accélère le mélange de  $\phi_1$  et  $\phi_2$ . Cependant, une analyse des JPDFs montre que, loin en aval, ces effets sont inversés. De plus, des différences importantes se

révèlent entre des jets coaxiaux où  $M < 1$ , et ceux où  $M > 1$ . Ceci est certainement dû au fait que le jet annulaire est entraîné dans le jet central quand  $M < 1$ , alors que le jet central est entraîné dans le jet annulaire quand  $M > 1$ . Finalement, il convient de noter que  $M$  peut avoir un effet important sur la forme et l'évolution des JPDFs des scalaires, alors même que les coefficients de corrélation des différents cas soient égaux. L'ensemble de ces constatations conduit donc à souligner l'importance des mesures multi-scalaires simultanées lorsqu'il est question d'étudier un mélange multi-scalaire.

## TABLE OF CONTENTS

ACKNOWLEDGEMENTS . . . . .	iii
ABSTRACT . . . . .	iv
RÉSUMÉ . . . . .	vii
LIST OF TABLES . . . . .	xiii
LIST OF FIGURES . . . . .	xiv
NOMENCLATURE . . . . .	xviii
1 Introduction . . . . .	1
1.1 Background, Motivation, and Overall Objectives . . . . .	1
1.2 Specific Objectives . . . . .	3
1.3 Organization of the Thesis . . . . .	5
2 Literature Review . . . . .	6
2.1 Measurement Techniques . . . . .	6
2.1.1 Velocity Measurements . . . . .	6
2.1.2 Scalar Measurements . . . . .	9
2.1.3 Velocity-Scalar Measurements . . . . .	12
2.1.4 Multi-Scalar Measurements . . . . .	13
2.2 Scalar Mixing . . . . .	15
2.2.1 Mixing of a Single Passive Scalar . . . . .	15
2.2.2 Two-Scalar Mixing Experiments . . . . .	19
2.2.3 Two-Scalar Mixing Simulations . . . . .	24
2.3 Jets . . . . .	26
2.3.1 Velocity Field of a Single Round Jet . . . . .	27
2.3.2 Scalar Field of a Single Round Jet . . . . .	29
2.3.3 Jet with Variable Fluid Properties . . . . .	32
2.3.4 Coaxial Jets . . . . .	36
3 Experimental Apparatus . . . . .	44
3.1 Calibration Apparatus . . . . .	44

3.1.1	Overview . . . . .	44
3.1.2	He/Air Mixing System . . . . .	46
3.1.3	Automation of the He/Air Mixing System . . . . .	48
3.1.4	Heating System . . . . .	50
3.1.5	Calibration Jet . . . . .	50
3.2	Coaxial Jet Apparatus . . . . .	51
3.2.1	Interface with Calibration Jet Apparatus . . . . .	53
3.2.2	Enclosure . . . . .	55
3.2.3	Coaxial Jet Streams . . . . .	56
3.2.4	Traversing Mechanisms . . . . .	59
3.3	Data Acquisition . . . . .	61
4	Instrumentation . . . . .	63
4.1	Single-Normal Hot-Wire and Cold-Wire Probes . . . . .	63
4.1.1	Single-Normal Hot-Wire Probe . . . . .	64
4.1.2	Cold-Wire Probe . . . . .	64
4.2	Interference Probe . . . . .	68
4.2.1	Background . . . . .	68
4.2.2	Theory . . . . .	71
4.2.3	Design . . . . .	78
4.2.4	Calibration and Data Reduction . . . . .	80
4.2.5	Experiments . . . . .	87
4.2.6	Optimal Design of Interference Probes . . . . .	94
4.3	3-Wire Probe . . . . .	95
4.3.1	Cold-Wire in Flows of Helium . . . . .	95
4.3.2	Use of Interference Probes in Non-Isothermal Flows . . . . .	97
4.3.3	Operation of 3-wire Probe . . . . .	105
5	Validation of the Experimental Apparatus and Measurement Techniques	107
5.1	Validation of the Experimental Apparatus . . . . .	107
5.1.1	Single-Normal Hot-Wire Measurements in an Axisymmetric Jet . . . . .	107
5.1.2	Exit Profiles . . . . .	113
5.2	Validation of Measurement Techniques . . . . .	115
5.2.1	Interference Probe Measurements in Axisymmetric Jets . . . . .	117
5.2.2	3-Wire Probe Measurements in Coaxial Jets . . . . .	123
6	Results . . . . .	131
6.1	Experimental Conditions . . . . .	131
6.2	Statistical Moments . . . . .	133

6.2.1	Mean Quantities . . . . .	133
6.2.2	Second-Order Quantities . . . . .	140
6.2.3	Third-Order Quantities . . . . .	150
6.3	Probability Density Functions . . . . .	153
6.4	Scalar-Scalar Joint Probability Density Functions . . . . .	161
6.4.1	JPDFs of $\phi_1$ and $\phi_2$ . . . . .	162
6.4.2	JPDFs of $\phi_1$ and $\phi_3$ . . . . .	171
6.4.3	JPDFs of $\phi_2$ and $\phi_3$ . . . . .	175
6.5	Velocity-Scalar Joint Probability Density Functions . . . . .	176
6.6	Conditional Expectations of the Fluctuating Velocity . . . . .	180
7	Conclusions . . . . .	189
7.1	Thermal-Anemometry-Based Measurement Techniques . . . . .	189
7.2	Multi-Scalar Mixing in Coaxial Jets . . . . .	191
7.3	Novel Contributions of the the Present Study . . . . .	195
7.3.1	Thermal-Anemometry-Based Measurement Techniques . . . . .	195
7.3.2	Multi-Scalar Mixing in Coaxial Jets . . . . .	196
7.4	Future Work . . . . .	197
7.4.1	Extension of Measurements Pertaining to the Current Experimental Conditions . . . . .	197
7.4.2	Additional Multi-scalar Mixing Studies in Coaxial Jets . . . . .	198
7.4.3	Variable Viscosity and Variable Thermal Diffusivity . . . . .	199
	REFERENCES . . . . .	200
	Appendix A: Derivation of King's Law . . . . .	218
	Appendix B: LabVIEW Program automating the He/Air Mixing System . . . . .	221
	Appendix C: Uncertainty Analysis . . . . .	223
	Appendix D: Confirmation of Statistical Convergence of the Measurements . . . . .	232
	Appendix E: Rarified Gas and Accommodation Effects . . . . .	234
	Appendix F: Calculations of Fluid Properties in He/Air Mixtures . . . . .	240

## LIST OF TABLES

<u>Table</u>		<u>page</u>
3.1	Properties of the center and annular jet streams . . . . .	57
4.1	Summary of thermal-anemometry-based probes developed in the literature capable of simultaneously measuring velocity and concentration in turbulent flows . . . . .	72
4.2	Summary of interference probe designed for the present work . . . . .	79
5.1	Comparison of characteristics of axisymmetric jets . . . . .	109
5.2	Experimental properties of axisymmetric jets in validation experiments for the interference probe . . . . .	118
5.3	Experimental properties of the center jet, annular jet, and coflow in validation experiments for the 3-wire probe . . . . .	123
6.1	Experimental properties of the center jet, annular jet and coflow in multi-scalar mixing experiments . . . . .	132
C.1	Summary of various sources of error in the calibration apparatus and the corresponding uncertainties. . . . .	225
C.2	Summary of various sources of error for the PCI-6143 A/D DAQ board and the corresponding uncertainties. . . . .	227
C.3	Summary of various sources of error for the instantaneous measurements and the corresponding uncertainties. . . . .	228
E.1	Typical Knudsen numbers of hot-wires . . . . .	235

## LIST OF FIGURES

<u>Figure</u>		<u>page</u>
2.1	Schematic representation of a variable-density jet . . . . .	34
2.2	Schematic representation of the near-field of coaxial jets . . . . .	37
3.1	Schematic of the calibration apparatus . . . . .	45
3.2	Data acquisition system for the helium/air mixing system . . . . .	49
3.3	Coaxial jet apparatus . . . . .	52
3.4	Schematic of fluid flow in the calibration apparatus during experiments	54
3.5	Coaxial jet apparatus design . . . . .	57
3.6	Stand with three traversing mechanisms . . . . .	60
4.1	Typical calibration for a single-normal hot-wire . . . . .	66
4.2	Typical calibration for a cold-wire sensor and response of a cold-wire to the current injection technique of Lemay and Benaïssa (2001) . .	66
4.3	Theoretical dependence of $E_2^2$ on $E_1^2$ for two hot-wires of different diameters . . . . .	76
4.4	Theoretical dependence of $E_2^2$ on $E_1^2$ for two hot-wires at different temperatures . . . . .	76
4.5	Schematic representation of an interference probe . . . . .	79
4.6	Typical calibration map for an interference probe . . . . .	81
4.7	Comparison of the effects of the overheat ratio on the calibration map of the 2.5W-1.2Pt-35 probe . . . . .	82
4.8	Comparison of the effects of the overheat ratio on the calibration map of the 10W-5W-10 probe . . . . .	83
4.9	Additional calibration plots for the interference probe . . . . .	86

4.10	Velocity spectra measured using a single-normal hot-wire and interference probe . . . . .	88
4.11	Concentration spectra measured using an interference probe in He/air mixtures and pure air . . . . .	88
4.12	Comparison of interference probe designs . . . . .	91
4.13	Image of interference probe with and without heating wires . . . . .	93
4.14	Cold-wire measurements in flows of different helium concentrations . .	96
4.15	Theoretical sensitivity ratios ( $s_u/s_t$ , $s_c/s_t$ ) for a cold-wire . . . . .	96
4.16	Typical non-isothermal calibration map for an interference probe . . .	99
4.17	The calibration constants $A$ and $B$ plotted as a function of temperature	101
4.18	Temperature compensated voltages of the upstream wire of an interference probe . . . . .	101
4.19	The calibration constants $F$ and $G$ plotted as a function of temperature	103
4.20	The calibration constants $T_{w,F}$ and $T_{w,G}$ plotted as a function of temperature . . . . .	103
4.21	Temperature-normalized calibration map of an interference probe . . .	104
5.1	Downstream evolution of the centerline axial mean velocity of an axisymmetric jet . . . . .	110
5.2	Downstream evolution of the centerline turbulence intensity of an axisymmetric jet . . . . .	110
5.3	Normalized radial profiles of the mean velocity . . . . .	111
5.4	Downstream evolution of an axisymmetric jet's half-width . . . . .	111
5.5	Velocity profiles for the coaxial jet apparatus at $x = 1.5$ mm . . . . .	114
5.6	Temperature profiles for the coaxial jet apparatus at $x = 1.5$ mm . . .	116
5.7	Downstream evolution of the mean centerline axial velocity in axisymmetric jets with different density ratios . . . . .	120
5.8	Downstream evolution of the turbulence intensity in axisymmetric jets with different density ratios . . . . .	120

5.9	Downstream evolution of the mean centerline concentration in axisymmetric jets with different density ratios . . . . .	121
5.10	Downstream evolution of the intensity of concentration fluctuations in axisymmetric jets with different density ratios . . . . .	121
5.11	Downstream evolution of $\langle U \rangle$ and $u_{rms}/\langle U \rangle$ in the coaxial jets . . . . .	125
5.12	Downstream evolution of $\langle C \rangle$ and $c_{rms}$ in the coaxial jets . . . . .	125
5.13	Downstream evolution of $\langle \Delta T \rangle$ and $t_{rms}$ in the coaxial jets . . . . .	126
5.14	PDFs of $\Delta T$ in the coaxial jets . . . . .	126
5.15	Temperature spectra in the coaxial jets . . . . .	128
6.1	Schematic representation of the experimental flow . . . . .	134
6.2	Downstream evolution of mean quantities . . . . .	135
6.3	Downstream evolution of rms quantities . . . . .	141
6.4	Downstream evolution of fluctuating intensities . . . . .	143
6.5	Downstream evolution of correlation coefficients . . . . .	147
6.6	Downstream evolution of triple moments . . . . .	151
6.7	PDFs of $U$ . . . . .	154
6.8	Schematic representation of the evolution of the radial velocity profiles of coaxial jets . . . . .	155
6.9	PDFs of $\phi_1$ . . . . .	158
6.10	PDFs of $\phi_2$ . . . . .	159
6.11	PDFs of $\phi_3$ . . . . .	160
6.12	JPDFs of $\phi_1$ and $\phi_2$ for case I . . . . .	163
6.13	JPDFs of $\phi_1$ and $\phi_2$ for case II . . . . .	164
6.14	JPDFs of $\phi_1$ and $\phi_2$ for case III . . . . .	165
6.15	Schematic representation of the effects of the area and momentum ratios of the coaxial jets on the flow . . . . .	168
6.16	Effect of $M$ on JPDFs of $\phi_1$ and $\phi_2$ . . . . .	170

6.17	JPDFs of $\phi_1$ and $\phi_3$ . . . . .	172
6.18	JPDFs of $\phi_2$ and $\phi_3$ . . . . .	174
6.19	JPDFs of $U$ and $\phi_1$ . . . . .	177
6.20	JPDFs of $U$ and $\phi_2$ . . . . .	178
6.21	JPDFs of $U$ and $\phi_3$ . . . . .	179
6.22	Downstream evolution of $\langle u \phi_1, \phi_2\rangle/u_{rms}$ for case I . . . . .	181
6.23	Downstream evolution of $\langle u \phi_1, \phi_2\rangle/u_{rms}$ for case II . . . . .	182
6.24	Downstream evolution of $\langle u \phi_1, \phi_2\rangle/u_{rms}$ for case III . . . . .	183
6.25	Downstream evolution of $\langle u \phi_1, \phi_3\rangle/u_{rms}$ . . . . .	186
6.26	Downstream evolution of $\langle u \phi_2, \phi_3\rangle/u_{rms}$ . . . . .	187
D.1	Convergence of $\langle u^6 \rangle$ . . . . .	232
D.2	Convergence of $\langle \phi_1'^6 \rangle$ . . . . .	233
D.3	Convergence of $\langle \phi_2'^6 \rangle$ . . . . .	233
D.4	Convergence of $\langle \phi_3'^6 \rangle$ . . . . .	233

## NOMENCLATURE

### Roman Symbols

$A$	Calibration constant in King's Law equation
$A^*$	Component of $A$ which is insensitive to temperature
$A_1, A_i$	Area of center jet
$A_2, A_o$	Area of annular jet
$A_c$	Calibration constant for cold-wire
$A_J$	Area of jet
$A_r$	Area of room/enclosure
$B$	Calibration constant in King's Law equation
$B^*$	Component of $B$ which is insensitive to temperature
$B_c$	Calibration constant for cold-wire
$B_u$	Centerline velocity decay constant
$B_{u,e}$	Centerline velocity decay constant in variable-density jets
$C$	Instantaneous concentration (i.e. He mass fraction)
$c$	Fluctuating concentration ( $C - \langle C \rangle$ )
$C_1$	He mass fraction at the exit of the center jet
$C_{\text{set}}$	He mass fraction set with LabVIEW program
$c_w$	Specific heat of the wire
$D$	Diameter of the jet
$d$	Diameter of the wire
$D_e$	Effective diameter

$D_h$	Hydraulic diameter
$D_i$	Inner diameter of the jet
$D_o$	Outer diameter of the jet
$E$	Anemometer output voltage
$E_c$	Cold-wire voltage
$E_{c,\text{meas}}$	Measured (actual) cold-wire voltage
$E_{c,\text{theory}}$	Theoretical cold-wire voltage ( $\tau_w = 0$ )
$E_{\text{down}}$	Interference probe downstream wire voltage
$E_{\text{down},20}$	Normalized value of the downstream wire voltage
$E_{\text{up}}$	Interference probe upstream wire voltage
$E_w$	Wire voltage
$F$	Froude number
$F$	Calibration constant for non-isothermal interference probes
$F^*$	Component of $F$ which is insensitive to temperature
$f$	Frequency
$f_c$	Cut-off frequency
$f_{HP}$	High-pass frequency
$f_{LP}$	Low-pass frequency
$f_\eta$	Kolmogorov frequency
$f_{\eta\phi}$	Maximum frequency of the scalar field
$f_\phi$	Scalar PDF
$f_{U_j\phi}$	Velocity-Scalar JPDF
$f_{\phi_\alpha\phi_\beta}$	Scalar-Scalar JPDF
$G$	Calibration constant for non-isothermal interference probes
$G^*$	Component of $G$ which is insensitive to temperature

$g$	Gravitational constant
$h$	Heat transfer coefficient
$H(f)$	Filter function for frequency compensation of cold-wire
$I$	Electrical current in the wire
$k$	thermal conductivity of the fluid
$k^\circ$	“Frozen” thermal conductivity ( $\mu/M_{MM}$ )
$k_{air}$	Thermal conductivity of air
$K_c$	Centerline scalar decay constant
$k_{He}$	Thermal conductivity of helium
$k_{mix}$	Thermal conductivity of a He/air mixture
$l$	Length of the wire
$L_c$	Length of the potential core of the center jet
$M$	Mach number of the flow
$M$	Momentum ratio of coaxial jets
$M_\infty$	Momentum flow rate of a jet in an infinite environment
$M_{air}$	Molecular weight of air
$M_{He}$	Molecular weight of helium
$M_J$	Momentum flow rate at the exit of the jet
$m_J$	Mass flow rate at the exit of the jet
$M_{MM}$	Molar mass of the fluid
$n$	Calibration constant in King’s Law equation
$N(f)$	Spectra of the noise
$Nu$	Nusselt number
$Nu_c$	Continuum Nusselt number
$OH$	Overheat ratio of wire

$P$	(Instantaneous) pressure
$p$	Fluctuating pressure
$Pe$	Péclet number
$Pr$	Prandtl number
$q$	Heat flux
$Q$	Volumetric flow rate
$Q_{air}$	Volume flow rate of air
$Q_{air,J}$	Volume flow rate of air at the jet exit
$Q_{air,MFM}$	Volume flow rate of air recorded by the MFM
$Q_{He}$	Volume flow rate of helium
$Q_{He,J}$	Volume flow rate of helium at the jet exit
$Q_{He,MFC}$	Volume flow rate of helium recorded by the MFC
$Q_{tot,J}$	Total volume flow rate at the jet exit
$\dot{Q}_c$	Conductive heat-transfer rate
$\dot{Q}_e$	Electrical heat-generation rate
$\dot{Q}_{fc}$	Forced-convective heat-transfer rate
$\dot{Q}_r$	Radiation heat-transfer rate
$\dot{Q}_s$	Heat storage rate
$R$	Velocity ratio of coaxial jets ( $U_o/U_i, U_2/U_1$ )
$r_{1/2}$	Jet half-width
$r_{\phi_{1/2}}$	Jet half-width defined from scalar measurements
$R_{20}$	Resistance of the wire at 20°C
$R_a$	Cold-resistance of the wire
$R_{cr}$	Critical velocity ratio in coaxial jets
$Re$	Reynolds number

$Re_D$	Reynolds number of the jet ( $Re_D = U_J D / \nu$ )
$Re_{D_h}$	Reynolds number of the jet based on the hydraulic diameter
$R_L$	Resistance of cable connecting hot-wire to CTA
$R_T$	Top-resistance of the Wheatstone bridge of a CTA
$R_{univ}$	Universal gas constant
$R_w$	Resistance of the wire (while being operated)
$S$	Density ratio ( $\rho_J / \rho_\infty, \rho_o / \rho_i, \rho_2 / \rho_1$ )
$S(f)$	Spectra of the signal
$Sc$	Schmidt number
$s_c$	Wire sensitivity to concentration ( $\partial E / \partial C$ )
$s_t$	Wire sensitivity to temperature ( $\partial E / \partial U$ )
$S_u$	Jet spreading rate
$s_u$	Wire sensitivity to velocity ( $\partial E / \partial U$ )
$S_\phi$	Chemical source term in PDF transport equations
$T$	(Instantaneous) temperature of the fluid
$t$	Fluctuating temperature ( $T - \langle T \rangle$ )
$T_1$	Temperature at the exit of the center jet
$T_2$	Temperature at the exit of the annular jet
$T_3$	Temperature at the exit of the coflow
$T_f$	Film temperature of the wire
$\Delta T_{max}$	Maximum temperature difference in the coaxial jet apparatus ( $T_3 - T_1$ )
$Tw_A$	Calibration constant for non-isothermal interference probes
$Tw_B$	Calibration constant for non-isothermal interference probes
$Tw_F$	Calibration constant for non-isothermal interference probes
$Tw_G$	Calibration constant for non-isothermal interference probes

$Tw_{up}$	Calibration constant for non-isothermal interference probes
$U$	Instantaneous (axial) velocity
$u$	Fluctuating (axial) velocity ( $U - \langle U \rangle$ )
$U_0$	Centerline axial velocity
$U_1, U_i$	Average velocity at the exit of the center jet
$U_2, U_o$	Average velocity at the exit of the outer jet
$U_3$	Velocity at the exit of the coflow
$U_j$	Instantaneous velocity components
$u_j$	Fluctuating velocity components
$u_x$	Uncertainty of quantity $x$
$v$	radial component of fluctuating velocity
$V_{MFC}$	Voltage sent to mass flow controller
$V_{MFM}$	Voltage acquired from mass flow meter
$x$	Cartesian or cylindrical coordinate / denotes axial direction of jet
$x_0$	Virtual origin of jet
$x_{0\phi}$	Virtual origin of the jet defined from scalar measurements
$x_1$	Parameter quantifying buoyancy effects in turbulent jets
$x_{air}$	Mole fraction of air
$x_{FD}$	Entrance length of pipe
$x_{He}$	Mole fraction of helium
$Y$	Volumetric fraction of helium
$y$	Cartesian coordinate
$z$	Cartesian coordinate

### Greek Symbols

$\alpha$	Accommodation coefficient
----------	---------------------------

$\alpha_{20}$	Temperature coefficient of resistivity of the wire at 20°C
$\alpha_{air}$	Accommodation coefficient in air
$\alpha_{He}$	Accommodation coefficient in helium
$\beta$	Slip parameter
$\beta_{air}$	Slip parameter in air
$\beta_{He}$	Slip parameter in helium
$\gamma$	Diffusivity of the scalar
$\gamma_R$	Ratio of specific heats of the fluid
$\Delta$	Temperature jump distance in slip conditions
$\epsilon$	Dissipation of turbulent kinetic energy
$\epsilon_\phi$	Dissipation of scalar variance
$\epsilon_{VV}$	Dissipation of turbulent kinetic energy in variable viscosity flows
$\theta(f)$	Wiener filter
$\eta$	Kolmogorov length scale
$\lambda$	Mean free path
$\mu$	(Dynamic) viscosity of the fluid
$\mu_{air}$	(Dynamic) viscosity of air
$\mu_{He}$	(Dynamic) viscosity of helium
$\mu_{mix}$	(Dynamic) viscosity of a He/air mixture
$\nu$	Kinematic viscosity of the fluid
$\Phi$	Parameter quantifying accommodation effects
$\phi$	Instantaneous scalar
$\phi_0$	(Instantaneous) centerline scalar
$\phi_1$	Normalized helium concentration (scalar of the center jet)
$\phi_2$	Cold, helium-free scalar (scalar of the annular jet)

$\phi_3$	Normalized temperature (scalar of the coflow)
$\phi'$	Fluctuating scalar ( $\phi - \langle \phi \rangle$ )
$\phi'_1$	Fluctuating component of $\phi_1$ ( $\phi_1 - \langle \phi_1 \rangle$ )
$\phi'_2$	Fluctuating component of $\phi_2$ ( $\phi_2 - \langle \phi_2 \rangle$ )
$\phi'_3$	Fluctuating component of $\phi_3$ ( $\phi_3 - \langle \phi_3 \rangle$ )
$\rho$	Density of the fluid
$\rho_1, \rho_i$	Density of the center jet (at the exit)
$\rho_\infty$	Density of ambient surroundings
$\rho_2, \rho_o$	Density of the annular jet (at the exit)
$\rho_{\phi_\alpha \phi_\beta}$	Scalar cross-correlation coefficient
$\rho_{air}$	Density of air
$\rho_{air,J}$	Density of air at the jet exit
$\rho_{air,MFM}$	Density of air recorded by the MFM
$\rho_{He}$	Density of helium
$\rho_{He,J}$	Density of He at the jet exit
$\rho_{He,MFC}$	Density of helium recorded by the MFC
$\rho_J$	Density at the exit of the jet
$\rho_{mix}$	Density of a He/air mixture
$\rho_w$	Density of the wire
$\tau_w$	Time constant of the wire
$\chi_w$	Resistivity of the wire material

### Operators, Superscripts, Subscripts

$\langle \phi \rangle$	Mean of $\phi$
$\hat{\phi}$	Sample-space variable for $\phi$
$\phi_{rms}$	Root mean square of $\phi$

## CHAPTER 1 Introduction

### 1.1 Background, Motivation, and Overall Objectives

The vast majority of fluid flows, whether natural or industrial, are turbulent. Although there is no complete and precise definition of turbulence, turbulent flows all share certain, specific characteristics. They (i) are irregular or random, (ii) occur at large Reynolds numbers, (iii) exhibit three-dimensional vorticity fluctuations, (iv) are always dissipative, such that a constant supply of energy is required to maintain them, and (v) are highly diffusive, leading to enhanced mixing of mass, momentum, and energy (Tennekes and Lumley 1972). This final characteristic of turbulence is one of its most important, and the turbulent mixing of scalars, such as temperature, humidity, pollutants, or any other chemical species, plays an essential role in many engineering and scientific fields, including heat transfer, combustion, environmental pollution dispersion, and oceanic and atmospheric sciences.

Significant attention has been given to the turbulent mixing of scalars, however most studies have focused only on the mixing of a single passive scalar.<sup>1</sup> Yet, many of flows of interest contain more than one scalar (e.g. mixing of temperature and salinity in the ocean, mixing of temperature and humidity in the atmosphere, mixing

---

<sup>1</sup> Given the complex, non-linear, and chaotic nature of both turbulent flows and the subsequent mixing of scalars therein, it is first preferable to neglect the effects of buoyancy and chemical reactions, which further complicate a difficult problem, and consider only the mixing of non-reacting, passive scalars (i.e. scalars whose presence does not alter the dynamics of the flow under consideration).

of multiple reactants and products in combusting flows). Previous studies have demonstrated that mixing between multiple scalars, *even multiple passive scalars*, is complex and highly dependent on initial conditions (e.g. the initial separation distance between scalars or their source location(s)), the type of flow (isotropic, homogeneous, inhomogeneous), and the diffusivities of the scalars. Moreover, there is evidence that common mixing models used with PDF methods may not be suitable for extension to multi-scalar mixing (Cai *et al.* 2011; Meyer and Deb 2012; Rowinski and Pope 2013). Accordingly, there is a need for additional experimental work on multi-scalar mixing; first to better understand these complex mixing processes and, second, to ensure that new or existing models adequately account for the mixing of multiple scalars.

To date, there have only been a handful of experimental studies on multi-scalar mixing, and a similar number of computational ones. Most of these, with the notable exception of the experiments of Sirivat and Warhaft (1982), have only focused on the scalar fields, despite the fact that simultaneous velocity-scalar measurements are required to fully describe turbulent scalar mixing. As can be seen from the advection-diffusion equation, which governs the evolution of a scalar ( $\phi$ ) in a flow:

$$\frac{\partial \phi}{\partial t} + U_j \frac{\partial \phi}{\partial x_j} = \gamma \frac{\partial^2 \phi}{\partial x_j \partial x_j}, \quad (1.1)$$

as well as the Reynolds-averaged advection-diffusion equation for the mean scalar ( $\langle \phi \rangle$ ),

$$\frac{\partial \langle \phi \rangle}{\partial t} + \langle U_j \rangle \frac{\partial \langle \phi \rangle}{\partial x_j} + \frac{\partial \langle \phi' u_j \rangle}{\partial x_j} = \gamma \frac{\partial^2 \langle \phi \rangle}{\partial x_j \partial x_j}, \quad (1.2)$$

and the scalar variance ( $\langle \phi'^2 \rangle$ ) budget:

$$\frac{\partial \langle \phi'^2 \rangle}{\partial t} + \langle U_j \rangle \frac{\partial \langle \phi'^2 \rangle}{\partial x_j} + 2 \langle \phi' u_j \rangle \frac{\partial \langle \phi \rangle}{\partial x_j} + \frac{\partial \langle u_j \phi'^2 \rangle}{\partial x_j} = \gamma \frac{\partial^2 \langle \phi'^2 \rangle}{\partial x_j \partial x_j} - 2 \gamma \left\langle \frac{\partial \phi'}{\partial x_j} \frac{\partial \phi'}{\partial x_j} \right\rangle, \quad (1.3)$$

where  $U_j$  is the velocity of the flow and  $\gamma$  is the diffusivity of the scalar, the transport of a scalar depends on the dynamics of the velocity field, as well as interactions between the velocity and scalar fields.<sup>2</sup>

Given the scarcity of simultaneous, turbulent, multi-scalar measurements in the literature, and the even greater scarcity of simultaneous, turbulent, multi-scalar and velocity measurements, the overall objective of this work is to enhance our understanding of multi-scalar mixing by way of measurements of two scalars and velocity in a turbulent flow. The experiments herein are carried out in turbulent coaxial jets emanating into a coflow. These jets are widely used in applications in which multiple fluid streams (each of which may carry one or more scalars) need to be mixed (e.g. fuel injectors within combustion systems), and consequently are well suited to a study of multi-scalar mixing. More specifically, it should be noted that the configuration of the flow studied within this work mimics that of piloted flames, in which a center and pilot jet are surrounded by a coflowing stream. Because turbulent scalar mixing is a critical factor affecting the operation of such burners — which are of interest due to their stability (Dunn *et al.* 2007) and/or high efficiency (Dally *et al.* 2002) — the present work, while fundamental in nature, nevertheless has significant practical applications .

## 1.2 Specific Objectives

The objective of the current work is to study the evolution of multiple scalars (*viz.* helium concentration and temperature) *and* velocity in turbulent coaxial jets.

---

<sup>2</sup> Note that equations (1.1), (1.2), and (1.3) are each written in a form that assumes constant properties, a reasonable assumption if  $\phi$  is considered to be a passive scalar.

Although multi-scalar mixing has previously been studied in coaxial jets, it is emphasized that the present study is the first to measure the scalar fields in conjunction with the velocity field.

Two specific objectives for the work are proposed:

- The first objective is to develop an experimental technique capable of simultaneously measuring two scalars and velocity in turbulent flows with high spatial and temporal resolution. As will be discussed in §2.1, thermal anemometry-based techniques, which are known for their relatively high spatial resolution, temporal resolution, and signal-to-noise ratio, can be used to measure the velocity, gas species, or temperature of a fluid. In the current work, a novel 3-wire thermal-anemometry-based probe is designed to simultaneously measure velocity, helium concentration, and temperature in a turbulent flow. Additional work, on the optimization and design of thermal-anemometry-based interference probes (see §2.1.3 and §4.2) capable of concurrently measuring velocity and helium concentration, is also presented, as is a study of the use of cold-wire thermometers in heterogeneous gas mixtures, with the objective of extending the capabilities of thermal-anemometry-based techniques.
- The second objective involves using the 3-wire probe to obtain simultaneous two-scalar and velocity measurements in the coaxial jets by way of single and multivariable/joint statistics. Mean and rms values, correlation coefficients, mixed velocity-scalar triple moments, probability density functions (PDFs), joint probability density functions (JPDFs), and conditional expectations of the fluctuating velocity are measured along the axis of the coaxial jets for three different momentum ratios (defined as the ratio of the momentum flow rate of the annular jet to that of the center jet), ranging from 0.77 to 4.2.

By way of mixed velocity-scalar and multi-scalar measurements, the current work provides valuable experimental data for the testing of numerical simulations of multi-scalar mixing. Furthermore, the results presented herein are used to describe in detail the mixing of multiple scalars in turbulent coaxial jets, and the effect the momentum ratio of the jets (which, as will be discussed in §2.3.4, governs the behavior of the flow) has on the mixing of these scalars.

### **1.3 Organization of the Thesis**

The remainder of the thesis is organized as follows. A literature review pertaining to measurement techniques for turbulent flows, scalar mixing in turbulent flows, and turbulent jets is presented in Chapter 2. The experimental apparatus is described in Chapter 3. Details of the instrumentation, including the design and optimization of interference probes and development of the novel 3-wire probe, are provided in Chapter 4. Subsequently, validation measurements, for both the experimental apparatus and instrumentation, are described in Chapter 5. The mixing of multiple scalars in turbulent coaxial jets is finally examined in Chapter 6, where the results of the present study, including measurements of mean and rms quantities, correlation coefficients, mixed velocity-scalar triple moments, PDFs, JPDFs, and conditional expectations of the fluctuating velocity, are presented. Conclusions, novel contributions, and future work are then discussed in Chapter 7.

## **CHAPTER 2**

### **Literature Review**

Given the previously defined objectives of the present work, a literature review of the following subjects is provided: (i) measurement techniques for turbulent flows, (ii) scalar mixing in turbulent flows, and (iii) turbulent jets. The focus herein is on multi-scalar mixing in turbulent coaxial jets, but more general overviews of the fields of scalar mixing and turbulent jets are also included, as these are essential to understanding the work presented in this thesis.

### **2.1 Measurement Techniques**

The current section discusses experimental techniques for the measurement of the velocity and scalar fields of turbulent flows. Brief overviews of existing techniques used to measure these respective fields are presented in §2.1.1 and §2.1.2, and extensions to simultaneous-velocity scalar measurements and multi-scalar measurements are examined in §2.1.3 and §2.1.4, respectively. Hot-wire anemometry and cold-wire thermometry are described in greater detail as these were the techniques adopted in the present work.

#### **2.1.1 Velocity Measurements**

In turbulent flows, the fluid's velocity is commonly measured by way of thermal anemometry (including hot-wire and hot-film anemometry), laser Doppler anemometry (LDA), or particle image velocimetry (PIV). Thermal anemometry, the oldest of these three techniques, remains one of the principal tools of turbulence research due to its (i) high temporal and spatial resolutions and (ii) high signal-to-noise ratio.

A brief summary of this technique is given here; for a more complete description of the principles of thermal anemometry, the reader is referred to the works of Perry (1982), Lomas (1986), Bruun (1995), and Tropea *et al.* (2007), all of which contain excellent reviews of the subject.

Thermal anemometry is based on the principles of convective heat transfer. The heat generated by passing a current through a fine metal wire (or film) is equal to the heat convected away by the fluid flow (assuming heat transfer by radiation and heat transfer by conduction to the prongs, to which the wire is attached, are neglected), such that the anemometer output voltage ( $E$ ) can be expressed as a function of the fluid velocity ( $U$ ) in what is often referred to as King's Law:

$$E^2 = A + BU^n. \quad (2.1)$$

$A$ ,  $B$ , and  $n$  can be treated as constants, and are typically determined from calibrations of the hot-wire (or hot-film) in flows of known, constant velocity. However, it should be noted that  $A$  and  $B$  are actually functions of the fluid temperature and composition, as well as the wire properties. For a constant temperature anemometer (i.e. one in which the wire's temperature/resistance is maintained constant by the anemometer), these can be expressed as:

$$A = 0.24\pi \left( \frac{OH - 1}{OH} \right) \left( \frac{T_f}{T} \right)^{0.17} k \left( \frac{1}{\alpha_{20} R_{20}} \right) (R_T + R_L + R_w)^2 l, \quad (2.2)$$

$$B = 0.56\pi \left( \frac{OH - 1}{OH} \right) \left( \frac{T_f}{T} \right)^{0.17} k \left( \frac{\rho}{\mu} \right)^n \left( \frac{1}{\alpha_{20} R_{20}} \right) (R_T + R_L + R_w)^2 l d^n, \quad (2.3)$$

where  $T$  is the temperature of the fluid and  $T_f$ <sup>1</sup> is the film temperature of the wire;  $k$ ,  $\mu$ , and  $\rho$  are respectively, the thermal conductivity, viscosity, and density of the fluid evaluated at  $T_f$ ;  $l$  and  $d$  are the respective length and diameter of the wire;  $\alpha_{20}$  and  $R_{20}$  are the temperature coefficient of resistivity and resistance of the wire at 20°C;  $R_T$  is the top-resistance of the Wheatstone bridge of a constant temperature anemometer (CTA);  $R_L$  is the resistance of the cable connecting the hot-wire to the CTA;  $R_w$  is the resistance of the wire while being operated; and finally,  $OH$  is the overheat ratio of the wire.<sup>2</sup> The derivation of equations (2.2) and (2.3) is provided in Appendix A.

The hot-wire sensor is generally made of tungsten, platinum, or a platinum alloy. It is recommended that the length-to-diameter ratio ( $l/d$ ) of hot-wires be at least 200 to minimize heat transfer by conduction from the wire to the prongs of the sensor to which it is attached (Bruun 1995). Moreover, the wire length ( $l$ ) should also be small enough that the Kolmogorov length scale ( $\eta$ ) can be resolved. Thus, hot-wires are designed to have very small diameters, typically 2.5 – 5  $\mu\text{m}$ , so that their lengths are roughly 0.5 – 1 mm long. Although spatial resolution errors may occur in some flows when measuring fine-scale turbulence, it is important to note that compared to many other common techniques for measuring velocity, hot-wires have comparable or superior spatial resolution.

As hot-wire anemometry has certain limitations — for example, hot-wires cannot be used without modifications in flows of high turbulence intensity, or in hostile environments (i.e. combusting flows, flows with particles) — alternative techniques may

---

<sup>1</sup>  $T_f \equiv 0.5(T_w + T)$ , where  $T_w$  is the temperature of the wire.

<sup>2</sup>  $OH \equiv R_w/R_a$ , where  $R_a$  is the cold-resistance of the wire.

be preferred. Popular alternatives to hot-wire anemometry include LDA and PIV. Both have the advantage of being non-intrusive, but LDA is a point-measurement technique with good spatial and temporal resolution,<sup>3</sup> whereas PIV can be used to measure the full velocity field, albeit with a generally limited temporal resolution.<sup>4</sup>

### 2.1.2 Scalar Measurements

The most common scalar measurement techniques in turbulent flows are cold-wire thermometry and LIF (laser induced fluorescence) / PLIF (planar laser induced fluorescence). The former is used to measure temperature fluctuations and involves a very fine wire operated as a resistance temperature detector (RTD) in conjunction with a constant current source. If the current is low, the cold-wire is nearly insensitive to the fluctuating velocity field, and, assuming the temperature differences are not overly large, the cold-wire voltage ( $E_{c,\text{theory}}$ ) can be theoretically expressed as a linear function of temperature ( $T$ ) (Bruun 1995):

$$E_{c,\text{theory}} = A_c + B_c T. \quad (2.4)$$

In practice, cold-wires have a non-zero velocity-dependent time constant ( $\tau_w$ ) such that the theoretical wire voltage is related to the measured wire voltage ( $E_{c,\text{meas}}$ ) in

---

<sup>3</sup> The temporal resolution of HWA and LDA are comparable, with the former on the order of 100 kHz and the latter in the 10 – 100 kHz range. Similarly, the spatial resolution of LDA is on par with that of HWA, with a typical measurement volume of 50  $\mu\text{m}$  by 0.25 mm (Bruun 1995; Jensen 2004).

<sup>4</sup> The velocity field is commonly sampled at frequencies below 100 Hz, but measurements at frequencies up to 50 kHz are also possible (Jensen 2004).

the following manner:

$$\tau_w \frac{dE_{c,\text{meas}}}{dt} + E_{c,\text{meas}} = E_{c,\text{theory}}, \quad (2.5)$$

where,

$$\tau_w \simeq \frac{\rho_w c_w d^2}{4k\text{Nu}}, \quad (2.6)$$

and  $\rho_w$  and  $c_w$  are, respectively, the density and specific heat of the cold-wire material and Nu is the Nusselt number of the flow over the wire.<sup>5</sup> Accordingly, cold-wires are small ( $\leq 1 \mu\text{m}$  in diameter) to ensure that  $\tau_w$  is also small. The frequency response of a cold-wire is typically in the 5 – 10 kHz range (depending on the wire diameter and flow velocity), and characterized by the cut-off frequency ( $f_c = 1/(2\pi\tau_w)$ ). As a result, compensation techniques may be necessary to accurately measure small-scale statistics, such as the scalar dissipation rate, in certain flows of interest (Lemay and Benaïssa 2001).

In contrast to cold-wire thermometry, LIF / PLIF can be used to measure both instantaneous temperature and chemical species concentration. The latter is of particular interest to the study of multi-scalar mixing (given that at least one of the scalars may represent chemical species concentration), and is done by seeding a flow with a fluorescent tracer, which emits photons when excited by a laser. When the tracer concentration is low, the intensity of the fluorescence emitted by the excited

---

<sup>5</sup> It should be emphasized that this results from the fact that cold-wires are operated in constant-current mode. This is in contrast to hot-wires, which are typically operated in constant-temperature mode, where the thermal inertia of the wire is automatically re-adjusted when flow conditions vary and the unsteady term appearing in equation (2.5) can be neglected.

tracer molecules is a linear function of species concentration. Like LDA and PIV, LIF techniques have the advantage of being non-intrusive. Furthermore they can be used to make both point and planar measurements, and unlike cold-wires, which are fragile and not recommended for use in liquids, LIF can be used in both gases and liquids. However, improving the spatial resolution of this technique comes at the expense of the signal-to-noise ratio (Wang and Fiedler 2000). Additionally, the accuracy and quality of LIF measurements can be affected by a variety of factors, including (i) photobleaching, which is the reduction of fluorescence intensity with time, (ii) thermal blooming, which occurs when the laser beam used to excite the dye heats the fluid, changing its density and causing the beam to diverge, (iii) attenuation, which occurs when the laser beam must cross non-negligible amounts of dyed fluid (and have its intensity reduced) before reaching the measurement section, and finally, (iv) drift, if using photomultiplier tubes (Lavertu 2006).

In addition to LIF, chemical species concentration can be measured by other laser scattering techniques, such as Raman scattering and Rayleigh scattering (Tropea *et al.* 2007), as well as by thermal-anemometry-based aspirating probes (Bruun 1995). These probes consist of a hot-wire or hot-film (which are typically used to measure velocity) placed in a sample tube, and upstream or downstream of a nozzle. During operation, a vacuum is applied to the tube, such that a choked-nozzle condition is achieved. The hot-wire (or hot-film) directly measures the sonic speed in the nozzle, which is itself a function of gas mixture concentration. Aspirating probes have successfully been used to measure gas concentration in a large number of studies, including, but not limited to, those of Ng and Epstein (1983), Ahmed and So (1986), White (1987), Ninnemann and Ng (1992), Favre-Marinet and Schettini (2001), and Guibert and Dicocco (2002).

### 2.1.3 Velocity-Scalar Measurements

The experimental techniques of §2.1.1 can be combined with those of §2.1.2 to simultaneously measure the velocity and scalar of interest. For example, hot-wires can be placed side-by-side with cold-wires to simultaneously measure velocity and temperature (Bruun 1995); LDA can be combined with aspirating probes (So *et al.* 1990; Zhu *et al.* 1988) and LIF (Lemoine *et al.* 1996); and PIV, DPIV (digital particle image velocimetry), or DPTV (digital particle tracking velocimetry) can be combined with LIF and other laser-based techniques (Frank *et al.* 1996; Law and Wang 2000; Webster *et al.* 2001; Hu *et al.* 2004).

In addition to the above examples, simultaneous velocity and concentration measurements have also been developed using only thermal-anemometry-based techniques. In equations (2.1) - (2.3), the output voltage of a hot-wire anemometer is shown to be a function of the gas composition of the fluid. Special thermal-anemometry-based probes, in which two hot-wires are operated at different overheat ratios, or one sensing element (either a hot-wire or hot-film) is placed in the thermal field of another, have been successfully used to simultaneously measure velocity and gas concentration in turbulent flows (Way and Libby 1970; Way and Libby 1971; McQuaid and Wright 1973, 1974; Stanford and Libby 1974; Aihara *et al.* 1974; Siritvat and Warhaft 1982; Panchapakesan and Lumley 1993b; Riva *et al.* 1994; Harion *et al.* 1996; Sakai *et al.* 2001; Jonáš *et al.* 2003). The latter are known as interference or “Way-Libby” probes, and are discussed in more detail in §4.2. The advantage of using interference probes (or other thermal-anemometry-based techniques) for simultaneous velocity-scalar measurements, is that only a single measurement technique is needed (whereas the techniques discussed at the beginning of this subsection all combine different measurement techniques). Moreover, the advantages of thermal

anemometry are also retained. For example, Sirivat (1983) showed that the interference probes used in their work had excellent temporal<sup>6</sup> and spatial resolution, which was comparable to that of a single-normal hot-wire probe.

#### 2.1.4 Multi-Scalar Measurements

In most prior studies of multi-scalar mixing (which, by definition, involve two or more scalars), the scalars were not measured simultaneously, but with a technique developed by Warhaft (1981), known as the inference method. (Warhaft 1981; Sirivat and Warhaft 1982; Warhaft 1984; Tong and Warhaft 1995; Grandmaison *et al.* 1996; Costa-Patry and Mydlarski 2008). Warhaft (1981) proposed that the covariance between two thermal (or otherwise identical scalar) sources ( $\langle \phi'_\alpha \phi'_\beta \rangle$ , where  $\phi'_\alpha$  and  $\phi'_\beta$  are the fluctuations of two scalar fields of the same type) could be inferred from measurements of the scalar variance of both scalar sources operating simultaneously ( $\langle (\phi'_\alpha + \phi'_\beta)^2 \rangle$ ), along with those of each scalar source operating alone ( $\langle \phi_\alpha^2 \rangle$ ,  $\langle \phi_\beta^2 \rangle$ ), as follows:

$$\langle \phi'_\alpha \phi'_\beta \rangle = \frac{1}{2} \left[ \langle (\phi'_\alpha + \phi'_\beta)^2 \rangle - \langle \phi_\beta'^2 \rangle - \langle \phi_\alpha'^2 \rangle \right]. \quad (2.7)$$

Although the inference method permits measurements of the scalar covariance (or when normalized the correlation coefficient), as well as cospectra and coherency spectra, other statistics, such as joint probability density functions (JPDFs), necessitate simultaneous measurement of both scalars. Accordingly, this measurement technique cannot be used to fully describe the mixing of multiple scalars in turbulent flows.

---

<sup>6</sup> This follows from the fact that the interference probe designed by Sirivat (1983) consisted of two hot-wires operated in constant-temperature mode, both of which therefore had a very high frequency response.

The first simultaneous turbulent multi-scalar measurements appear to have been obtained by Sirivat and Warhaft (1982), who developed a 3-wire thermal-anemometry-based probe capable of concurrently measuring velocity, helium concentration, and temperature in turbulent flows. Subsequent simultaneous multi-scalar measurements were performed using laser techniques, including two-channel LIF (Saylor and Sreenivasan 1998; Lavertu *et al.* 2008; Soltys and Crimaldi 2011, 2015; Shoaie and Crimaldi 2017) and a combination of PLIF and planar laser Rayleigh scattering (Cai *et al.* 2011; Li *et al.* 2017). Thus, it should be emphasized that while there are many well established techniques to measure the mixing of a single scalar, and a considerable amount of research demonstrating various ways in which the velocity and scalar fields can be measured simultaneously, there has been far less work on the subject of multi-scalar mixing measurement techniques.

Moreover, to the author’s knowledge, the only prior experimental technique capable of simultaneously measuring multiple scalars *and* velocity in turbulent flows is the 3-wire probe developed by Sirivat and Warhaft (1982). This probe consists of an interference probe to measure velocity and helium concentration and a hot-wire operated at a low overheat ratio ( $OH = 1.05$ ) to measure temperature. The 3-wire probe designed by Sirivat and Warhaft (1982) is somewhat limited in its use. To effectively measure the three quantities of interest (velocity, helium concentration, temperature), the interference probe is assumed to be insensitive to the surrounding temperature of the flow. Although this assumption is valid in the experiments of Sirivat and Warhaft (1982), since temperature fluctuations in their flow were very small ( $t_{rms} < 0.1^\circ\text{C}$ ), it is unlikely to hold in most non-isothermal flows. Consequently, novel techniques are needed to make simultaneous two-scalar and velocity

measurements in such flows. As stated in Chapter 1, this will therefore be the first objective of the present work.

## 2.2 Scalar Mixing

Turbulent scalar mixing, once considered to merely be a “footnote to the turbulence problem” (Warhaft 2000), has instead become its own, vast field of study, as previous research has demonstrated significantly different characteristics for the velocity and scalar fields. Most studies of scalar mixing have focused on the mixing of a single passive scalar, and excellent reviews of this subject already exist, including those of Sreenivasan (1991), Shraiman and Siggia (2000), Warhaft (2000), and Dimotakis (2005). Nevertheless, a brief summary of the available literature, as well as a few pertinent references, is presented in §2.2.1 The subject of multi-scalar mixing is then discussed in detail in §2.2.2 - §2.2.3.

### 2.2.1 Mixing of a Single Passive Scalar

The simplest case of mixing is the mixing of a single passive scalar, which, by definition has no effect on the material properties of the fluid (density, viscosity, etc...), and consequently no effect on the flow (Pope 2000). This subject has been studied in a wide variety of flows, including homogeneous isotropic turbulence (Taylor 1935; Uberoi and Corrsin 1953; Townsend 1954; Warhaft and Lumley 1978; Sreenivasan *et al.* 1980; Warhaft 1984; Stapountzis *et al.* 1986; Mydlarski and Warhaft 1998), homogeneous (but not isotropic) flows (Chung and Kyong 1989; Karnik and Tavoularis 1989; Stapountzis and Britter 1989), and inhomogeneous flows. The later can be further subdivided into studies of free-shear flows (Dowling and Dimotakis 1990; Veeravalli and Warhaft 1990; Grandmaison *et al.* 1991; Tong and Warhaft 1995; Darisse *et al.* 2015), as well as wall-bounded shear flows (Shlien and Corrsin 1976; Fackrell and Robins 1982; Paranthoen *et al.* 1988; Lavertu and Mydlarski 2005;

Lepore and Mydlarski 2011).<sup>7</sup> Although the previously mentioned studies are mainly experimental in nature, a significant amount of research on scalar mixing has also been performed using numerical approaches. Direct numerical simulation (DNS) has emerged as one the principal research tools for turbulent flows, and has, for example, been employed to study the evolution of the scalar’s PDF (Eswaran and Pope 1988), the small-scale structure of a passive scalar field (Kerr 1985), and mixing in the presence of a mean scalar gradient (Pumir 1994).

In both experimental and numerical studies, the manner in which a scalar evolves downstream of the source from which it is released, the basic statistics that characterize this evolution (mean and rms quantities, skewnesses, kurtoses, PDFs, etc.), and the effects of initial or boundary conditions on the scalar field, have all been of particular interest. This will be further expanded upon in §2.3.2 - §2.3.4 for jets specifically. Numerous studies have also focused on assessing the accuracy of the various turbulence models that have been proposed over the years and/or developing new ones. Common modeling techniques include Reynolds-average-Navier-Stokes (RANS), Large Eddy Simulation (LES), and PDF methods (Pope 2000). The latter, which are described in greater detail by Pope (1985, 1991, 1994a), Pope and Chen (1990), and Haworth (2010), involve solving a model transport equation for the PDF (or JPDF) of the quantity (or quantities) of interest. In the context of scalar mixing, this may involve the one-point, one-time Eulerian PDF of a scalar ( $f_\phi$ ), the one-point, one-time Eulerian JPDF of two scalars ( $f_{\phi_\alpha\phi_\beta}$ ), or the one-point, one-time Eulerian JPDF of the velocity and scalar ( $f_{U_j\phi}$ ), each of which are respectively governed by

---

<sup>7</sup> Note that the list of sources cited is not by any means exhaustive, and merely provides examples of scalar mixing studies involving a single passive scalar.

the following equations:

$$\begin{aligned} \frac{\partial f_\phi}{\partial t} + \frac{\partial}{\partial x_j} [f_\phi (\langle U_j \rangle + \langle u_j | \hat{\phi} \rangle)] &= - \frac{\partial}{\partial \hat{\phi}} \left( f_\phi [\langle \gamma \nabla^2 \phi | \hat{\phi} \rangle + S_\phi(\hat{\phi})] \right) \\ &= \gamma \nabla^2 f_\phi - \frac{1}{2} \frac{\partial^2}{\partial \hat{\phi}^2} \left( f_\phi \left\langle \gamma \frac{\partial \phi}{\partial x_j} \frac{\partial \phi}{\partial x_j} \middle| \hat{\phi} \right\rangle \right) - \frac{\partial}{\partial \hat{\phi}} [f_\phi S_\phi(\hat{\phi})], \end{aligned} \quad (2.8)$$

$$\begin{aligned} \frac{\partial f_{\phi_\alpha \phi_\beta}}{\partial t} + \frac{\partial}{\partial x_j} [f_{\phi_\alpha \phi_\beta} (\langle U_j \rangle + \langle u_j | \hat{\phi}_\alpha, \hat{\phi}_\beta \rangle)] &= \\ - \frac{\partial}{\partial \hat{\phi}_\alpha} \left( f_{\phi_\alpha \phi_\beta} [\langle \gamma_\alpha \nabla^2 \phi_\alpha | \hat{\phi}_\alpha, \hat{\phi}_\beta \rangle + S_{\phi_\alpha}(\hat{\phi}_\alpha, \hat{\phi}_\beta)] \right) & \\ - \frac{\partial}{\partial \hat{\phi}_\beta} \left( f_{\phi_\alpha \phi_\beta} [\langle \gamma_\beta \nabla^2 \phi_\beta | \hat{\phi}_\alpha, \hat{\phi}_\beta \rangle + S_{\phi_\beta}(\hat{\phi}_\alpha, \hat{\phi}_\beta)] \right), & \end{aligned} \quad (2.9)$$

$$\begin{aligned} \frac{\partial f_{U_j \phi}}{\partial t} + \hat{U}_j \frac{\partial f_{U_j \phi}}{\partial x_j} - \frac{1}{\rho} \frac{\partial \langle P \rangle}{\partial x_j} \frac{\partial f_{U_j \phi}}{\partial V_j} + \frac{\partial}{\partial \hat{\phi}} [f_{U_j \phi} S_\phi(\hat{\phi})] &= \\ - \frac{\partial}{\partial \hat{U}_j} \left( f_{U_j \phi} \left\langle \nu \nabla^2 U_j - \frac{1}{\rho} \frac{\partial p}{\partial x_j} \middle| \hat{U}_j, \hat{\phi} \right\rangle \right) - \frac{\partial}{\partial \hat{\phi}} [\langle \gamma \nabla^2 \phi | \hat{U}_j, \hat{\phi} \rangle], & \end{aligned} \quad (2.10)$$

where  $\hat{U}_j$  and  $\hat{\phi}$  are the sample-space variables (Pope 1985, 2000). Since nonlinear chemical reactions ( $S_\phi$ ) appear in closed form in the equations above, PDF methods are frequently used for dealing with turbulent reactive flows, and consequently, have been studied in detail.<sup>8</sup> To account for the effects of molecular diffusion ( $\langle \gamma \nabla^2 \phi | \hat{\phi} \rangle$ ,  $\langle \gamma_\alpha \nabla^2 \phi_\alpha | \hat{\phi}_\alpha, \hat{\phi}_\beta \rangle$ ,  $\langle \gamma_\beta \nabla^2 \phi_\beta | \hat{\phi}_\alpha, \hat{\phi}_\beta \rangle$ ,  $\langle \gamma \nabla^2 \phi | \hat{U}_j, \hat{\phi} \rangle$ ), which are not in closed form, these

---

<sup>8</sup> Note that while reactive flows are not the focus of the current work/subsection, a large number of studies involving the mixing of passive scalars are motivated by the need to validate and/or develop models for these flows. Moreover, in flows with passive scalars, PDF methods may be of interest where exceedance probabilities are desired (e.g. when studying environmental pollution dispersion).

methods must be used with mixing models,<sup>9</sup> common examples of which include the Interaction by Exchange with the Mean (IEM) (Villermaux and Devillon 1972; Dopazo and O’Brien 1974), Modified Curl (MC) (Curl 1963; Janicka *et al.* 1979), Euclidean Minimum Spanning Tree (EMST) (Subramaniam and Pope 1998), and Interaction by Exchange with the Conditional Mean (IECM) (Pope 1994b, 1998) models.

Given the discussion above, it is reasonable to conclude that many studies of scalar mixing have been motivated by a desire to describe or accurately predict the behavior of the scalar in a specific flow of interest. However, it goes without saying that many others have been motivated by the need to achieve an improved theoretical and universal understanding of this subject. Traditionally, scalar mixing theory is based on the Kolmogorov cascade phenomenology, which predicts that the scalar field will be isotropic at small scales for high Reynolds (Re) and Péclet (Pe) numbers (Kolmogorov 1941; Oboukhov 1949; Corrsin 1951). However, many experimental studies have identified either limitations or departures from Kolmogorov-Oboukhov-Corrsin (KOC) phenomenology for the scalar field (Sreenivasan 1991; Warhaft 2000)). Previous investigations have demonstrated that: (i) the small scales are not locally isotropic, and (ii) this phenomenon is tied to the effects of internal intermittency, which is characterized by strong fluctuations and non-Gaussian statistics for small quantities like the dissipation of turbulent kinetic energy ( $\epsilon$ ) and scalar variance ( $\epsilon_\phi$ ). Although both the velocity and scalar field exhibit internal intermittency, it is more pronounced for the scalar field than the velocity field, and present even when the

---

<sup>9</sup> These models are also referred to as molecular mixing models, or micromixing models.

velocity field is Gaussian (Warhaft 2000). Accordingly, it has been suggested that the complexity of scalar mixing is not inherited from the velocity field (Shraiman and Siggia 2000), and that the two fields have different characteristics.

### 2.2.2 Two-Scalar Mixing Experiments

As was discussed in the previous section, the mixing of even a single passive scalar is complex, and distinct from the more extensively studied velocity field. Extension to multi-scalar mixing adds other levels of complexity, as the initial arrangement of the scalars and their respective diffusivities play an important role in the mixing process. Given the limited capabilities to simultaneously measure two scalars, the earliest multi-scalar mixing studies made use of the inference method described in §2.1.4, and, as a result, investigated the behavior of one type of scalar (typically temperature) introduced at two different locations in turbulent flows. (This is essentially the simplest case of multi-scalar mixing, given that the diffusivities of the two scalars are equal.) A major focus of these studies was characterizing the evolution of the scalar cross-correlation coefficient ( $\rho_{\phi_\alpha\phi_\beta}$ ):

$$\rho_{\phi_\alpha\phi_\beta} = \frac{\langle \phi'_\alpha \phi'_\beta \rangle}{\langle \phi'^2_\alpha \rangle^{1/2} \langle \phi'^2_\beta \rangle^{1/2}}, \quad (2.11)$$

which is a non-dimensionalized form of the scalar covariance often used to quantify the mixing between two scalars (or scalar sources). The correlation coefficient is bounded between  $-1$  and  $1$ , with the former indicating that the scalars are perfectly anti-correlated and the latter indicating that they are fully correlated (and thus, mixed).

Multi-scalar mixing was first studied by Warhaft (1981) in decaying grid turbulence. He showed that the cross-correlation coefficient (and the covariance) from two longitudinally separated arrays of fine heated wires (mandolines) was initially high,

and then decreased downstream. Sirivat and Warhaft (1982) went on to clarify that, for the same flow, there existed certain situations, depending on the relative scalar and velocity length scales, in which the scalar cross-correlation coefficient (but not the covariance) could remain constant, or even increase in the downstream direction. They found that the cross-correlation coefficient decayed more rapidly when the two scalars were injected into the flow at different downstream locations than when they were injected at the same downstream location. These experiments, along with those of Warhaft (1981), demonstrated the importance of initial conditions on the evolution of scalar fields in grid turbulence. A study of the interference of thermal fields from two or more (laterally separated) line sources in grid turbulence by Warhaft (1984) further supported this conclusion — the cross-correlation coefficient was found to be a function of source spacing and distance from the grid, as well as the probe measurement location. The source spacing was shown to have a particularly significant effect on the evolution of the cross-correlation coefficient, since for the range of downstream distances investigated, the cross-correlation coefficient asymptoted towards a value of 1 for small source spacings, but decreased for large source spacing. In the more general case (i.e. for intermediate source spacing), the cross-correlation coefficient initially decreased, before eventually increasing farther downstream.

Tong and Warhaft (1995) and Costa-Patry and Mydlarski (2008) extended the work of Warhaft (1984) to a turbulent jet and turbulent channel, respectively. Both these experiments, as well as those of Warhaft (1984), have helped to establish consistent or “universal” behavior for the mixing of two laterally separated scalar sources: (i) initially the cross-correlation coefficient is undefined, as the measurement probe is rarely exposed to either of the thermal plumes produced by the scalar sources, (ii)

farther downstream, the initially “thin” thermal plumes begin to meander and “flap” due to motions of the largest eddies in the flow, and the measurement probe begins to alternatively sample each plume, but not both at the same time, so that the correlation coefficient becomes increasingly negative, and finally, (iii) the plumes begin to overlap and mix, and the cross-correlation coefficient starts to increase, eventually becoming positive and tending towards an asymptotic value of 1. Additional studies on the evolution of the cross-correlation coefficient between two scalar sources confirm that far downstream the correlation coefficient asymptotes to 1 (Grandmaison *et al.* 1996), and, at a fixed downstream distance, decreases with increasing separation distance between the sources (Sawford *et al.* 1985; Davies *et al.* 2000).

Both Tong and Warhaft (1995) and Costa-Patry and Mydlarski (2008) observed that mixing is enhanced in their respective inhomogeneous flows (a turbulent jet and turbulent channel) compared to the grid turbulence experiments of Warhaft (1984). Tong and Warhaft (1995) found that for comparable separation distances between scalar sources, complete mixing is accomplished much more rapidly in a jet than in grid turbulence (1.5 eddy turnover times vs. 3-4 eddy turnover times), likely due to the presence of mean shear in their flow. On the other hand, Costa-Patry and Mydlarski (2008) attributed the enhanced mixing of their flow to the bounded nature of channel flow. Furthermore, Costa-Patry and Mydlarski (2008) noted that although Warhaft (1984) was able to collapse the evolution of the cross-correlation coefficient as function of two non-dimensionalized parameters, the same non-dimensionalization fails when applied to their results — an indication of the non-negligible effects of inhomogeneity on the mixing process. Thus, while the earliest studies of multi-scalar mixing (Warhaft 1981; Sirivat and Warhaft 1982; Warhaft 1984) demonstrated that the mixing of multiple scalars is highly dependent on initial conditions (a fact which,

as discussed earlier, has been confirmed by many subsequent studies), the work of Tong and Warhaft (1995) and Costa-Patry and Mydlarski (2008) demonstrated that this mixing process is also sensitive to the type of flow in which the scalars are mixed.

Further insight into the multi-scalar mixing process can be obtained by examining statistics other than the scalar cross-correlation coefficient. For example, analysis of the coherency spectra and cospectra of scalar fields emitted from two laterally separated scalar sources indicated that mixing evolved more quickly at large scales than at small ones (Tong and Warhaft 1995; Costa-Patry and Mydlarski 2008). More recent studies, employing experimental techniques that allow for simultaneous measurement of both scalars (see §2.1.4), have focused on (i) the scalar-scalar JPDF, which contains information on all the statistical moments of the scalars, and (ii) unclosed mixing terms in the scalar-scalar JPDF transport equation (equation (2.9)), such as the conditional scalar diffusion ( $\langle \gamma_\alpha \nabla^2 \phi_\alpha | \hat{\phi}_\alpha \hat{\phi}_\beta \rangle$ ,  $\langle \gamma_\beta \nabla^2 \phi_\beta | \hat{\phi}_\alpha, \hat{\phi}_\beta \rangle$ ) and conditional scalar dissipation ( $\langle \gamma_\alpha \frac{\partial \phi_\alpha}{\partial x_j} \frac{\partial \phi_\alpha}{\partial x_j} | \hat{\phi}_\alpha, \hat{\phi}_\beta \rangle$ ,  $\langle \gamma_\beta \frac{\partial \phi_\beta}{\partial x_j} \frac{\partial \phi_\beta}{\partial x_j} | \hat{\phi}_\alpha, \hat{\phi}_\beta \rangle$ ). These studies have so far been limited to turbulent jets — specifically, coaxial (Cai *et al.* 2011; Li *et al.* 2017) and parallel (Soltys and Crimaldi 2015; Shoaie and Crimaldi 2017) jets in a coflow. Cai *et al.* (2011) demonstrated that the conditional scalar diffusion, which transports the JPDF in scalar space and thus represents components of a diffusion (or transport) velocity, quickly converged to a manifold (mixing path), along which it continued at a slower rate. Since two of the scalars in their experiments were initially separated (the center jet and coflow were separated by the annular jet<sup>10</sup>), the mixing path had to make a detour in scalar space. As discussed

---

<sup>10</sup> Note that in the experiments of Cai *et al.* (2011), the center jet consisted of acetone-doped air, the annular jet consisted of pure ethylene, and the outer coflow was composed of pure air, such that the flow could be described as containing three

by Cai *et al.* (2011), this presents difficulties for standard mixing models, like the IEM model, which depend on scalar-space variables, but do not take into account the physical-space structure. Accordingly, as was mentioned in §1.1, there is a need to ensure that our current mixing models are suitable for extension to multi-scalar mixing. This is especially important given that this detour in the mixing path was also observed by Soltys and Crimaldi (2015), who studied mixing between two jets in a coflow, and Li *et al.* (2017), who extended the work of Cai *et al.* (2011) to different velocity and length-scale ratios.

In their work on turbulent coaxial jets, Li *et al.* (2017) also found that increasing the velocity ratio of the jets lead (i) to increased turbulent transport, so that the scalar evolution was initially faster, and (ii) decreased small-scale mixing, so that the scalar evolution was delayed far downstream. Increasing the width of the annular jet increased the effects of the velocity ratio, and also delayed the progression of mixing. These experiments provided some evidence of the limitations of the scalar cross-correlation coefficient in describing the state of mixing of a flow, as Li *et al.* (2017) showed that where the correlation coefficients for the different cases studied were nearly equal, the JPDFs still exhibited clear qualitative differences. Soltys and Crimaldi (2015) also noted that merely focusing on the correlation coefficient “lends no insight into the direct role of instantaneous flow processes on the development of the scalar covariance.” Using scalar-scalar JPDFs, as well as instantaneous images of the scalar field, they were able to better explain the mixing process in their flow,

---

different scalars. Accordingly, the mixing of two scalars in a separate, ambient fluid may be referred to as three-scalar or ternary mixing. Similarly, the mixing of a single scalar in ambient fluid is often referred to as binary mixing. These two conventions are used arbitrarily throughout the field of scalar mixing.

concluding that the two scalars are initially distributed into separate filaments, before being brought together in attracting regions, where they coalesce as a result of diffusive flux. It is therefore reasonable to suggest that a complete study of multi-scalar mixing necessitates more than just correlation coefficients, and will require simultaneous multi-scalar measurements.

### 2.2.3 Two-Scalar Mixing Simulations

In addition to the aforementioned experimental works, many two-scalar mixing studies have been computational in nature. Juneja and Pope (1996) used DNS to study the mixing of two passive scalars in homogenous, isotropic turbulence, where the scalar fields were initially arranged in a “triple delta function” JPDF, with “blobs” of fluid in three distinct states. They found that mixing mainly took place between adjacent pairs of “blobs,” and that changing the diffusivity or length scale of one scalar with respect to another, resulted in faster mixing towards the scalar with the higher diffusivity or smaller length scale. Later, Vrieling and Nieuwstadt (2003) confirmed Warhaft’s (1984) results by using DNS to study the mixing of two scalar sources located in the homogeneous region of a channel, and concluded that the variance resulting from separate scalar sources could not be obtained from the sum of the variances of the individual scalar sources (since the covariance of the scalars was not necessarily zero). More recently, DNS from Oskouie *et al.* (2015, 2017) of near-ground and elevated point sources in an open channel was used to identify four stages of mixing similar to those described in §2.2.2: a zero interference stage, a negative interference stage, a positive interference stage, and a complete mixing state. Additionally, in Oskouie *et al.* (2015), cospectra and coherency spectra were used to lend greater insight into the physical processes occurring in each stage of mixing. In contrast to Tong and Warhaft (1995) and Costa-Patry and Mydlarski (2008), who

observed that mixing occurred fastest at large scales, Oskouie *et al.* (2015) found that mixing occurred fastest at smaller scales (approximately  $2\eta - 10\eta$ ). This was attributed to the fact that plume meandering, which initially takes place at large scales, was dominant in the studies of Tong and Warhaft (1995) and Costa-Patry and Mydlarski (2008), but negligible in the work of Oskouie *et al.* (2015). Instead, they suggested that internal turbulent mixing, which occurs at smaller scales, was more important. As may be inferred from the discussion above, these computational studies (i.e the works of Juneja and Pope 1996; Vrieling and Nieuwstadt 2003; Oskouie *et al.* 2015, 2017) all help confirm some of the findings discussed in the previous subsection — which is that the mixing of multiple scalars depends on their initial conditions and the type of flow in which they mix.

A reasonably large number of other computational works on two-scalar mixing have taken a different approach, and focused on identifying or developing mixing models for these complex mixing processes. This includes the work of Sawford (2006), Sawford and de Bruyn Kops (2008) and Meyer and Deb (2012) in three-stream mixing layers, Viswanathan and Pope (2008) in grid turbulence, and Rowinski and Pope (2013) in coaxial jets. Sawford (2006) found that the DNS results of Cha *et al.* (2006) in a double mixing layer<sup>11</sup> could be modeled using a Lagrangian stochastic model coupled to the IECM mixing model. Sawford and de Bruyn Kops (2008) extended this work to a more general three-stream mixing layer, and showed good agreement between the aforementioned model and DNS results in the near field, but observed some significant differences in statistics in the far field. Thus, although this

---

<sup>11</sup> The double mixing layers is arguably the simplest case of three stream mixing. The middle of three mixing layers, each of which carries an arbitrary concentration of two or more scalars, is a mixture of the outer two.

mixing model worked well for the simple double mixing layer, it failed to fully capture the behavior of the more complex three-stream mixing layer. Interestingly however, a modified IECM mixing model agreed well with the experimental results of Warhaft (1984) obtained in homogeneous, isotropic turbulence. Following these experiments, Meyer and Deb (2012) reproduced the results of Sawford and de Bruyn Kops (2008), and highlighted the importance of velocity conditioning in predicting concentration JPDFs. They found that the generalized mixing model of Meyer (2010) was more accurate, with similar computational expense, compared to the IECM mixing model employed by Sawford and de Bruyn Kops (2008). Finally, in a somewhat more comprehensive study of the application of different mixing models to multi-scalar mixing, Rowinski and Pope (2013) investigated the accuracy of the IEM, MC, and EMST models using RANS-PDF calculations, and showed that none of the mixing models accurately estimated the JPDFs of the two scalars. However, they did find that JPDFs calculated from LES-PDF calculations agreed well with the experimental data of Cai *et al.* (2011), especially when using the attenuation of variance production model developed in their work. Accordingly, although certain specific models may adequately account for the mixing of multiple scalars (like those developed by Meyer and Deb (2012) or Rowinski and Pope (2013)), for the most part, common mixing models (e.g. the IEM, MC, EMST or IECM models) do not.

### 2.3 Jets

In the previous section, an overview of scalar mixing and multi-scalar mixing in a wide variety of flows was provided. As the subject of the present thesis is on multi-scalar mixing in turbulent coaxial jets, the behavior of the velocity and scalar fields of turbulent jets is examined in greater detail in the current section. Specific attention is given to the dynamics of (i) the velocity field of a single round jet, (ii) the

scalar field of a single round jet, (iii) jets with variable fluid properties, and finally, (iv) the velocity and scalar fields of coaxial round jets.

### 2.3.1 Velocity Field of a Single Round Jet

The turbulent jet is one of the most commonly studied free-shear flows. It is generated from a continuous source of momentum (as opposed to a plume, which is generated from a continuous source of buoyancy); (Lee and Chu 2003), and as its name implies, is “free” of any wall or boundary. A thorough description of the dynamics of jets can be found in Tennekes and Lumley (1972), Pope (2000), and Lee and Chu (2003). Herein, a brief discussion of the characteristics of the velocity field is provided. Moreover, it should be noted that this discussion, and subsequent discussions presented in §2.3.2 - §2.3.4 are limited to axisymmetric (round) jets.

A statistically stationary and axisymmetric jet is two-dimensional and depends only on the axial and radial coordinates. The mean flow is predominately in the axial direction and spreads gradually. As a result, radial gradients are much larger than axial gradients, and boundary-layer equations can be used in place of the full RANS equations (Pope 2000). When issuing into quiescent flow, the jet eventually reaches an asymptotic, self-similar state in the far-field. In this region ( $x/D \gtrsim 30$ , Pope 2000), the (normalized) shape of the velocity profiles do not change, although the jet continues to decay and spread. Non-dimensionalized radial profiles of the mean axial velocity ( $\langle U \rangle$ ) evaluated at different downstream distances have been found to all collapse onto each other (Wyganski and Fiedler 1969; Panchapakesan and Lumley 1993a; Hussein *et al.* 1994; Ferdman *et al.* 2000; Khorsandi *et al.* 2013). Similarly, so do radial profiles of appropriately non-dimensionalized higher order statistics including  $u_{rms}$ ,  $v_{rms}$ , and  $\langle uv \rangle$  (Wyganski and Fiedler 1969; Panchapakesan and Lumley 1993a; Hussein *et al.* 1994; Ferdman *et al.* 2000; Khorsandi *et al.*

2013), although these reach a self-similar state farther downstream than the mean quantities (Ferdman *et al.* 2000; Xu and Antonia 2002). Furthermore, the centerline turbulence intensity asymptotes to a constant value of approximately 0.25 (Panchapakesan and Lumley 1993a), and although this value varies slightly from experiment to experiment, it does not appear to be significantly affected by the Reynolds number ( $Re_D \equiv U_J D / \nu$ ); (Pope 2000).

The self-similar nature of turbulent jets predicts (either through dimensional analysis or manipulation of the continuity and momentum equations) that the mean centerline axial velocity ( $\langle U_0 \rangle$ ) scales inversely with the downstream distance ( $x$ ) such that:

$$\frac{\langle U_0 \rangle}{U_J} = \frac{B_u}{x - x_0}, \quad (2.12)$$

where  $x_0$  is a virtual origin and  $B_u$  is an empirical scaling constant (Pope 2000). Moreover, the jet's half-width ( $r_{1/2}$ ) scales with the downstream distance ( $x$ ) such that:

$$r_{1/2} = S_u(x - x_0), \quad (2.13)$$

where  $S_u$  is the jet's spreading rate (Pope 2000). Given the above equations, the mass flow rate of the mean flow also scales with  $x$ , while the local Reynolds number ( $Re_0 = r_{1/2} \langle U_0 \rangle / \nu$ ) and the momentum flow rate of the mean flow are independent of  $x$ . Both equations (2.12) and (2.13) have been verified experimentally in numerous studies (Wyganski and Fiedler 1969; Panchapakesan and Lumley 1993a; Hussein *et al.* 1994; Ferdman *et al.* 2000; Khorsandi *et al.* 2013; Xu and Antonia 2002; Darisse *et al.* 2013); and it is generally accepted that  $B_u \approx 6$  and  $S_u \approx 0.1$  in a round jet.

It has been a long-held belief that the flow in the self-similar region of the jet exhibits universal behavior that is independent of initial conditions (Townsend 1980). However, more recent studies, including those of Boersma *et al.* (1998) and Xu and Antonia (2002), have shown otherwise. Xu and Antonia (2002) found differences in the self-similar regions of (i) smooth contraction nozzle jets (with a “top-hat” velocity profile at the exit), and (ii) fully-developed pipe jets, resulting in faster decay (i.e. lower  $B_u$ ) and a larger spreading rate (i.e. higher  $S_u$ ) for the contraction nozzle jet. Moreover, they also found that the contraction nozzle jet developed more quickly, and approached self-similarity before the pipe jet. These results were consistent with the earlier DNS studies of Boersma *et al.* (1998). Additionally, Hussein *et al.* (1994) has suggested that differences between experiments may arise from differences in Reynolds number, and both George and Arndt (1989) and George (2012) have proposed analytical arguments supporting the idea that the similarity solutions of turbulent jets depend on initial conditions, and are therefore not universal.

### 2.3.2 Scalar Field of a Single Round Jet

The scalar field of turbulent jets bears many similarities to the velocity field. When discussing scalar mixing in jets, it should be emphasized that there is a distinction between turbulent jets, which are generated by a continuous source of momentum, and buoyant plumes, which are generated by a continuous source of buoyancy, as will subsequently be discussed in §2.3.3. The current discussion is primarily limited to the transport of scalars in turbulent jets. Although the scalars in the studies discussed herein are not always exactly passive by definition, density differences remain small enough that the effects of buoyancy can be neglected. In most cases, these scalars can still be considered to be passive.

Like the velocity field, the scalar field also tends towards self-similarity in the far-field of the jet. Previous experimental studies have shown that (i) the mean scalar ( $\langle\phi\rangle$ ) becomes self-similar beyond a certain distance (approximately  $x/D = 10$ ,  $x/D = 20$ , depending on the study), (ii) the mean centerline scalar ( $\langle\phi_0\rangle$ ) is inversely related to  $x$ , and (iii) the scalar half-width ( $r_{\phi_{1/2}}$ ) is proportional to  $x$  (Wilson and Danckwerts 1964; Lockwood and Moneib 1980; Dowling and Dimotakis 1990; Panchapakesan and Lumley 1993b; Mi *et al.* 2001). The rms statistics and scalar fluxes also become self-similar, although this occurs somewhat farther downstream than the mean statistics (Wilson and Danckwerts 1964; Lockwood and Moneib 1980; Panchapakesan and Lumley 1993b).

In many jets transporting scalars, the density of the jet differs from that of the ambient surroundings (i.e.  $\rho_J \neq \rho_\infty$ ), which has an effect on the self-similar solutions of the jet, even when buoyancy effects are negligible. For example, Pitts (1991a) demonstrated that  $\langle\phi_0\rangle$  decays more quickly as the density ratio ( $S = \rho_J/\rho_\infty$ ) decreases. To account for the effects of density, in addition to other initial conditions (such as the exit velocity profile), the use of an effective diameter ( $D_e$ ), defined below, is suggested in place of the diameter  $D$  (Dowling and Dimotakis 1990; Mi *et al.* 2001):

$$D_e = \frac{2m_J}{\sqrt{\pi\rho_\infty M_J}} \approx \sqrt{\frac{\rho_J}{\rho_\infty}} D, \quad (2.14)$$

where  $m_J$  is the mass flow rate at the exit of the jet and  $M_J$  is the momentum flow rate at the exit of the jet. Accordingly, the decay of the mean centerline scalar ( $\langle\phi_0\rangle$ ) in the self-similar region can be expressed as follows:

$$\frac{\langle\phi_0\rangle}{\phi_J} = K_c \left( \frac{D_e}{x - x_{0_\phi}} \right), \quad (2.15)$$

where  $K_c$  is the centerline decay constant and  $x_{0_\phi}$  is the virtual origin for the scalar measurements. Using the above scaling, universal values of  $K_c$  can be observed for flows of different densities, although there is some scatter in the reported data (Pitts 1991a). A thorough review of previous measurements in the self-similar region of scalar jets by Mi *et al.* (2001) reveals that the value of  $K_c$  may vary between 4.42 and 5.59. Similarly, there is considerable scatter in measurements of  $\phi_{rms,0}/\langle\phi_0\rangle$ , which have been observed to asymptote to values between approximately 0.19 and 0.36 (Mi *et al.* 2001).

Although some of the aforementioned variability may be due to experimental uncertainty, there is nevertheless substantial evidence that the scalar field of jets is still sensitive to initial conditions far downstream (i.e. in what is considered the self-similar region), lending additional credence to the arguments put forth by George and Arndt (1989) and George (2012). For example, Dowling and Dimotakis (1990) observed a  $Re_D$  dependence for the mean scalar centerline decay rate, which Mi *et al.* (2001) later clarified may exist for  $Re_D < Re_{D,cr}$  (where  $Re_{D,cr}$  is some critical Reynolds number) in contraction nozzle jets, but is negligible in fully developed pipe jets. Similarly, Miller and Dimotakis (1991) found that measurements of  $\phi_{rms,0}/\langle\phi_0\rangle$  scaled inversely with  $Re_D$  in liquid flows, asymptotically approaching a value of approximately 0.23 only at the highest Reynolds numbers. Yet no such Reynolds number dependencies were observed in the gas-phase experiments of Dowling and Dimotakis (1990) and Pitts (1991b), an indication of the importance of Schmidt number (Sc) effects on the flow. Moreover, in agreement with the velocity-field measurements of Xu and Antonia (2002), Mi *et al.* (2001) found non-negligible differences in the scalar fields of contraction nozzle jets and fully-developed pipe jets. However,

although Xu and Antonia (2002) primarily observed differences between the spreading and decay rates of the jets (both of which are obtained from measurements of the mean quantities of the flow), Mi *et al.* (2001) discovered additional differences in the asymptotic values of  $\phi_{rms,0}/\langle\phi_0\rangle$ , which support a suggestion made at the beginning of their work — that the scalar field is more sensitive than the velocity field to differences in the underlying turbulence structure, and consequently is more sensitive to the initial conditions of the flow.

### 2.3.3 Jet with Variable Fluid Properties

The effects of variable fluid properties on turbulent jets are discussed in greater detail in the current section. In particular, attention is given to variable density and variable viscosity jets.

#### Variable Density

As previously discussed, in many scalar jets, the density ( $\rho_J$ ) may differ from the density of the ambient surrounding ( $\rho_\infty$ ), resulting in buoyancy effects. The relative importance of inertial to buoyancy forces can be characterized by the densimetric Froude number (F) (Chen and Rodi 1980):

$$F = \frac{U_J}{gD(\rho_\infty - \rho_J)/\rho_J}, \quad (2.16)$$

where  $g$  is the gravitational constant. A pure jet, where  $\rho_J = \rho_\infty$  is characterized by  $F = \infty$ , whereas a pure plume, which has zero initial momentum, is characterized by  $F = 0$ . For variable density jets, for which  $0 < F < \infty$ , three regions of flow can be identified: (i) an initial non-buoyant region in which momentum forces dominate, (ii) an intermediate region, and (iii) finally a buoyant region in which buoyancy forces dominate (see figure 2.1). To delineate these three regions Chen and Rodi (1980)

defined a non-dimensional axial parameter ( $x_1$ ):

$$x_1 = F^{-1/2} \left( \frac{\rho_J}{\rho_\infty} \right)^{-1/4} \frac{x}{D}, \quad (2.17)$$

and determined that the non-buoyant region occurred for  $x_1 < 0.5$ , the intermediate region for  $0.5 < x_1 < 5$ , and the buoyant region for  $x_1 > 5$ . It was suggested by Chen and Rodi (1980) that self-similarity is only possible in the first and last regions, although the experiments of Panchapakesan and Lumley (1993b), which were performed in the intermediate region, suggest otherwise. Different scaling laws have been proposed for the non-buoyant and buoyant regions of the jet. In the former, the dynamics of the jet are similar to those of a pure jet, so  $\langle U_0 \rangle \sim x^{-1}$  and  $\langle \phi_0 \rangle \sim x^{-1}$ , whereas in the latter, the dynamics of the jet are similar to those of a pure plume, so  $\langle U_0 \rangle \sim x^{-1/3}$  and  $\langle \phi_0 \rangle \sim x^{-5/3}$  (Chen and Rodi 1980). The effects of density on these scaling relations can be taken into account through the density ratio ( $S = \rho_J/\rho_\infty$ ), and, in the buoyant region, also  $F$ .

Amielh *et al.* (1996) and Pitts (1991a) respectively studied the velocity and scalar field of variable density jets. In accordance with what was discussed in §2.3.2, Amielh *et al.* (1996) showed that the centerline mean velocity ( $\langle U_0 \rangle$ ) decays more quickly as the density ratio ( $S = \rho_J/\rho_\infty$ ) decreases, and that (in the non-buoyant region at least) the effective diameter ( $D_e$ ) collapses measurements of  $\langle U_0 \rangle$ . Additionally, both Amielh *et al.* (1996) and Pitts (1991a) observed that although the asymptotic values of  $u_{rms,0}/\langle U \rangle$  and  $\phi_{0,rms}/\langle \phi_0 \rangle$  were independent of  $S$ , lighter jets (with smaller  $S$ ) would approach these asymptotic values faster. These results suggest that lighter jets (e.g. a helium jet issuing into ambient air) develop more quickly, and that mixing in these jets is more efficient. Djeridane *et al.* (1996) measured the entrainment in

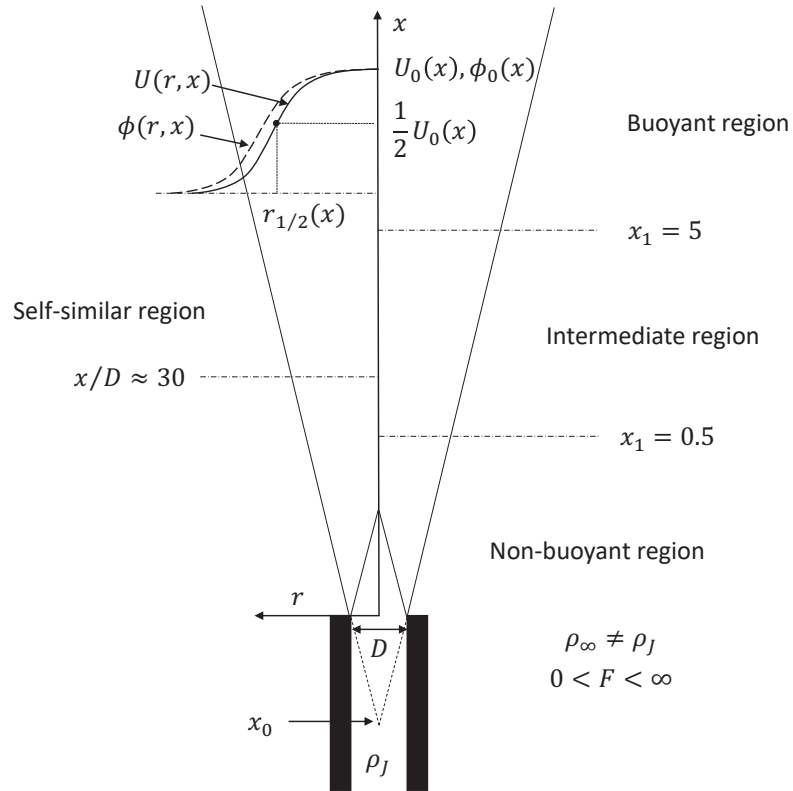


Figure 2.1: Schematic representation of the three regions of flow observed in variable-density jets: (i) the non-buoyant region, (ii) the intermediate region, and (iii) the buoyant region. On the left-hand side, a more generalized depiction of scalar jets (which could also apply to constant-density jets) is provided.

variable density density jets and found it was much higher in lighter jets, confirming this hypothesis.

### Variable Viscosity

Variable viscosity jets, in which a less viscous jet issues into a more viscous coflow, have been observed to develop more quickly than constant viscosity jets; the mean axial velocity decays more quickly, mean energy dissipation is enhanced, and self-similarity is reached earlier (Talbot *et al.* 2013). It was suggested that as the more viscous fluid is entrained into the jet, the presence of viscous “blobs” creates enhanced velocity gradients, and consequently increases the dissipation and production of lateral velocity fluctuations. The influence of variable viscosity on dissipation was derived analytically, such that when two streams of different viscosities and speeds mix, the following expression for variable viscosity dissipation ( $\epsilon_{VV}$ ) was suggested:

$$\epsilon_{VV} \approx \frac{\nu_s}{\nu_f} \left\langle \nu \left( \frac{\partial u_i}{\partial x_j} \right)^2 \right\rangle, \quad (2.18)$$

where  $\nu_s$  is the viscosity of the slow stream (i.e. the coflow) and  $\nu_f$  is the viscosity of the fast stream (i.e. the jet); (Talbot *et al.* 2013). Thus, dissipation is enhanced for a jet mixing in a more viscous (slower) fluid, whereas it is diminished for a jet mixing in a less viscous (slower) fluid.

A subsequent study by Voivenel *et al.* (2016) for a jet of propane issuing into a coflow of nitrogen ( $\nu_s/\nu_f = 3.5$ ,  $S = \rho_s/\rho_f \approx 1$ ) confirmed the findings of Talbot *et al.* (2013), noting that self-similarity of the mean velocity was achieved as early as  $x/D = 4.5$  in a variable viscosity jet. It was argued, however, that this self-similarity is only possible in regions of uniform viscosity, such as the jet axis, and not in regions where viscosity gradients are important, such as the jet boundaries (Danaila *et al.* 2017). These viscosity gradients were shown to profoundly alter the dynamics of

the jet, such that the effects of viscosity are felt at all scales, including the largest (Voivenel *et al.* 2016). It should be emphasized that this is in contradiction to Kolmogorov theory, in which viscosity is a small scale quantity and has no effect on the inertial scales of a turbulent flow.

### 2.3.4 Coaxial Jets

Coaxial jets consist of an (inner) center and (outer) annular jet. In addition to the factors that influence the behavior of single jets – e.g. the Reynolds number and the initial velocity profile — coaxial jets are characterized by the velocity ( $R = U_o/U_i$ ), density ( $S = \rho_o/\rho_i$ ), and area ( $A_o/A_i$ ) ratios of the jets. In coaxial jets of varying density ( $S \neq 1$ ), the effects of density are incorporated into the momentum ratio ( $M$ ) defined below:

$$M = SR^2. \tag{2.19}$$

Previous studies indicate that the behavior of coaxial jets is best characterized by the momentum ratio (as might be expected, given that jets are a momentum-driven flow), which, for constant-density coaxial jets, reduces to the velocity ratio (Schumaker and Driscoll 2012; Favre-Marinet and Schettini 2001; Favre-Marinet *et al.* 1999).

As depicted in figure 2.2, close to the jet exit, coaxial jets exhibit two potential cores — for the inner and outer jet, respectively — separated by an inner mixing region in which the center and annular jets mix with each other, but not the ambient fluid. The potential core of the annular jet is surrounded by an outer mixing region in which the annular jet and ambient fluid mix. Farther downstream, the cores disappear, and the coaxial jets behave as a single jet, and can exhibit self-similarity (Champagne and Wygnanski 1971). In the self-similar region, Champagne

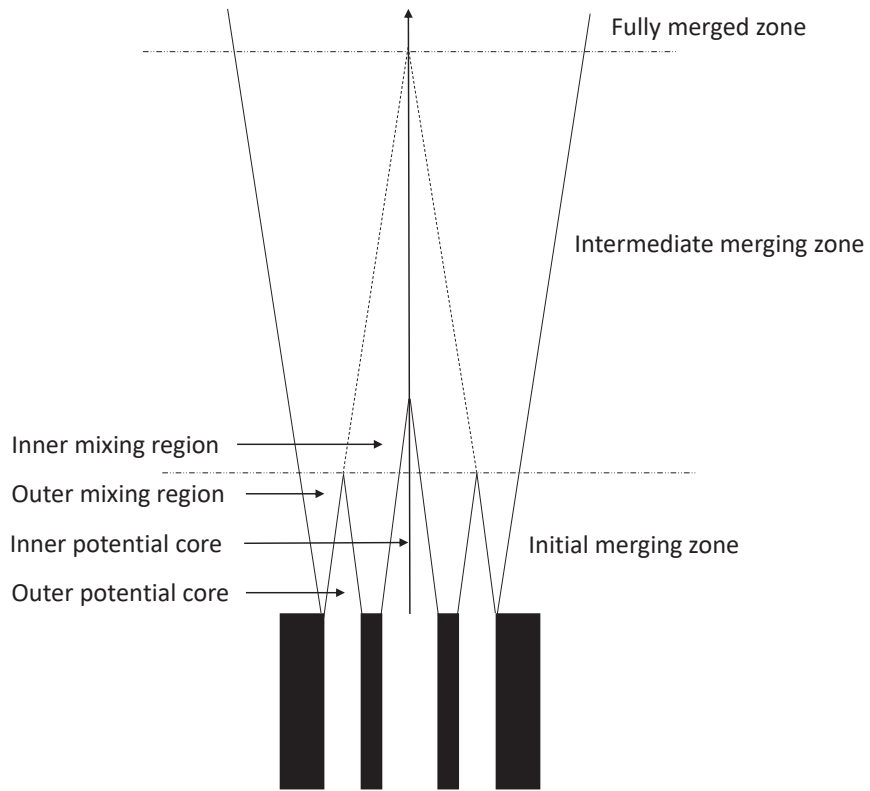


Figure 2.2: Schematic representation of the near-field of coaxial jets based on the descriptions of Champagne and Wagnanski (1971), Ko and Kwan (1976), and Ko and Au (1985).

and Wygnanski (1971) observed that, when properly non-dimensionalized, the centerline velocity decay and half-width of the coaxial jets were independent of initial conditions, such as the velocity and area ratios, and behave similarly to single jets. Thus, the focus of many studies of coaxial jets has been on the mixing that takes place in the developing region of the jet — i.e. before self-similarity is observed.

Champagne and Wygnanski (1971) showed that although the outer core did not appear to be affected by the velocity ratio ( $R = U_0/U_i$ ) (nor  $M$ , since their experiments were performed in constant-density jets), the inner core was significantly affected by  $R$ . For  $0 < R < 1$ , the inner core was slightly longer than the potential core of a single jet, probably due to decreased shear between the center jet and the fluid around it, whereas the length of the inner core decreased as  $R$  increased when  $R > 1$ . Champagne and Wygnanski (1971) suggested that this was because the lower pressure in the center jet causes the annular jet to bend inwards. This effect appeared to be more significant for small area ratios (i.e. a thinner annular jet), as the pressure differential between the jets is increased. A subsequent study by Ko and Au (1981) confirmed the findings of Champagne and Wygnanski (1971) — the outer core did not depend on  $R$  (nor  $M$ ), whereas the inner core decreased from  $4.1D_o$  (where  $D_o$  is the diameter of outer/annular jet) to  $2.1D_o$  as  $R$  increased from 1.25 to 2.50. In studies of the scalar fields of coaxial jets, the length of potential core was again observed to vary inversely with  $R$  for  $R > 1$  (Villermaux and Rehab 2000), or inversely with  $M^{1/2}$  for  $M > 1$ , when density effects were incorporated (Favre-Marinet and Schettini 2001; Schumaker and Driscoll 2012).

Ko and Kwan (1976) studied the dynamics of the developing region of coaxial jets for  $R < 1$ , and suggested that it be split up into the three zones: (i) an initial merging zone, containing the inner and outer cores, and inner and outer mixing regions, as

described by Champagne and Wygnanski (1971), (ii) an intermediate merging zone beyond the end of the outer core, in which the inner core may remain, and the inner and outer mixing regions mix, and (iii) a fully merged region, in which the center (inner) and annular (outer) jets have merged and behave as a single jet. In a related study by Ko and Au (1985) for coaxial jets in which  $R > 1$ , the intermediate merging zone was defined to end where the maximum velocity intercepts the centerline — a location referred to as the reattachment point, since it marks the point where the outer mixing regions reach the centerline and “reattach.” Given that both the length of the outer core and reattachment point were shown to be mostly unaffected by  $R$ , the three zones are nearly independent of the velocity ratio (although note this may only be true for  $R > 1$ , since when  $R < 1$ ,  $\langle U_0 \rangle$  monotonically decreases along the centerline, and the aforementioned definition for the intermediate merging zone cannot be used). Significant parts of the works of Ko and Kwan (1976) and Ko and Au (1985), as well as similar studies by Kwan and Ko (1976) and Au and Ko (1987) were devoted to detailing the behavior of coherent structures generated in coaxial jets, given that, according to Kwan and Ko (1976), mixing, entrainment, and energy transfer processes in jets are related to the interaction and amalgamation of these structures. In each of the previously mentioned studies, differences were observed between vortices originating from the outer mixing region (“outer vortices”) and those originating from the inner mixing region (“inner vortices”). For example, both Ko and Au (1985) and Au and Ko (1987) found that the “outer vortices” were independent of  $R$  and exhibited characteristics similar to those of single jets, whereas the “inner vortices” were dependent on  $R$ , and at high  $R$  exhibited characteristics similar to those of annular jets. Accordingly, the behavior of the flow within coaxial

jets lies somewhere between that of single jets and that of annular jets (Au and Ko 1987).

Both Rehab *et al.* (1997) and Villermaux and Rehab (2000) studied the dynamics of the developing region of coaxial jets in which  $R > 1$  and  $S = 1$ . The near-field of these jets is dominated by the annular (outer) jet and can be divided into two regimes (Rehab *et al.* 1997). In the first regime, which occurs for  $1 < R < R_{cr}$ , where  $R_{cr}$  is a critical velocity ratio, the flow dynamics were similar to those observed by Champagne and Wygnanski (1971), Ko and Au (1981), and Ko and Au (1985). Therein, Rehab *et al.* (1997) showed that the length of the inner potential core varied as  $A_R/R$ , where  $A_R$  is a constant that is weakly dependent on initial conditions. (Note that this is analogous to the argument that the potential core varies as  $A_R/M^{1/2}$ , in accordance with later work performed by Favre-Marinet *et al.* (1999), Favre-Marinet and Schettini (2001), and Schumaker and Driscoll (2012) for variable-density coaxial jets.) Transition to the second regime occurs beyond  $R_{cr}$ , and can be predicted by a simple model based on turbulent entrainment and mass conservation (see also Villermaux and Rehab (2000), for more information on this model). This regime is characterized by an unsteady recirculation bubble, resulting from the balance between the radial Reynolds stress gradient accelerating the flow forward and the axial mean static adverse pressure gradient decelerating the flow. This recirculation region, which Rehab *et al.* (1997) found to begin at  $R \approx 8$  (i.e.  $M \approx 64$ ), was also observed by Favre-Marinet *et al.* (1999), who found that it occurred for  $M > 50$ .

Favre-Marinet *et al.* (1999) succinctly described the dynamics of the near field of coaxial jets with high velocity ratio ( $R > 1$ ), suggesting that an important feature of these jets is the entrainment of the lower-speed center jet into the mixing layer surrounding the inner potential core. This process consists of a “mass transfer”

across the interface separating the inner core and mixing layer, in which the mass flow rate associated with the former ( $m_i(x)$ ) decreases with the distance from the jet exit. The entrainment velocity, which is proportional to  $M^{1/2}$ , and slightly dependent on  $S$  (especially for small  $M$ ), controls this process, and thus the length of the inner potential core. For high  $R$ , a decrease in  $m_i(x)$  causes the centerline velocity ( $\langle U_0 \rangle$ ) to decrease until the end of the potential core. After this point, the inner mixing layers merge and  $\langle U_0 \rangle$  increases. Farther downstream, when the coaxial jets behave as a single jet,  $\langle U_0 \rangle$  once more decreases.

The scalar field of variable density coaxial jets ( $S < 1$ ) with high velocity ratios ( $R > 1$ ) was investigated by Favre-Marinet and Schettini (2001) and Schumaker and Driscoll (2012), the latter being perhaps the most comprehensive and thorough investigation of coaxial jets, given that up to 56 combinations of velocity ratios, density ratios, and Reynolds numbers were examined. Schumaker and Driscoll (2012) concluded that the entrainment model developed by Rehab *et al.* (1997) and Villermaux and Rehab (2000) best describes the behavior of coaxial jets. Moreover, as previously discussed, both Favre-Marinet and Schettini (2001) and Schumaker and Driscoll (2012) found that, in general, the effects of the density ratio were accounted for by considering the momentum ratio, meaning that coaxial jets with the same momentum ratio behave similarly even if their density ratios vary. However, it should be noted that some secondary density effects were observed by Favre-Marinet and Schettini (2001) when the momentum ratio was small ( $M < 4$ ) and/or when the density ratio was very small ( $S = 0.028$ ). Under the former conditions, the length of the potential core decreased (departing from its expected value) as  $S$  decreased, whereas under the latter conditions, the length of the potential core increased (also departing from its expected value). Thus, although decreasing  $S$  appeared to initially enhance

entrainment and increase mixing, this effect was reversed for very small  $S$ . Significant deviations in the behavior for coaxial jets with very small  $S$  were also observed by Favre-Marinet *et al.* (1999), who showed that recirculation did not occur until at least  $M = 100$  for  $S = 0.028$  — a value of  $M$  twice that observed for coaxial jets with larger  $S$ .

Finally, as discussed in §2.2.2, coaxial jets have also been used to study multi-scalar mixing (Grandmaison *et al.* 1996; Cai *et al.* 2011; Li *et al.* 2017). These studies confirm some of the findings presented in the current section — the mixing of multiple scalars was shown to dependent on  $R$  (as well as  $M$ , given that  $S = 1$  in the aforementioned studies) and, far downstream, resembled that of single jets. However, some contradictions can be observed between the work of Li *et al.* (2017), in which  $R < 1$ , and that of Grandmaison *et al.* (1996), in which  $R > 1$ . The former found that the scalar correlation coefficient increased more slowly along the centerline as  $R$  increased, whereas the latter showed that the initially the opposite was true — the correlation coefficient increased more quickly with increasing  $R$ . Consequently, the effects of  $R$  (or  $M$ ) on multi-scalar mixing are not exactly clear, and merit additional investigation. Furthermore, as may be apparent from the above discussion, it is worth pointing out that there have been relatively few studies of coaxial jets (focusing on the turbulent properties of the flow) involving (i) scalar mixing, (ii) variable density jets, (iii) simultaneous velocity-scalar measurements, and (iv) multi-scalar mixing. In particular, there do not appear to be studies of coaxial jets in which  $S > 1$  (as is the case in the current work), or in which mixed velocity-scalar statistics were measured. Thus, it is expected that the present work, which focuses on simultaneous two-scalar and velocity measurements in turbulent

coaxial jets where  $0.77 < M < 4.2$ ,  $0.75 < R < 1.75$ , and  $S = 1.37$ , should not only enhance our understanding of multi-scalar mixing, but also that of coaxial jets.

## **CHAPTER 3**

### **Experimental Apparatus**

The present chapter describes the experimental apparatus used in this thesis. A description of the (i) calibration apparatus, in which the thermal-anemometry-based probes used herein were calibrated, (ii) coaxial jet apparatus, in which experiments were performed, and (iii) data acquisition equipment is provided below.

#### **3.1 Calibration Apparatus**

The calibration apparatus depicted in figure 3.1 was used to generate constant velocity flows of different, known helium concentrations and temperatures. It was primarily designed by Hewes (2016), and modified to connect with the coaxial jet apparatus described in §3.2. Accordingly, only a brief overview of the apparatus, focusing on recent modifications is given here. Specific components of the apparatus, including the He/air mixing system, heating system, and calibration jet, are discussed in detail, as these are also used during experiments.

##### **3.1.1 Overview**

Calibrations in the current work are performed by setting the valves on the calibration apparatus so that compressed air and helium flow through pathway A to the calibration jet, as depicted by the arrows in figure 3.1. The air is supplied from a compressed air supply and filtered to remove dust and/or particles which could damage either the mass flow meters/mass flow controllers in the system or the thermal-anemometry-based probes being calibrated. Downstream of the filters,

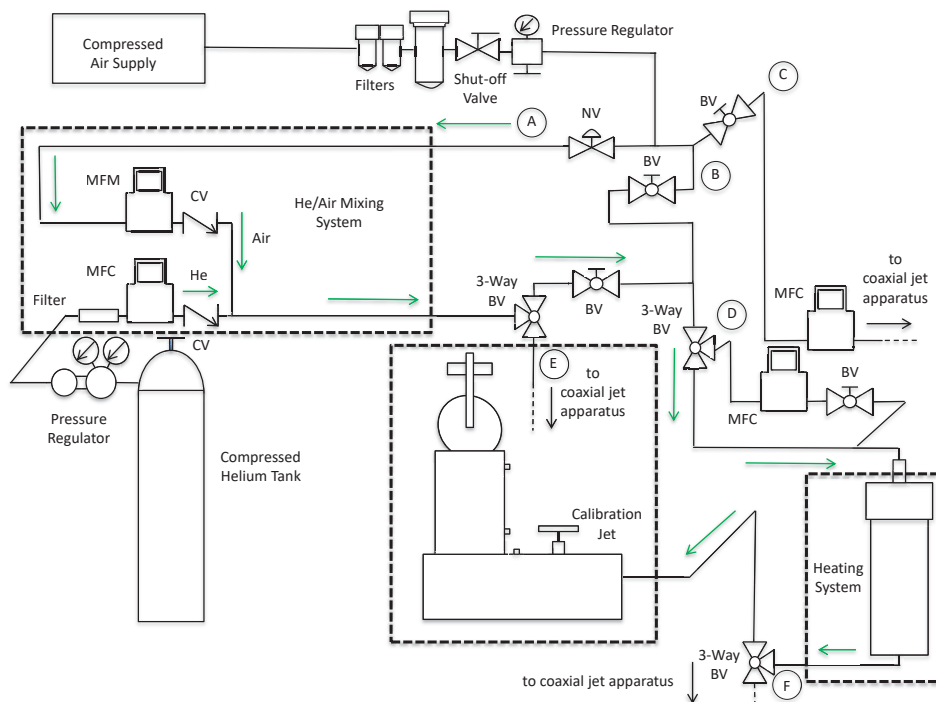


Figure 3.1: Schematic of the calibration apparatus. During calibrations, air flows through branch A, and into the He/air mixing system, heating system, and, finally, the calibration jet, as depicted by the green arrows. The abbreviations are defined as follows: BV: ball valve, NV: needle valve, CV: check valve, MFM: mass flow meter, MFC: mass flow controller.

a pressure regulator is used and set to a pressure of roughly 25 psi, per the specifications of the calibration jet. Following the pressure regulator, a T-junction splits the flow into 3 different branches: A, B, and C, labeled in figure 3.1. The latter two are closed during calibrations, so that all the air flows into branch A, which contains the He/air mixing system described in §3.1.2 and §3.1.3. After passing through the mixing system, fluid flows to the heating system, which is described in §3.1.4. As depicted in figure 3.1, branch D is bypassed, as the mass flow controller located therein is not needed during calibrations. Finally, the fluid flows to the calibration jet, which will be discussed in greater detail in §3.1.5.

### 3.1.2 He/Air Mixing System

The He/air mixing system consists of continuous stream of helium which joins a continuous stream of air by way of a T-junction. The two gases mix via the naturally occurring turbulence in the piping system. The desired He/air concentrations can be maintained at specific concentrations by continuously adjusting the flow rate of helium relative to the measured flow rate of air. A description of the this process will be given in the following subsection. First, the physical components of the mixing system are described.

The compressed air entering the mixing system is controlled with a needle valve and the flow rate is measured downstream with a commercial mass flow meter (Alicat M-100SLPM-D) rated to 100 slpm. This mass flow meter is designed to measure the differential pressure drop ( $\Delta P$ ) across a laminar flow element consisting of hundreds of small-diameter tubes (of radius  $r$  and length  $L$ ) designed specifically to have laminar flow. The volumetric flow rate ( $Q$ ) is then calculated from the Poiseuille equation below:

$$Q = \frac{\Delta P \pi r^4}{8 \mu L}, \quad (3.1)$$

and converted to a “mass flow rate” expressed in standard liters per minute (slpm). (This is the volume flow rate at a standard temperature and pressure of 25°C and 14.696 psia, respectively.) The mass flow meter automatically compensates for changes in temperature and has an accuracy of 0.2% of full scale + 0.8% of flow rate.

The flow rate of pure 99.995% compressed helium gas entering the mixing system is controlled by a 20 slpm commercial mass flow controller (Alicat MC-20SLPM-D) operating under the same principles as the 100 slpm mass flow meter just described. Upstream of the mass flow controller, a high-purity, dual-stage pressure regulator sets the delivery pressure of the helium to between 25 – 45 psi, depending on flow requirements. An inline 20 micron filter removes any particles that might have been introduced into the system (for example, when an empty helium tank is replaced with a full one).

Following the T-junction, where the air and helium streams join, a long straight length of tubing allows both gases to mix. Past studies have found that sufficient mixing of fluids is obtained anywhere from 2 to 150 diameters downstream of a T-junction (Ger and Holley 1974; Forney and Kwon 1979; Forney and Lee 1982). As the experimental conditions of these studies differ from those herein, they cannot be used to predict the exact mixing length necessary for the present work. Nevertheless, the total length of tubing between the T-junction and the calibration jet exceeds 400 diameters and includes a number bends that create or enhance the turbulence. As a result, it is assumed that the helium and air are fully mixed at the exit of the

calibration jet. This assumption is supported by Hewes (2016), in which the PDF of the measured He mass fraction was observed to be effectively approximated by a Dirac delta function.

### 3.1.3 Automation of the He/Air Mixing System

The mixing system was automated so that specified helium concentrations would be maintained, regardless of the air flow rate set by the needle valve. The mass flow meter (used to measure the air flow rate) and mass flow controller (used to control the helium flow rate) communicate with a LabVIEW program via an 8-pin Mini-DIN connector located on each of the devices. Single-ended 8-pin male Mini-DIN connector cables were used to connect the devices to a computer. One end was connected to each device and the other was cut to expose the wires of interest. (For the mass meter these are the output and ground signals; for the mass controller these are the input and ground signals.) These were then soldered to a bulkhead BNC jack and connected to a BNC 2110 shielded connector block with BNC cables, as depicted in figure 3.2. A National Instrument PCI-MIO-16-E-4 12-bit A/D DAQ board was used to convert analog signals to digital signals, or vice versa.

The LabVIEW program automating the mixing system allows the user to input a desired helium mass fraction ( $C_{\text{set}}$ ) at which the system will be maintained. Voltages from the mass flow meter are sampled at a rate of 500 Hz and averaged in sets of 100 to attenuate the effects of electronic noise. The program then uses this averaged data to calculate the helium flow rate necessary to maintain the required helium mass fraction in the flow. This information is sent to the mass flow controller and the cycle repeats, as the LabVIEW program is designed to run continuously. For additional information on the LabVIEW program, the reader is referred to Appendix B. As may be seen in the uncertainty analysis described in Appendix C, the helium

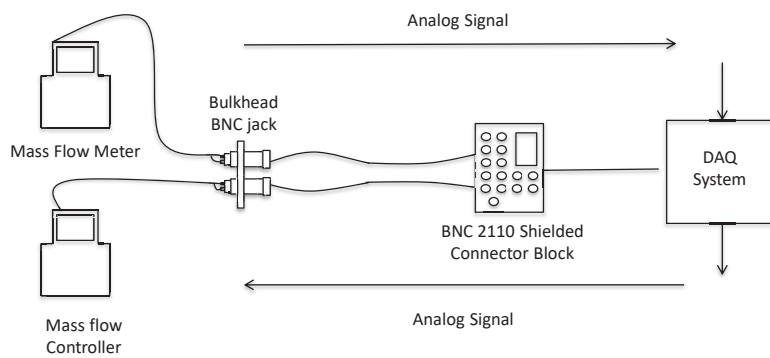


Figure 3.2: Data acquisition system for the helium/air mixing system

mass fraction can be set with accuracies of  $2.5 \cdot 10^{-7} - 9.3 \cdot 10^{-5}$ , depending on the flow rate (Given that the helium mass fraction is generally set to a value on the order of 0.01, this corresponds to a relative accuracy of approximately 0.001 – 1%.)

### 3.1.4 Heating System

The heating system consists of a long copper cylinder, 5.08 cm in diameter, around which three 80  $\Omega$  strip heaters have been wrapped. During calibrations, the strip heaters are powered by a 105 V, 4A variable AC heater. The fluid passing through the cylinder can be heated up to a temperature of 100°C, as per the material constraints of the heating system. Although the tubing downstream of the heating system is insulated, some heat loss occurs between the heating system and the calibration jet. Consequently, for typical calibration velocities (1 - 20 m/s), the fluid at the exit of the calibration jet can be heated to a maximum temperature of roughly of 50°C.

### 3.1.5 Calibration Jet

The calibration jet is a commercially produced TSI Model 1128B Air Velocity Calibrator. It is a manually-operated, bench-top system designed to produce a jet with a top-hat velocity profile for calibrations of single, dual, and triple sensor hot-wire probes. The model comes with 10 and 14 mm diameter exit nozzles, the former of which is currently installed. The calibration jet is typically operated using (i) fine and coarse adjustment valves located on the actual apparatus to control the flow rate, and (ii) a pressure transducer to infer the velocity at the jet exit. However, modifications have been made to the typical mode of operation so that the system can be used for He/air mixtures. The fine and coarse adjustment valves are left open, and, as previously discussed, the air flow rate is set using a needle valve, whereas the helium flow rate is set with the mass flow controller. The exit velocity ( $U_J$ ) is determined from the total volume flow rate at the jet exit ( $Q_{tot,J} = Q_{air,J} + Q_{He,J}$ ),

and the area of the exit nozzle:

$$U_J = \frac{Q_{tot,J}}{0.25\pi D^2}, \quad (3.2)$$

where  $D$  is the diameter of the exit nozzle, and  $Q_{air,J}$  and  $Q_{He,J}$  are the respective flow rates of the air and helium at the jet exit. These are calculated by adjusting the flow rates recorded by the mass flow meter ( $Q_{air,MFM}$ ) and mass flow controller ( $Q_{He,MFC}$ ) (which are given in slpm) using the densities measured at the jet exit ( $\rho_{air,J}$ ,  $\rho_{He,J}$ ):

$$Q_{air,J} = \frac{\rho_{air,MFM}}{\rho_{air,J}} Q_{air,MFM}, \quad (3.3)$$

$$Q_{He,J} = \frac{\rho_{He,MFC}}{\rho_{He,J}} Q_{He,MFC}. \quad (3.4)$$

Note that  $\rho_{air,MFM}$  and  $\rho_{He,MFC}$  refer to the densities associated with the mass flow meter and mass flow controller, and given that their flow rates are expressed in slpm, these are respectively, the densities of air and helium at standard temperature and pressure (STP). The densities at the jet exit ( $\rho_{air,J}$ ,  $\rho_{He,J}$ ) are calculated using the temperature measured by a type E thermocouple installed at the jet exit and the pressure measured by a mercury barometer in the laboratory. The calibration system therefore can measure velocities in both heterogeneous *and* non-isothermal flows.

### 3.2 Coaxial Jet Apparatus

The coaxial jet apparatus, shown in figure 3.3, consists of 3 concentric jets: (i) a center jet containing a mixture of helium and air, (ii) an annular jet containing pure (unheated) air, and (iii) a coflow containing (pure) heated air. The entire apparatus is housed in a large 1.8 m  $\times$  1.7 m  $\times$  2.4 m enclosure, that is connected to the calibration apparatus, as discussed previously.

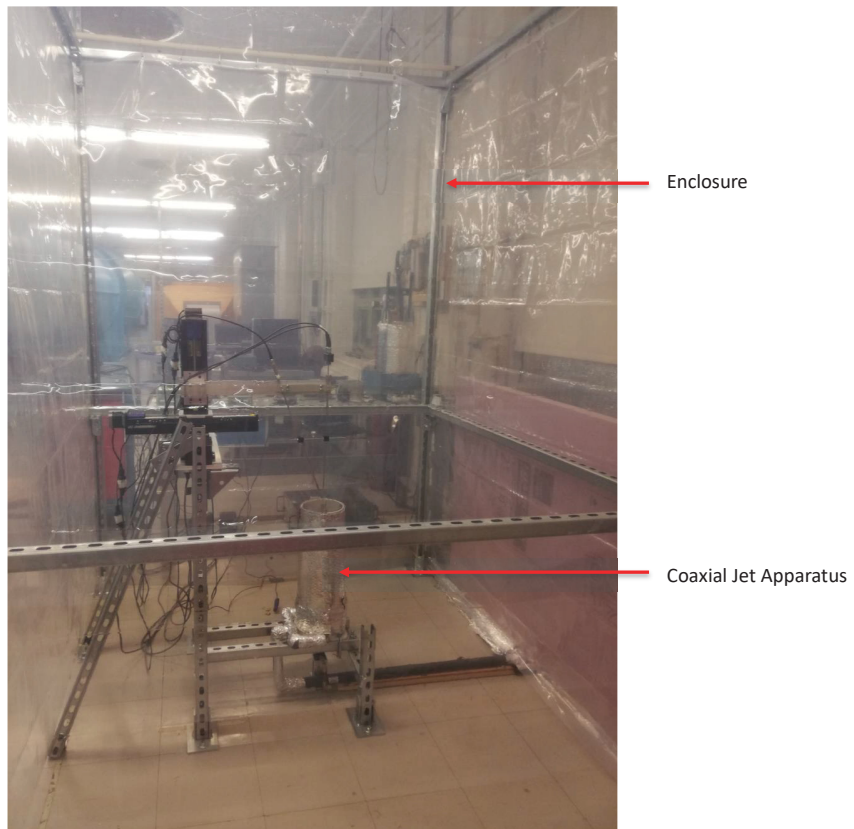


Figure 3.3: Coaxial jet apparatus within its enclosure

### 3.2.1 Interface with Calibration Jet Apparatus

During experiments, the valves on the calibration apparatus are set to supply the three jets with their respective flows via branches C, E, and F (as depicted in figures 3.1 and 3.4, the latter of which has been reproduced from figure 3.1 to show fluid flow during experiments). The mixing system described in §3.1.2 is used to supply flow to the center jet. Accordingly, the flow rate for this jet is set by adjusting the needle valve located at the beginning of branch A and setting the desired helium mass fraction in the LabVIEW program described in §3.1.3. The flow rates for the annular jet and coflow are set by 500 slpm mass flow controllers (Alicat MC-500SLPM-D), located in branches C and D, respectively. Both of these mass flow controllers operate under the same principles as the mass flow meter and mass flow controller described in §3.1.2, however the flow rates are set directly on the units instead of from a LabVIEW program.

During experiments, the heating system is powered with a 15A, 75V DC power supply, as the cold-wires used herein are sensitive to electronic noise generated by the AC power supply.<sup>1</sup> The tubing beyond the heating system in branch F, as well as the coflow jet, is insulated to minimize heat loss before the heated coflow. A thermocouple is installed in the coflow to monitor its temperature.

---

<sup>1</sup> This is not a concern during calibrations, since the AC power supply is merely used to heat the fluid flow before the actual calibration procedure takes place. Moreover, the DC power supply is not powerful enough to reach the required temperatures (up to approximately 45°C) necessary for calibrations. Thus, the two power supplies are interchanged regularly, depending on the use of the heating system.

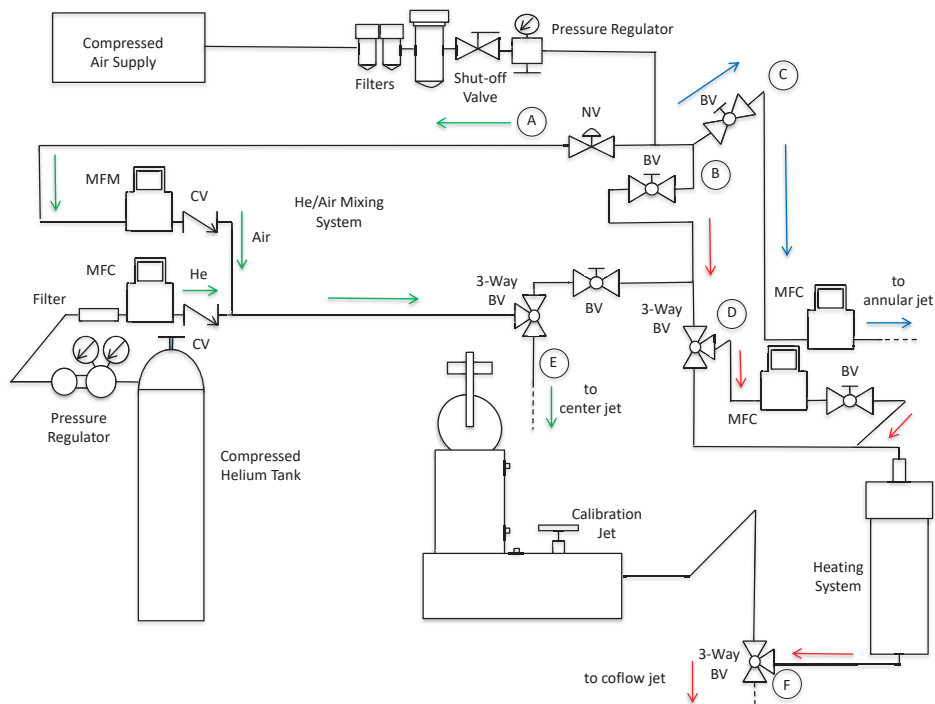


Figure 3.4: Schematic of fluid flow in the calibration apparatus during experiments.  $\rightarrow$  : path of flow for the center jet,  $\rightarrow$  : path of flow for the annular jet,  $\rightarrow$  path of flow for the coflow jet. The abbreviations are defined as follows: BV: ball valve, NV: needle valve, CV: check valve, MFM: mass flow meter, MFC: mass flow controller.

### 3.2.2 Enclosure

An enclosure with a cross-sectional area of 1.8 m × 1.7 m and a height of approximately 2.4 m was constructed to shield the coaxial jet apparatus from exterior flow perturbations emanating from the room in which it is located (i.e. circulating air from HVAC vents, other experimental equipment). The walls of the enclosure are made of plastic sheeting, and a distance of roughly 5 cm was left between the base of the plastic sheeting and the floor so that air can be entrained into the enclosure. The top of the enclosure is open, allowing the coaxial jets to discharge into the surrounding room.

The coaxial jet apparatus is roughly centered within the enclosure, such that there is approximately 0.9 m between the apparatus and the walls on 3 sides, and 0.76 m between the apparatus and the wall on the final side. The area of the enclosure was specifically designed to be large enough that it has no effect on the dynamics of the jet. This was verified using the following equation derived by Hussein *et al.* (1994) to quantify the effect of room size on a jet emanating into it:

$$\frac{M_\infty}{M_J} = \left[ 1 + \frac{16}{\pi B_u^2} \left( \frac{x}{D} \right)^2 \frac{A_J}{A_r} \right]^{-1}, \quad (3.5)$$

where  $M_\infty$  is the momentum flow rate of a jet in an infinite environment,  $M_J$  is the momentum flow rate of a jet in a room of cross-sectional area  $A_r$ ,  $B_u$  is the slope of the centerline velocity decay,  $D$  is the diameter of the jet, and  $A_J$  is the area of the jet. The ratio  $M_\infty/M_J$  was calculated for the center jet, annular jet, and coflow assuming a maximum downstream distance of  $x = 0.4$  m (although most measurements herein are limited to  $x = 0.16$  m) and a centerline decay slope of  $B_u = 6$ .  $M_\infty/M_J$  was found to be approximately equal to 0.99 in each case, indicating that the enclosure has

a negligible effect on the dynamics of each jet. This is further confirmed through validation measurements presented in §5.1.1

### 3.2.3 Coaxial Jet Streams

The coaxial jet streams are depicted in detail in figure 3.5, and their specifications are listed in table 3.1. The design of this apparatus was inspired by that of Cai *et al.* (2011), however, a number of modifications were made to minimize heat conduction between the three jets, as the current work includes temperature as a scalar. First, it was decided that the coflow would contain the heated air instead of the annular jet. In preliminary designs, the air in the annular jet was heated. However, excessive amounts of heat were conducted to the center jet through the wall separating the two flows. Substantially less heat was transferred to the other jets when the coflow was heated instead. In the final design of the apparatus, a steel tube with an inner diameter of 6.22 mm and an outer diameter of 9.525 mm was placed in the center of an acrylic tube with an inner diameter of 12.7 mm and an outer diameter of 19.05 mm to generate the center and annular jets. The material and wall thicknesses were chosen to minimize heat transfer between the jets, while still ensuring that the jets remain rigid and straight. 3D-printed and machined parts were designed to align the two jets concentrically at their base and maintain their vertical orientation. Additionally, two sets of three holes were drilled into the annular jet (roughly equally spaced, so that the sets of holes are located about  $1/3$  and  $2/3$  of the way up from the base of the annular jet). Fine screws were inserted into these holes, and used to adjust the alignment of the center and annular jets until their exit velocity profiles were verified to be symmetric and concentric. (See §5.1.2 for the exit velocity profiles).

Both the center and annular jets were designed to have fully developed turbulent flow at their respective exits. In the experiments conducted herein, the Reynolds

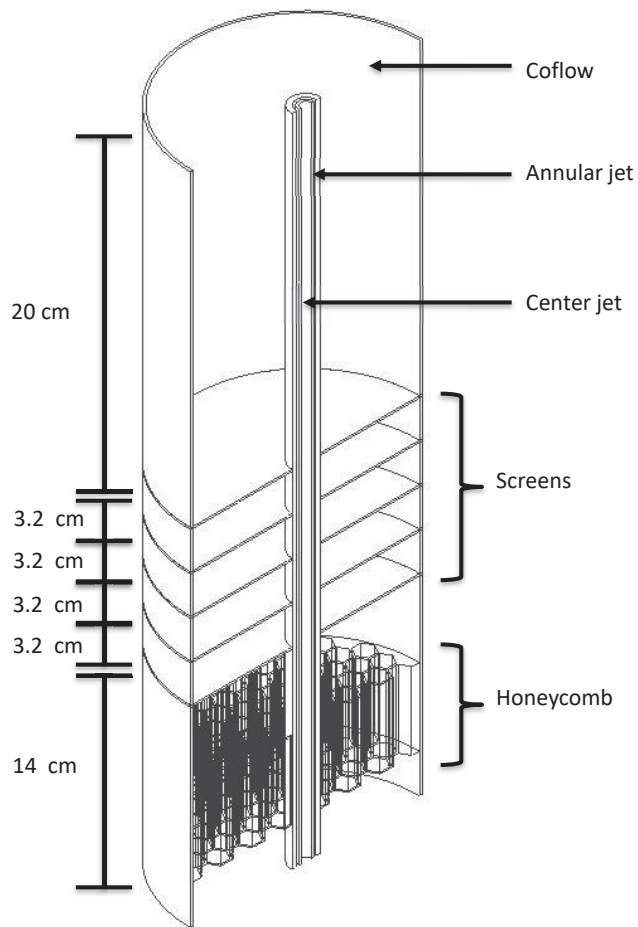


Figure 3.5: Coaxial jet apparatus consisting of (i) a center jet containing a mixture of He and air, (ii) an annular jet containing pure air, and (iii) a coflow containing heated air. Honeycomb and screens are installed in the coflow to give it a uniform velocity profile at the jet exit.

Table 3.1: Properties of the center and annular jet streams

Jet	$D_i$ (mm)	$D_o$ (mm)	$D_h$ (mm)	$l/D_h$	$Re_{D_h} (\equiv U_J D_h / \nu)$
Center		6.22	6.22	100	3700 - 10700
Annular	9.525	12.7	3.175	160	2000 - 4700

number, based on the hydraulic diameter ( $Re_{D_j} = UD_h/\nu$ ) ranged from 3700 to 10700 in the center jet, and from 2000 to 4700 in the annular jet. The entrance lengths ( $x_{FD}/D_h$ ) (for turbulent pipes), calculated as follows:

$$\frac{x_{FD}}{D_h} = 4.4Re_{D_h}^{1/6}, \quad (3.6)$$

ranged from 17 – 21 in the center jet and 16 – 18 in the annular jet. As can be seen in table 3.1, the length-to-diameter ratios of both jets greatly exceed these values, and thus the flows of each jet are assumed to be fully developed and turbulent.

In contrast, the coflow was designed to have a uniform velocity profile at the jet exit. A series of flow-conditioning elements were incorporated into the coflow to generate a uniform velocity profile with minimal velocity fluctuations at the exit. These include:

- a 3D-printed component at the base of the coflow tube jet, designed to axisymmetrically redistribute flow from two inlets,
- marbles in the center of the 3D-printed part to continue distributing the flow uniformly,
- a perforated plate,
- a honeycomb section composed of hexagonal cells with opposing walls 6.35 mm apart to reduce transverse velocity fluctuations and swirl, and
- five 50×50 aluminum mesh screens<sup>2</sup> each spaced 3.2 cm apart.

The screens were held between sections of the coflow jet (a polycarbonate tube with  $D_i = 149.2$  mm and  $D_o = 152.4$  mm), and a thin PVC pipe ( $D_i = 152.4$  mm), was

---

<sup>2</sup> The mesh size is determined by counting the number openings per square inch. Thus, a 50x50 mesh is one which contains 50x50 openings per square inch.

mounted around the coflow jet to hold everything together. Due to the elements mentioned above, the coflow has a nearly uniform velocity of approximately 0.4 m/s and a turbulence intensity of  $< 5\%$ , as measured by a single-normal hot-wire probe (see §5.1.2)

### 3.2.4 Traversing Mechanisms

Three traversing mechanisms were assembled so that the thermal-anemometry-based probes used herein could be translated in three directions. The traversing mechanisms, labeled  $x$ ,  $y$ , and  $z$ , corresponding to their direction of travel, are commercial, motor-driven Velmex BiSlide assemblies. Each of the traversing mechanisms is capable of moving in increments of 0.01 mm. The range of travel of the  $y$  and  $z$  traversing mechanisms is 254 mm, so the entire cross-sectional area of the coaxial jet apparatus can be covered, whereas the vertically oriented ( $x$ ) traversing mechanism has a 508 mm range of travel.

The three traversing mechanisms are mounted on an adjustable stand. The height is set so the entire range of the  $x$  traversing mechanism can be used. Particular care was taken to ensure that the stand was perfectly level, as well as the traversing mechanisms mounted on it. The stand is located roughly 0.5 m away from the coaxial jet apparatus to ensure it will not interfere with the flow. A long metal bar extending from the  $x$  traversing mechanism is used to support up to two hot-wire probes. The first probe is oriented vertically and mounted on a long probe support (approximately 0.45 m long) to again ensure that interference with the flow is minimal. When utilized, the second probe is mounted on a similar probe support (also approximately 0.45 m long), and oriented at an angle of  $20^\circ$  from the vertical. When two probes are used, a small threaded rod with two cubical mounts passing through it, as depicted in figure 3.6, is used to set the separation between the sensors

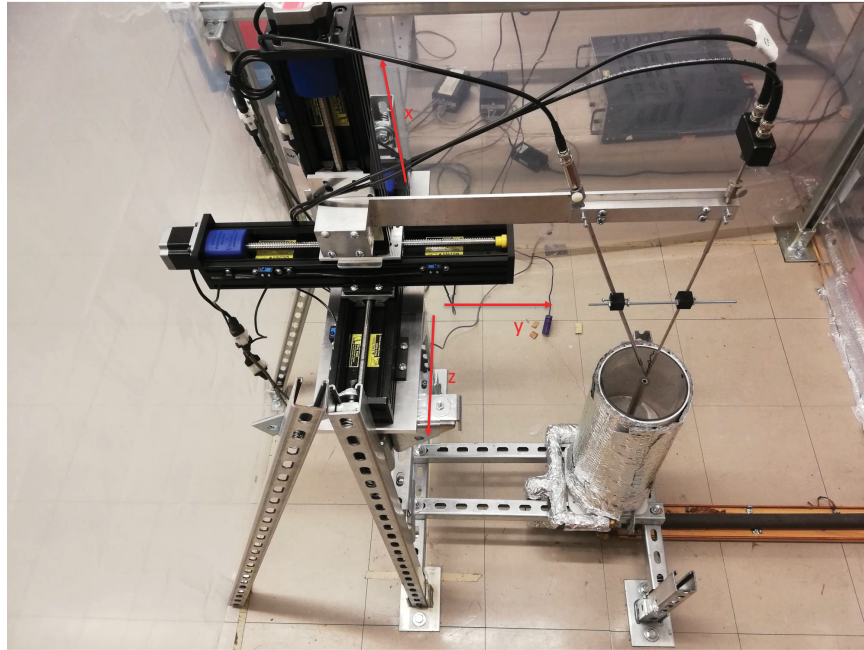


Figure 3.6: Stand with three traversing mechanisms to move probes in the  $x$ ,  $y$ , and  $z$  directions. In the image above, an interference probe and cold-wire thermometer are installed side-by-side, with sensors 1 mm apart. Note that the associated supports and traversing mechanisms used to hold these probes in place do not significantly interfere with the flow given that measurements are performed upstream of all obstructions.

attached to the two probes. Set screws in the cubical mounts are used to hold the probe supports in place, and hex nuts on both sides of the cubical mounts can be turned to either bring the mounts (and thus probes) closer together, or move them further apart. The distance between the two probes was generally set to 1 mm.

### 3.3 Data Acquisition

The output signals of the thermal-anemometry-based probes used herein were filtered using Krohn-Hite 3382 and 3384 filters. For each wire, the mean and fluctuating components of the signal were acquired using two separate data acquisition channels. The former was low-passed filtered to remove high-frequency electronic noise, while the latter was band-passed filtered (additionally removing the DC component of the signal) and, if necessary, amplified to minimize discretization errors. The low-pass frequency was set to the maximum (Kolmogorov) frequency of the flow ( $f_\eta$ ), which can be estimated from the dissipation spectrum (proportional to  $f^2E(f)$ ). According to Tennekes and Lumley (1972), the dissipation should peak close to  $f_\eta/5$  and monotonically decrease at higher frequencies. In practice, electronic noise will cause the measured dissipation spectrum (as well as  $f^2E(f)$ ) to begin increasing at frequencies beyond the Kolmogorov frequency. Assuming the signal-to-noise ratio of the thermal-anemometry-based probe is good,  $f_\eta$  can be estimated to occur at the minimum in the spectrum of  $f^2E(f)$  (for frequencies beyond its peak). The high-pass frequency should be selected such that there is no significant turbulent kinetic energy at frequencies below this value. This will occur where the spectrum  $fE(f)$  (which when plotted on a log-linear plot has an area that is proportional to the turbulent-kinetic energy) approaches zero. As  $f_{HP}$  is generally small ( $< 1$  Hz in the present work), it is set to 0.1 Hz in all measurements.

After being filtered, the output signal of the probe was digitized using a 16-bit National Instrument PCI-6143 DAQ board controlled with LabVIEW. Voltage samples from multiple wires were sampled simultaneously at twice the low-pass filter frequency (as specified by the Nyquist criterion) to obtain time series of the data. A sufficient number of points (typically  $3.3 \cdot 10^7 - 1.3 \cdot 10^8$ ) was taken to ensure the total sampling time (typically 5 - 10 min) was long enough that the statistics reported herein are converged. (See Appendix D for confirmation of statistical convergence).

## **CHAPTER 4**

### **Instrumentation**

As stated in §1.2, the first objective of the present work was to develop an experimental technique capable of simultaneously measuring two scalars and velocity in turbulent flows. Given that thermal-anemometry-based techniques can be used to measure velocity, gas species concentration, and/or temperature, these techniques were adapted to create a novel 3-wire probe to simultaneously measure velocity, helium concentration, and temperature. As will be subsequently discussed, the 3-wire probe consists of an interference probe combined with a cold-wire thermometer. Although the use of the latter is well established, that of the former is not, nor is it particularly well understood. Therefore a large portion of this chapter is devoted to extending the work of Hewes (2016) on the optimization and design of interference probes. In addition to the aforementioned objectives, the current chapter also discusses the design, calibration, and operation of all instrumentation used in the present experiments, including (i) single-normal hot-wire and cold-wire probes, (ii) interference probes, and (iii) the novel 3-wire probe.

#### **4.1 Single-Normal Hot-Wire and Cold-Wire Probes**

Single-normal hot-wire and cold-wire probes, which respectively measure velocity and temperature, were used to make some of the validation measurements (in flows of pure air) that are presented in the following chapter. Given that the use of such probes is well established, their design, calibration, and operation is only discussed briefly in this subsection.

### 4.1.1 Single-Normal Hot-Wire Probe

Single-normal hot-wire probes, with sensors consisting of either  $2.5\ \mu\text{m}$  diameter platinum-rhodium wires or  $5\ \mu\text{m}$  diameter tungsten wires, were used to measure the instantaneous longitudinal velocity of the flow. Both types of wires were constructed to have  $l/d$  ratios of 200, so the platinum-rhodium wires were approximately 0.5 mm in length whereas the tungsten wires were roughly 1 mm in length. Although the platinum-rhodium wires have better spatial resolution, the tungsten wires are more robust and less prone to drift (see Hewes *et al.* 2020), and thus were preferred in certain cases.

The single-normal hot-wires were mounted on TS1 1210 hot-wire probes. When connected to a TSI IFA300 Constant Temperature Anemometer, they form one arm of a Wheatstone bridge, and are maintained at a constant resistance. As discussed in §2.1.1, a semi-theoretical relationship known as King’s Law (equation (2.1)) is used to relate the anemometer output voltage ( $E$ ) to the flow’s velocity ( $U$ ). The constants  $A$ ,  $B$ , and  $n$ , in this equation were found by calibrating the wires at roughly 20 different velocities in the calibration jet described in §3.1.5. Figure 4.1 presents an example of a typical calibration, with equation (2.1) fit to the data. To minimize drift, the single-normal hot-wires were calibrated frequently — generally before and after each experiment.

### 4.1.2 Cold-Wire Probe

Cold-wire thermometers are used to measure temperature, most commonly in flows of pure air. The cold-wire sensing element consists of a platinum wire with a diameter of  $0.625\ \mu\text{m}$  and a length of approximately 0.5 mm, yielding a length-to-diameter ratio ( $l/d$ ) of about 800. Although Browne and Antonia (1987) recommend a length-to-diameter ratio of 1500 to minimize finite-wire-length conduction effects,

the wire must also be small enough to resolve the smallest features of the flow, which are on the order of the Kolmogorov length scale ( $\eta$ ). In the current work,  $\eta$  is on the order of  $10^{-1}$  mm, and for  $0.625\ \mu\text{m}$  diameter wires (the smallest diameter commercially available),  $l/d$  of 1500 yields a wire length of nearly 1 mm. As a compromise, and because it has been found that spatial-resolution errors are more significant than finite-wire conduction effects (Mydlarski and Warhaft 1998), a length-to-diameter ratio of 800 is employed herein, like in the work of Lepore and Mydlarski (2011).

Like the aforementioned hot-wires, the cold-wire sensors were mounted on TSI 1210 single-wire probes. They were operated using a constant current anemometer (CCA) built at the Université Laval in Québec, Canada, which supplied a constant current of 0.1 mA to the wires. This value has been determined to be low enough that the wires in question will be nearly insensitive to the fluctuating velocity field (Bruun 1995). As was discussed in §2.1.2, the temperature of the flow ( $T$ ) can be linearly related to the voltage measured by the cold-wire:

$$T = A_c + B_c E_c. \quad (4.1)$$

The constants  $A_c$  and  $B_c$  in the equation above were determined by heating the calibration jet to a temperature of  $30 - 40^\circ\text{C}$ , and then letting it slowly cool while maintaining a constant velocity. Although the cold-wire should not be sensitive to velocity (due to the low current supplied by the CCA), the velocity during calibration was nevertheless set to be close to the average velocity during experiments, to best match the experimental conditions. As the jet cooled, the voltage of the cold-wire and temperature of the flow were measured every  $0.5^\circ\text{C}$ , and equation (4.1) was fit to the data, like in figure 4.2(a).

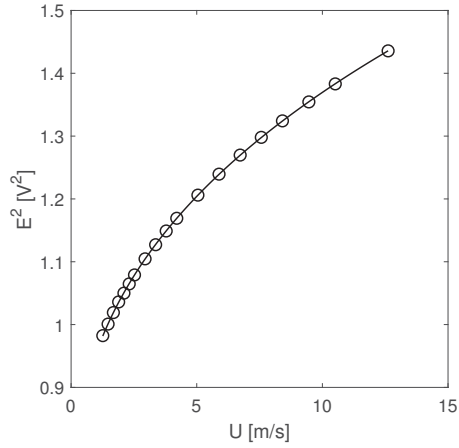


Figure 4.1: Typical calibration for a single-normal hot-wire with equation (2.1) ( $E^2 = A + BU^n$ ) fit to the data.

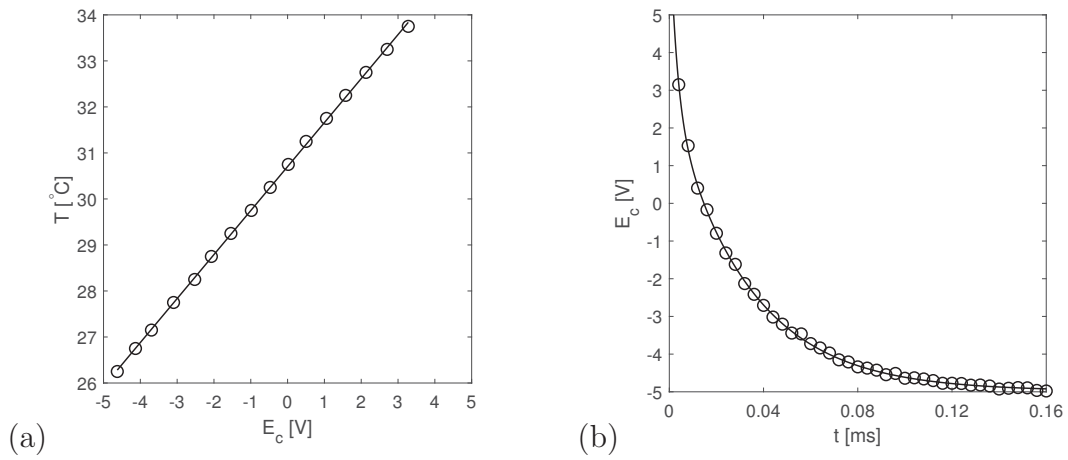


Figure 4.2: Typical (a) calibration for a cold-wire sensor, with equation 4.1 fit to the data, and (b) response of a cold-wire to the current injection technique of Lemay and Benaïssa (2001), with equation (4.2) fit to the data.

As mentioned in §2.1.2, the frequency response of cold-wires may be limited. In the current work, the cut-off frequency ( $f_c$ ) was determined experimentally using the current injection technique of Lemay and Benaïssa (2001). In this technique, a square-wave current is supplied to the cold-wire, and its response is recorded during the cooling phase of this process. Lemay and Benaïssa (2001) suggest that the cooling period of the wire can be described by an exponential decay due to the electronics of the CCA (with a time constant  $\tau_E = 3 \mu\text{s}$ ) superimposed on an exponential decay due to the wire's time constant ( $\tau_w$ ):

$$E_c = C_1 e^{-t/\tau_E} + C_2 e^{-t/\tau_w} + C_3. \quad (4.2)$$

The cut-off frequency ( $f_c$ ) is related to  $\tau_w$  and defined as:

$$f_c = \frac{1}{2\pi\tau_w}. \quad (4.3)$$

Using the technique of Lemay and Benaïssa (2001), an example of which is shown in figure 4.2(b),  $f_c$  was found to be approximately 4–6 kHz over the range of velocities typically encountered during experiments. For situations in which the frequencies are greater than  $f_c$ , the compensation method developed by Lemay and Benaïssa (2001) may be used to improve the accuracy of small-scale measurements. This consists of taking the Fourier transform of the original signal, multiplying it by the filter function  $H_f(f)$  defined below:

$$H_f(f) = |H_f(f)| e^{-i\phi(f)}, \quad (4.4)$$

where

$$|H_f(f)| = \sqrt{\frac{1 + (f/f_c)^2}{1 + (f/f'_c)^2}}, \quad (4.5)$$

and then taking the inverse Fourier transform of this product. The overall result is to artificially extend the frequency response of a cold-wire to a desired frequency  $f'_c$  (typically the low-pass frequency set by the filter). However, given that (i) the present work primarily measured large-scale quantities, and (ii) the compensation method described above also amplified electronic noise, ultimately it was not used herein.

## 4.2 Interference Probe

As discussed in §2.1.3, interference (or “Way-Libby”) probes have successfully been used in a handful of studies to simultaneously measure velocity and species concentration in gaseous turbulent flows. However, there is relatively little documentation on the design and operation of these probes, making it difficult to design, construct, and/or improve them. To rectify this situation, Hewes (2016) investigated the essential design characteristics of an interference probe. The present work further improves upon the recommendations in Hewes (2016), and, as a result, the design of interference probes is examined in detail in the subsequent subsections.

### 4.2.1 Background

The design of interference probes was primarily influenced by early theoretical work by Corrsin (1949) and experimental work by Way and Libby (1970). The former posited that the fluctuating velocity ( $u$ ) and concentration ( $c$ ) fields in a turbulent flow could be inferred from the voltages of two hot-wire probes of differing diameters ( $d$ ). Corrsin’s (1949) suggestions were based on the idea that, in a heterogeneous isothermal gas mixture, the fluctuating voltage of a hot-wire ( $e$ ):

$$e = s_u u + s_c c, \tag{4.6}$$

is a function of  $u$  and  $c$ , where  $s_u = \partial E/\partial U$  and  $s_c = \partial E/\partial C$  are the sensitivity of velocity and concentration, respectively. The fluctuating velocity and concentration can therefore be determined from two linearly independent forms of the above equation, which is possible when using two hot-wires with differing  $s_u/s_c$  ratios. Using equation 2.1, the ratio  $s_u/s_c$  is derived to be:

$$\frac{s_u}{s_c} = \frac{nB(C)U^{n-1}}{A'(C) + B'(C)U^n}, \quad (4.7)$$

where  $A'(C)$  and  $B'(C)$  are the derivatives of  $A$  and  $B$  with respect to the instantaneous concentration ( $C$ ). Consequently, since  $s_u/s_c \sim B$  and  $B \sim d$ , Corrsin (1949) proposed that different values of  $s_u/s_c$  could be obtained with hot-wires of different diameters.

The first to implement the ideas of Corrsin (1949) were Way and Libby (1970). They designed a thermal-anemometry-based probe consisting of a hot-wire ( $d_w = 2.5 \mu\text{m}$ ) and hot-film ( $d_f = 25 \mu\text{m}$ ) to simultaneously measure the instantaneous velocity ( $U$ ) and helium concentration ( $C$ ) in turbulent flows. Initially, the two sensors were placed far enough apart that they could both be assumed to follow King's Law:

$$E_w^2 = A_w(C) + B_w(C)U^{0.5}, \quad (4.8a)$$

$$E_f^2 = A_f(C) + B_f(C)U^{0.5}, \quad (4.8b)$$

where the subscript “ $w$ ” refers to the hot-wire, and the subscript “ $f$ ” refers to the hot-film. In theory, the above equations can be re-expressed as follows:

$$E_w^2 = A_w \left[ 1 - \left( \frac{B_w}{B_f} \right) \left( \frac{A_w}{A_f} \right) \right] E_f^2 = m(C)E_f^2 + b(C), \quad (4.9)$$

to solve for  $C$ . In practice, however, Way and Libby (1970) found that  $m(C)$  and  $b(C)$  were relatively weak functions of concentration, and it was difficult to distinguish voltage pairs arising from high concentrations and low velocities from those arising from low concentrations and high velocities. This was explained by the low thermal accommodation coefficient<sup>1</sup> of helium on common hot-wire materials (i.e. tungsten, platinum), which causes thermal slip effects and may render equations (4.8a) and (4.8b) invalid.

Way and Libby (1970) found that when the hot-wire and hot-film were moved sufficiently close together, so that their thermal fields interfered, the sensitivity to concentration was greatly enhanced. Although the behavior of the hot-film was relatively unaffected — it still followed King’s Law — the behavior of the hot-wire was strongly influenced by the presence of the hot film’s thermal wake. For example, the voltage measured across a hot-wire normally increases as the concentration of helium ( $C$ ) increases. However, when the hot-wire was placed in the thermal wake of the hot-film, the voltage measured across the hot-wire was mostly unaffected by helium concentration, and in some circumstances even decreased as concentration increased. By bringing the hot-wire and hot-film close together, the two sensors of the probe had sufficiently different responses to  $U$  and  $C$  that simultaneous measurements of both these quantities was possible. Note that this is analogous to saying that the

---

<sup>1</sup> The thermal accommodation coefficient relates the energy transferred between a surface and colliding gas molecules. It is the ratio of the average increase in energy of the molecules after striking the surface to the increase in energy if the molecules were to have time to come into thermal equilibrium with the surface (i.e. the maximum possible energy increase based on thermodynamics). It is bound between 0, where no energy is transferred from the surface, and 1, where the surface and gas molecules are in thermal equilibrium. See Appendix E for additional information.

$s_u/s_c$  ratios of the two sensors were sufficiently different, and can therefore be related to the work of Corrsin (1949).

Subsequent designs of thermal-anemometry-based probes that simultaneously measure velocity and gas concentration are based on the ideas of both Corrsin (1949) and Way and Libby (1970). The designs of these probes, of which there are few, are summarized in table 4.1. Therein, it can be observed that the sensing elements of the probes (i.e. the hot-wire and hot-film) (i) mostly have different diameters and (ii) are generally placed close together ( $\leq 50 \mu\text{m}$ ) (so that their thermal fields interfere, and the probe can accordingly be referred to as an interference or “Way-Libby” probe). Although the advantage of diameter differences was briefly discussed by McQuaid and Wright (1973) and Harion *et al.* (1996), there has been no comprehensive investigation into the design constraints and criteria required for thermal-anemometry-based probes capable of successfully measuring velocity and concentration, with the exception of Hewes (2016) (on which the present work expands). Moreover, it should be noted that most of the probes presented in table 4.1 use hot-films (most likely to obtain large diameter ratios) and therefore have a poor frequency response. Accordingly, the ideal probe consists of two hot-wires, like in the work of Sirivat and Warhaft (1982), so that its temporal and spatial resolution is as high as possible.

### 4.2.2 Theory

Before discussing the design of interference probes (which, by definition, consist of two sensing elements placed close enough together that their thermal fields interfere), the theory underlying the use of thermal anemometry for making simultaneous velocity and concentration measurements is examined. Although this subject has already been treated by Corrsin (1949), a different approach will be taken herein since  $s_u/s_c$  ratios are complex functions of concentration and cannot be easily calculated.

Table 4.1: Summary of thermal-anemometry-based probes developed in the literature capable of simultaneously measuring velocity and concentration in turbulent flows.

Authors	Gas mixture	Upstream sensor: diameter and material	Downstream sensor: diameter and material	Diameter ratio	Separation distance	Upstream sensor: overheat ratio / wire temperature	Downstream sensor: overheat ratio / wire temperature	Angle
Way and Libby (1970)	He/air	2.5 $\mu\text{m}$ platinum	25 $\mu\text{m}$ platinum	10	50 $\mu\text{m}$	$\sim 120^\circ\text{C}$	$\sim 295^\circ\text{C}$	perpendicular
Way and Libby (1971)	He/air	2.5 $\mu\text{m}$ platinum	25 $\mu\text{m}$ quartz coated platinum	10	25 $\mu\text{m}$	$\sim 145^\circ\text{C}$	$\sim 320^\circ\text{C}$	perpendicular
Stanford and Libby (1974)	He/air	2.5 $\mu\text{m}$ platinum	25 $\mu\text{m}$	10	25 $\mu\text{m}$	85 $^\circ\text{C}$	305 $^\circ\text{C}$	10 $^\circ$
McQuaid and Wright (1974)	Ar/air	2.5 $\mu\text{m}$ platinum	10 $\mu\text{m}$ platinum	4	Not given	1.3	2.5	Not given
Sirivat and Warhaft (1982)	He/air	5 $\mu\text{m}$ platinum-rhodium	3 $\mu\text{m}$ tungsten	1.7	5 $\mu\text{m}$	1.6	1.2	10 $^\circ$
Panchapakesan and Lumley (1993)	He/air	9 $\mu\text{m}$ tungsten	3 $\mu\text{m}$ tungsten	3	5 $\mu\text{m}$	1.8	1.6	nearly parallel
Riva <i>et al.</i> (1994)	He/air	2.5 $\mu\text{m}$	70 $\mu\text{m}$	28	25 $\mu\text{m}$	100 $^\circ\text{C}$	250 $^\circ\text{C}$	perpendicular
Harion <i>et al.</i> (1996)	He/air	2.5 $\mu\text{m}$	70 $\mu\text{m}$	28	25 $\mu\text{m}$	250 $^\circ\text{C}$	100 $^\circ\text{C}$	perpendicular
Sakai <i>et al.</i> (2001)	CO <sub>2</sub> /air	5 $\mu\text{m}$ tungsten	5 $\mu\text{m}$ platinum	1	500 $\mu\text{m}$	1.3	2.4	parallel
Jonáš <i>et al.</i> (2003)	He/air	5 $\mu\text{m}$ tungsten	70 $\mu\text{m}$ nickel film plated quartz fiber	14	1000 $\mu\text{m}$	250 $^\circ\text{C}$	100 $^\circ\text{C}$	Not given

It is important to note that interference probes are not necessary for making simultaneous velocity and concentration measurements, as may be observed in table 4.1 (see the work of McQuaid and Wright (1974) or Sakai *et al.* (2001)). However, due to the choice of gas mixture for the proposed experiments, as well as constraints on the probe's design (sensor length, diameter...), it will be shown that in the present work, interference probes will be necessary to accurately and precisely make simultaneous velocity and concentration measurements.

To develop the theory behind such measurements, one can start by following the approach of Way and Libby (1970), in which two hot-wires are placed side-by-side and far enough apart that their thermal fields do not interfere. In this situation both wires follow King's Law such that for each wire  $i$ :

$$E_i^2 = A_i(C) + B_i(C)U^n, \quad (4.10)$$

where  $A_i(C)$  and  $B_i(C)$  are defined in equations (2.2) and (2.3), respectively. For simplicity, the exponent  $n$  is assumed to be the same for both wires (which is reasonable given that  $n$  is often assumed to have a constant value of either 0.45 or 0.5), and the wire voltages ( $E_1$  and  $E_2$ ) can be expressed as functions of each other, independent of the velocity ( $U$ ):

$$E_2^2 = m(C)E_1^2 + b(C). \quad (4.11)$$

To obtain simultaneous velocity and concentration measurements, one must ensure that  $m$  and/or  $b$  are functions of concentration ( $C$ ), so that distinct iso-concentration curves for  $E_2$  can be obtained in the  $E_2$ - $E_1$  plane. Using the definitions of  $A$  and  $B$

provided in equations (2.2) and (2.3),  $m(C)$  and  $b(C)$  can be expressed as:

$$m(C) = \left[ \frac{(OH_2 - 1)/OH_2}{(OH_1 - 1)/OH_1} \right] \left( \frac{T_{f,2}}{T_{f,1}} \right)^{0.17} \frac{k_2}{k_1} \left( \frac{\rho_2 \mu_1}{\rho_1 \mu_2} \right)^n \times \left[ \frac{R_T + R_L + OH_2 R_{a,2}}{R_T + R_L + OH_1 R_{a,1}} \right] \left( \frac{\alpha_{20,1} R_{20,1}}{\alpha_{20,2} R_{20,2}} \right) \left( \frac{l_2}{l_1} \right) \left( \frac{d_2}{d_1} \right)^n, \quad (4.12)$$

$$b(C) = 0.24\pi \left( \frac{OH_2 - 1}{OH_2} \right) \left( \frac{T_{f,2}}{T_a} \right)^{0.17} k_2 (R_T + R_L + OH_2 R_{a,2}) \times \left( \frac{l_2}{\alpha_{20,2} R_{20,2}} \right) \left[ 1 - \left( \frac{\rho_2 \mu_1}{\rho_1 \mu_2} \right)^n \left( \frac{d_1}{d_2} \right)^n \right], \quad (4.13)$$

where the fluid properties of gas mixtures are evaluated using the expressions provided in Appendix F. As may be observed from the above equations,  $m$  is generally a weak function of concentration, and becomes independent of concentration for the specific case in which the wire temperatures are equal (so  $T_{f,1} = T_{f,2}$ ,  $k_1 = k_2$ ,  $\mu_1 = \mu_2$ ,  $\rho_1 = \rho_2$ ). Accordingly, to concurrently measure velocity and concentration,  $b$  must therefore be a function of concentration (and non-zero), which necessitates that:

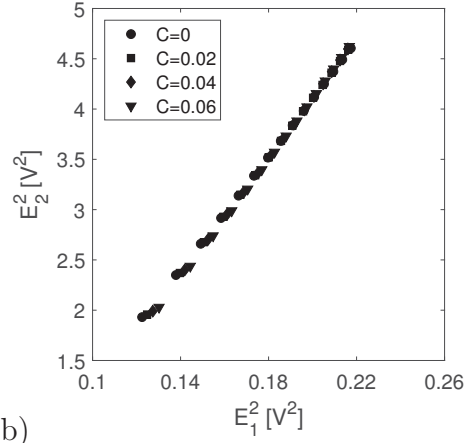
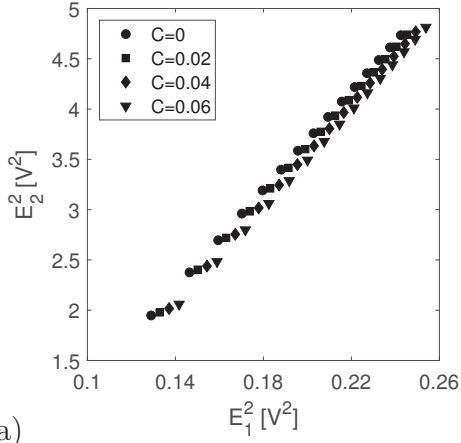
$$\left( \frac{\rho_2 \mu_1}{\rho_1 \mu_2} \right)^n \left( \frac{d_1}{d_2} \right)^n \neq 1. \quad (4.14)$$

Consequently, simultaneous measurements of velocity and concentration are theoretically possible if (i)  $d_1 \neq d_2$ , or (ii)  $T_{f,1} \neq T_{f,2}$ . It is worth noting that the latter is in contradiction with the analysis Corrsin (1949), who found that  $s_u/s_c$  was independent of the choice of wire temperature.

Neither equation (4.12) nor (4.13) take into account rarified gas or accommodation effects, which Way and Libby (1970) suggest may be significant in flows of helium, causing experimental results to depart from theoretical predications. Given that the gases of interest in the current work are air and helium, some discussion of

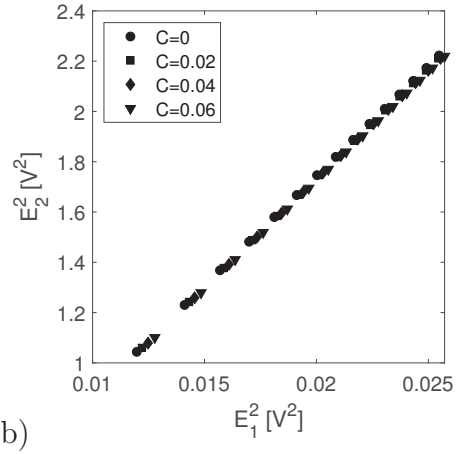
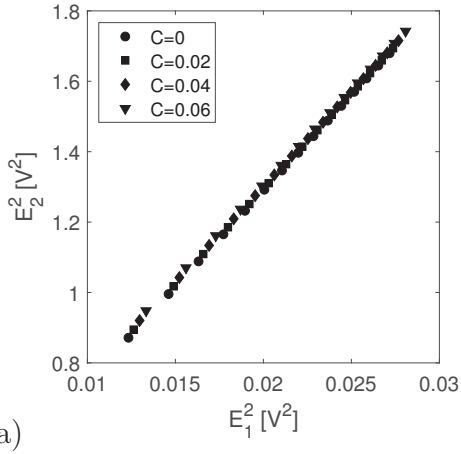
these effects will be presented herein. Rarified gas effects can be quantified by the Knudsen number ( $\text{Kn} = \lambda/d$ , where  $\lambda$  is the mean free path of a gas), which increases as the diameter of a hot-wire ( $d$ ) decreases, or as the concentration of helium (in helium/air mixtures) increases (see Appendix E). Previous research has shown that as  $\text{Kn}$  increases, the flow may transition from continuum flow to slip flow, resulting in a decrease of the Nusselt number (Collis and Williams 1959; Andrews *et al.* 1972). Furthermore, thermal slip has also been observed, even in what is normally considered continuum flow ( $\text{Kn} < 0.01$ ), when the accommodation coefficient for the gas on the wire is small (Kassoy 1967; Aihara *et al.* 1967; Wu and Libby 1971). A study by Pitts and McCaffrey (1986) on the response of hot-wires in different gases reveals that although accommodation effects are negligible in most common gases, including air, they are particularly strong in helium. Due to a combination of higher Knudsen numbers and significant accommodation effects, the actual heat transfer from a hot-wire in flows of helium may be lower than what is predicted by equation (4.10). As a result, equations (4.12) and (4.13), which are derived from the preceding equation, may not be valid in mixtures involving helium.

Returning to the analysis at hand, to gain further insight into the design of thermal-anemometry-based probes capable of simultaneously measuring velocity and helium concentration, the theoretical voltages ( $E_1$ ,  $E_2$ ) of a couple select configurations of commercially available hot-wires were calculated over the range of velocities and helium mass fractions typically encountered in the experiments performed herein ( $1 \text{ m/s} < U < 15 \text{ m/s}$  and  $0 < C < 0.06$ ), and are plotted in figures 4.3 and 4.4. These theoretical calibration maps were calculated using equation (4.10) (from which (4.12) and (4.13) are derived), as well as a technique described in Appendix E to correct for rarified gas and accommodation effects. The results for a probe consisting of



(a) (b)

Figure 4.3: Theoretical dependence of  $E_2^2$  on  $E_1^2$  (a) not correcting for, and (b) correcting for rarified gas and accommodation effects. The first wire is made of platinum ( $d_1 = 1.2 \mu\text{m}$ ) and the second wire is made of tungsten ( $d_2 = 10 \mu\text{m}$ ). Both are operated at  $OH = 1.8$ .



(a) (b)

Figure 4.4: Theoretical dependence of  $E_2^2$  on  $E_1^2$  (a) not correcting for, and (b) correcting for rarified gas and accommodation effects. The first wire is made of tungsten and operated at  $OH = 1.05$  ( $T_{w,1} = 34^\circ\text{C}$ ) and the second wire is made of platinum-rhodium and operated at  $OH = 1.8$  ( $T_{w,2} = 520^\circ\text{C}$ ). Both are  $2.5 \mu\text{m}$  in diameter.

two wires with a large diameter ratio ( $d_2/d_1 = 8.3$ ) are depicted in figure 4.3. As may be seen in figure 4.3(a), equation (4.10) (in which rarified gas and accommodation effects are neglected) predicts distinct iso-concentration curves. However, as demonstrated in figure 4.3(b), when rarified gas and accommodation effects are accounted for, the iso-concentration curves all collapse onto a single line, such that simultaneous measurement of velocity and concentration is not possible. This is consistent with experimental data presented by Way and Libby (1970) for a probe with a similar diameter ratio ( $d_f/d_w = 10$ ), and suggests that Way and Libby (1970) were indeed correct in assuming that accommodation effects caused the experimental data to deviate from the theoretical predictions. The theoretical effects of large differences in wire temperature are considered in figure 4.4, and it is shown that even if the difference in wire temperature is extremely large ( $T_{w,2} - T_{w,1} = 486^\circ\text{C}$ ), the iso-concentration curves all collapse onto each other and simultaneous velocity and concentration measurements are, once again, not possible.

From the above analysis it can be concluded that for the range of helium concentrations of interest, neither a large diameter ratio ( $d_2/d_1 = 8.3$ ), nor an extremely large wire temperature difference ( $T_{w,2} - T_{w,1} = 486^\circ\text{C}$ ) is sufficient for making simultaneous velocity and concentration measurements, despite what was inferred earlier from equations (4.12) and (4.13). Not only are theoretical thermal-anemometry-based probes nearly insensitive to differences in wire temperature, but rarified gas and accommodation effects in helium/air mixtures have a significant effect on these probes, and render differences in wire diameter imperceptible. Accordingly, the suggestions put forth by Corrsin (1949) do not appear to be well suited to flows containing helium (although they should apply to other gas mixtures). Furthermore, it is worth pointing out that the diameter ratio of the hot-wires investigated in figure 4.3 was

chosen to be as large as realistically possible, and cannot be increased significantly beyond its current value (since the dimensions of the wires are limited due to end conduction effects, spatial resolution requirements, and the specifications of the CTA used herein). Given the results presented in figures 4.3 and 4.4, and practical constraints for hot-wire designs, it is suggested that the only way to increase sensitivity to helium concentration is to bring the two wires close enough together that one is in the thermal field of the other, thus forming an interference probe. It will be shown experimentally in §4.2.4 and §4.2.5 that this solution is effective.

### 4.2.3 Design

Over the course of this work, a large number of interference probes were designed, constructed, and tested for the purpose of making simultaneous velocity and helium concentration measurements with high temporal and spatial resolution. The interference probes are mounted on TSI 1240 X-wire probes which were modified to place the downstream wire of the probe in the thermal field of the upstream wire, as depicted in figure 4.5. Creating these probes was delicate work. Each was built by hand using the techniques described in Hewes (2016) and, as can be seen in table 4.2, require that two hot-wires be separated by a distance on the order of  $10\ \mu\text{m}$ . Analysis of initial designs revealed that the probes adequately measured mean velocities and concentrations, but the same was not true for the fluctuating velocities and concentrations. These probes exhibited spurious measurements of concentration in flows of pure air, similarly to what is observed when a cold-wire is used in turbulent isothermal flows, where velocity fluctuations can then be misinterpreted as temperature fluctuations. One of the goals of this work was therefore to design an interference probe in which erroneous concentration measurements were minimized. To this end, a large number of different designs, which are summarized in table 4.2,

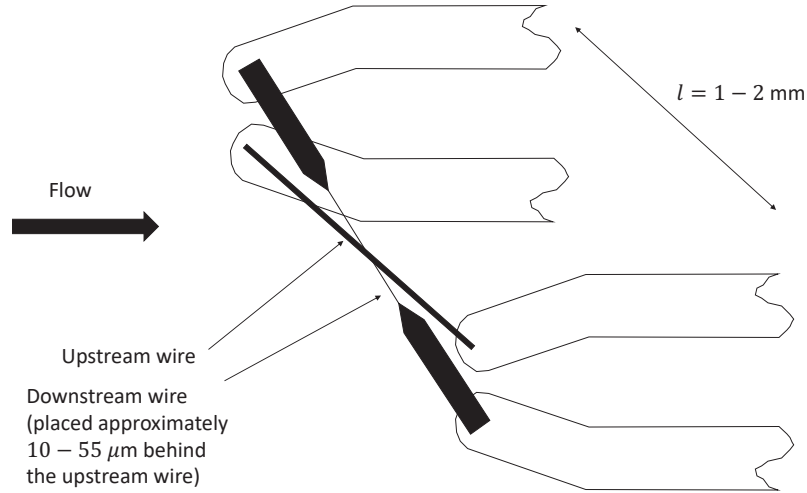


Figure 4.5: Schematic representation of an interference probe mounted on a modified TSI 1240 X-wire probe. Note that the prongs are bent, so that the wires cross at an angle of  $20 - 30^\circ$ . This helps ensure that a large portion of the downstream wire is located within the thermal field of the upstream wire.

Table 4.2: Summary of interference probe designed for the present work. The diameter (in  $\mu\text{m}$ ) and wire material (tungsten - W, platinum- Pt, platinum-rhodium- Pt/Rh) of the upstream and downstream wire is provided, as is the diameter ratio and the separation distance of the two wires.

Upstream Wire	Downstream Wire	Diameter Ratio	Separation Distances ( $\mu\text{m}$ )
2.5 W	2.5 W	1	10, 25, 55
5 W	5 W	1	10, 10
2.5 W	1.2 Pt	2	35
5 W	2.5 W	2	10, 20
5 W	2.5 Pt/Rh	2	10, 10, 10, 15, 15
10 W	5 W	2	10, 10, 10, 15, 25
10 W	2.5 W	4	25, 25, 35

were tested and analyzed to identify the necessary and optimal design parameters for an interference probe. Note that these probes are henceforth described using abbreviations pertaining to the upstream wire diameter and material, downstream wire diameter and material, and separation distance (i.e. 2.5W-2.5W-10, 5W-5W-10, 2.5W-1.2Pt-35, etc...).

It is important to stress that the designs listed table 4.2 are limited due to (i) constraints in which types of hot-wires may used (e.g. spatial resolution requirements and limitations of the CTA used herein, as previously discussed), and (ii) the capability to construct the probe (fragile wires do not survive the construction process). Nevertheless, the variation of design parameters studied herein is far more comprehensive than any other published work on the design of interference probes (Way and Libby 1970; Harion *et al.* 1996).

#### 4.2.4 Calibration and Data Reduction

The probes in table 4.2 were operated using two channels of the IFA300 Constant Temperature Anemometer and are calibrated in the calibration jet, similarly to the single-normal hot-wire probes described in §4.1.1. Calibrations were performed for velocities ranging from approximately 1 to 13 m/s and concentrations (in terms of the He mass fraction) of 0, 0.02, 0.04, and 0.06. The voltages of both wires were recorded for each velocity and concentration, forming a calibration map like the one shown in figure 4.6. The interference probe is well designed when distinct iso-concentration curves can be identified, indicating that simultaneous velocity and concentration measurements are possible (as is the case for the probe used for figure 4.6).

The overheat ratios at which the wires were operated were observed to have a significant effect on the shape of the calibration map. Two examples are presented to demonstrate this. The first involves a probe consisting of a 2.5  $\mu\text{m}$  diameter tungsten

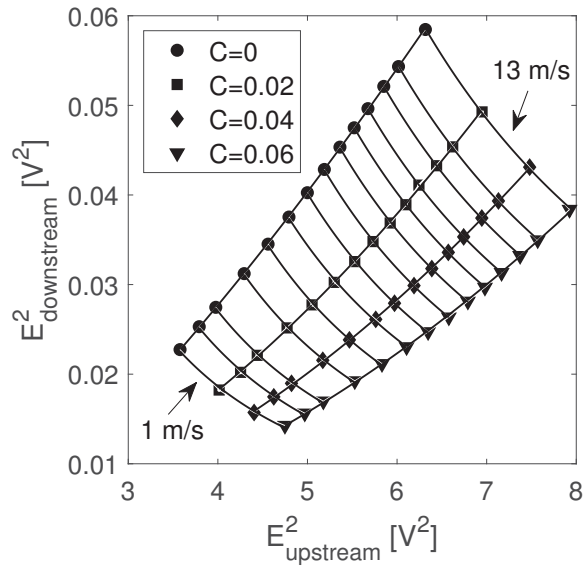


Figure 4.6: Calibration map for an interference probe consisting of a  $10\ \mu\text{m}$  diameter tungsten wire placed  $10\ \mu\text{m}$  upstream of a  $5\ \mu\text{m}$  diameter tungsten wire (10W-5W-10). The squared voltage of the downstream wire is plotted as a function of the squared voltage of the upstream wire for velocities ranging from 1 to 13 m/s and concentrations of  $\bullet$ : 0,  $\blacksquare$ : 0.02,  $\blacklozenge$ : 0.04, and  $\blacktriangledown$ : 0.06 He mass fraction. Power laws are fit to the data along iso-concentration and iso-velocity lines.

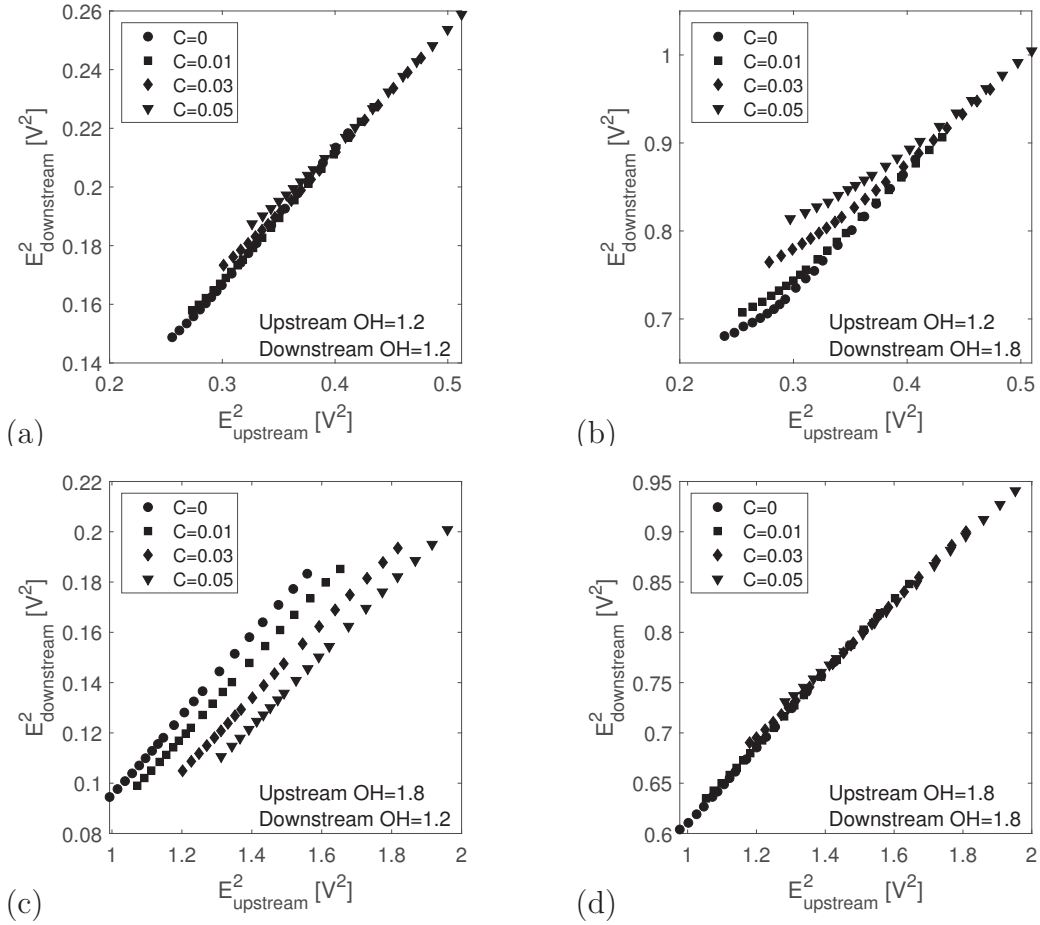


Figure 4.7: Comparison of the effects of the overheat ratio on the calibration map of the 2.5W-1.2Pt-35 probe. (a) Upstream wire OH=1.8 and downstream wire OH=1.8. (b) Upstream wire OH=1.8 and downstream wire OH=1.2. (c) Upstream wire OH=1.2 and downstream wire OH=1.8. (d) Upstream wire OH=1.2 and downstream wire OH=1.2.

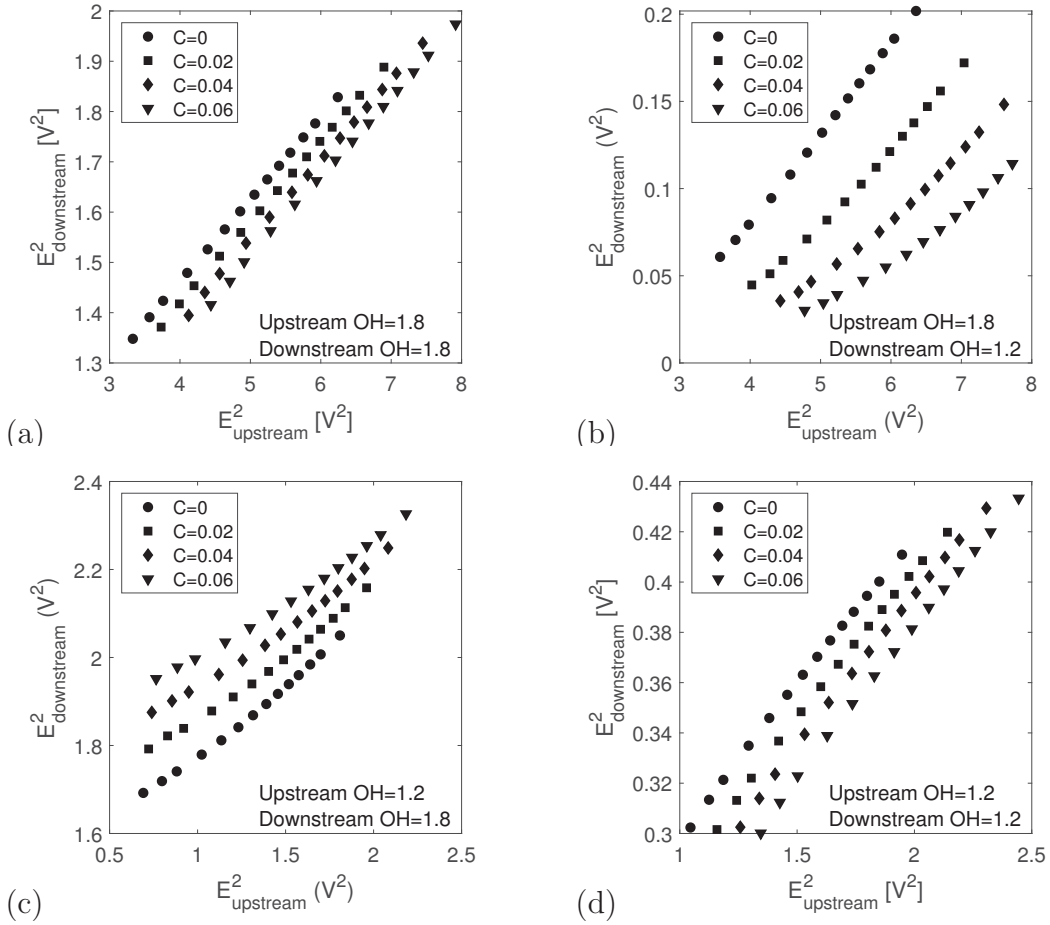


Figure 4.8: Comparison of the effects of the overheat ratio on the calibration map of the 10W-5W-10 probe. (a) Upstream wire OH=1.8 and downstream wire OH=1.8. (b) Upstream wire OH=1.8 and downstream wire OH=1.2. (c) Upstream wire OH=1.2 and downstream wire OH=1.8. (d) Upstream wire OH=1.2 and downstream wire OH=1.2.

wire placed  $35\ \mu\text{m}$  upstream of a  $1.2\ \mu\text{m}$  diameter platinum wire (accordingly labelled 2.5W-1.2Pt-35) and the second involves a probe consisting of a  $10\ \mu\text{m}$  diameter tungsten wire placed  $10\ \mu\text{m}$  upstream of a  $5\ \mu\text{m}$  diameter tungsten wire (accordingly labelled 10W-5W-10). Both probes were calibrated with:

- both wires operated at overheat ratios of 1.8,
- the upstream wire operated at an overheat ratio of 1.8 and the downstream wire operated at an overheat ratio of 1.2,
- the upstream wire operated at an overheat ratio of 1.2 and the downstream wire operated at an overheat ratio of 1.8, and
- both wires operated at overheat ratios of 1.2.

As demonstrated in figures 4.7 and 4.8, the calibration maps for each combination of overheat ratios are quite different. Similar results were also observed by Harion *et al.* (1996), who also studied the effect of overheat ratio (i.e. sensor temperature) on an interference probe consisting of a hot-wire and a hot-film. They found that choices in the sensor temperature could be used to design probes in which (i) neither sensor was significantly influenced by the other, (ii) the hot-film was influenced by the hot-wire, and (iii) the hot-wire was influenced by the hot-film. In the current work, it appears that sensitivity to concentration is enhanced when the (smaller) downstream wire is operated at a low overheat ratio and the (larger) upstream wire is operated at a high overheat ratio, such that the former is influenced by the latter. This is especially apparent for the 2.5W-1.2Pt-35 probe, for which simultaneous velocity and concentration measurements are only possible when the upstream wire overheat ratio is high and the downstream wire overheat ratio is low. Consequently, the interference probes designed herein are operated with the aforementioned combination of overheat ratios. Differences between the calibration maps of the 2.5W-1.2Pt-25 probe and

those of the 10W-5W-10 probe are most likely due to differences in the separation distance between the two wires of the probe. Since the wires of the 10W-5W-10 probe are much closer together, simultaneous velocity and concentration measurements are possible for each combination of overheat ratios. The effects of separation distance, as well as other design parameters, are investigated in greater detail in the following subsection. However, the data reduction for the interference probe is first presented.

To obtain concentration ( $C$ ), a two-dimensional fit of the following form was applied to the calibration map of the two wire voltages ( $E_{up}$ ,  $E_{down}$ ):

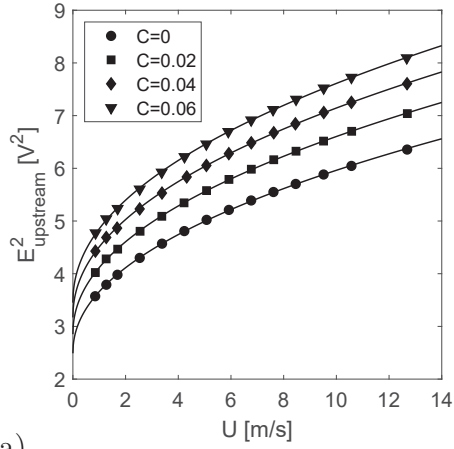
$$C = c_1(\ln E_{up}^2)^3 + c_2(\ln E_{down}^2)^3 + c_3(\ln E_{up}^2)^2 \ln E_{down}^2 + c_4 \ln E_{up}^2 (\ln E_{down}^2)^2 + c_5 \ln E_{up}^2 \ln E_{down}^2 + c_6(\ln E_{up}^2)^2 + c_7(\ln E_{down}^2)^2 + c_8 \ln E_{up}^2 + c_9 \ln E_{down}^2 + c_{10}. \quad (4.15)$$

Although polynomial fits were suggested in earlier works (Sirivat and Warhaft 1982; Hewes 2016), analysis of different curve fits revealed that the fit at low velocities was improved when taking logarithms of the voltages. Moreover, as may be observed in figure 4.6, which is representative of most calibration maps, the iso-concentration and iso-velocity curves each exhibit power-law behaviors, which suggests that a fit of the form of equation (4.15) is more representative of the relationship between  $C$ ,  $E_{up}$ , and  $E_{down}$  than a two-dimensional polynomial fit.

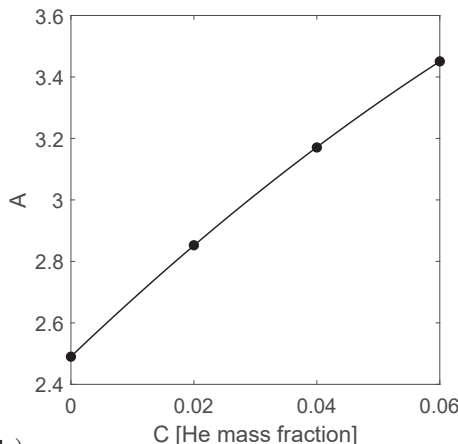
The velocity ( $U$ ) was calculated by applying an inversion of equation (4.10) (or (2.1)) to the upstream wire:

$$U = \left[ \frac{E_{up}^2 - A(C)}{B(C)} \right]^{1/n}. \quad (4.16)$$

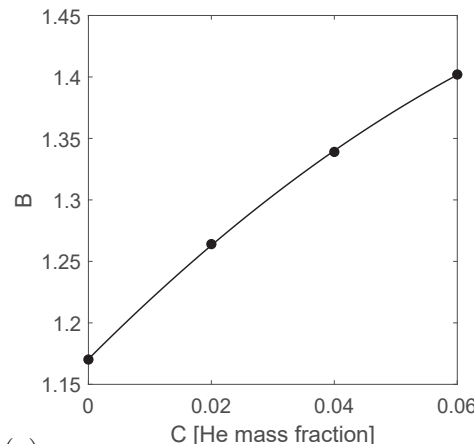
The functions  $A(C)$  and  $B(C)$  were determined by fitting King's Law (equation (4.10)) to iso-concentration curves of the upstream wire, as shown in figure 4.9. The process is similar to what occurs when calibrating a hot-wire in non-isothermal flows.



(a)



(b)



(c)

Figure 4.9: (a) King's Law fits ( $E^2 = A(C) + B(C)U^n$ ) of the upstream wire at 0, 0.02, 0.04, and 0.06 helium mass fractions. (b) Values of  $A$  calculated from the King's Law fits in (a) plotted as a function of  $C$ . (c) Values of  $B$  calculated from the King's Law fits in (a) plotted as a function of  $C$ . Both  $A$  and  $B$  are fit with second-order polynomials.

As may be observed in figures 4.9b and 4.9c,  $A(C)$  and  $B(C)$  were found to be fit well by second-order polynomial functions of  $C$ .

Assuming that no drift has occurred since the wires were calibrated, the above data reduction scheme can be used to infer the velocity and concentration at each point in the flow from the measured voltages of both wires ( $E_{up}$ ,  $E_{down}$ ). First, equation (4.15) is used to calculate  $C$ , and then, using that value of  $C$ , equation (4.17) is used to calculate  $U$ . As assessed by applying the data reduction scheme to flows with known conditions, the calculated values of  $U$  and  $C$  deviate from their true by values by no more than 1%.

#### 4.2.5 Experiments

The interference probes listed in table 4.2 were tested in the turbulent region of the calibration jet, at downstream distances of  $x/D = 10$  from the jet exit. Before discussing the effects of the various design parameters, validation measurements are presented in figures 4.10 and 4.11, to demonstrate the accuracy of the interference probe. These results were measured with an interference probe consisting of a  $5 \mu\text{m}$  diameter tungsten wire placed  $10 \mu\text{m}$  upstream of a  $2.5 \mu\text{m}$  diameter tungsten wire, which compared to other designs, had high signal-to-noise ratio (SNR). (Note that for the present discussion on interference probes, this refers to the signal-to-noise ratio of the concentration measurements.) As may be observed in figure 4.10, the velocity field measured by an interference probe agrees well with that measured by a single-normal hot-wire probe, for which the accuracy is already well established. Moreover, given that the velocity spectra measured by the two probes are very similar, it can

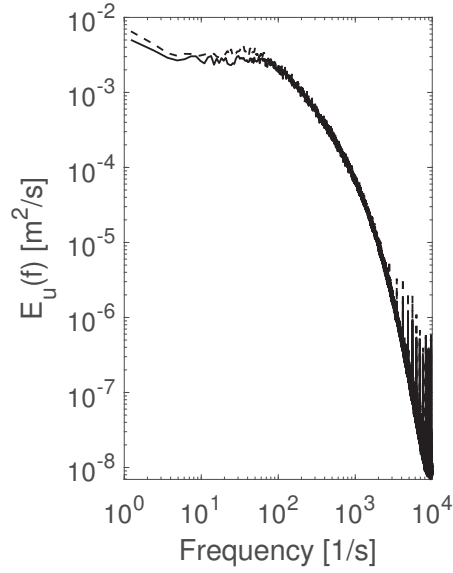


Figure 4.10: Velocity spectra measured in a turbulent jet of pure air with  $Re_D = 4500$  using a single-normal hot-wire (---) and an interference probe (—). Measurements were performed at  $x/D = 10$ .

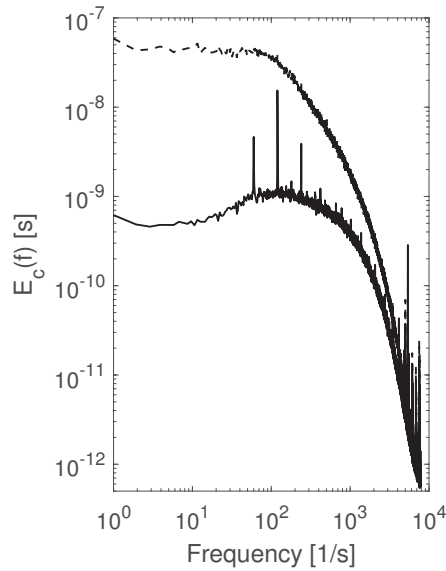


Figure 4.11: Concentration spectra measured using an interference probe in a turbulent jet of He/air (---), where  $C = 0.04$  at the jet exit and  $Re_D = 3800$ , and a comparable jet of pure air (—). Measurements were performed at  $x/D = 10$ .

be concluded that the frequency response of the interference probe<sup>2</sup> is comparable to that of conventional hot-wire anemometry, at least over the range of frequencies measured, which extended up to 10 kHz.

As discussed in §4.2.3, spurious concentration measurements can be recorded in flows of pure air, similarly to what occurs when a cold-wire thermometer is used in isothermal turbulent flows. In figure 4.11, the concentration spectrum measured in He/air mixtures is compared with the concentration spectrum measured in pure air under the same nominal flow conditions (i.e. the noise spectrum of the concentration). It should be noted that the data in figure 4.11 is measured with the same low pass frequency ( $f_{LP} = 10$  kHz) and sampled at the same frequency ( $2f_{LP}$ ) as the velocity data presented in figure 4.10 (since both velocity and concentration are measured using the same interference probe).  $f_{LP}$  approximates  $f_\eta$ , the Kolmogorov frequency, such that the highest frequencies in the flow represent actual velocity fluctuations and not electronic noise. However, given that the Schmidt number (Sc) of helium is 0.22,  $f_{LP}$  is much larger than  $f_{\eta_\phi}$ , the analogous frequency for the scalar field (since  $f_{\eta_\phi} = \text{Sc}^{3/4} f_\eta = 0.32 f_\eta$ ). Thus, the highest frequencies in figure 4.11 (i.e. frequencies in the range  $f_{\eta_\phi} < f < f_{LP}$ ) primarily represent electronic noise, and not concentration fluctuations. This explains why the signal-to-noise ratio approaches 1 at high frequencies. In contrast, at low frequencies, the noise spectrum is approximately two decades lower than the concentration spectrum measured in a He/air mixture, which is comparable to what Sirivat and Warhaft (1982) obtained for their interference probe. Given that the signal-to-noise ratio of other interference probes

---

<sup>2</sup> Note that this frequency response is assumed to apply to both the velocity *and* the concentration measurements, given that the same two wires are used to measure both of these quantities.

designed herein was much lower, the remainder of this subsection is therefore focused on understanding the design requirements for an interference probe with high SNR.

The probes in table 4.2 were each analyzed in a similar fashion. Measurements were (i) made at a distance  $x/D = 10$  from the jet exit, where the He mass fraction was 0.04 and the velocity was 6.8 m/s, and (ii) compared with measurements made at the same location for a comparable jet of pure air. The quality of the measurements of each probe was assessed by calculating the signal-to-noise ratio of the concentration spectra at low frequencies ( $\text{SNR}_0$ )<sup>3</sup> :

$$\text{SNR}_0 = E_c(0)/E_n(0), \quad (4.17)$$

where  $E_c(0)$  and  $E_n(0)$  are respectively the concentration spectrum measured in the He/air mixture and the noise spectrum measured in pure air in the limit as the frequency tends to 0 Hz.

The first, and most important observation from these experiments is that the SNR does not improve as the diameter ratio increases. In fact, as observed from figure 4.12(a), the best results are obtained when the diameter ratio is equal to 1. Note that this does not suggest that large SNR is correlated with small diameter ratios, since it is difficult to infer any trends in the data of figure 4.12(a) when other parameters (separation distance, wire material) vary. The second important observation, gleaned from figure 4.12(b), is that in order to have high SNR, the

---

<sup>3</sup> Although not a perfect measure of the SNR, given that (i) the largest scales (i.e the smallest frequencies) contribute the most to the total scalar variance, and (ii) the highest frequencies ( $f_{\eta\phi} < f < f_{LP}$ ) primarily contain electronic noise (and thus should not be taken into account),  $\text{SNR}_0$  reasonably and simply approximates it without the need for more complex post-processing of the data.

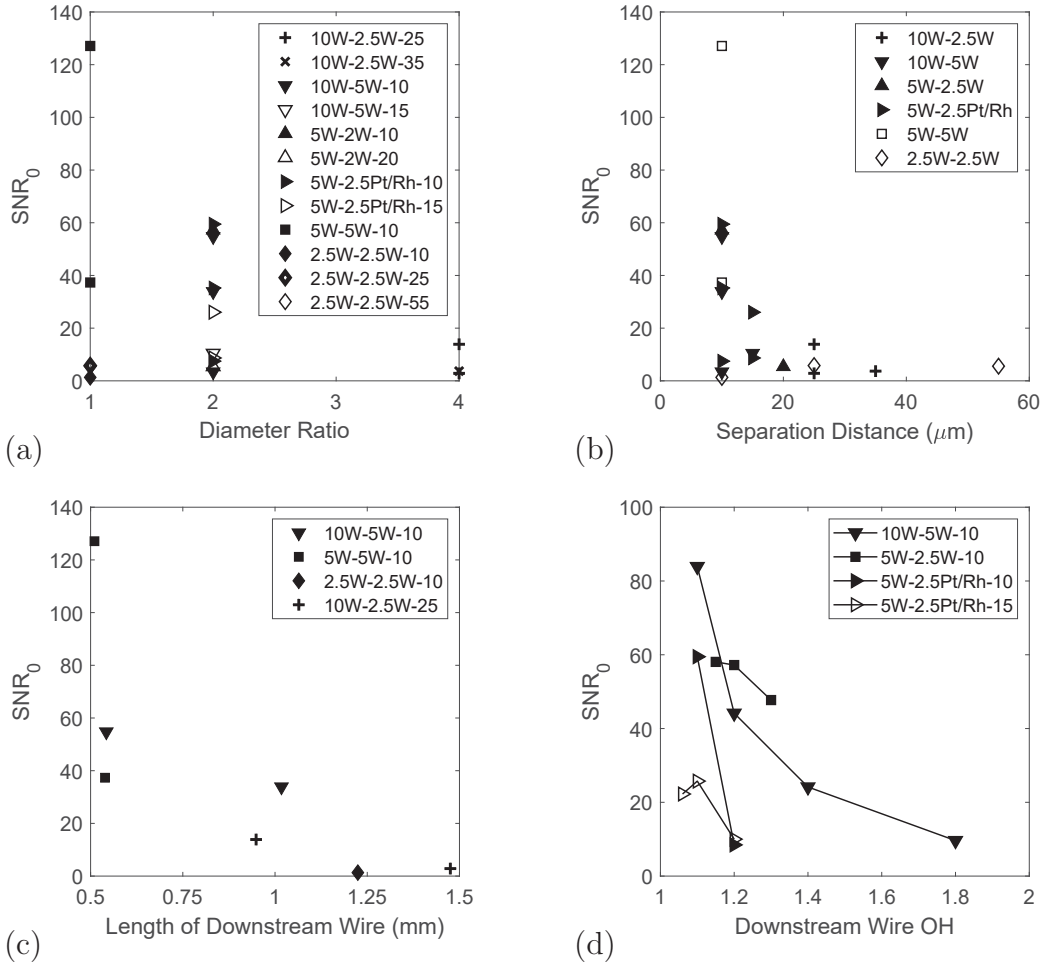
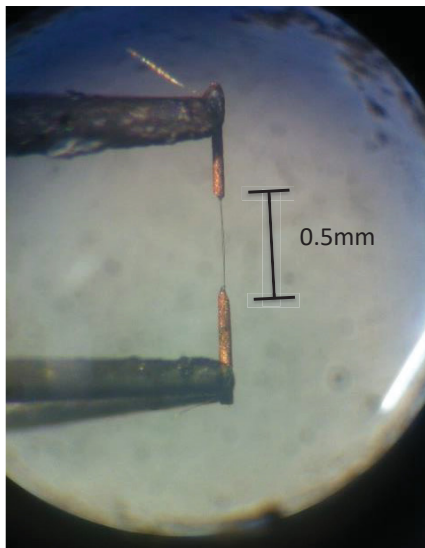


Figure 4.12:  $SNR_0$  of the interference probes listed in table 4.2 plotted as a function of (a) the diameter ratio, (b) the separation distance between the wires, (c) the length of the downstream wire, and (d) the overheat ratio of the downstream wire. In (a), (b), and (c) the overheat ratios are kept constant as the parameter of interest is varied (1.8 for the upstream wire, and 1.2 or 1.1 for the downstream wire). In (d) the overheat ratio of the upstream wire is held constant at a value of 1.8.

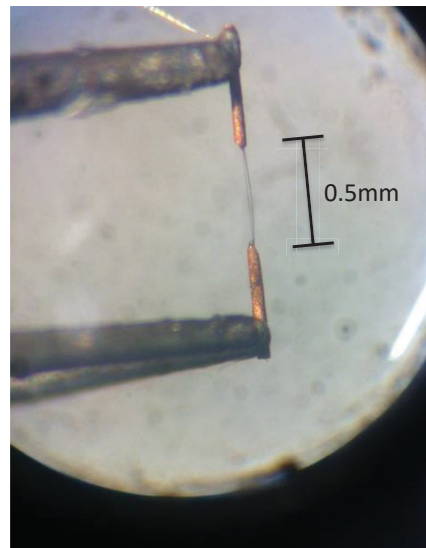
separation distance between the two wires should be  $\lesssim 10 \mu\text{m}$ . However, it should be emphasized that a small separation distance does not necessarily imply high SNR, as  $\text{SNR}_0$  ranges from 1.3 to 127.1 when the separation distance is  $10 \mu\text{m}$ .

The relationship between separation distance and  $\text{SNR}_0$  is further complicated by the fact that it is difficult to accurately measure the separation distance between the wires of the probe. This distance is only estimated with an accuracy  $\pm 5 \mu\text{m}$  *before* the wires of the probe are operated. Furthermore, when the wires are heated, they deflect away from each other, such that the actual separation distance may be larger than what is recorded. An example of the effect of heating on the separation distance of the two wires is shown in figure 4.13. Although it is not clear why the wires deflect away from each other, the fact that hot-wires may buckle when operated is known, and has been discussed by Perry (1982). To fix this issue, the length of the downstream wire was reduced, as shorter wires will buckle less. The positive impact of the reduction of the downstream wire length is documented in figure 4.12(c), where it can be seen that  $\text{SNR}_0$  is inversely related to the length of the downstream wire.

One final point must be made regarding the design of interference probes. In the previous section, the choice of overheat ratio for each wire was shown to have an impact on the shape of the calibration map. Further analysis shows that it also has an effect on the SNR of the concentration measurements. Figure 4.12(d) demonstrates that as the overheat ratio of the downstream wire is lowered while keeping the overheat ratio of the upstream wire remains constant,  $\text{SNR}_0$  generally increases. This is due to the fact that the wire is more sensitive to changes in fluid temperature (resulting from changes in the thermal field of the upstream wire) when the overheat ratio (and thus the wire temperature) of the downstream wire is lowered. In some cases, diminishing returns from the effects of lowering the downstream wire



(a)



(b)

Figure 4.13: (a) Interference probe before each of the two wires are heated. The separation distance is measured to be  $\lesssim 10\ \mu\text{m}$ . (b) The same interference probe with both wires heated to approximately  $220^\circ\text{C}$  above the ambient temperature, depicting a significantly larger separation distance.

overheat ratio may occur. This is because the voltage measured by the downstream wire decreases as the overheat ratio decreases (in some cases even approaching 0 if interference effects are too strong, Harion *et al.* 1996), such that the wire becomes more sensitive to electronic noise.

#### 4.2.6 Optimal Design of Interference Probes

Based on the data presented in the previous subsection, it was concluded that interference probes can successfully be used to measure velocity and helium concentration in turbulent flows, as long as the hot-wires of the probe are placed close enough together that one is in the thermal field of the other. Wires of different diameters are not necessary, unlike what has been suggested in the literature, which greatly simplifies the design of the probe. The best results are obtained when (i) the separation distance between the wires is  $\lesssim 10 \mu\text{m}$ , and (ii) the downstream wire overheat ratio is low. Moreover, to ensure the separation distance between the wires remains small enough, short wires are recommended. In the present work, two different interference probes were used: a 10W-5W-10 probe, which was used for the validation measurements presented in Chapter 5, and a 5W-2.5W-10 probe, which was used in the experiments described in Chapter 6. The former is composed of an upstream wire with a length of 2 mm and downstream wire with a length of 0.5 mm, whereas the latter is composed of an upstream wire with a length of 1 mm and a downstream with a length of 0.25 mm, such that the spatial resolution<sup>4</sup> is significantly improved.

---

<sup>4</sup> Note that the spatial resolution of the interference probe will not exceed the length of the upstream wire, which in the present work ranges from 1 mm (during the actual experiments) to 2 mm (during the validation measurements).

### 4.3 3-Wire Probe

The novel 3-wire thermal anemometry-based probe designed herein to simultaneously measure velocity, helium concentration, and temperature is composed of an interference probe and cold-wire thermometer. Developing this probe required extending (i) the use of cold-wire thermometers to binary mixtures of air and helium, and (ii) the use of interference probes in non-isothermal flows. Both are described in the remainder of this section, as is the operation of the 3-wire probe.

#### 4.3.1 Cold-Wire in Flows of Helium

It is demonstrated herein that cold-wires, which have principally been used in flows of pure air, can also be used in flows of helium. For a cold-wire operated at a constant current ( $I$ ), the (steady-state) voltage measured across the wire ( $E_c$ ) can be expressed as:

$$E_c = IR_{c,w} = I \frac{\pi l k \text{Nu}}{\pi l k \text{Nu} - \alpha_{20} R_{c,20} I^2} R_{c,a}. \quad (4.18)$$

Since  $I$  is very small (0.1 mA in the present work),  $R_{c,w} \approx R_{c,a}$  and the equation above can be approximated as the linear relationship below:

$$E_c \approx IR_{c,a} = IR_{20}[1 + \alpha_{20}(T - T_{20})], \quad (4.19)$$

which does not depend on helium concentration. As depicted in figure 4.14, where calibrations performed at different concentrations all collapse onto a single straight line, the cold-wire is indeed insensitive to the presence of helium (at least for  $0 \leq C \leq 0.06$ , the range of concentrations studied herein).

To further confirm this, the sensitivity ratios ( $s_u/s_t$ ,  $s_c/s_t$ ) were assessed. According to Wyngaard (1971), the ratio of the sensitivity of velocity to that of temperature

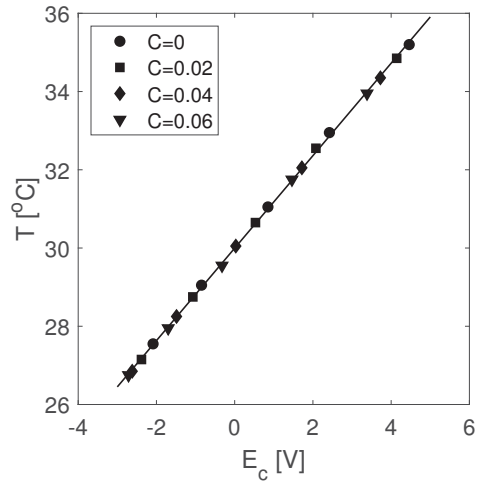


Figure 4.14: Calibration of a cold-wire in flows of different helium concentrations with a linear best-fit line fit to the data.

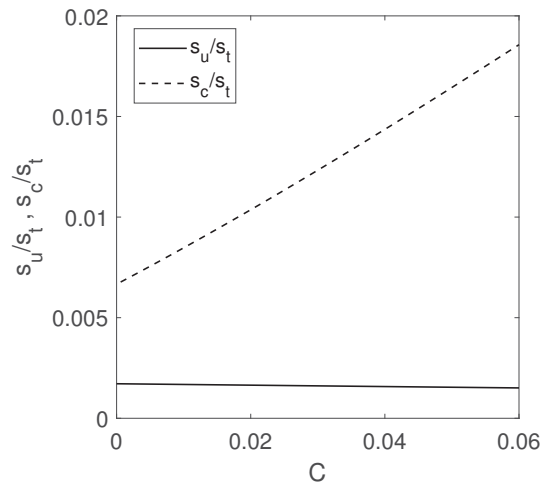


Figure 4.15: Theoretical sensitivity ratios ( $s_u/s_t$ ,  $s_c/s_t$ ) for a  $0.625 \mu\text{m}$  diameter cold-wire operated with a current of  $0.1 \text{ mA}$ . The velocity of the flow is  $10 \text{ m/s}$ .

$(s_u/s_t)$  can be expressed as:

$$\frac{s_u}{s_t} = -\frac{\chi_w Re^{0.45}}{\pi^2 k \langle U \rangle (0.24 + 0.56 Re^{0.45})^2} \frac{I^2}{d^2}. \quad (4.20)$$

A similar analysis was performed to find the ratio of the sensitivity of concentration to that of temperature ( $s_c/s_t$ ):

$$\frac{s_c}{s_t} = -\frac{4\chi_w (A'_c(C) + B'_c(C)U^{0.45})}{\pi^2 k (0.24 + 0.56 Re^{0.45})^2} \frac{I^2}{d^2}, \quad (4.21)$$

where  $\chi_w$  is the resistivity of the wire material. Both  $s_u/s_t$  and  $s_c/s_t$  are plotted in figure 4.15 assuming that  $d = 0.625 \mu\text{m}$  and  $I = 0.1 \text{ mA}$  (the value suggested to minimize velocity sensitivity). It is apparent that  $s_u/s_t$  is extremely small (and nearly constant), and that  $s_c/s_t$ , although larger than  $s_u/s_t$ , is nevertheless also very small. Consequently, given that both experimental results (figure 4.14) and theoretical analysis suggest that the cold-wire is insensitive to helium concentration, it is concluded that the cold-wire can be employed to measure temperature in heterogeneous mixtures of air and helium using the same techniques as those used to measure temperature in pure air (i.e. the techniques described in §4.1.2).

### 4.3.2 Use of Interference Probes in Non-Isothermal Flows

The hot-wire sensor is generally sensitive to changes in ambient temperature, as may be seen from this re-arrangement of King's Law (equation (2.1)) below:

$$E^2 = \left[ A^* k + k \left( \frac{\rho}{\mu} \right)^n B^* U^n \right] (T_w - T), \quad (4.22)$$

where  $A^*$  and  $B^*$  are insensitive to changes in temperature. Since the interference probe consists of two hot wires, it must also be sensitive to changes in ambient temperature, as may be observed in the non-isothermal calibration map presented in figure 4.16. The degree to which an interference probe is sensitive to temperature

depends in part on its design, since both the overheat ratio and wire material affect the wire temperature. Sirivat and Warhaft (1982) were able to design an interference probe that was insensitive to very small temperature fluctuations ( $t_{rms} < 0.1^\circ\text{C}$ ), by heating the upstream wire to a very high temperature ( $375^\circ\text{C}$ ). In the current work, however, the temperature fluctuations are larger ( $t_{rms} \sim 0.5^\circ\text{C}$ ), and such an approach was not possible.<sup>5</sup> Consequently, a temperature compensation method was developed for the interference probes.

Compensating for temperature changes in the upstream wire of the interference probe is relatively straightforward and can be done using compensation techniques developed for single-normal hot-wire probes. (See Bruun (1995) for additional information on temperature compensation for hot-wire probes.) The interference probe is calibrated over a range of fixed temperatures, and King's Law, with constant values of  $n$ , is fit at each of the temperatures. The coefficients  $A$  and  $B$  from each of these calibrations are (approximately) linear functions of the flow temperature ( $T$ ), as may be observed in figure 4.17. As a result,  $A$  and  $B$  can be expressed as:

$$A = A^*(T_{w,A} - T), \quad (4.23)$$

$$B = B^*(T_{w,B} - T). \quad (4.24)$$

---

<sup>5</sup> Although interference probes with platinum-rhodium wires were found to be somewhat insensitive to the moderate changes of temperature typical of the experiments conducted herein, these probes were far too fragile to be of practical use, and this approach was therefore ultimately abandoned.

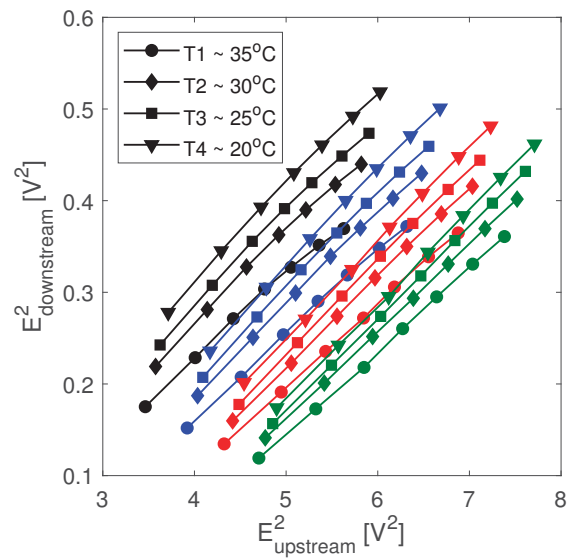


Figure 4.16: Typical calibration map for an interference probe (10W-5W-10) at different temperatures. The squared voltage of the downstream wire is plotted as a function of the squared voltage of the upstream wire for (i) velocities ranging from 1 to 13 m/s, (ii) concentrations of 0 (black), 0.02 (blue), 0.04 (red), and 0.06 (green) He mass fraction, and (iii) temperatures of approximately 35°C (○), 30°C (◊), 25°C (◻), and 20°C (◻).

The constants  $T_{w,A}$  and  $T_{w,B}$ , determined from fits of equations (4.23) and (4.24) to the data, are used to define the average temperature for the upstream wire ( $T_{w,up}$ ):

$$T_{w,up} = \frac{1}{2}(T_{w,A} + T_{w,B}), \quad (4.25)$$

which can then be used to compensate for the effects of temperature on the upstream wire. As shown in figure 4.18, the term  $E_{upstream}/(T_{w,up} - T)$  is independent of temperature. It should be noted that the method described above does not account for changes in the thermophysical properties of the fluid ( $k$ ,  $\rho$ , and  $\mu$ ) due to temperature, which will affect a hot-wire's response, as shown in equation (4.22). However, given that the range of temperatures present during experiments is relatively small ( $\Delta T \leq 15^\circ\text{C}$ ), these effects can be assumed to be negligibly small.

Compensating for the effects of temperature on the downstream wire is more complex, as King's Law does not apply to this wire. In §4.2.4 it was shown that the iso-concentration curves of the calibration map exhibit power law behaviors. As a result, it is suggested herein that the downstream wire voltage can be expressed as a function of the upstream wire voltage as follows:

$$E_{downstream}^2 = F + G \left( \frac{E_{upstream}^2}{T_{w,up} - T} \right)^{n_{down}}, \quad (4.26)$$

where  $F$ ,  $G$ , and  $n_{down}$  are coefficients determined from power-law fits of the calibration map depicted in figure 4.16. Similarly to the upstream wire,  $F$  and  $G$  are also linear functions of the fluid temperature ( $T$ ):

$$F = F^*(T_{w,F}(C) - T), \quad (4.27)$$

$$G = G^*(T_{w,G}(C) - T). \quad (4.28)$$

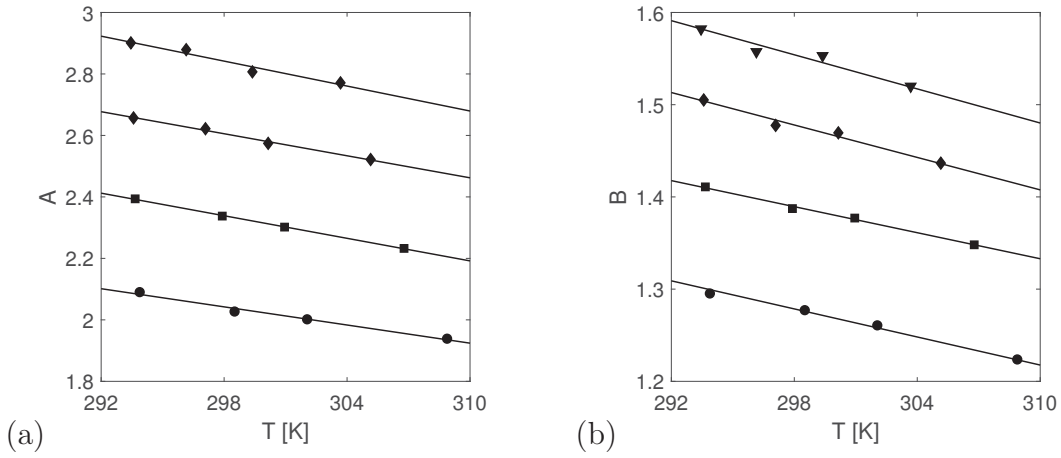


Figure 4.17: (a) The coefficient  $A$  plotted as a function of  $T$  and fit with equation (4.23). (b) The coefficient  $B$  plotted as a function of  $T$  and fit with equation (4.24). The concentrations of helium correspond to:  $C = 0$ :  $\bullet$ ;  $C = 0.02$ :  $\blacksquare$ ;  $C = 0.04$ :  $\blacklozenge$ ; and  $C = 0.06$ :  $\blacktriangledown$ .

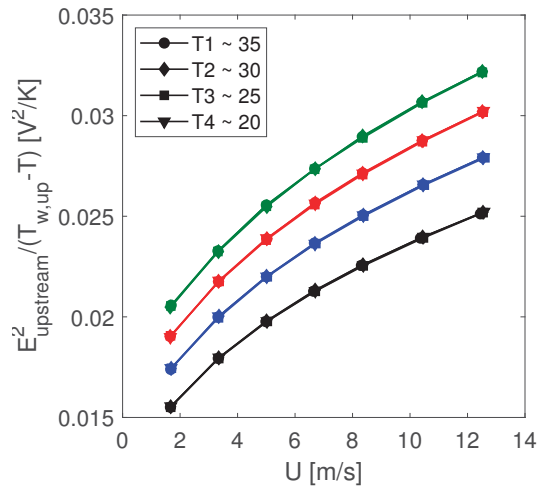


Figure 4.18: Compensated voltages ( $E_{upstream}/(T_{w,up}-T)$ ) plotted as function of  $U$  for (i) velocities ranging from 1 to 13 m/s, (ii) concentrations of 0 (black), 0.02 (blue), 0.04 (red), and 0.06 (green) He mass fraction, and (iii) temperatures of approximately 35°C ( $\circ$ ), 30°C ( $\square$ ), 25°C ( $\diamond$ ), and 20°C ( $\nabla$ ).

However, the constants  $T_{w,F}$  and  $T_{w,G}$  depend on helium concentration ( $C$ ), as may be observed in figure 4.20. This adds some complexity to the compensation process, as compensating for temperature effects requires knowledge of the concentration, and solving for concentration requires compensating for temperature.

To compensate for temperature, the following method is therefore proposed and utilized. The coefficients  $F$  and  $G$  are re-adjusted to their values at 20°C (an arbitrary reference value to reduce the complexity of the calibration map) using  $T_{w,G}$  and  $T_{w,F}$  such that the expected downstream wire voltage at 20°C ( $E_{down,20}$ ) can be expressed as follows:

$$E_{down,20}^2 = F \frac{T_{w,F} - T_{20}}{T_{w,F} - T} + G \frac{T_{w,G} - T_{20}}{T_{w,G} - T} \left( \frac{E_{upstream}^2}{T_{w,up} - T} \right)^{n_{down}}. \quad (4.29)$$

Analysis of calibration data, for which the concentration is known, and for which  $F$ ,  $G$ ,  $T_{w,F}$ , and  $T_{w,G}$  can easily be calculated, has shown that when this normalized voltage is plotted as a function of the corresponding normalized voltage for the upstream wire ( $E_{up,20}$ ), calibrations at different temperatures collapse exceptionally well (see figure 4.21) and resemble those in the isothermal calibration map presented in §4.2.4. Equation (4.15) can therefore be applied to find the concentration, provided the upstream and downstream wire voltages in this equation are replaced by their normalized values.

As knowledge of the concentration ( $C$ ) is required to find the normalized value of the downstream wire ( $E_{down,20}$ ), an iterative process must be applied in which the concentration is first guessed. This is used to estimate  $F$ ,  $G$ ,  $T_{w,F}$  and  $T_{w,G}$ , which are all assumed to be second-order polynomial functions of concentration. Once  $E_{down,20}$  is calculated, it can be applied to equation (4.15) to find the concentration ( $C$ ). More accurate values of  $F$ ,  $G$ ,  $T_{w,G}$  and  $T_{w,F}$  can then be estimated using the new value

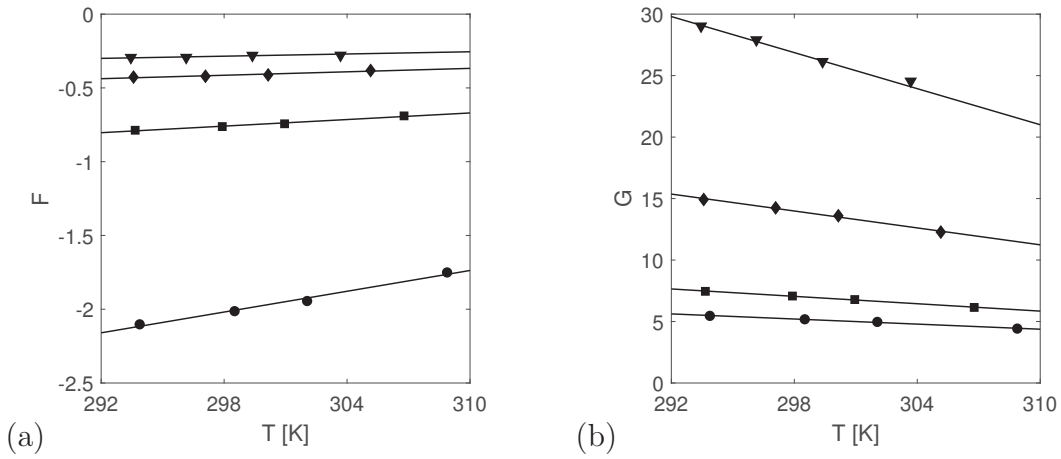


Figure 4.19: (a) The coefficient  $F$  plotted as a function of  $T$  and fit with equation (4.27). (b) The coefficient  $G$  plotted as a function of  $T$  and fit with equation (4.28). The concentrations of helium correspond to:  $C = 0$ :  $\bullet$ ;  $C = 0.02$ :  $\blacksquare$ ;  $C = 0.04$ :  $\blacklozenge$ ; and  $C = 0.06$ :  $\blacktriangledown$ .

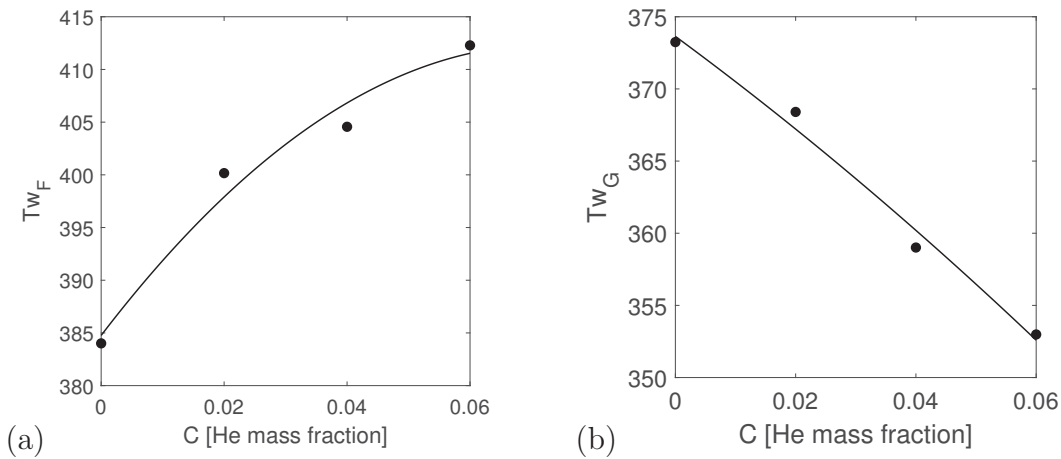


Figure 4.20: (a) The coefficient  $T_{w,F}$  plotted as function of  $C$ . (b) The coefficient  $T_{w,G}$  plotted as function of  $C$ . Second order polynomials are fit to the data.

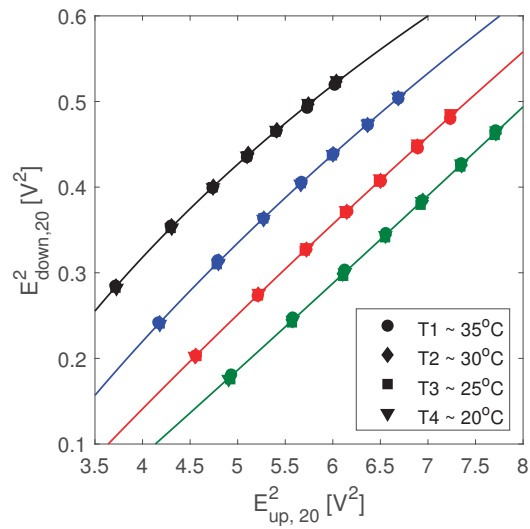


Figure 4.21: Temperature-normalized calibration map of the interference probe (10W-5W-10). The expected downstream wire voltage at 20°C ( $E_{down,20}$ ) is plotted against the expected upstream wire voltage at 20°C ( $E_{up,20}$ ) for (i) velocities ranging from 1 to 13 m/s, (ii) concentrations of 0 (black), 0.02 (blue), 0.04 (red), and 0.06 (green) He mass fraction, and (iii) temperatures of approximately 35°C (○), 30°C (◻), 25°C (◊), and 20°C (◻).

of  $C$ , and the process repeats until satisfactory accuracy for the concentration value is achieved. In §5.2.2, it will be demonstrated that the effects of temperature on the interference probe are well compensated for using this technique.

### 4.3.3 Operation of 3-wire Probe

As stated earlier, the 3-wire probe is composed of an interference probe (either 10W-5W-10 or 5W-2.5W-10) and a cold-wire thermometer. Both probes are placed approximately 1 mm apart, with the cold-wire placed very slightly upstream ( $< 0.25$  mm) of the interference probe. This design is similar to what is used when combining a cold-wire and single-normal hot-wire, or a cold-wire and an X-wire, which is done to minimize the possibility of the wake of the hot-wire affecting the cold-wire measurements, while still ensuring that the spatial resolution remains high. Both probes are operated simultaneously, such that three channels of data are measured at the same time: voltages from the upstream wire, voltages from the downstream wire, and voltages from the cold-wire. Since, the cold-wire is assumed to be insensitive to velocity and helium concentration, temperature can be measured independently of the first two quantities. Measurements from the cold-wire are therefore used to compensate for temperature effects on the interference probe, so that  $U$  and  $C$  can then be calculated.

Lastly, to account for noise present in the interference probe measurements a Wiener filter was applied to the data. Measurements were performed in the flow of interest, as well as in a comparable flow of pure air (i.e. one with the same total initial momentum flow rate), to quantify the noise of the concentration measurements. Both sets of data were Fourier transformed to obtain spectra of the signal ( $S(f)$ ) and noise

$(N(f))$ , and the following optimal filter was applied to the data:

$$\theta(f) = \frac{|S(f)|^2}{|S(f)|^2 + |N(f)|^2}. \quad (4.30)$$

An inverse Fourier transform was then used to convert the data back to the time domain. This process was used to obtain noise-corrected values of  $C$ , which also result in more accurate values of  $U$ . In §5.2.1, it is shown that application of the Wiener filter correctly accounts for noise, and that the velocity and concentration fields of turbulent jets can be accurately measured using the interference probe. Similarly, it is shown in §5.2.2 that the velocity, concentration, and temperature fields of a turbulent jet can be accurately measured with the 3-wire probe.

## CHAPTER 5

### Validation of the Experimental Apparatus and Measurement Techniques

Before discussing the multi-scalar mixing experiments that are the focus of the research, the current chapter presents a validation of (i) different elements of the experimental apparatus (given that it was specifically constructed for the present work), and (ii) the novel measurement techniques developed in the previous chapter.

#### 5.1 Validation of the Experimental Apparatus

In this section, two sets of measurements are presented to examine certain aspects of the experimental design. The first was performed in the center jet of the coaxial jet apparatus. Given that (single) axisymmetric jets issuing into quiescent air have been extensively studied, this flow is an excellent reference for validation measurements. The latter were performed using a single-normal hot-wire to verify the alignment of the jet axis and traversing mechanism, and to confirm the (negligible) effects of the enclosure surrounding the jet on its dynamics. The second set of measurements involved measuring the exit velocity and temperature profiles of the full coaxial jet apparatus (i.e. the center jet, annular jet, and coflow), with the aim of establishing the exit conditions, and ensuring the symmetry of the flow.

##### 5.1.1 Single-Normal Hot-Wire Measurements in an Axisymmetric Jet

Measurements were undertaken using a single-normal hot-wire in a jet of pure air, where  $Re_D = U_J D / \nu = 10,700$  and the average velocity at the jet exit ( $U_J$ ) was 25.7 m/s. Mean and rms velocities were recorded along the centerline for  $1.6 \leq x/D \leq 56.3$  and along radial profiles at  $x/D = 16.1, 24.1, \text{ and } 32.2$ . These were used to

characterize the jet, including a calculation of the centerline decay rate constant ( $B_u$ ), virtual origin ( $x_0/D$ ), spreading rate ( $S_u$ ), and centerline turbulent intensity ( $u_{rms}/\langle U_0 \rangle$ ), which are all reported in table 5.1. Although data from other turbulent jet studies (such as the commonly cited works of Panchapakesan and Lumley (1993a) and Hussein *et al.* (1994)) are also included in table 5.1, the results herein are primarily compared to studies with similar initial conditions, since these may affect the dynamics of a turbulent jet, even into its self-similar region (George and Arndt 1989; Xu and Antonia 2002; George 2012). Accordingly, the fully-developed pipe jet studies of Xu and Antonia (2002) and Ferdman *et al.* (2000), which were also performed using stationary hot-wire anemometry, are principally used to benchmark the current measurements.

Measurements of the mean axial ( $\langle U_0 \rangle$ ) and rms ( $u_{rms}$ ) velocities at the centerline are presented in figures 5.1 and 5.2, along with those of Xu and Antonia (2002) and Ferdman *et al.* (2000). When  $U_J/\langle U_0 \rangle$  is plotted as a function of  $x/D$ , the resulting downstream evolution of  $U_J/\langle U \rangle$  is (i) linear far downstream, as predicted from equation 2.12, and (ii) shows excellent agreement with the results reported by Xu and Antonia (2002) and Ferdman *et al.* (2000). A best-fit line is fit to the data for  $x/D \geq 12.9$  to calculate the centerline decay rate constant ( $B_u$ ) and virtual origin ( $x_0/D$ ) (defined in equation (2.12)). These were respectively found to be 6.32, and 3.8, which are consistent with previous results of fully-developed pipe jets (see table 5.1). The rms velocities, which were non-dimensionalized to give the turbulence intensity ( $u_{rms}/\langle U_0 \rangle$ ), also agree with previous results, and in particular, those of Xu and Antonia (2002). As may be observed in figure 5.2, in both the current work and that of Xu and Antonia (2002),  $u_{rms}/\langle U_0 \rangle$  asymptotes to very similar values far downstream — approximately 0.24 to 0.25.

Table 5.1: Comparison of characteristics of axisymmetric jets, including the virtual origin ( $x_0/D$ ), centerline decay constant ( $B_u$ ), spreading rate ( $S_u$ ), and asymptotic centerline turbulence intensity  $u_{rms}/\langle U_0 \rangle$  for different studies. The exit velocity profile (i.e. top-hat or fully-developed pipe flow), Reynolds number ( $Re_D$ ), and measurement type (stationary hot-wire anemometry - SHWA; flying hot-wire anemometry - FHWA; laser Doppler anemometry - LDA; pitot-tube - PT; stationary hot-film anemometry - SHFA; flying hot-film anemometry - FHFA; acoustic Doppler velocimetry - ADV) are also provided for the purpose of comparison.

Author	Jet Exit Velocity Profile	Meas. Type	$Re_D$	$x_0/D$	$B_u$	$S_u$	$u_{rms}/\langle U_0 \rangle$
Wynanski & Fieldler (1969) <sup>1</sup>	Top-hat	SHWA	100,000	3-7	5-5.7	0.084	0.28
Panchapakesan & Lumley (1993)	Top-hat	FHWA	11,000	0	6.06	0.096	0.24
Hussein et al. (1994)	Top-hat	SHWA LDA	95,500	2.7 4	5.9 5.8	0.102 0.094	0.28 0.28
Darisse et al. (2013)	Top-hat	PT/LDA	150,000	1.6	6.18	0.091	0.25
Xu & Antonia (2002)	Top-hat FD pipe	SHWA	86,000	3.7 2.6	5.8 6.5	0.095 0.086	0.25 0.24
Ferdman et al. (2000)	FD pipe	SHWA	24,000	2.5	6.7	0.089	0.24
Khorsandi et al. (2013) <sup>2</sup>	FD pipe	SHFA FHFA ADV	10,600	4.18 2.89 5.5	5.9 6.05 5.43	- 0.101 0.099	0.27 0.27 0.35
Current Work	FD pipe	SHWA	10900	3.8	6.32	0.102	0.25

<sup>1</sup> Due to enclosure effects, two different values were obtained for  $x_0/D$  and  $B_u$ . For  $x/D < 50$ ,  $x_0/D = 3$  and  $B_u = 5.7$ , which is consistent with other studies. For  $x/D > 50$ ,  $x_0/D = 7$ , and  $B_u = 5$ .

<sup>2</sup> Different values of  $B_u$  were reported depending on the value chosen for  $x_0/D$ . Only values from the best-fit lines of the data are reported here.

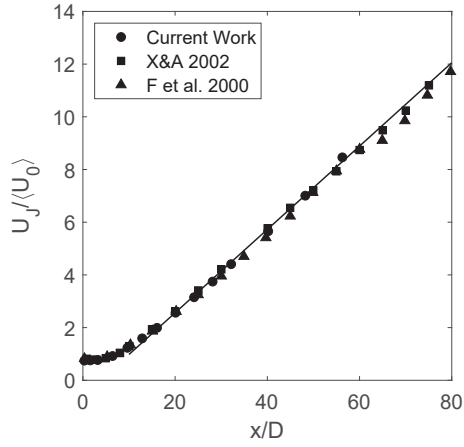


Figure 5.1: Downstream evolution of the centerline axial mean velocity  $\langle U_0 \rangle$  in an axisymmetric jet at  $Re_D = 10700$ . Results are compared with those of Xu and Antonia (2002) at  $Re_D = 86000$  and Ferdman *et al.* (2000) at  $Re_D = 24000$ . A linear best-fit line is applied to the data of the current work to calculate  $B_u$  and  $x_0/D$ .

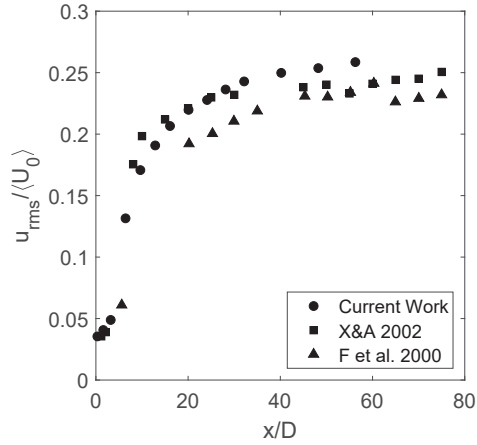


Figure 5.2: Downstream evolution of the centerline turbulence intensity  $(u_{rms}/\langle U_0 \rangle)$  in an axisymmetric jet at  $Re_D = 10700$ . Results are compared with those of Xu and Antonia (2002) at  $Re_D = 86000$  and Ferdman *et al.* (2000) at  $Re_D = 24000$ .

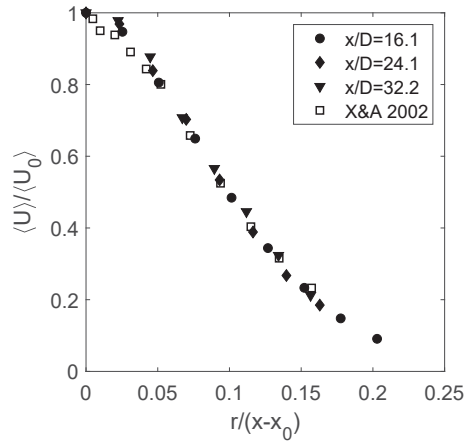


Figure 5.3: Normalized radial profiles of the mean velocity at  $x/D = 16.1$ ,  $x/D = 24.1$ , and  $x/D = 32.2$  for an axisymmetric jet at  $Re_D = 10700$ , where  $x_0/D = 3.8$ . Results are compared with those of Xu and Antonia (2002) at  $Re_D = 86000$ , where  $x_0/D = 2.6$ .

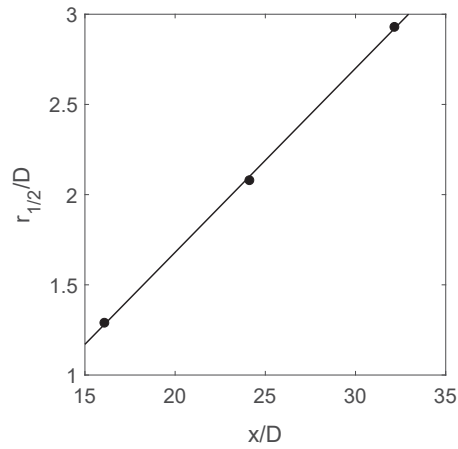


Figure 5.4: Downstream evolution of the jet's half-width ( $r_{1/2}$ ) for an axisymmetric jet at  $Re_D = 10700$ . A linear best-fit line is fit to the data to calculate the spreading rate  $S_u$ .

Measurements of the mean velocity ( $\langle U \rangle$ ) along radial profiles located at  $x/D = 16.1, 24.1,$  and  $32.2$  are depicted in figure 5.3. The radial profiles (which are all located in the self-similar region of the jet) all collapse onto the same curve and agree well with the radial profile of Xu and Antonia (2002) measured at  $x/D = 20$ . The jet's half-width ( $r_{1/2}$ ) is calculated by fitting a Gaussian curve to the data of figure 5.3, so that the location at which  $\langle U \rangle = \frac{1}{2}\langle U_0 \rangle$  can be identified. The results are plotted in figure 5.4, and are consistent with what is predicted from equation (2.13);  $r_{1/2}$  varies linearly with respect to  $x$  in the self-similar region of the jet. The jet's spreading rate ( $S_u$ ), calculated from a best-fit line of the data presented in figure 5.4, is approximately 0.102, which is slightly higher than the values of  $S_u$  reported by Xu and Antonia (2002) and Ferdman *et al.* (2000), 0.095 and 0.089, respectively. However, as may be observed from table 5.1, the value of  $S_u$  calculated herein agrees very well with that of other turbulent jet studies.<sup>1</sup>

Given that the jet characteristics ( $B_u, x_0/D, S_u,$  and  $u_{rms}/\langle U_0 \rangle$ ) reported in the current subsection fall within the range of quantities measured in the literature (as demonstrated in table 5.1) and, in particular, agree very well with studies undertaken using stationary hot-wire measurements in fully-developed turbulent pipe jets, it is concluded that the surrounding enclosure does not have a significant effect on the dynamics of the center jet, as predicted from equation (3.5). Consequently, it is assumed that similar predictions for the annular jet and coflow are also valid,

---

<sup>1</sup> Considering the turbulence intensity ( $u_{rms}/\langle U \rangle$ ) in these profiles is, for the most part, high (approaching a maximum of 66% at the furthest radial locations, which affects the accuracy of a stationary hot-wire probe), the agreement with other results, in this context, is in fact excellent.

such that the effects of the enclosure on the dynamics of the coaxial jets should be negligible.

### 5.1.2 Exit Profiles

Typical velocity and temperature profiles at the exit of the coaxial jet apparatus were measured and are provided in this subsection. Note that these measurements were performed to verify the design of the coaxial jet apparatus, and the conditions under which they were obtained (i.e. Reynolds numbers, temperatures) may differ slightly from those used in the subsequent experiments.

#### Velocity Profiles

Velocity profiles at the exit of the coaxial jet apparatus were measured using a single-normal hot-wire. The results are presented in figure 5.5. To verify the symmetry of the apparatus, measurements were performed along four different cross-sections of the apparatus (labeled  $y+$ ,  $y-$ ,  $z+$ , and  $z-$ , as depicted in figure 5.5). The collapse of the mean velocity and turbulence intensity profiles for the four cross-sections is excellent in the regions of the flow directly above the center jet, annular jet, and coflow. Small differences are observed between the  $y$  and  $z$  profiles in the shear layers between jets, in part due to differences in the hot-wire probe's orientation. During these measurements, the hot-wire probe was positioned such that it was parallel to the  $z$  axis and perpendicular to the  $y$  axis. As a result, the hot-wire probe is exposed to much larger velocity gradients when measurements are made in the shear layer along the  $y$  axis. Accordingly, flow symmetry only necessitates that the  $z+$  and  $z-$  profiles collapse onto each other, and the  $y+$  and  $y-$  profiles collapse onto each other. This can be observed in figure 5.5, although as stated earlier, the collapse of the data for all four cross-sectional profiles is excellent in the regions of the flow which are not immediately downstream of the jet walls.

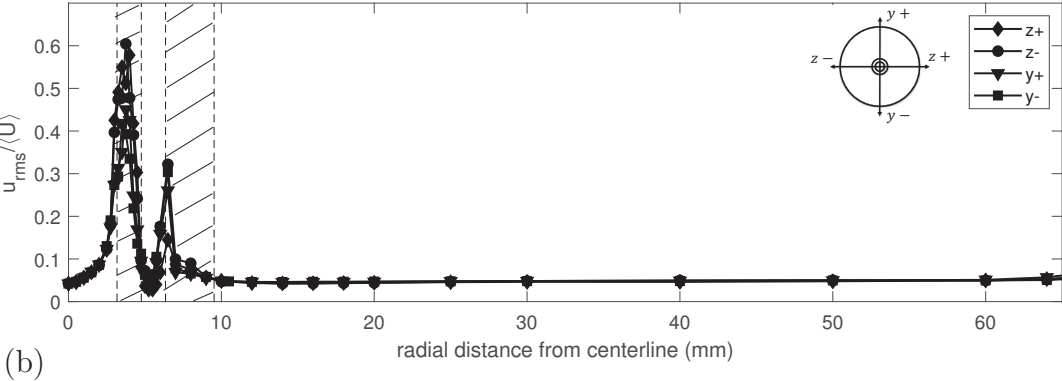
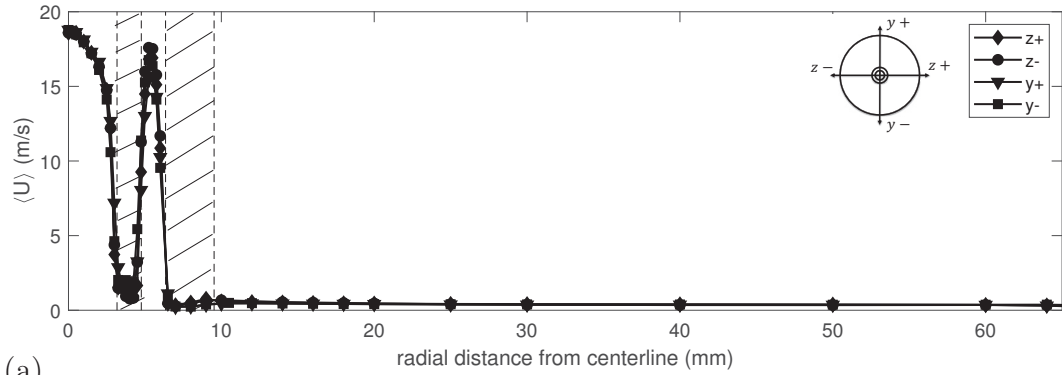


Figure 5.5: (a) Mean velocity ( $\langle U \rangle$ ), and (b) turbulence intensity ( $u_{rms}/\langle U \rangle$ ) at  $x = 1.5$  mm along the  $y^+$ ,  $y^-$ ,  $z^+$ , and  $z^-$  axes. The Reynolds numbers ( $Re_{D_h} = U_J D_h / \nu$ ) of the center and annular jets are 5300 and 2600, respectively, and the velocity in the coflow is 0.4 m/s. The locations of the jet walls are denoted by shading for clarity.

Finally, it should be noted that the coflow has a top-hat velocity profile, validating the choice of flow conditioning elements presented in §3.2.3. The mean velocity in the coflow is approximately 0.4 m/s, which agrees well with the average velocity predicted from the mass flow rate (0.43 m/s), and the turbulence intensity is less than 5%. As the rms velocities are extremely small (0.02 m/s), the effects of electronic noise on the measurements are notably larger here. Thus, the actual turbulence intensity of the coflow is expected to be lower than its measured value.

### Temperature Profiles

Mean and rms temperature profiles at the exit of the coaxial jet apparatus were measured using a cold-wire thermometer and are presented in figure 5.6. The coflow was heated such that the temperature of the center jet was approximately 4.5 degrees below the temperature of the coflow. Although the temperature in the center jet is nearly uniform, this is not the case in the annular jet due to either (i) radial (conductive or convective) heat transfer from the fluid emanating from the heated coflow to the unheated flow from the annular jet and/or (ii) heat transfer through the wall of the annular jet. Nevertheless, the difference between the temperature in the center and annular jets is relatively small, and the vast majority of heated air is contained in the coflow. Moreover, analysis of the rms temperatures ( $t_{rms}$ ) reveals that these are extremely small ( $t_{rms} < 0.05^\circ\text{C}$ ) and of the same magnitude as values of  $t_{rms}$  measured in flows where no fluid is heated, in addition to being nearly uniform (with the exception of regions close to the shear layers).

## 5.2 Validation of Measurement Techniques

Having validated the quality of the flow in the experimental apparatus, the current section focuses on validating the novel instrumentation used herein — specifically, the interference probe and 3-wire probe. Validation measurements for the

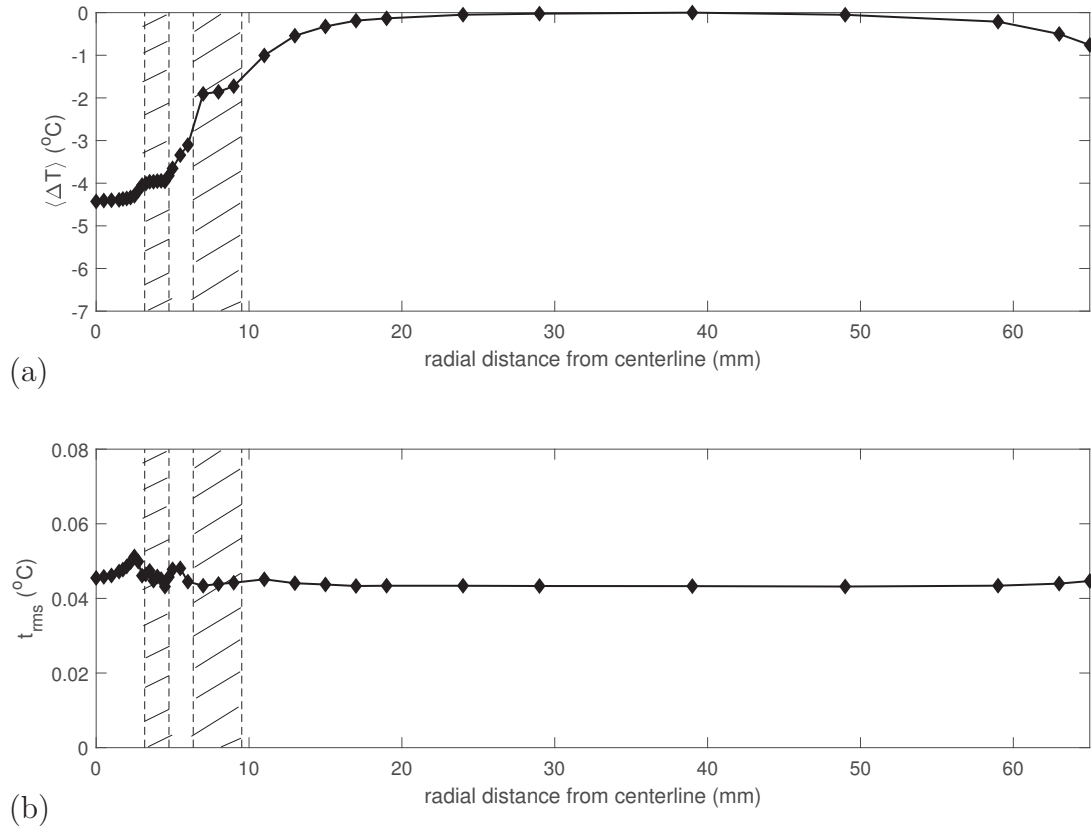


Figure 5.6: (a) Mean and (b) rms temperature profiles at  $x = 1.5$  mm. The Reynolds numbers ( $Re_{D_h} = U_J D_h / \nu$ ) of the center and annular jets are 5300 and 2600, respectively, and the velocity in the coflow is 0.4 m/s. The locations of the jet walls are denoted by shading for clarity.

interference probe were performed in the center jet, which, as mentioned earlier, is well suited to making such measurements, whereas validation measurements for the 3-wire probe were performed with all three jets of the coaxial jet apparatus (i.e. the center jet, annular jet, and coflow).

### 5.2.1 Interference Probe Measurements in Axisymmetric Jets

Measurements were undertaken using an interference probe in axisymmetric jets of varying helium concentration. The purpose of these experiments was to demonstrate the accuracy of these probes, and in particular, verify that the Wiener Filter described in the previous chapter adequately filters out the noise. Three cases are studied: (i) a jet initially containing 0% He by mass (i.e. pure air), (ii) a jet initially containing 4% He by mass, and (iii) a jet initially containing 6% He by mass. The Reynolds numbers ( $Re_D = U_J D / \nu$ ) of these flows are summarized in table 5.2, and were specifically chosen to ensure the momentum flow rate was the same for each case. Measurements were performed along the centerline and limited to  $1.6 \leq x/D \leq 32.2$ , as the SNR of the interference probe degraded farther downstream. Since the (i) the density ratios of the jet and ambient fluid ( $S = \rho_J / \rho_\infty$ ) are close to unity, and (ii) Froude Numbers (F) are relatively large, momentum forces are assumed to dominate over buoyancy forces in the jet. This was verified in two different ways. First, the non-dimensional parameter ( $x_1$ ) defined by Chen and Rodi (1980) (see §2.3.3) was calculated. Given that it is less than 0.5 at the farthest downstream location, the jet can be quantitatively classified as non-buoyant in the region of investigation. Second, the ratio of production of turbulent kinetic energy by buoyancy ( $g\langle u\rho\rangle/\langle\rho\rangle$ ) to the dissipation of turbulent kinetic energy ( $\epsilon$ ) was also calculated. As may be observed in table 5.2, the maximum value of this ratio does not exceed 0.3%, further confirming that buoyancy effects are small.

Table 5.2: Experimental properties of axisymmetric jets in validation experiments for the interference probe, including the initial concentration of helium ( $C_J$ ), the density ratio ( $S = \rho_J/\rho_\infty$ ), the Reynolds number ( $Re_D$ ), the Froude number (F), the maximum value of ( $x_1$ ) as defined by Chen and Rodi (1980), and the maximum ratio of production of turbulent kinetic energy by buoyancy ( $g\langle u\rho\rangle/\langle\rho\rangle\epsilon$ ) to the dissipation of turbulent kinetic energy ( $\epsilon$ ).

Case	$C_J$	$S$	$Re_D$	F	$x_{1,max}$	$(g\langle u\rho\rangle/\langle\rho\rangle\epsilon)_{max}$
I	0	1	4600	$\infty$	0	0
II	0.04	0.8	3900	10100	0.34	0.2%
III	0.06	0.73	3700	7400	0.4	0.3%

Measurements of the decay of the inverse of the normalized velocity ( $U_J/\langle U_0\rangle$ ) and turbulence intensity ( $u_{rms}/\langle U_0\rangle$ ) are presented in figures 5.7 and 5.8, respectively. The mean centerline velocity decays faster as the density ratio decreases, which is consistent with previous work on variable density jets, such as that of Amielh *et al.* (1996). The latter also observed faster decay of  $\langle U_0\rangle$  as the density ratio decreased and concluded that lighter gases mix more rapidly compared to heavier gases. The effects of density on the mean centerline velocity are accounted for by non-dimensionalizing the results in terms of the effective diameter ( $D_e$ ), defined below:

$$D_e = \sqrt{\frac{\rho_J}{\rho_\infty}} D. \quad (5.1)$$

Measurements of  $\langle U_0\rangle$  for jets with different density ratios collapse when plotted as a function of  $x/D_e$  (see figure 5.7(b)). Moreover, the centerline decay constant defined in terms of the effective diameter ( $B_{u,e}$ ) was inferred from:

$$\frac{\langle U_0\rangle}{U_j} = \frac{B_{u,e}}{(x - x_0)/D_e}, \quad (5.2)$$

and found to be constant and approximately equal to 6.0 for the three cases presented in figure 5.7(b). The same non-dimensionalization has been used in previous studies of variable-density jets and a similar collapse for the decay of  $\langle U_0 \rangle$  was also observed in these studies (Amielh *et al.* 1996; Panchapakesan and Lumley 1993b). Furthermore, note that for the pure air case ( $S = 1$ ),  $B_{u,e} = B_u$  (since  $D_e = D$ ), which agrees well with the data presented in §5.1.1.

Measurements of  $u_{rms}/\langle U_0 \rangle$  for each of the three cases investigated collapse in the far-field, and asymptote to a value of approximately 0.23. The centerline turbulence intensity approaches its asymptotic value faster as the density ratio  $S$  decreases, similarly to what was observed by Amielh *et al.* (1996), who demonstrated that  $u_{rms}/\langle U_0 \rangle$  increased more quickly as (i)  $S$  decreased and, to a lesser extent, (ii) as  $Re_D$  decreased. It should be noted that small differences (in  $B_u$  and the asymptotic value  $u_{rms}/\langle U_0 \rangle$ , for example) are observed between the velocity field measured with an interference probe in pure air ( $S = 1$ ) and the single-normal hot-wire measurements presented in §5.1.1. This may be explained by the fact the single normal hot-wire measurements were performed farther downstream, allowing for greater accuracy in calculating  $B_u$  and identifying the asymptotic value of  $u_{rms}/\langle U_0 \rangle$ . Moreover, experimental uncertainty, from identifying the location of the jet's centerline or hot-wire drift, may also account for differences observed between the two set of experiments. Given that these differences are small, and that the velocity measurements presented in the current subsection agree well with those reported by previous studies (see table 5.1), it can be concluded that the interference probe accurately measures the velocity field of a turbulent jet.

Measurements of the downstream evolution of the mean centerline concentration ( $\langle C_0 \rangle$ ) and the intensity of concentration fluctuations ( $c_{rms}/\langle C_0 \rangle$ ) are presented

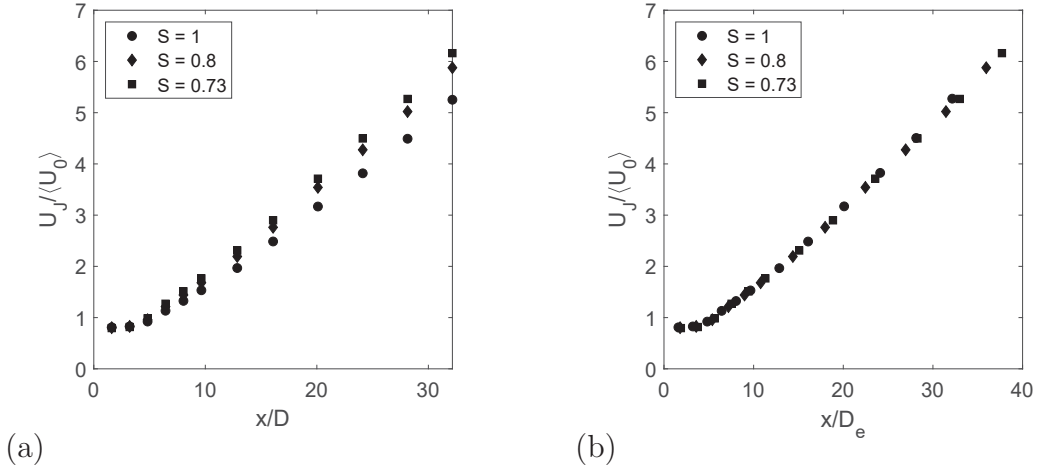


Figure 5.7: Downstream evolution of the mean centerline axial velocity ( $\langle U_0 \rangle$ ) in axisymmetric jets with density ratios of  $S = 1, 0.8,$  and  $0.73$ . The data are plotted as a function of (a)  $x/D$ , and (b)  $x/D_e$ .

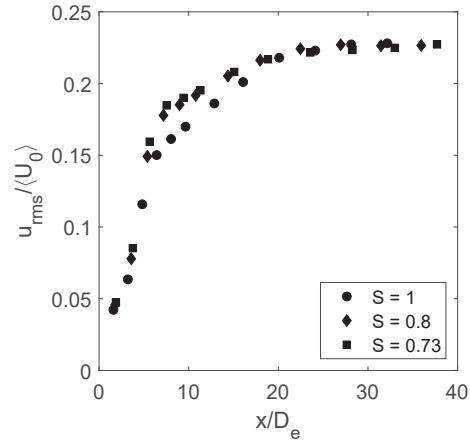


Figure 5.8: Downstream evolution of the turbulence intensity ( $u_{rms} / \langle U_0 \rangle$ ) in axisymmetric jets with density ratios of  $S = 1, 0.8,$  and  $0.73$ .

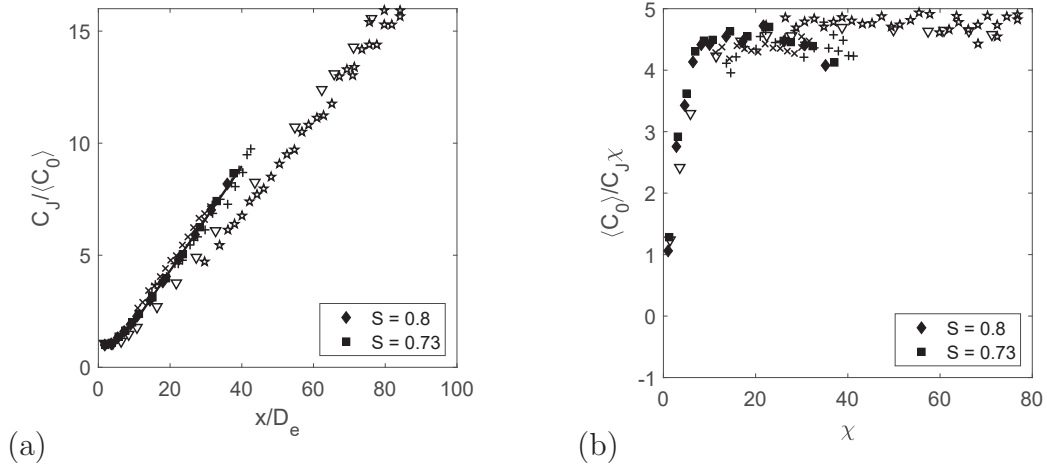


Figure 5.9: Downstream evolution of the mean centerline concentration ( $\langle C_0 \rangle$ ) in axisymmetric jets with density ratios of  $S = 0.8$  and  $0.73$ . The current data, ( $\blacklozenge$ :  $S = 0.8$ ,  $\blacksquare$ :  $S = 0.73$ ) are plotted along with the data of Pitts (1991a) ( $\times$ :  $S = 1.55$ ,  $+$ :  $S = 0.55$ ,  $\star$ :  $S = 0.14$ ) and Mi *et al.* (2001) ( $\nabla$ :  $S = 0.85$ ) for the purposes of comparison. In (a),  $C_J / \langle C_0 \rangle$  is plotted as a function of  $x/D_e$ . In (b),  $\langle C_0 \rangle / C_J \chi$  is plotted as a function of  $\chi$ , where  $\chi = (x - x_{0,c})/D_e$ . In the latter case, self-similarity is indicated by an asymptotic approach to a horizontal straight line.

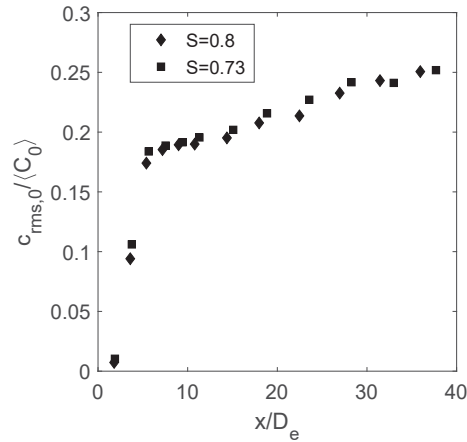


Figure 5.10: Downstream evolution of  $c_{rms} / \langle C_0 \rangle$  in axisymmetric jets with density ratios of  $S = 0.8$  and  $0.73$ .

in figures 5.9 and 5.10, respectively. Like  $\langle U_0 \rangle$ ,  $\langle C_0 \rangle$  is nominally expected to be inversely proportional to  $x$ . A best-fit line is fit to the data in figure 5.9(a) for ( $x/D_{1,e} > 10$ ) and used to calculate the centerline concentration decay constant ( $K_c$ ), which is found to be 4.33 for the jet in which  $S = 0.8$ , and 4.27 for the jet in which  $S = 0.73$ . These values are on the lower end of what has previously been previously observed in fully-developed pipe jets, where the values of  $K_c$  were found to fall between 4.42 and 5.44 (Mi *et al.* 2001). However, the current measurements were limited to  $x/D_{1,e} < 40$ , which also affects the calculated value of  $K_c$ . (As mentioned previously, measurements farther downstream are affected by SNR issues. Increasing the initial He concentration to offset this would have introduced other complications, including buoyancy effects.) Despite slight differences in the calculated values of  $K_c$ , the decay of  $(C_J/\langle C_0 \rangle)$ , when plotted as a function of  $x/D_{1,e}$ , agrees well with the results of Pitts (1991a) for jets of  $CH_4$  ( $S = 0.55$ ) and  $C_3H_8$  ( $S = 1.55$ ) flowing into air. The fact that the current measurements do not agree as well with the results of Pitts (1991a) for a He jet flowing into air ( $S = 0.14$ ), or the results of Mi *et al.* (2001) for a heated jet ( $S = 0.85$ ), may simply reflect the importance that initial conditions have on the evolution of a scalar jet (see §2.3.2). Finally, given that measurements of  $c_{rms,0}/\langle C_0 \rangle$ , which asymptote to a value of approximately 0.25 at the farther downstream position, are in good agreement with the aforementioned works, it can be inferred that the Wiener Filter used in post-processing correctly filters out noise in the concentration measurements. Consequently, like the velocity field, the concentration field of a turbulent jet can be accurately measured with an interference probe.

Table 5.3: Experimental properties of the center jet, annular jet, and coflow for the four cases of the validation experiments. The initial helium concentration of the center jet ( $C_1$ ), the maximum temperature difference between the coflow and center jet ( $\Delta T_{max} = T_1 - T_3$ ), the Reynolds numbers of the center and annular jets ( $Re_{D_{h,1}}$ ,  $Re_{D_{h,2}}$ ), the density ratio of the annular to center jets ( $S = \rho_2/\rho_1$ ), the velocity ratio of the annular to center jets ( $R = U_2/U_1$ ), the coflow velocity ( $U_3$ ), and the maximum ratio of the production of turbulent kinetic energy by buoyancy ( $g\langle u\rho\rangle/\langle\rho\rangle$ ) to the dissipation of turbulent kinetic energy ( $\epsilon$ ) are provided<sup>1</sup>.

Case	$C_1$	$\Delta T_{max}(\text{°C})$	$Re_{D_{h,1}}$	$Re_{D_{h,2}}$	$S$	$R$	$U_3$ (m/s)	$\frac{g\langle u\rho\rangle}{\langle\rho\rangle\epsilon}$
I: H & T	0.04	-5.95	3900	2300	1.25	0.9	0.4	0.03%
II: nH & T	0	-5.95	4500	2300	1	1	0.4	0.01%
III: H & nT	0.04	1.10	3900	2300	1.25	0.9	0.4	0.03%
IV: nH & nT	0	1.10	4500	2300	1	1	0.4	0.002%

<sup>1</sup> Note that the subscripts 1, 2, and 3 are respectively used to refer to the center jet, annular jet, and coflow, that H and nH are respectively used to refer to cases with and without helium, and that T and nT are respectively used to refer to cases with and without the heated coflow.

## 5.2.2 3-Wire Probe Measurements in Coaxial Jets

Measurements were conducted along the axis of the coaxial jets to assess the accuracy of the 3-wire probe. The objective of these experiments was to show that the effects of temperature on the interference probe are adequately compensated, and to further investigate the behavior of the cold-wire thermometer in turbulent flows of uniform and variable compositions (i.e. with and without helium fluctuations). Four cases are specifically investigated, and the relevant experimental parameters of the jets are summarized in table 5.3 for each case. In cases I and III, a He/air mixture ( $C_1 = 0.04$ ) is supplied to the center jet, whereas in cases II and IV, pure air is supplied to the center jet. In cases I and II, the coflow is heated such that the center jet is 5.95°C cooler than the coflow, whereas in cases III and IV, the coflow is not heated. Due to the Joule-Thompson effect in the coflow (in which the temperature of the air drops after being throttled through a valve, orifice, or porous plug), when the coflow is not heated, the temperature of the center jet is

slightly higher. Accordingly, the flow in cases III and IV is not isothermal, but the temperature fields of these cases are distinct from those of cases I and II. As was the case in the previous subsection, which presents validation measurements for the interference probe, the flow rate was held constant for the jets described in table 5.3. Again, momentum forces are assumed to dominate over buoyancy forces, and this is confirmed by calculating the ratio of the production of turbulent kinetic energy by buoyancy ( $g\langle u\rho\rangle/\langle\rho\rangle$ ) to the dissipation of turbulent kinetic energy ( $\epsilon$ ). As may be seen in table 5.3, the effects of buoyancy are indeed small.

Velocity and concentration measurements for the four cases are presented in figures 5.11 and 5.12. Similarly to the measurements presented in §5.2.1, some differences are observed between cases with helium fluctuations (I&III) and those without (II & IV). Accordingly, both velocity and concentration measurements are plotted as a function of the effective diameter of the center jet ( $D_{1,e}$ ). Whereas profiles of  $\langle U \rangle$  collapse when plotted as a function of  $x/D_{1,e}$ , small differences remain between profiles of  $u_{rms}/\langle U \rangle$  with helium fluctuations (I & III) and those without (II & IV). In particular,  $u_{rms}/\langle U \rangle$  approaches its asymptotic value faster in jets with helium fluctuations (cases I&III) than in jets of pure air (cases II & IV), consistent with the results presented in §5.2.1. Since temperature is a passive scalar (maximum temperature differences in the flow are  $< 6^\circ\text{C}$ , and do not have a significant impact on the density and other fluid properties), it is expected that the velocity and concentration fields will not be affected by the temperature field. This is confirmed in figures 5.11 and 5.12 — cases in which the coflow is heated (I & II) collapse onto the equivalent cases in which the coflow is not heated (III & IV). Consequently, it can be assumed

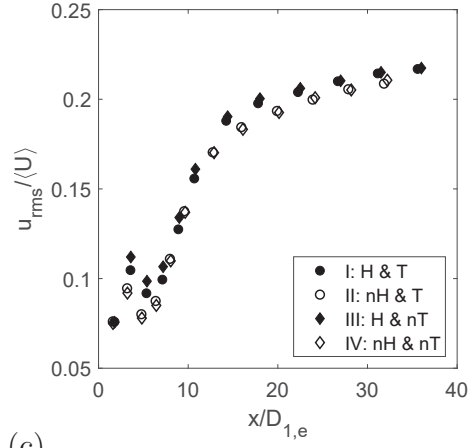
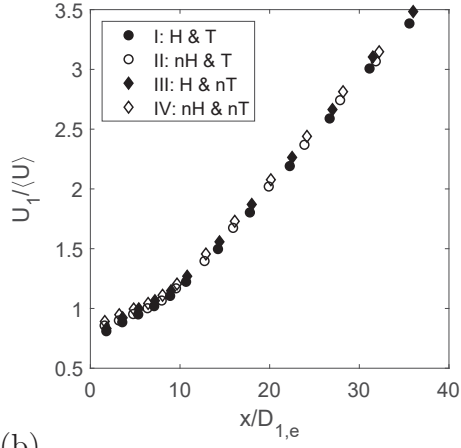


Figure 5.11: Downstream evolution of (a)  $\langle U \rangle$ , and (b)  $u_{rms} / \langle U \rangle$  in the coaxial jets for the four cases presented in table 5.3.

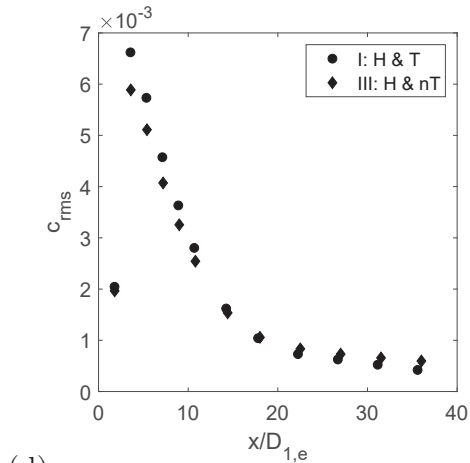
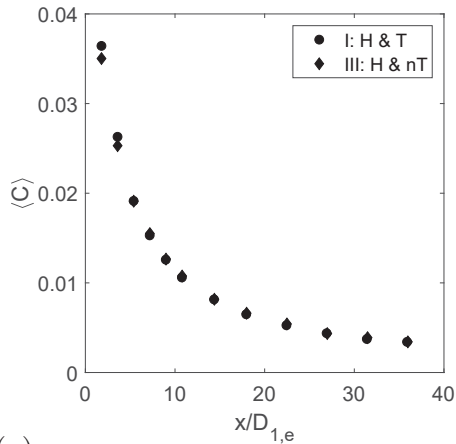


Figure 5.12: Evolution of (a)  $\langle C \rangle$ , and (b)  $c_{rms}$  in the coaxial jets for the two cases presented in table 5.3 in which a He/air mixture ( $C_1 = 0.04$ ) was supplied to the center jet.

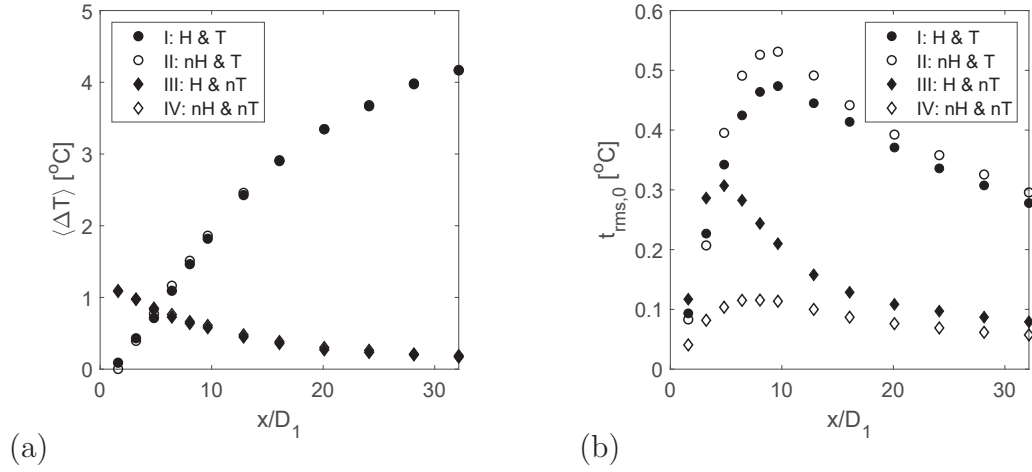


Figure 5.13: Downstream evolution of (a)  $\langle \Delta T \rangle$ , where  $\Delta T = T - T_{ref}$ , and (b)  $t_{rms}$  in the coaxial jets for the four cases presented in table 5.3.  $T_{ref}$  is defined to be the temperature at the exit of the center jet ( $T_1$ ).

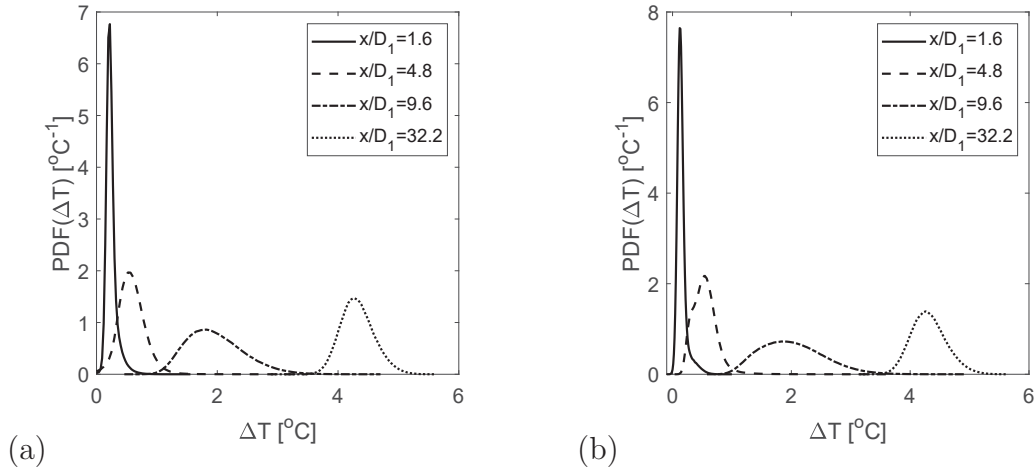


Figure 5.14: PDFs of  $\Delta T$  for (a) Case I (helium fluctuations), and (b) Case II (no helium fluctuations). Note that measurements are bounded between 0 and  $\Delta T_{max} = 5.95$ , as expected.

that the temperature compensation method described in §4.3.2 correctly accounts for the effect of temperature on the interference probe.

Temperature measurements along the axis of the jets are presented in figure 5.13. The collapse of mean temperature measurements ( $\langle T \rangle$ ) for cases with different concentration fields is excellent, consistent with what was observed for the cold-wire in laminar flow. Accordingly, the results presented in figure 5.13(a) may serve as additional proof that the cold-wire thermometer is insensitive to the presence of helium concentration in the jet. In contrast, significant differences in  $t_{rms}$  are observed for flows with different concentration fields. It is emphasized that this does not necessarily mean that the cold-wire thermometer is sensitive to helium. There is substantial evidence suggesting that the data of figure 5.13(b) are not the result of measurement error, but rather a representation of physical differences in the transport of temperature in flows with different concentration fields. This will be explained subsequently (although it should be noted that the current discussion is primarily limited to the cases in which the coflow was heated (I & II), since the temperature fluctuations are sufficiently large that the SNR of the measurements is high).

If the cold-wire were actually sensitive to helium and erroneously interpreting helium fluctuations as temperature fluctuations, then  $t_{rms}$  would consistently be higher in flows with helium fluctuations (cases I & III). However, the opposite is observed for cases in which the coflow is heated — for  $x/D_1 > 3.2$ ,  $t_{rms}$  is larger in flows of pure air (case II) than when they are not (case I). Moreover, at  $x/D_1 = 3.2$ , where helium fluctuations are largest (see figure 5.13(b)), the values of  $t_{rms}$  for cases I and II are similar. Inspection of the PDFs of cases I & II, some of which are presented in figure 5.14, show that measurements of  $\Delta T$  remain for the most part

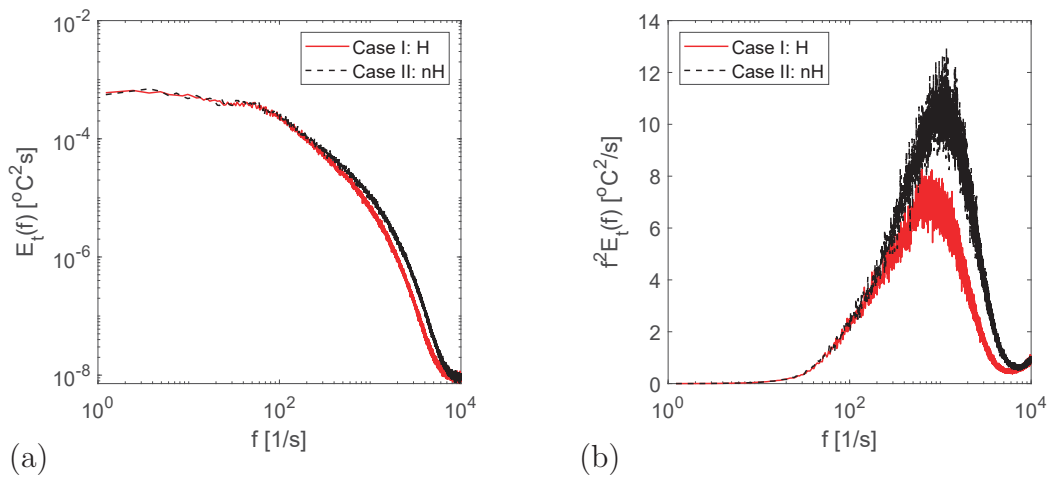


Figure 5.15: Temperature spectra for cases I (helium fluctuation) and II (no helium fluctuations) at  $x/D_1 = 32.2$ . In (a), the temperature spectrum  $E_t(f)$  is plotted as function of  $f$ . In (b),  $f^2 E_t(f)$ , which is proportional to the dissipation spectrum, is plotted as a function of  $f$ . The area under the curve is proportional to the dissipation and is observed to be larger for case II (no helium fluctuations) than for case I (helium fluctuations).

bounded between 0 and  $\Delta T_{max} = 5.95$ , as they should be. The temperature field is therefore measured with a reasonable degree of accuracy.

In figures 5.7, 5.8, and 5.11, it was observed that the presence of helium concentration has a small effect on the dynamics of the velocity field. It should therefore not be surprising that the dynamics of the temperature field are affected as well, given that it is advected by the velocity field. Examination of the temperature spectra of cases in which the coflow is heated (see figure 5.15) reveals that differences between the cases are greatest at small scales, which implies that these may be attributed to the effects of variable viscosity or variable thermal diffusivity, and not to buoyancy effects, or other phenomena that cause large-scale differences. Talbot *et al.* (2013) observed differences between variable viscosity jets (in which the initial viscosity of the jet,  $\nu_J$ , and surrounding fluid,  $\nu_\infty$ , are not equal) and constant density jets (in which  $\nu_J = \nu_\infty$ ). Through careful analysis of the kinetic energy budget, they demonstrated that the dissipation is affected by variable viscosity effects and, for the specific case of jets issuing into quiescent air or a slow coflow, proportional to  $\nu_\infty/\nu_J$ . Consequently, dissipation is reduced for a jet mixing in a less viscous fluid, and enhanced for a jet mixing in a more viscous fluid. Although the work of Talbot *et al.* (2013), and other related studies (Voivenel *et al.* 2016; Danaila *et al.* 2017) focused on the velocity field, it is likely that these findings can be extended to the scalar field. This notion is supported by figure 5.15(b), which demonstrates that the dissipation of temperature in case I, in which the more viscous and thermally diffusive center jet mixes with the less viscous and thermally diffusive annular jet and coflow, is lower than that observed in case II, where the variations in fluid properties are minimal.

A more thorough investigation of the effects of variable viscosity and variable thermal diffusivity on passive scalars, such as temperature, is beyond the scope of

the current work, but nevertheless merits consideration given the complex behavior of the temperature field observed herein. For example, the presence of helium has a significantly different effect on cases in which the heated fluid emanates from the coflow (I & II) and cases in which the heated fluid emanates from the center jet (III & IV). Given the results presented in this subsection, it is concluded that there is ample evidence that differences in the physical properties of the flow explain differences in the measured temperature field for cases with (I & III) and without (II & IV) helium fluctuations. Moreover, it was shown that even in the presence of helium fluctuations, the temperature appears to be measured correctly (no spurious measurements of temperature are recorded). Accordingly, the 3-wire probe, consisting of an interference probe combined with a cold-wire thermometer, can be used to accurately measure velocity, helium concentration, and temperature in a turbulent flow.

## CHAPTER 6

### Results

As stated in Chapter 1, the second objective of this work was to study multi-scalar mixing in coaxial jets by way of simultaneous velocity-scalar measurements. The present chapter discusses the evolution of multiple scalars and velocity along the axis of coaxial jets with different momentum ratios:  $M_2/M_1 = 0.77$ ,  $M_2/M_1 = 2.1$ , and  $M_2/M_1 = 4.2$ , where  $M_1$  and  $M_2$  are the momentum flow rates of the center and annular jets, respectively. The experimental conditions are described in §6.1, and the results, including mean and rms quantities, correlation coefficients, third-order moments, PDFs, JPFDs, and conditional expectations, are presented in §6.2-§6.6. The aforementioned measurements were chosen (i) to describe the mixing processes occurring in the coaxial jets, and, in some cases, (ii) for their relevance to turbulence modeling.

### 6.1 Experimental Conditions

The 3-wire probe developed as part of this work was used to make measurements for the three cases presented in table 6.1. The center jet was supplied with a mixture composed of 6% helium and 94% air by mass ( $C_1 = 0.06$ ), and the coflow was heated such that there was a 7.0°C difference in temperature between the coflow and center jet ( $\Delta T_{max} = T_3 - T_1 = 7.0^\circ\text{C}$ , where  $T_1$  and  $T_3$  are the temperatures at the exits of the center jet and coflow, respectively). This temperature difference was kept constant (to within 0.1°C) between the three different experiments. Note that the momentum ratio ( $M$ ) is principally used to describe the different coaxial jets, given that when

Table 6.1: Properties of the flow in the center jet, annular jet and coflow for the three cases investigated, including the He mass fraction at exit of the center jet ( $C_1$ ), the temperature difference between the center jet and coflow ( $\Delta T_{max}$ ), the Reynolds number of the center and annular jets (respectively  $Re_{D_h,1}$ ,  $Re_{D_h,2}$ ), the velocity of coflow ( $U_3$ ), the density ( $S = \rho_2/\rho_1$ ) and velocity ( $R = U_2/U_1$ ) ratios of the center and annular jets, and the maximum ratio of production of turbulent kinetic energy by buoyancy ( $g\langle u\rho\rangle/\langle\rho\rangle$ ) to the dissipation of turbulent kinetic energy ( $\epsilon$ ).

Case	$C_1$	$\Delta T_{max}$ ( $^{\circ}\text{C}$ )	$Re_{D_h,1}$	$Re_{D_h,2}$	$U_3$ (m/s)	$S$	$R$	$\frac{g\langle u\rho\rangle}{\langle\rho\rangle\epsilon}$
I: M=0.77	0.06	7.0	3700	2000	0.4	1.37	0.75	0.03%
II: M=2.1	0.06	7.0	3700	3400	0.4	1.37	1.25	0.03%
III: M=4.2	0.06	7.0	3700	4700	0.4	1.37	1.75	0.02%

<sup>1</sup> As before, note that the subscripts 1, 2, and 3 are respectively used to refer to the center jet, annular jet, and coflow.

the densities of these jets differ (i.e.  $S \neq 1$ ), their behavior is best characterized by  $M$ , and not  $R$  (see, for example, Favre-Marinet and Schettini 2001).

The 3-wire probe simultaneously measured velocity ( $U$ ), helium concentration ( $C$ ), and temperature ( $T$ ). The two scalars (helium concentration and temperature), were normalized to be 1 at the exit of their respective jets, thus, effectively representing the mixture fractions of these flows. The normalized scalars are defined as follows:  $\phi_1 = C/C_1$  and  $\phi_3 = (T - T_1)/\Delta T_{max}$ . For flows in which multiple scalars are mixed, such as the one herein, the flow can be thought of as  $n$  scalars mixing in an additional fluid, or as  $n + 1$  scalars, where the additional fluid also transports a scalar. The latter convention is used in the present experiments, and the flow is accordingly viewed as containing three scalars.  $\phi_2$  therefore represents the ‘‘scalar’’ of the (cold, helium-free) annular jet. Given that the scalars are defined as mixture

fractions, which must sum to one assuming (i) the ambient (unheated) air surrounding the coaxial jets does not penetrate the measurement domain,<sup>1</sup> and (ii) differential diffusion effects are negligible,<sup>2</sup> the value of  $\phi_2$  can be inferred from measurements of the other two scalars:

$$\phi_2 = 1 - \phi_1 - \phi_3. \quad (6.1)$$

## 6.2 Statistical Moments

The discussion of the results obtained herein begins with statistical moments measured along the axis of the jets. Measurements of (i) mean quantities, (ii) second-order quantities, and (iii) third-order quantities are therefore subsequently described.

### 6.2.1 Mean Quantities

The downstream evolution of the mean quantities ( $\langle U \rangle$ ,  $\langle \phi_1 \rangle$ ,  $\langle \phi_2 \rangle$ ,  $\langle \phi_3 \rangle$ ) is presented in figure 6.2. As per the discussion in §2.3.4, the centerline of coaxial jets can be characterized by three different regions (see figure 6.1): (i) the potential core of the center jet, (ii) the inner mixing region, where the center and annular jets mix with each other, but not the coflowing fluid, and (iii) the fully merged region, where the coaxial jets behave similarly to a single jet with the same initial momentum.

---

<sup>1</sup> This is a reasonable assumption given that measurements are limited to  $x \leq 160$  mm, a value slightly larger than one coflow diameter (149.2 mm).

<sup>2</sup> Herein, like in the work of Rowinski and Pope (2013), it is assumed that turbulent diffusion dominates over molecular diffusion, and  $\phi_1$ , which represents the fraction of mass emanating from the center jet and consists of both helium and air, is effectively equal to  $C/C_1$ .

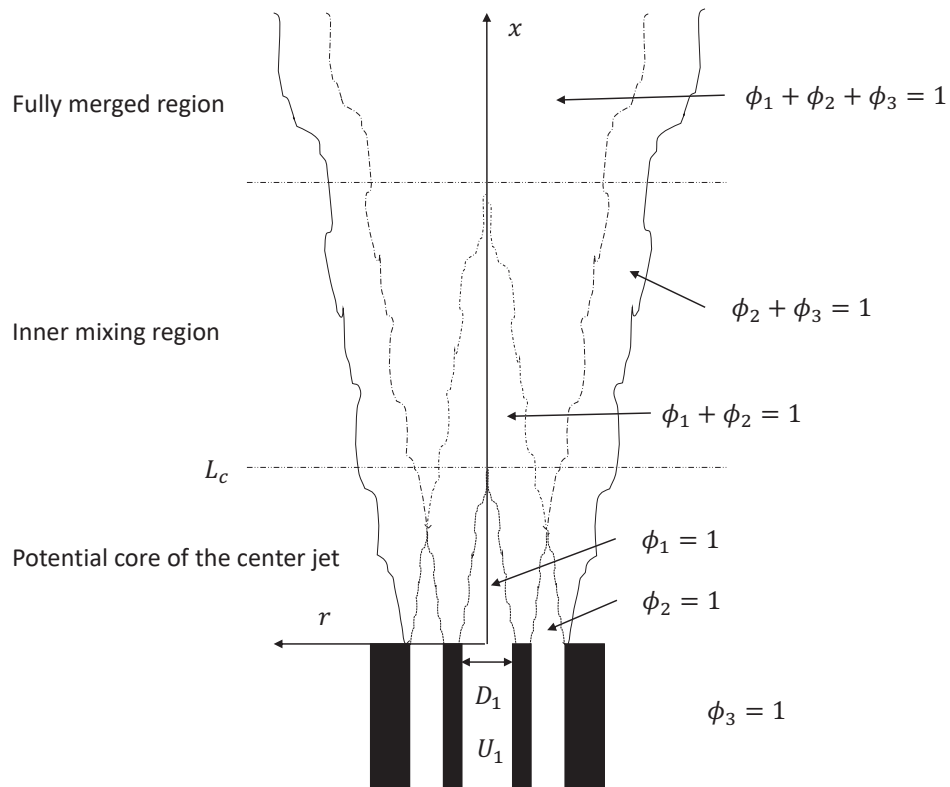
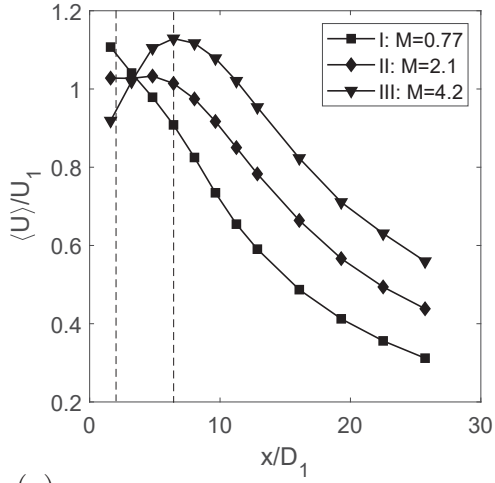
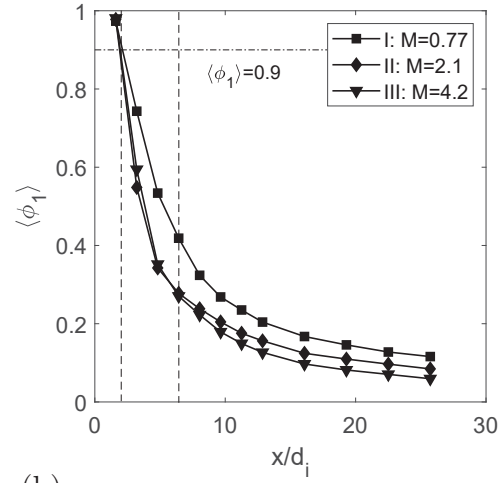


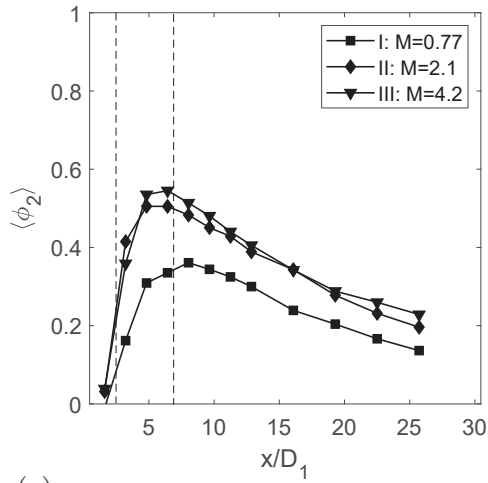
Figure 6.1: Schematic representation of the experimental flow depicting the three regions of interest *along the centerline*: (i) the potential core of the center jet (whose length is denoted by  $L_c$ ), (ii) the inner mixing region, and (iii) the fully-merged region.



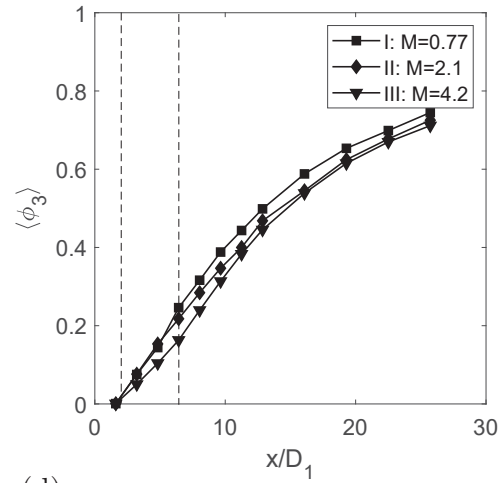
(a)



(b)



(c)



(d)

Figure 6.2: Downstream evolution of (a)  $\langle U \rangle$ , (b)  $\langle \phi_1 \rangle$ , (c)  $\langle \phi_2 \rangle$ , and (d)  $\langle \phi_3 \rangle$  along the centerline. Note that measurements of  $\langle U \rangle$  are non-dimensionalized using  $U_1$ , the average velocity at the exit of the center jet, and that the dashed lines delineate the three regions of the jet (the potential core of the center jet, inner mixing region, and fully merged region).

General trends in  $\langle U \rangle$ ,  $\langle \phi_1 \rangle$ ,  $\langle \phi_2 \rangle$ , and  $\langle \phi_3 \rangle$  in each of the three regions are first discussed, before examining the effect that  $M$  has on these quantities.

### Potential Core of the Center Jet

In figure 6.2, it can be observed that  $\langle \phi_1 \rangle \approx 1$ ,  $\langle \phi_2 \rangle \approx 0$ , and  $\langle \phi_3 \rangle \approx 0$  immediately beyond the exit of the center jet, as expected, since the potential core of this jet, which is characterized by  $\phi = 1$ , generally extends a few diameters beyond its exit. According to Villermaux and Rehab (2000), the end of the potential core ( $L_c$ ) can be defined by the location at which  $\langle \phi_1 \rangle = 0.9$ , which corresponds to a downstream position of  $1.6 < L_c/D_1 < 3.2$ . Schumaker and Driscoll (2012) concluded that  $L_c/D_1 = 5/M^{0.5}$  based on measurements from their own work, in which  $0.07 < M < 14.3$ ,  $1.1 < R < 11$  and  $0.06 < S < 0.48$ , as well from previous studies, in which  $1 < M < 146$ ,  $1.1 < R < 70$ , and  $0.028 < S < 1$ . As predicted, one may infer from figure 6.2(b) that  $L_c$  decreases as  $M$  increases. However, the current estimates of  $L_c$  appear relatively small when compared to the correlation of Schumaker and Driscoll (2012), which predicts that  $2.4 \leq L_c/D_1 \leq 5.7$ . It is worth pointing out that the relationship for  $L_c$  developed by Schumaker and Driscoll (2012) is based on data in which there is a lot of scatter, and does not take into account other factors — secondary density effects, area ratios, exit velocity profiles — on which  $L_c$  is slightly dependent (see Rehab *et al.* 1997; Favre-Marinet and Schettini 2001). Although there is certainly convincing evidence that  $L_c \sim M^{0.5}$  (Rehab *et al.* 1997; Favre-Marinet *et al.* 1999; Villermaux and Rehab 2000; Favre-Marinet and Schettini 2001; Schumaker and Driscoll 2012), more complex relationships may be needed to accurately predict  $L_c$  in different coaxial jets.

### Inner Mixing Region

Beyond the potential core of the center jet, and until approximately  $x/D_1 = 6.4$ ,  $\langle\phi_1\rangle$  decreases, while  $\langle\phi_2\rangle$  and  $\langle\phi_3\rangle$  both increase. Although the scalars evolve similarly for all three cases, this is not true of  $\langle U\rangle$ . In case I,  $\langle U\rangle$  immediately decreases; in case II,  $\langle U\rangle$  remains constant until approximately  $x/D_1 = 6.4$  before decreasing; and in case III,  $\langle U\rangle$  increases until  $x/D_1 = 6.4$ , and then starts to decrease. As will subsequently be discussed, this region of the coaxial jets may be referred to as the inner mixing region.

Although the inner mixing region was previously described as the region of flow where the center and annular jets mix with each other, but not the surrounding fluid, it is important to note that herein the definition will be slightly less strict — it is merely considered to be the region of flow dominated by mixing between the center and annular jets, which therefore consists primarily (but not necessarily entirely) of  $\phi_1$  and  $\phi_2$ . If, as discussed in §5.1.2, a small amount of heat is transferred from the coflow to the annular jet, measurements of  $\phi_3$ , which represent the mixture fraction of the coflow, may be slightly overestimated. Consequently, it is difficult to determine exactly where the coflow truly penetrates the centerline and the inner mixing region ends. Nevertheless, between  $3.2 \leq x/D_1 \leq 6.4$ , one may observe behavior of the mean quantities, particularly  $\langle\phi_2\rangle$  and  $\langle U\rangle$ , consistent with the inner mixing region. For example, where the center and annular jets mix with each other, but not the coflow,  $\phi_1 + \phi_2 \approx 1$ , and  $\langle\phi_2\rangle$  is expected to increase as  $\langle\phi_1\rangle$  decreases. As can be seen in figure 6.2(b) and (c), this occurs until  $6.4 \leq x/D_1 \leq 8.0$ . Moreover, for coaxial jets in which  $R > 1$ , it is expected that, where the coflow has not yet reached the centerline, mixing with the faster annular jet will cause the mean centerline velocity to increase.

This can be observed for case III ( $R = 1.75$ ,  $M = 4.2$ ), and to a certain extent case II ( $R = 1.25$ ,  $M = 2.1$ ),<sup>3</sup> until approximately  $x/D_1 = 6.4$ .

### Fully Merged Region

As may be observed in figure 6.2,  $\langle U \rangle$ ,  $\langle \phi_1 \rangle$ , and  $\langle \phi_2 \rangle$  all decrease beyond  $x/D_1 = 6.4$ , and  $\langle \phi_3 \rangle$  increases, consistent with the behavior of a single jet of  $\phi_1$  and  $\phi_2$  emanating into a flow of  $\phi_3$ . Accordingly, it can be assumed that this point marks the the end of the inner mixing region and the beginning of the fully merged region.

### Effects of $M$ on the evolution of $\langle U \rangle$ , $\langle \phi_1 \rangle$ , $\langle \phi_2 \rangle$ and $\langle \phi_3 \rangle$

Increasing the momentum ratio (and thus the velocity ratio, since the density ratio is constant for the three cases) causes (i)  $\langle \phi_1 \rangle$  to decay more quickly, (ii)  $\langle \phi_2 \rangle$  to increase more quickly, and to higher values, and (iii)  $\langle \phi_3 \rangle$  to increase more slowly. It is important to note that  $M$  only increases by increasing  $M_2$  (the initial momentum flow rate of the annular jet), which has the result of increasing the proportion of  $\phi_2$  compared to  $\phi_1$  in the coaxial jets. It is therefore not surprising to see more significant amounts of  $\langle \phi_2 \rangle$  on the centerline as  $M$  increases. Moreover, the effects of  $M$  on the evolution of  $\langle \phi_1 \rangle$  are, in part, explained by the fact that the streamwise scalar flow rate ( $\approx \int_{-\infty}^{\infty} 2\pi r \rho \langle U \rangle \langle \phi \rangle dr$ , if the turbulent components are neglected<sup>4</sup>) must be conserved throughout the coaxial jets (Pope 2000). Given that (i) the streamwise scalar flow rate of  $\phi_1$  is the same for each of the three cases (since the initial conditions of the center jet are held constant), (ii)  $\langle U \rangle$  decays more slowly

---

<sup>3</sup> In case II, the velocity differences between the two jets are small. However, close inspection of  $\langle U \rangle$  reveals that its maximum value occurs at  $x/D_1 = 4.8$ .

<sup>4</sup> As the turbulent components are generally small in (single) jets, it reasonable to assume this is also true in coaxial jets, at least in the fully merged region.

as  $M$  increases (as may be observed in figure 6.2(a)), and (iii) the coaxial jets are expected to spread at same rate independent of  $M$  (as demonstrated by Ko and Au 1982), then  $\langle\phi_1\rangle$  is expected to decay faster with increasing  $M$  to conserve the streamwise scalar flow rate.

In addition to the aforementioned factors, it is suggested that increasing  $M$  may also result in decreased entrainment of the coflow into the coaxial jets. This follows from the behavior of single jets, where it is well established that up to a Reynolds number of  $2.5 \cdot 10^4$ , the Reynolds number and entrainment rate are inversely related (Ricou and Spalding 1961). If such behavior is extended to coaxial jets (a reasonable assumption given that in the fully merged region they resemble single jets), then one may conclude that  $M$  (which is proportional to both the total momentum flow rate and total Reynolds number characterizing the coaxial jets) is also inversely related to the entrainment rate. Consequently, it is possible that as  $M$  increases, decreased entrainment of the coflow into the coaxial jets causes  $\phi_3$  to evolve more slowly in the flow, such that, as depicted in figure 6.2(d),  $\langle\phi_3\rangle$  increases more slowly along the centerline.

The effects of  $M$  on  $\langle\phi_1\rangle$  and  $\langle\phi_2\rangle$ , and to a certain extent  $\langle\phi_3\rangle$ , described herein are consistent with those observed by Li *et al.* (2017) for coaxial jets in which  $M < 1$ . In their work, one can observe that  $\langle\phi_1\rangle$  also decreases more quickly as  $M$  increases, and that  $\langle\phi_2\rangle$  also peaks at higher values with increasing  $M$ , and decays more slowly. However, although Li *et al.* (2017) found that  $\langle\phi_3\rangle$  increased more slowly with  $M$  in coaxial jets with smaller area ratios ( $A_2/A_1 = 1$ ) (as was the case herein, where  $A_2/A_1 = 1.8$ ), they observed the opposite for coaxial jets with larger area ratios ( $A_2/A_1 = 2.6$ ). It is not exactly clear why such differences occur; it is possible that in the work of Li *et al.* (2017) the evolution of  $\phi_3$  along the axis is less affected by the

entrainment of the coflow into the coaxial jets, and more affected by other factors related to  $M$  (i.e. length of the inner potential core, amount of  $\phi_2$  in the jets, shear between the center and annular jets).

## 6.2.2 Second-Order Quantities

The current subsection describes the evolution of second-order quantities, including rms quantities ( $u_{rms}$ ,  $\phi_{1,rms}$ ,  $\phi_{2,rms}$ ,  $\phi_{3,rms}$ ), fluctuation intensities ( $u_{rms}/\langle U \rangle$ ,  $\phi_{1,rms}/\langle \phi_1 \rangle$ ,  $\phi_{2,rms}/\langle \phi_2 \rangle$ ,  $\phi_{3,rms}/\langle \phi_3 \rangle$ ) and correlation coefficients ( $\rho_{u\phi_1}$ ,  $\rho_{u\phi_2}$ ,  $\rho_{u\phi_3}$ ,  $\rho_{\phi_1\phi_2}$ ,  $\rho_{\phi_1\phi_3}$ ,  $\rho_{\phi_2\phi_3}$ ), each of which are discussed below.

### RMS Quantities

The rms profiles of  $U$ ,  $\phi_1$ ,  $\phi_2$ , and  $\phi_3$  are presented in figure 6.3. As depicted in figure 6.3(a),  $u_{rms}$  exhibits a local maximum at  $x/D_1 \approx 3.2$ , just beyond the end of the inner potential core; a local minimum at  $x/D_1 \approx 6.4$ , where the inner mixing region ends; and a second, much larger, local maximum between  $x/D_1 = 9.6$  and  $x/D_1 = 16.1$ . The first local maximum (approximately) coincides with the maximum values of  $\phi_{1,rms}$  and  $\phi_{2,rms}$ ,<sup>5</sup> whereas the second local maximum (approximately) coincides with the maximum values of  $\phi_{3,rms}$  (which occur at  $x/D_1 = 9.6$  for each of the three cases investigated herein). Accordingly, one may observe a clear relationship between the behavior of the velocity field and that of the scalar fields. Furthermore, consistent with the definition of the inner mixing region provided in the previous subsection, it is apparent that this zone is dominated by large fluctuations of  $\phi_1$  and  $\phi_2$ , most likely

---

<sup>5</sup> As inferred from figures 6.3(b) and (c), which may not display the true peaks of  $\phi_{1,rms}$  and  $\phi_{2,rms}$ , since data was sampled at discrete locations, and not continuously, along the centerline.

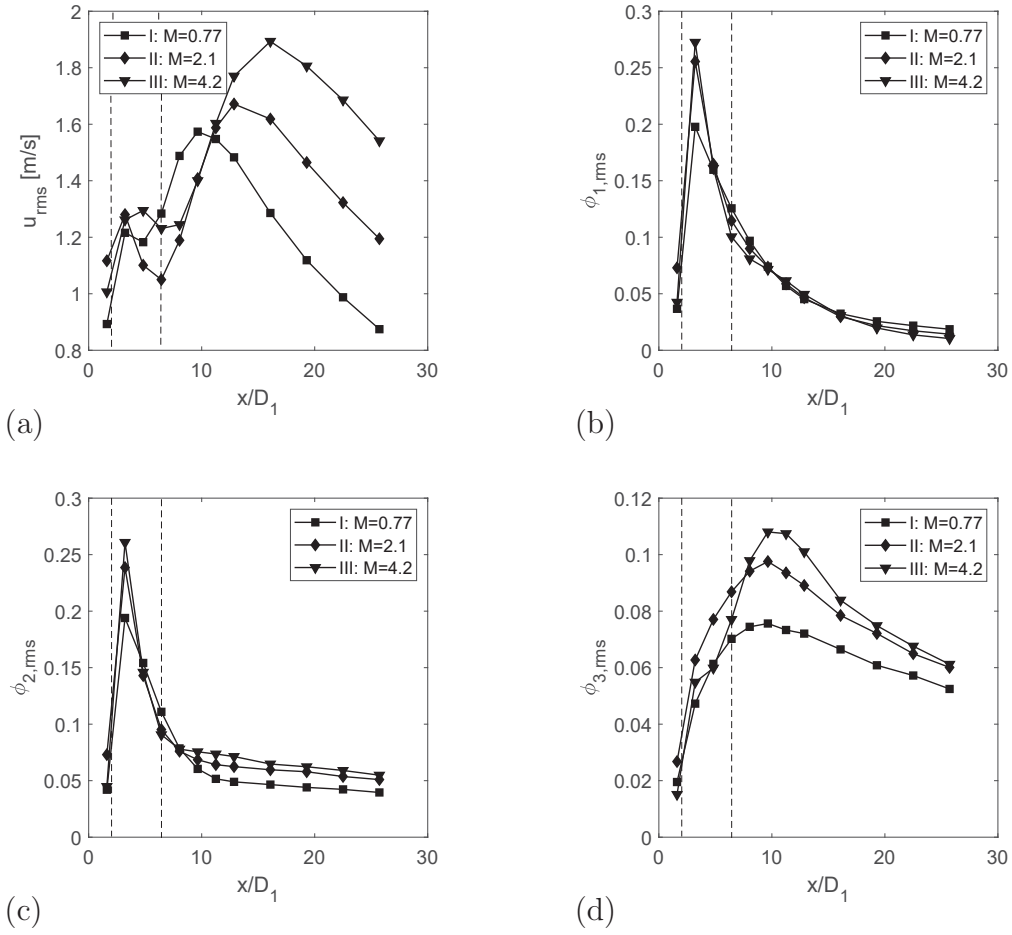


Figure 6.3: Downstream evolution of (a)  $u_{rms}$ , (b)  $\phi_{1,rms}$ , (c)  $\phi_{2,rms}$ , and (d)  $\phi_{3,rms}$  along the centerline. Note that the dashed lines delineate the three regions of the jet (the potential core of the center jet, inner mixing region, and fully merged region).

due to large-scale vortices associated with the Kelvin-Helmholtz layer that forms at the interfacial mixing layer between the center and annular jets.

In figure 6.3 it can be seen that increasing  $M$  increases the magnitude of the fluctuations;  $u_{rms}$ ,  $\phi_{1,rms}$ ,  $\phi_{2,rms}$ , and  $\phi_{3,rms}$  all get larger as  $M$  increases, with the most significant differences observed for  $u_{rms}$  and  $\phi_{3,rms}$ . Similar results were observed by Li *et al.* (2017) for  $\phi_{1,rms}$  and  $\phi_{2,rms}$ . They credit this to increased production rates in coaxial jets in which  $M$  is larger, since examination of the scalar cross-stream profiles reveals that the mean scalar gradients are larger in such jets. Although it is possible that production rates do increase as  $M$  increases, this cannot be concluded with certainty from the data of Li *et al.* (2017) since they did not measure scalar fluxes. Moreover, assuming molecular diffusion is negligibly small, the scalar variance budget along the centerline reduces to:

$$0 = -\langle U \rangle \frac{\partial \langle \phi'^2 \rangle}{\partial x} - 2\langle u\phi' \rangle \frac{\partial \langle \phi \rangle}{\partial x} - \left( \frac{\partial \langle u\phi'^2 \rangle}{\partial x} + \frac{1}{r} \frac{\partial \langle v\phi'^2 \rangle}{\partial r} \right) - \epsilon_\phi. \quad (6.2)$$

Production therefore results entirely from the streamwise mean scalar gradient ( $\frac{\partial \langle \phi \rangle}{\partial x}$ ) and the axial scalar flux ( $\langle u\phi' \rangle$ ), with no radial contribution.

### Fluctuation Intensities

The profiles of  $u_{rms}$ ,  $\phi_{1,rms}$ ,  $\phi_{2,rms}$ , and  $\phi_{3,rms}$  are non-dimensionalized by their mean values in figure 6.4, yielding profiles of the fluctuation intensities. The present discussion starts by considering the near-field, specifically focusing on the evolution of  $\phi_{1,rms}/\langle \phi_1 \rangle$ , which is strongly dependent on the choice of  $M$  (far more so than  $\phi_{1,rms}$ ). The far-field behavior of the fluctuation intensities is then subsequently discussed.

As may be observed in figure 6.4(b), although there are some commonalities in the centerline profiles of  $\phi_{1,rms}/\langle \phi_1 \rangle$  for the three cases —  $\phi_{1,rms}/\langle \phi_1 \rangle$  peaks relatively

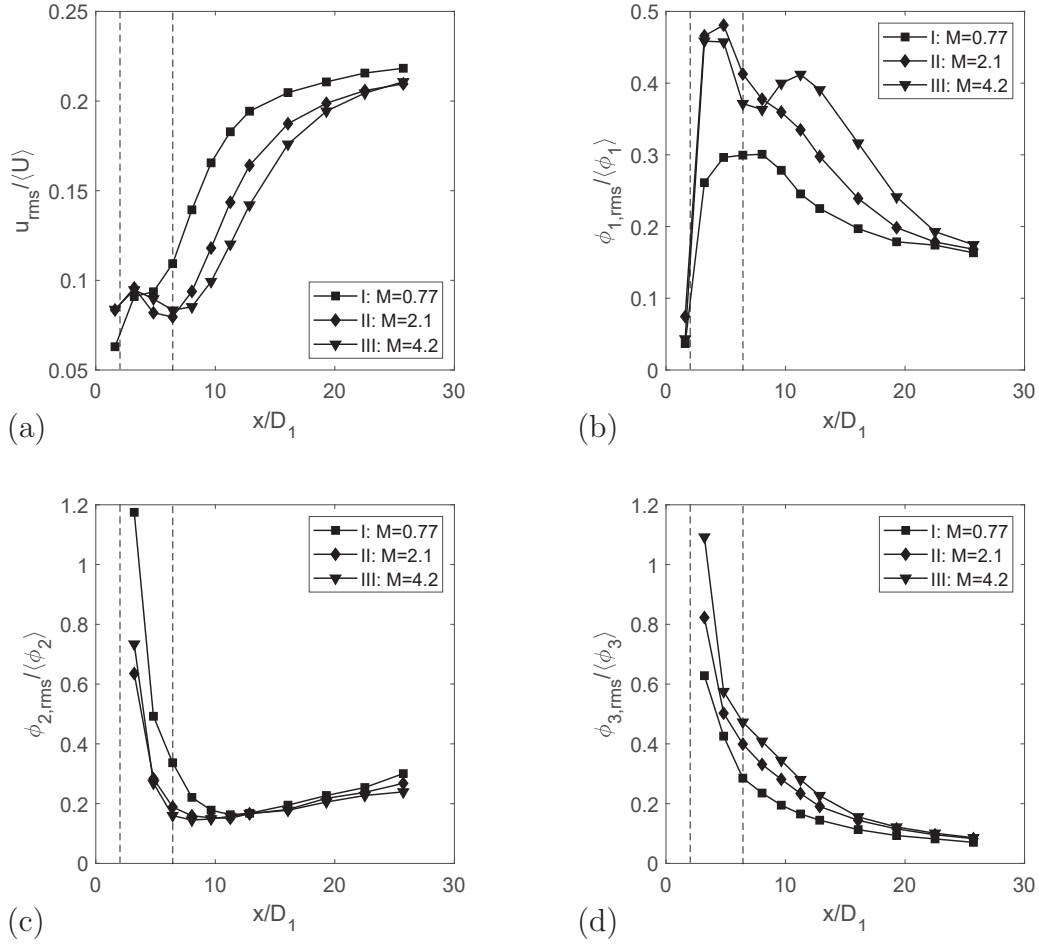


Figure 6.4: Downstream evolution of (a)  $u_{rms}/\langle U \rangle$ , (b)  $\phi_{1,rms}/\langle \phi_1 \rangle$ , (c)  $\phi_{2,rms}/\langle \phi_2 \rangle$ , and (d)  $\phi_{3,rms}/\langle \phi_3 \rangle$  along the centerline. Note that the dashed lines delineate the three regions of the jet (the potential core of the center jet, inner mixing region, and fully merged region).

close to the jet exit, and asymptotes to a constant far downstream at a lower value — the three profiles are generally distinct for different values of  $M$ . In cases I and II, only a single peak is observed, but in the former case it is much lower, and occurs farther downstream. Grandmaison *et al.* (1996), Cai *et al.* (2011), and Li *et al.* (2017) each observed evolutions of  $\phi_{1,rms}/\langle\phi_1\rangle$  similar to those depicted for cases I and II, and Li *et al.* (2017) showed that the peak of  $\phi_{1,rms}/\langle\phi_1\rangle$  in the near-field was (i) stronger when the annular jet was larger, and (ii) disappeared when  $M$  was much less than 1. Inspection of the results herein, as well as those of Grandmaison *et al.* (1996), Cai *et al.* (2011), and Li *et al.* (2017) suggests that the peak of  $\phi_{1,rms}/\langle\phi_1\rangle$  occurs just beyond the potential core of the center jet, in the inner mixing region. In (single) jets, it should be noted that a similar, but much smaller peak in  $\phi_{rms}/\langle\phi\rangle$  occurs just beyond the potential core of (single) smooth contraction nozzle jets (with a top-hat velocity profile at the jet exit) due to highly coherent vortex structures present in the near-field. Strong large-scale engulfment of the ambient fluid by these structures results in large scalar fluctuations and quick growth of  $\phi_{rms}$  (compared to fully-developed pipe jets, where there are few or no large-scale coherent structures); (Mi *et al.* 2001).

In contrast, two peaks are observed for  $\phi_{1,rms}/\langle\phi_1\rangle$  in case III, the first of which occurs between  $x/D_1 = 3.2$  and  $4.8$ , and coincides approximately with the peak observed in case II, and the second of which occurs between  $x/D_1 = 9.6$  and  $12.9$ . This double-peaked profile was not observed in previous studies of coaxial jets, even though Grandmaison *et al.* (1996) investigated jets with comparable values of  $M$ . The second peak in case III occurs at the beginning of the fully merged zone of the coaxial jets, just downstream of what may be considered the “potential core” of the coaxial jets — that is, the region consisting primarily of  $\phi_1$  and  $\phi_2$ . Thus, for coaxial

jets with large  $M$ , there appear to be two regions of intense fluctuations for  $\phi_1$ : first, where the center and annular jet begin mixing, and second, where both jets begin mixing with the coflow. As previously discussed, the potential core of the center jet decreases as  $M$  increases, so both the center and annular jets mix earlier, while  $\phi_3$  evolves more slowly along the centerline as  $M$  increases, delaying the point at which the center and annular jets mix with the coflow. This may explain why two distinct regions for the fluctuations of  $\phi_1$  are observed in case III, but not in cases I and II — as  $M$  decreases, these regions come close enough together to be indistinguishable.

Far downstream, the center and annular jets are expected to ultimately behave like a single jet of the same total momentum issuing in quiescent air. (Given the low initial velocity of the coflow, the dynamics of the two inner jets should not be strongly affected.) Thus it is expected that  $u_{rms}/\langle U \rangle$  will asymptote to approximately 0.25, and  $\phi_{1,rms}/\langle \phi_1 \rangle$  and  $\phi_{2,rms}/\langle \phi_2 \rangle$  will asymptote to approximately 0.21 – 0.23 (based on generally accepted values for  $\phi_{rms}/\langle \phi \rangle$  in single jets, although significant scatter exists in reported values of this quantity, Mi *et al.* 2001). Furthermore, one can additionally expect that with increasing  $x/D_1$ ,  $\phi_{3,rms}$  will tend to zero, and so will  $\phi_{3,rms}/\langle \phi_3 \rangle$ . In the current work, measurements are limited to  $x/D_1 \leq 25.7$ , and the asymptotic values are not yet fully achieved. Nevertheless, it can be observed that  $u_{rms}/\langle U \rangle$ ,  $\phi_{1,rms}/\langle \phi_1 \rangle$ , and  $\phi_{3,rms}/\langle \phi_3 \rangle$  all approach their asymptotic values more slowly as  $M$  is increased, further evidence that, as discussed in §6.2.1, the coaxial jets mix with the coflow more slowly as  $M$  increases.

The maximum measured values of  $u_{rms}/\langle U \rangle$  are 0.21 – 0.22, and, based on figure 6.4(a), likely to continue increasing farther downstream. At the same location,  $\phi_{1,rms}/\langle \phi_1 \rangle$  is approximately 0.17 for the three cases, and  $\phi_{2,rms}/\langle \phi_2 \rangle$  ranges between 0.24 and 0.30, depending on the value of  $M$ . Although these values may be slightly

lower (for  $\phi_{1,rms}/\langle\phi_1\rangle$ ) or higher (for  $\phi_{2,rms}/\langle\phi_2\rangle$ ) than those typically observed in the self-similar region of single jets, it should be emphasized that based on measurements of  $u_{rms}/\langle U\rangle$ , the coaxial jets do not appear to have fully reached self-similarity. Moreover, Cai *et al.* (2011) and Grandmaison *et al.* (1991), who also studied the mixing of multiple scalars in coaxial jets, measured asymptotic values of  $\phi_{1,rms}/\langle\phi_1\rangle$  consistent with those of the current work (0.21 and 0.16, respectively). Their measurements, which are also on the lower end of what is usually observed in single jets, suggest that there could also be actual physical differences between the far-field behavior of single and coaxial jets. That is, even if the behavior of coaxial jets ultimately resembles that of single jets, differences in their evolution in the near-field may nevertheless perpetuate far downstream, similarly to what can be observed when comparing fully-developed pipe jets with smooth contraction nozzle jets (see Mi *et al.* 2001; Xu and Antonia 2002), and in accordance with analytical arguments put forth by George and Arndt (1989) and George (2012) about the persistence of initial conditions in a jet.

### Correlation Coefficients

Velocity-scalar correlation coefficients ( $\rho_{u\phi_1}$ ,  $\rho_{u\phi_2}$ ,  $\rho_{u\phi_3}$ ) and scalar-scalar correlation coefficients ( $\rho_{\phi_1\phi_2}$ ,  $\rho_{\phi_1\phi_3}$ ,  $\rho_{\phi_2\phi_3}$ ) are presented in figure 6.5. The correlation coefficients are the normalized covariances of two turbulent quantities (and in the case of the mixed velocity-scalar statistics, the normalized turbulent scalar fluxes), and can be used to characterize the extent of mixing of these quantities. A correlation coefficient of  $-1$  indicates that the quantities of interest are perfectly anti-correlated, whereas a correlation coefficient of  $+1$  indicates they are perfectly correlated, and thus have fully mixed.

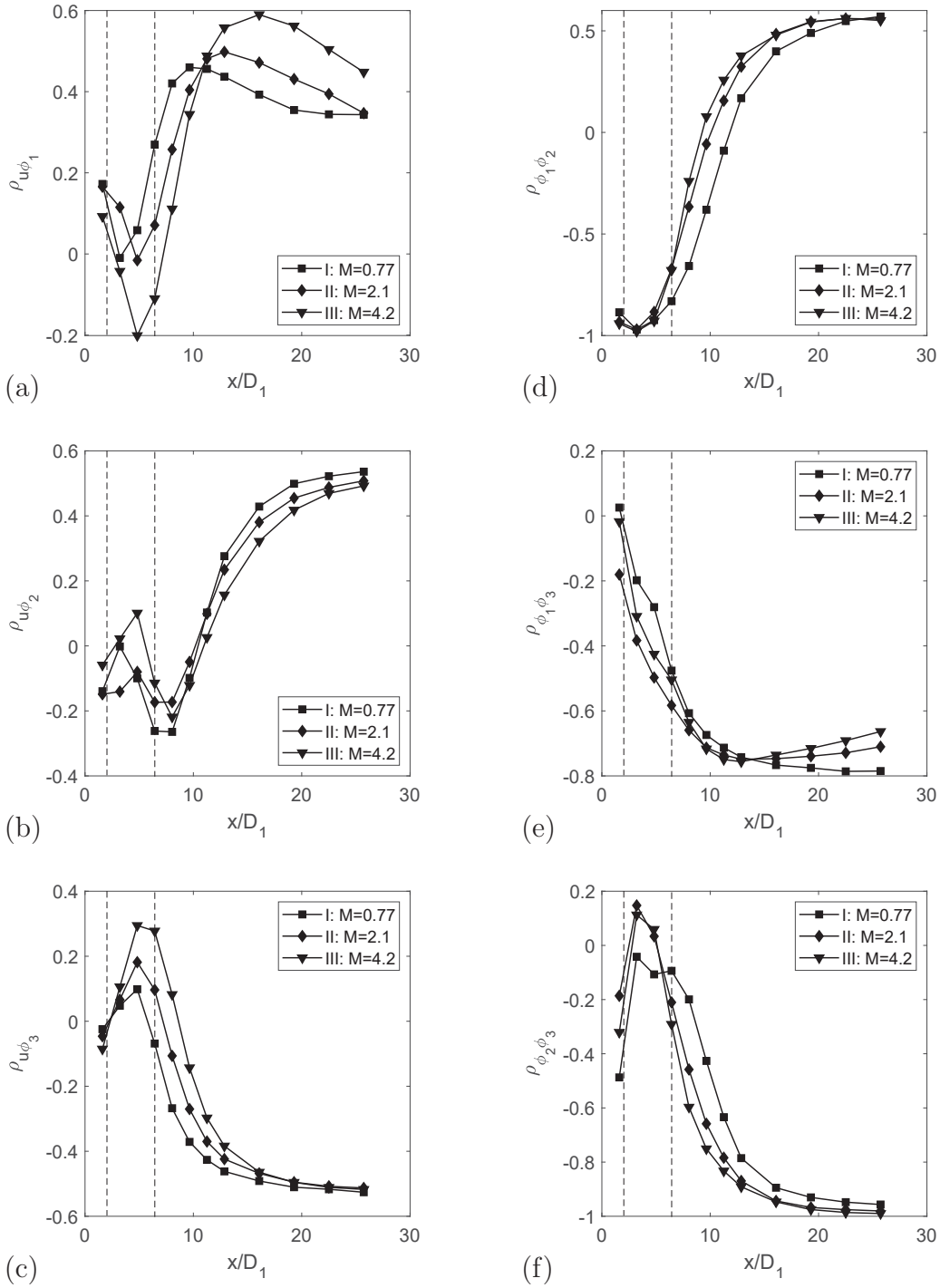


Figure 6.5: Downstream evolution of correlation coefficients along the centerline: (a)  $\rho_{u\phi_1}$ , (b)  $\rho_{u\phi_2}$ , (c)  $\rho_{u\phi_3}$ , (d)  $\rho_{\phi_1\phi_2}$ , (e)  $\rho_{\phi_1\phi_3}$ , (f)  $\rho_{\phi_2\phi_3}$ . Note that the dashed lines delineate the three regions of the jet (the potential core of the center jet, inner mixing region, and fully merged region).

One may observe that the velocity-scalar correlation coefficients  $(\rho_{u\phi_1}, \rho_{u\phi_2}, \rho_{u\phi_3})$ , as well as  $\rho_{\phi_1\phi_3}$  and  $\rho_{\phi_2\phi_3}$ , are initially approximately 0, indicating that these quantities are uncorrelated. (However, it should be noted that in the potential core of center jet there should be no  $\phi_2$  and  $\phi_3$ ; and in the inner mixing region there should be no, or relatively little  $\phi_3$ . This should be kept in mind when interpreting these correlation coefficients.) In contrast, it can be observed that close to the jet exit ( $1.6 \leq x/D_1 \leq 4.8$ ),  $\rho_{\phi_1\phi_2} = -1$ , such that measurement of  $\phi_1$  implies absence of  $\phi_2$ , and vice versa. This is expected given that the flow primarily consists of  $\phi_1$  and  $\phi_2$  (see figures 6.2(b),(c) and 6.3(b),(c)), and  $\phi_1 + \phi_2 \approx 1$ . In a binary mixture:

$$\langle \phi'_\alpha \phi'_\beta \rangle = -\langle \phi'^2_\alpha \rangle = -\langle \phi'^2_\beta \rangle, \quad (6.3)$$

and the correlation coefficient is therefore -1, by definition.

In the inner mixing region zone ( $3.2 \leq x/D_1 < 6.4$ ), values of the correlation coefficients do not vary significantly from those close to the jet exit:  $-0.2 \lesssim \rho_{u\phi_1} \lesssim 0.2$ ,  $-0.3 \lesssim \rho_{u\phi_2} \lesssim 0.1$  and  $\rho_{\phi_1\phi_2} = -1$ . As depicted in figures 6.5(a) and (b),  $\rho_{u\phi_1}$  exhibits a local minimum between  $x/D_1 = 3.2$  and  $x/D_1 = 4.8$ , whereas  $\rho_{u\phi_2}$  exhibits a local maximum. In cases I and II, it is unclear if these are of physical significance given the rather small differences in the values of  $\rho_{u\phi_1}$  and  $\rho_{u\phi_2}$  observed for these cases. However, in case III, the local minimum and maximum show  $U$  and  $\phi_1$  becoming slightly anti-correlated just beyond the center jet's potential core, and  $U$  and  $\phi_2$  becoming slightly positively correlated, as expected from the physics of the flow. Towards the end of the inner mixing region these trends reverse, presumably due to increasing incursions of  $\phi_3$  on the centerline.

As the coflow increasingly penetrates the centerline,  $\rho_{u\phi_1}$ ,  $\rho_{u\phi_2}$ , and  $\rho_{\phi_1\phi_2}$  all increase and tend towards positive values, while  $\rho_{u\phi_3}$ ,  $\rho_{\phi_1\phi_3}$ ,  $\rho_{\phi_2\phi_3}$  all decrease and

tend towards negative values, as expected when the coaxial jets increasingly behave like a single jet of  $\phi_1$  and  $\phi_2$  mixing in a fluid of  $\phi_3$ . As may be observed in figure 6.5(d),  $\rho_{\phi_1\phi_2}$  appears to asymptote to a value of 0.6, seemingly in contradiction with theoretical predictions, which suggest that far downstream  $\phi_1$  and  $\phi_2$  become fully mixed, such that  $\rho_{\phi_1\phi_2} = 1$  (Warhaft 1984). However, similarly to the profiles of the fluctuation intensities, it is possible that measurements were not obtained far enough downstream to observe the asymptotic values of  $\rho_{\phi_1\phi_2}$ . For example, Grandmaison *et al.* (1991) found that when  $M$  was large, far downstream,  $\rho_{\phi_1\phi_2}$  plateaued, and even decreased, before eventually increasing to 1 farther downstream. Alternatively, it is also possible that when  $x/D_1$  becomes sufficiently large, the SNR may fall to levels sufficiently low that the predicted asymptotic value is not observed. Such an evolution can be observed in the work Li *et al.* (2017) for cross-stream profiles of  $\rho_{\phi_1\phi_2}$  where the annular jet is large. Finally, it should be noted that in most previous studies of multi-scalar mixing, upon which our understanding of these processes have been developed, the density of the flow is nearly constant and the scalars have similar or identical diffusivities (e.g. the works of Warhaft 1984; Grandmaison *et al.* 1991; Tong and Warhaft 1995; Costa-Patry and Mydlarski 2008; Cai *et al.* 2011; Li *et al.* 2017). This is not the case in the current work, and it is not clear, how, or if, these factors have an effect on the evolution of  $\rho_{\phi_1\phi_2}$ .

Having discussed the downstream evolution of the correlation coefficients, it is also worth considering the effects of  $M$  on these correlation coefficients, specifically that of  $\rho_{\phi_1\phi_2}$ . As shown in figure 6.5(d), when  $M$  increases,  $\rho_{\phi_1\phi_2}$  increases more rapidly, achieving its asymptotic value faster. These results are somewhat consistent with those of Grandmaison *et al.* (1991) who found that *initially*  $\rho_{\phi_1\phi_2}$  increased faster as  $M$  increased. (In their work, this trend reversed far downstream;  $\rho_{\phi_1\phi_2}$  ultimately

approached 1 more slowly as  $M$  increased.) However, Li *et al.* (2017) observed the opposite — the scalar correlation coefficients in their experiments evolved more quickly to their asymptotic values as  $M$  decreased. The momentum ratios investigated in their experiments were approximately 0.94 and 0.47, and they attributed a faster evolution of  $\rho_{\phi_1\phi_2}$  at lower velocity ratios to increased shear between the center and annular jets. Although this could explain why  $\rho_{\phi_1\phi_2}$  evolves fastest for case III, it does not explain why case II evolves faster than case I. As will later be discussed herein, there appear to be differences between coaxial jets in which  $M < 1$  and those in which  $M > 1$ . Thus, the factors controlling the mixing of  $\phi_1$  and  $\phi_2$  appear to involve more than just differences in shear.

### 6.2.3 Third-Order Quantities

The downstream evolution of triple-velocity-scalar moments are presented in figure 6.6. Triple-velocity-scalar moments, including  $\langle u\phi'_\alpha{}^2 \rangle$  and  $\langle u\phi'_\alpha\phi'_\beta \rangle$ , appear in the budgets of  $\langle \phi'_\alpha{}^2 \rangle$  and  $\langle \phi'_\alpha\phi'_\beta \rangle$  and are related to the transport of scalar variance and covariance by turbulent diffusion (see equation (1.3)). There are relatively few measurements of  $\langle u\phi'_\alpha{}^2 \rangle$  in axisymmetric jets, and to the author’s knowledge, no existing measurements of  $\langle u\phi'_\alpha\phi'_\beta \rangle$ . Yet, models for the triple-velocity-scalar moments are required to close the budgets of  $\langle \phi'_\alpha{}^2 \rangle$  and  $\langle \phi'_\alpha\phi'_\beta \rangle$ . Accordingly, measurements of  $\langle u\phi_1'^2 \rangle$ ,  $\langle u\phi_2'^2 \rangle$ ,  $\langle u\phi_3'^2 \rangle$ ,  $\langle u\phi_1'\phi_2' \rangle$ ,  $\langle u\phi_1'\phi_3' \rangle$ ,  $\langle u\phi_2'\phi_3' \rangle$  are presented herein.

#### Evolution of $\langle u\phi_1'^2 \rangle$ , $\langle u\phi_2'^2 \rangle$ and $\langle u\phi_3'^2 \rangle$ along the centerline

The present discussion begins by describing the evolution of  $\langle u\phi_1'^2 \rangle$ ,  $\langle u\phi_2'^2 \rangle$ , and  $\langle u\phi_3'^2 \rangle$  along the centerline. As may be observed in figure 6.6(a) and (b),  $\langle u\phi_1'^2 \rangle$  and  $\langle u\phi_2'^2 \rangle$  are both largest in magnitude in the inner mixing region. In this region, differences can be observed between each of the three cases, although they are generally largest between cases II and III (in which  $M > 1$ ) and case I (in which  $M < 1$ ).

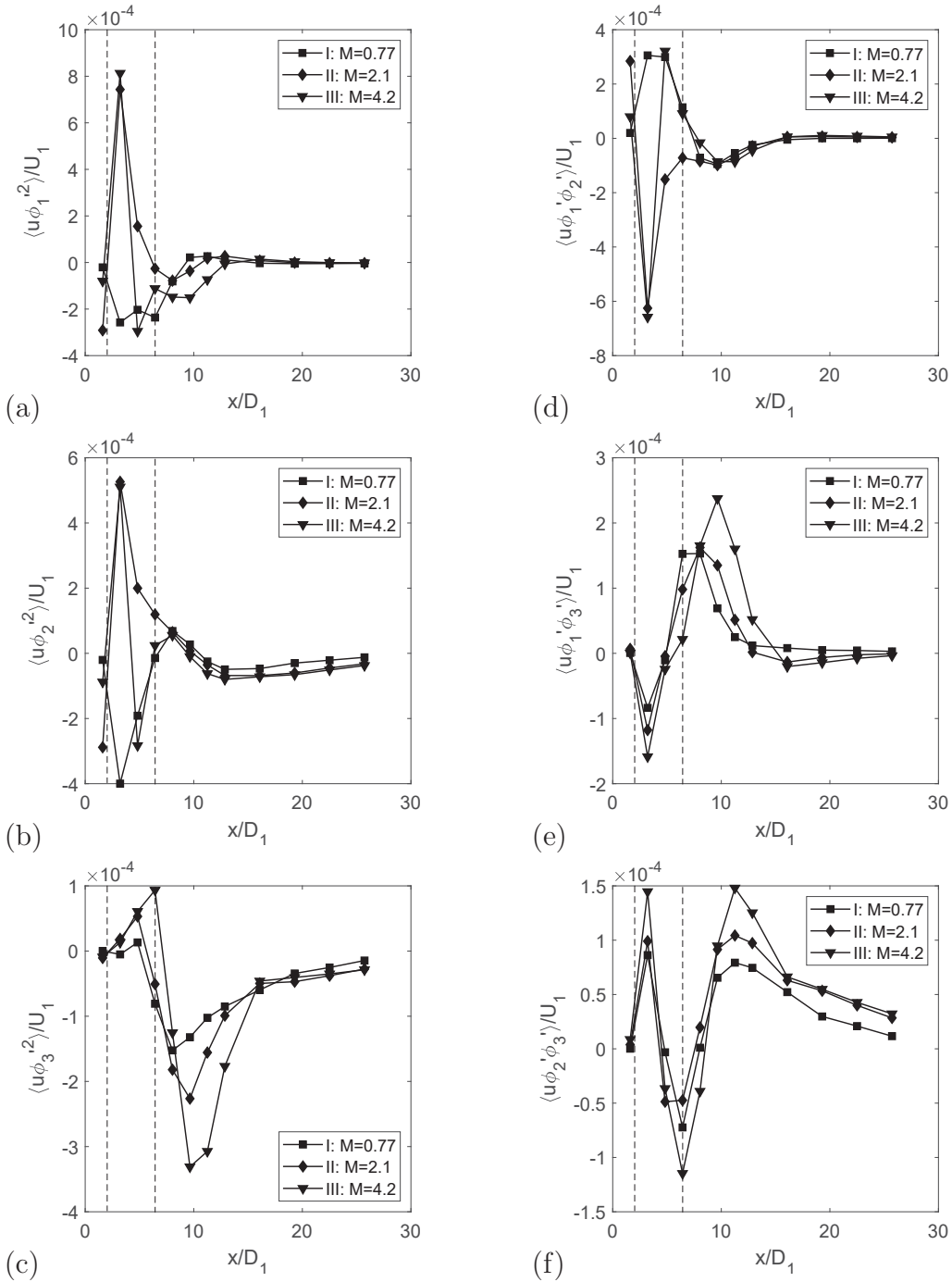


Figure 6.6: Downstream evolution of (a)  $\langle u\phi_1' \rangle$ , (b)  $\langle u\phi_2' \rangle$ , (c)  $\langle u\phi_3' \rangle$ , (d)  $\langle u\phi_1'\phi_2' \rangle$ , (e)  $\langle u\phi_1'\phi_3' \rangle$ , (f)  $\langle u\phi_2'\phi_3' \rangle$  along the centerline of the coaxial jets. Note that measurements of  $\langle U \rangle$  are non-dimensionalized using  $U_1$ , the average velocity at the exit of the center jet, and that the dashed lines delineate the three regions of the jet (the potential core of the center jet, inner mixing region, and fully merged region).

Contributions by the streamwise turbulent diffusion to the budgets of  $\langle \phi_1'^2 \rangle$  and  $\langle \phi_2'^2 \rangle$  can be inferred from the behavior of  $\partial \langle u \phi_1'^2 \rangle / \partial x$  and  $\partial \langle u \phi_2'^2 \rangle / \partial x$ . Again,  $\partial \langle u \phi_1'^2 \rangle / \partial x$  and  $\partial \langle u \phi_2'^2 \rangle / \partial x$  are largest in magnitude, and vary significantly with  $M$  in the inner mixing region. However, by the beginning of the fully merged region, all three cases begin to evolve similarly. Interestingly, in this region ( $8.0 \leq x/D_1 \leq 12.9$ ), contributions of the streamwise turbulent diffusion to the budget of  $\langle \phi_1'^2 \rangle$  are negative ( $\partial \langle u \phi_1'^2 \rangle / \partial x > 0$ ), whereas they are positive for the budget of  $\langle \phi_2'^2 \rangle$  ( $\partial \langle u \phi_2'^2 \rangle / \partial x < 0$ ). Finally, far downstream, both  $\partial \langle u \phi_1'^2 \rangle / \partial x \approx 0$  and  $\partial \langle u \phi_2'^2 \rangle / \partial x \approx 0$ , which is consistent with what occurs in single jets, where at such downstream distances, the contribution of the streamwise turbulent diffusion to the budget of  $\langle \phi_\alpha'^2 \rangle$  is negligible (see Darisse *et al.* 2014).

The behavior of  $\langle u \phi_3'^2 \rangle$ , which evolves similarly for all three cases, appears to be distinct from that of  $\langle u \phi_1'^2 \rangle$  and  $\langle u \phi_2'^2 \rangle$ . As demonstrated in figure 6.6(c),  $\langle u \phi_3'^2 \rangle$  peaks at the end of inner mixing region ( $4.8 \leq x/D_1 \leq 6.4$ ), subsequently decreases to a minimum at the beginning of the fully merged region ( $8.0 \leq x/D_1 \leq 9.6$ ), and finally increase to 0 far downstream. Consequently (excluding the inner mixing region, where  $\phi_3$  is not expected in large quantities) contributions by the streamwise turbulent diffusion to the budget of  $\langle \phi_3'^2 \rangle$  are first positive, then negative, and then tend to 0 far downstream.

### **Evolution of $\langle u \phi_1' \phi_2' \rangle$ , $\langle u \phi_1' \phi_3' \rangle$ , and $\langle u \phi_2' \phi_3' \rangle$ along the centerline**

The evolutions of  $\langle u \phi_1' \phi_2' \rangle$ ,  $\langle u \phi_1' \phi_3' \rangle$ , and  $\langle u \phi_2' \phi_3' \rangle$  along the centerline are depicted in figures 6.6(d), (e), and (f), respectively. In figure 6.6(d), once again, differences can be observed between cases II and III ( $M > 1$ ) and case I ( $M < 1$ ). In the former,  $\langle u \phi_1' \phi_2' \rangle$  immediately decreases to a minimum at  $x/D_1 = 3.2$ , whereas in the latter,  $\langle u \phi_1' \phi_2' \rangle$  increases to a maximum. Moreover, as may be inferred from figure

6.6(d), contributions by the streamwise turbulent diffusion to the budget of  $\langle \phi'_1 \phi'_2 \rangle$  vary widely with  $M$  in the inner mixing region. In contrast, the effects of  $M$  on the behavior of  $\langle u \phi'_1 \phi'_3 \rangle$  and  $\langle u \phi'_2 \phi'_3 \rangle$  are far less significant. Both  $\langle u \phi'_1 \phi'_3 \rangle$  and  $\langle u \phi'_2 \phi'_3 \rangle$  peak in the fully merged region, with the former reaching its maximum value at the beginning of the fully merged region ( $6.4 \leq x/D_1 \leq 9.6$ ), and the latter reaching its maximum value slightly farther downstream ( $x/D_1 = 11.3$ ). Thus, positive contributions by the streamwise turbulent diffusion to the budgets of  $\langle \phi'_1 \phi'_3 \rangle$  and  $\langle \phi'_2 \phi'_3 \rangle$  do not occur until the fully merged region of the jets.

Analysis of the evolutions of  $\langle u \phi'_1 \phi'_2 \rangle$ ,  $\langle u \phi'_1 \phi'_3 \rangle$ , and  $\langle u \phi'_2 \phi'_3 \rangle$ , as well as those of  $\langle u \phi_1'^2 \rangle$ ,  $\langle u \phi_2'^2 \rangle$  and  $\langle u \phi_3'^2 \rangle$ , suggest that mixed velocity-scalar triple moments which include  $\phi_1$  and  $\phi_2$  (i.e.  $\langle u \phi'_1 \phi'_2 \rangle$ ,  $\langle u \phi_1'^2 \rangle$ , and  $\langle u \phi_2'^2 \rangle$ ) are very sensitive to differences in  $M$  in the inner mixing region, whereas those including  $\phi_3$  (i.e.  $\langle u \phi'_1 \phi'_3 \rangle$ ,  $\langle u \phi'_2 \phi'_3 \rangle$ , and  $\langle u \phi_3'^2 \rangle$ ) are much less affected by  $M$ . Furthermore, as may be observed in figure 6.6, all mixed velocity-scalar triple moments tend to 0 far downstream, such that the most interesting behavior for the velocity-scalar moments appears to occur in the near-field. It should be noted that although the above discussion examined contributions of the streamwise turbulent diffusion to the budgets of the scalar variance or covariance, a complete investigation of the effects turbulent diffusion necessitates measurements of the radial components of velocity and the corresponding mixed velocity-scalar moments.

### 6.3 Probability Density Functions

Non-dimensionalized probability density functions (PDFs) of  $U$ ,  $\phi_1$ ,  $\phi_2$ , and  $\phi_3$  are presented in figures 6.7 - 6.11. The PDFs contain information on all the statistical moments of each quantity of interest ( $U$ ,  $\phi_1$ ,  $\phi_2$ , and  $\phi_3$ ), and can therefore be used to gain additional insight into the behavior of these quantities. Given that the most

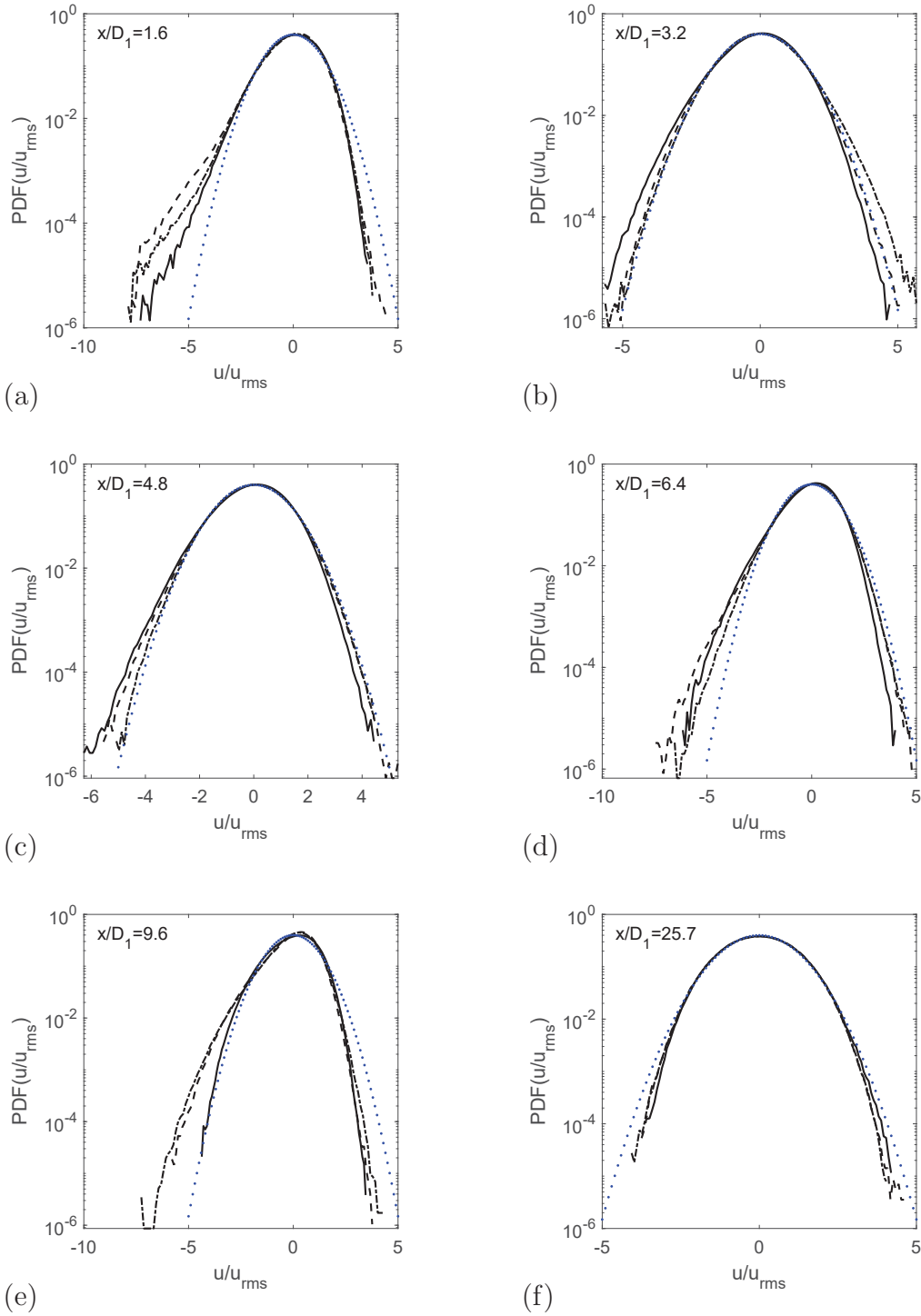


Figure 6.7: Non-dimensionalized PDFs of  $U$  measured along the centerline for case I:  $M = 0.77$  (—), case II:  $M = 2.1$  (---), case III:  $M = 4.2$  (---). Gaussian PDFs (⋯) are also provided for the purpose of comparison.

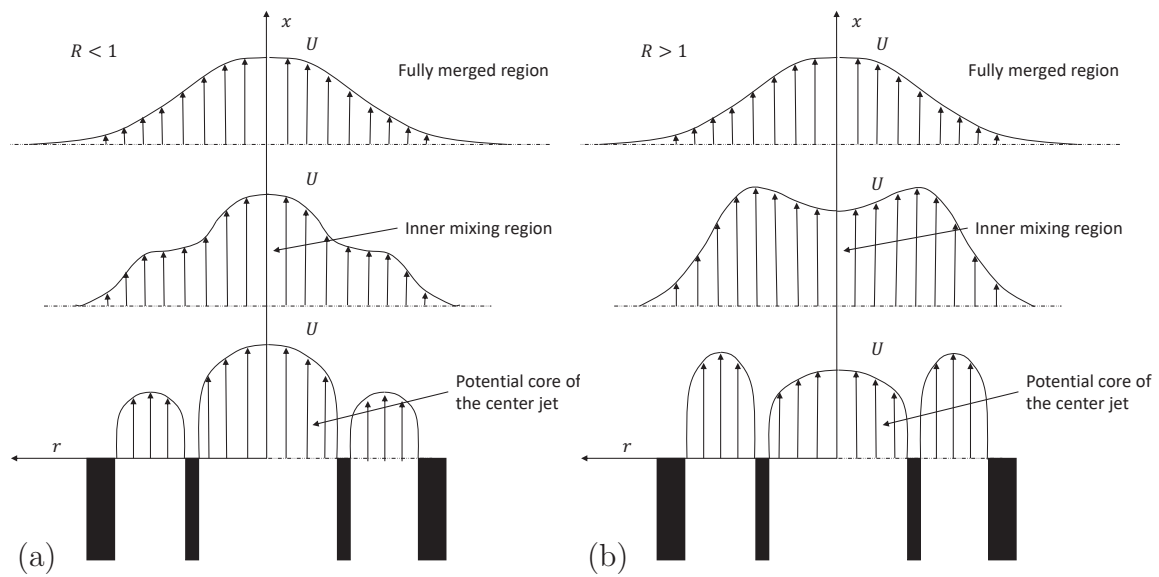


Figure 6.8: Schematic representation of the evolution of the radial velocity profiles of coaxial jets when (a)  $R < 1$  and (b)  $R > 1$  based on data from previous studies of coaxial jets (e.g., Ko and Kwan 1976; Ko and Au 1985). Note that this figure more specifically depicts the flow for cases in which  $R$  is either much less or much greater than 1.

unique behavior of coaxial jets occurs in the near-field, measurements in this section are mostly obtained close to the jet exit — at  $x/D_1 = 1.6, 3.2, 4.8, 6.4, 9.6$  — although the PDFs measured  $x/D_1 = 25.7$  are also presented, to quantify the behavior of  $U$ ,  $\phi_1$ ,  $\phi_2$ , and  $\phi_3$  far downstream.

The (non-dimensional) velocity PDFs are quasi-Gaussian, and are not significantly affected by the momentum ratio over the ranges studied herein, with the most notable differences being observed in the tails of the PDF. To better view these differences, the PDFs of  $U$  are plotted on semi-log plots, which do not obscure the PDF tails (as can be the case when the PDFs are plotted in fully linear coordinates). In the potential core of the center jet, at  $x/D_1 = 1.6$ , the PDFs are negatively skewed, as a consequence of the fully-developed velocity profile at the jet exit. (The flow first mixes with fluid from the edges of the center jet where, as depicted in figure 6.8, the velocity is lower. This induces negative velocity fluctuations, and therefore negative skew.) Farther downstream, in the inner mixing region ( $3.2 \leq x/D \leq 4.8$ ), the PDFs are still slightly negatively skewed, with the exception of case III at  $x/D = 3.2$ , which is slightly positively skewed. The latter results from mixing with the faster annular jet (or merely faster flowing surroundings, as can be observed in figure 6.8(b)), which causes increased positive fluctuations, and consequently positive skew. At the beginning of the fully merged region ( $6.4 \leq x/D \leq 9.6$ ), the PDFs are less Gaussian, and skewed more negatively, such that large negative velocity fluctuations of the velocity are more common, indicating that the slower moving fluid from the coflow has reached the centerline. Differences in the tails can be observed for the three cases in this region, but by  $x/D = 25.7$ , the velocity PDFs all collapse onto each other. At this location, the PDFs approach a Gaussian distribution once again, which suggests that the center jet, annular jet, and coflow are more fully mixed. Consistent with

the behavior of free-shear flows, the PDFs are not perfectly Gaussian, and are not expected to become so farther downstream (Pope 2000).

As can be seen in figures 6.9 and 6.10, close to the jet exit ( $x/D_1 = 1.6$ ), the PDFs of  $\phi_1$  and  $\phi_2$  are thin, with large tails. The kurtosis at these locations is therefore large ( $10.8 \leq K_{\phi_1} \leq 22.5$ ,  $8.3 \leq K_{\phi_2} \leq 18.2$ ), indicating that extreme events occur (relatively) frequently. As will be shown in the next section, there is evidence that  $\phi_1$  and  $\phi_2$  are just beginning to mix at  $x/D_1 = 1.6$ , and it is clear that the tails of the PDFs are not solely the result of noise. At this location, the PDFs of  $\phi_1$  are negatively skewed ( $-3.0 \leq S_{\phi_1} \leq -1.1$ ), while those of  $\phi_2$  are positively skewed ( $0.6 \leq S_{\phi_2} \leq 2.7$ ). In simple jets, negative skewness occurs where pockets of ambient fluid mix within the jet fluid (which contains the scalar), whereas positive skewness occurs where pockets of the jet fluid mix within the ambient fluid. This therefore implies that along the centerline of the current flow, at  $x/D_1 = 1.6$ , small pockets of  $\phi_2$  mix in fluid primarily composed of  $\phi_1$ . Farther downstream, at  $x/D_1 = 3.2$ , the PDFs of both  $\phi_1$  and  $\phi_2$  are bimodal, like those observed by Villermaux and Rehab (2000) for a scalar injected into the inner of two coaxial jets. One may therefore infer that the fluid at  $x/D_1 = 3.2$  consists principally of regions of high  $\phi_1$ /low  $\phi_2$  or low  $\phi_1$ /high  $\phi_2$ , an indication of the binary nature of the scalar field close to the jet exit. By  $x/D = 4.8$ , the PDFs of  $\phi_1$  and  $\phi_2$  become unimodal once again, with the former positively skewed and the latter negatively skewed. Furthermore, the degree to which the PDFs of  $\phi_1$  are positively skewed and the PDFs of  $\phi_2$  are negatively skewed increases with  $M$ . It can be inferred that pockets of  $\phi_1$  mix in a background preferentially composed of  $\phi_2$ , and that this become more pronounced as  $M$  increases — which is consistent with the fact that the coaxial jets initially mix faster as  $M$  increases. (As may be observed from the mean profiles, when  $M$

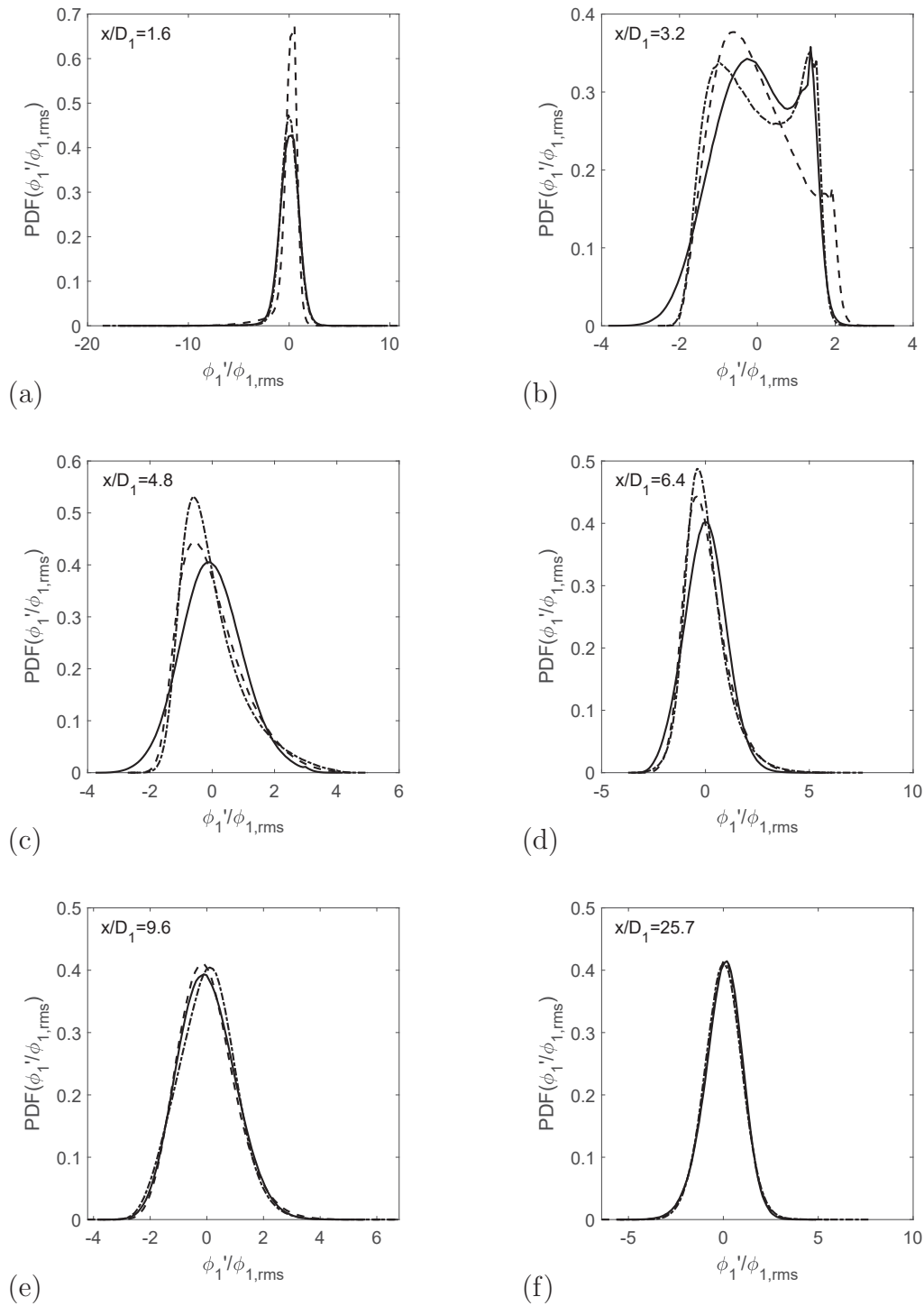


Figure 6.9: Non-dimensionalized PDFs of  $\phi_1$  measured along the centerline for case I:  $M = 0.77$  (—), case II:  $M = 2.1$  (---), case III:  $M = 4.2$  (-·-·-).

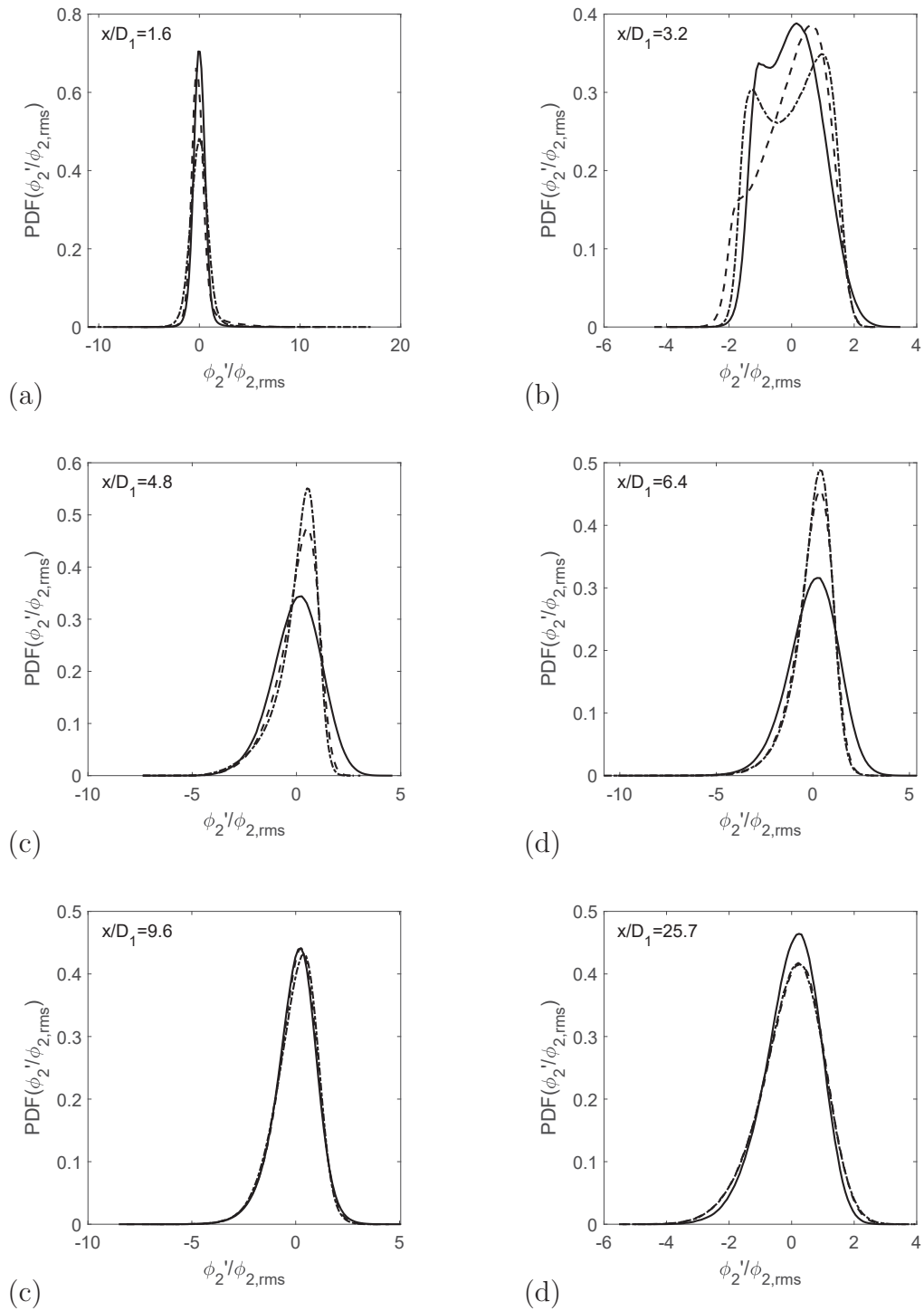


Figure 6.10: Non-dimensionalized PDFs of  $\phi_2$  measured along the centerline for case I:  $M = 0.77$  (—), case II:  $M = 2.1$  (---), case III:  $M = 4.2$  (-·-·-).

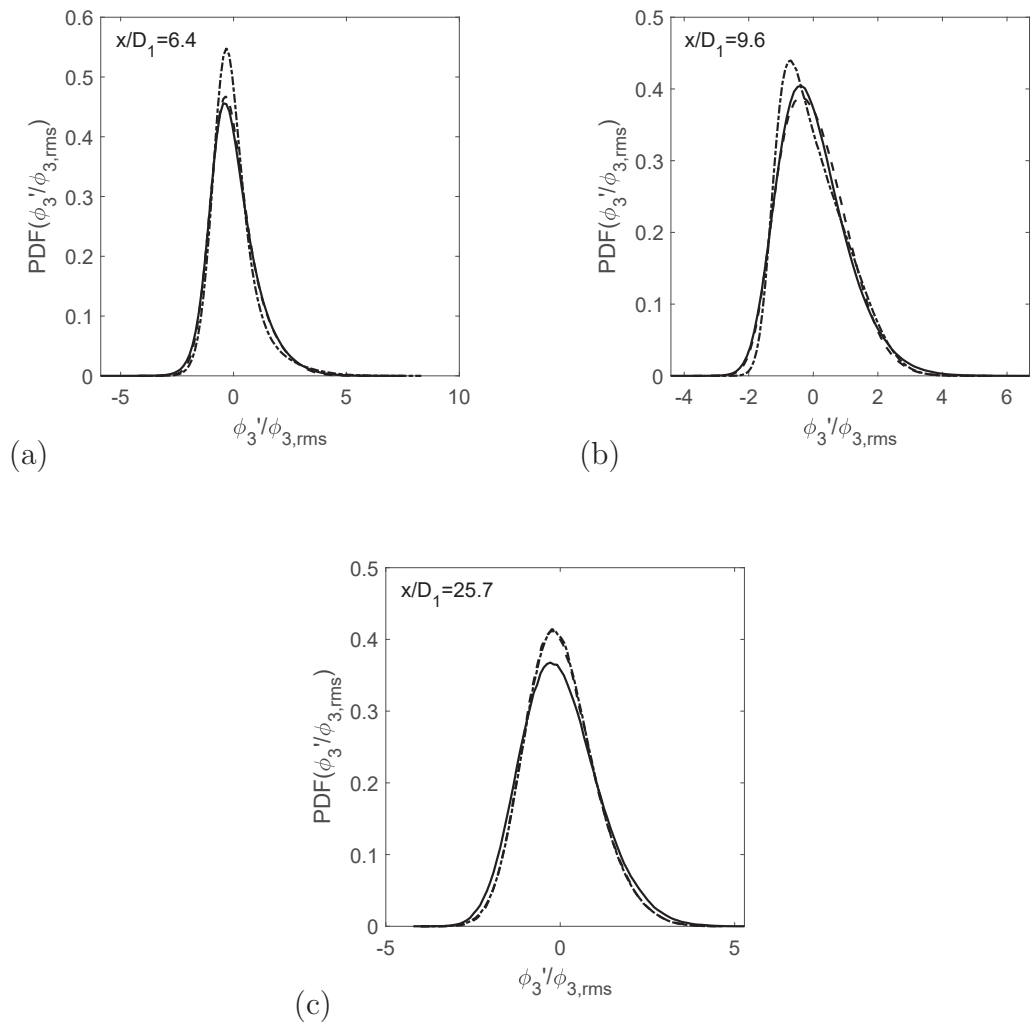


Figure 6.11: Non-dimensionalized PDFs of  $\phi_3$  measured along the centerline for case I:  $M = 0.77$  (—), case II:  $M = 2.1$  (---), case III:  $M = 4.2$  (-·-·).

increases, the potential cores decrease in length,  $\phi_1$  decays faster, and  $\phi_2$  increases faster). This behavior persists farther downstream, but by  $x/D = 9.6$  the PDFs of the three cases begin to collapse and are less markedly skewed. Far downstream (at  $x/D = 25.7$ ), the three PDFs of  $\phi_1$  are indistinguishable and nearly Gaussian, while small differences due to  $M$  can still be observed for the PDFs of  $\phi_2$ , which remain slightly negatively skewed.

The PDFs of  $\phi_3$  are only presented for the following locations:  $x/D_1 = 6.4$ ,  $x/D_1 = 9.6$ , and  $x/D_1 = 25.7$ . As discussed in §6.2.1, the inner mixing region should, by definition, consist primarily of  $\phi_1$  and  $\phi_2$ , and relatively little  $\phi_3$ . Nevertheless, small amounts of  $\phi_3$  are observed to reach the centerline before  $x/D_1 = 6.4$ , which marks the end of this region (see figures 6.2(d) and 6.3(d)). It is difficult to determine whether these measurements represent actual physical measurements of  $\phi_3$ , or if they are affected by (i) noise from the cold-wire (given that the SNR is low close to the jet exit) or (ii) temperature contamination of the annular jet (which causes  $\phi_3$  to be slightly overestimated and  $\phi_2$  to be slightly underestimated). Accordingly PDFs of  $\phi_3$  are not presented herein for  $x/D_1 < 6.4$ . As may be observed in figure 6.11, the PDFs of  $\phi_3$  are not strongly affected by  $M$ . Moreover, they are positively skewed, indicating more frequent large positive fluctuations of  $\phi_3$ , which is expected given that the flow at the centerline is lowest in  $\phi_3$ . Finally, similarly to what was observed for the PDFs of  $\phi_2$ , small differences due to  $M$  can still be observed in the PDFs of  $\phi_3$  at  $x/D_1 = 25.7$ .

#### 6.4 Scalar-Scalar Joint Probability Density Functions

Scalar-scalar joint probability density functions (JPDFs), including the JPDFs of  $\phi_1$  and  $\phi_2$  ( $f_{\phi_1\phi_2}$ ),  $\phi_1$  and  $\phi_3$  ( $f_{\phi_1\phi_3}$ ), and  $\phi_2$  and  $\phi_3$  ( $f_{\phi_2\phi_3}$ ), were measured along the axis of the coaxial jets, and are presented in the current section. Not only do the

scalar JPDFs provide valuable information about the state of mixing between scalars, given that they contain information related to statistical moments of all orders for *both* scalars, they are often of interest when modeling multi-scalar flows. As was discussed in §2.2.1, PDF methods which center on the scalar, joint-scalar-scalar, or joint-velocity-scalar PDFs, offer certain advantages compared to other modeling techniques: (i) the nonlinear chemical source term appears in closed form, in marked contrast to RANS models, and (ii) second- or higher-order moments can be readily modeled, as may be desired when studying the dispersion of pollutants or other toxic species. Despite their practical applications, there are relatively few measurements in the literature describing the evolution of scalar-scalar JPDFs in turbulent flows (in part because of difficulties associated with the simultaneous measurement of multiple scalars in turbulent flows); to the author’s knowledge, such measurements appear only in the works of Cai *et al.* (2011), Soltys and Crimaldi (2015), and Li *et al.* (2017).

#### 6.4.1 JPDFs of $\phi_1$ and $\phi_2$

The JPDFs of  $\phi_1$  and  $\phi_2$  ( $f_{\phi_1\phi_2}$ ) were measured at  $x/D_1 = 1.6, 3.2, 4.8, 6.4, 9.6$  and  $25.7$  for each of the three cases. Results are presented in figures 6.12 - 6.14. The evolution of  $f_{\phi_1\phi_2}$  along the centerline is first described. Subsequently, the effects of  $M$  on  $f_{\phi_1\phi_2}$  are discussed.

##### Downstream evolution of JPDFs of $\phi_1$ and $\phi_2$ along the centerline

Given that  $\phi_1 + \phi_2 + \phi_3 = 1$ ,  $\phi_1 + \phi_2$  must sum to less than 1, and the JPDFs should thus be confined to the triangle in the lower-left corner of  $\phi_1$ - $\phi_2$  space, which is bounded by the points  $(\phi_1 = 0, \phi_2 = 0)$ ,  $(\phi_1 = 1, \phi_2 = 0)$  and  $(\phi_1 = 0, \phi_2 = 1)$ . Nevertheless, certain small deviations are observed, which are primarily attributed to measurement noise. As was discussed in the previous subsection, measurements

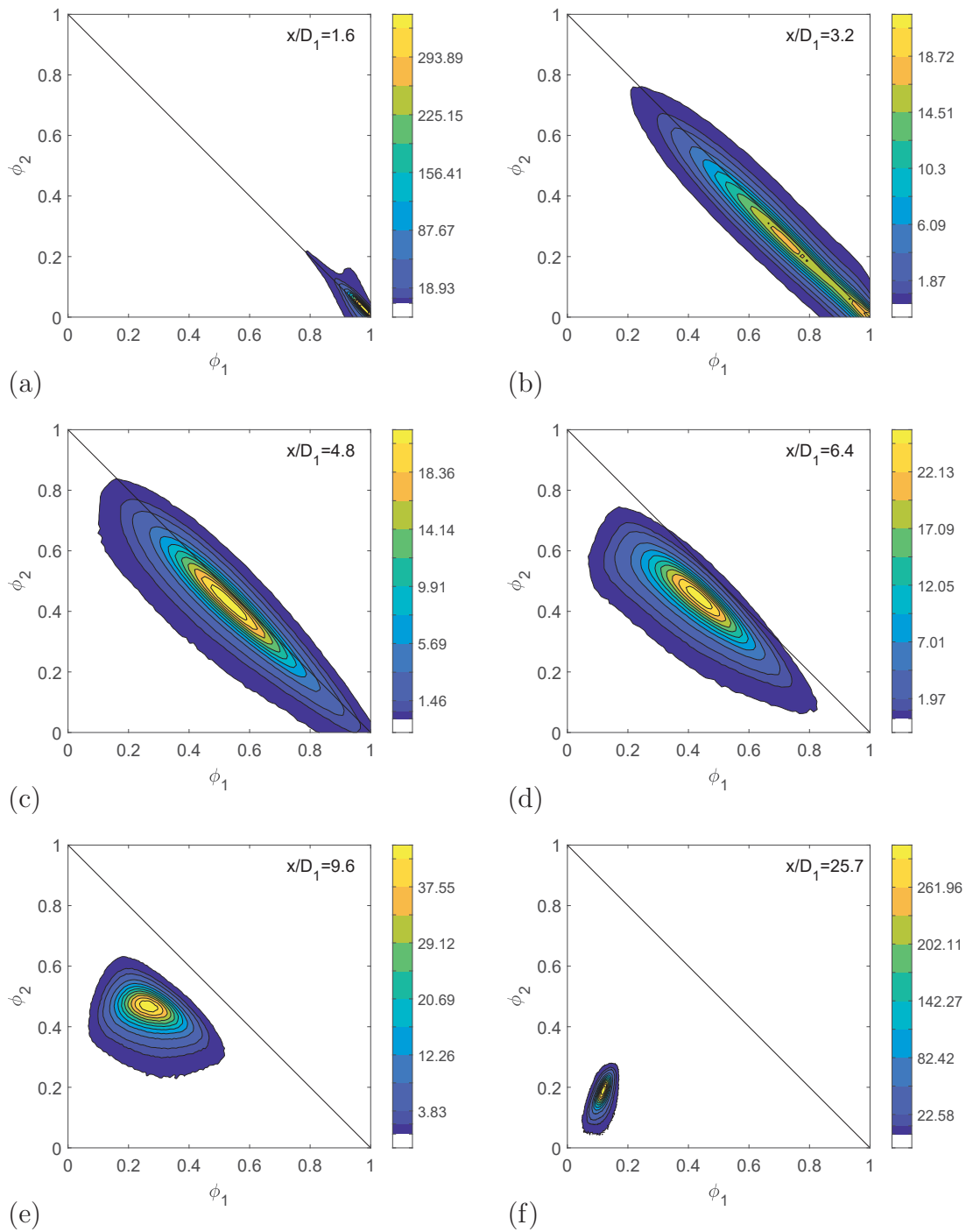


Figure 6.12: JPDFs of  $\phi_1$  and  $\phi_2$  for case I ( $M = 0.77$ ). The 3 last contours contain 99%, 95%, and 90% of the JPDF.

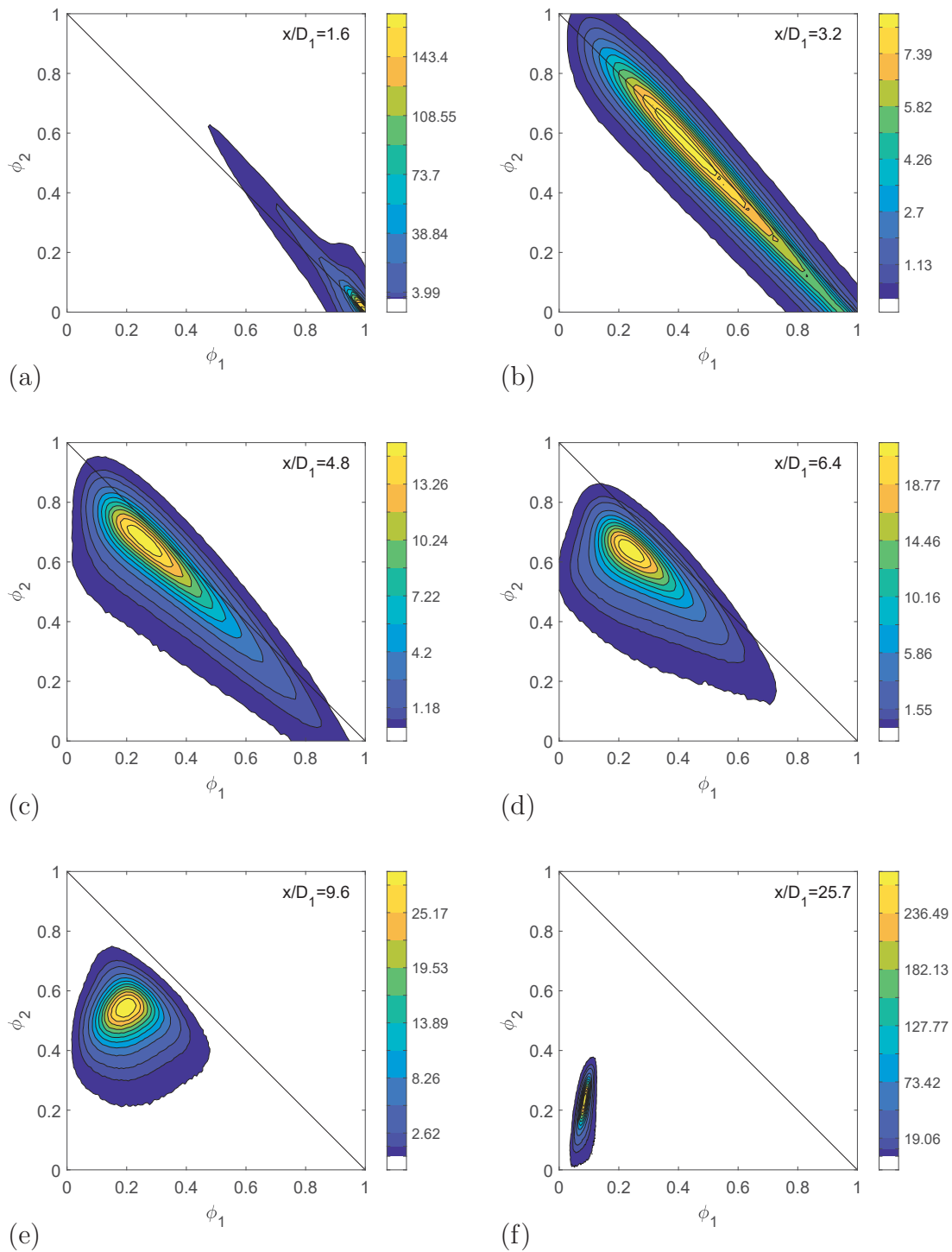


Figure 6.13: JPDFs of  $\phi_1$  and  $\phi_2$  for case II ( $M = 2.1$ ). The 3 last contours contain 99%, 95%, and 90% of the JPDF.

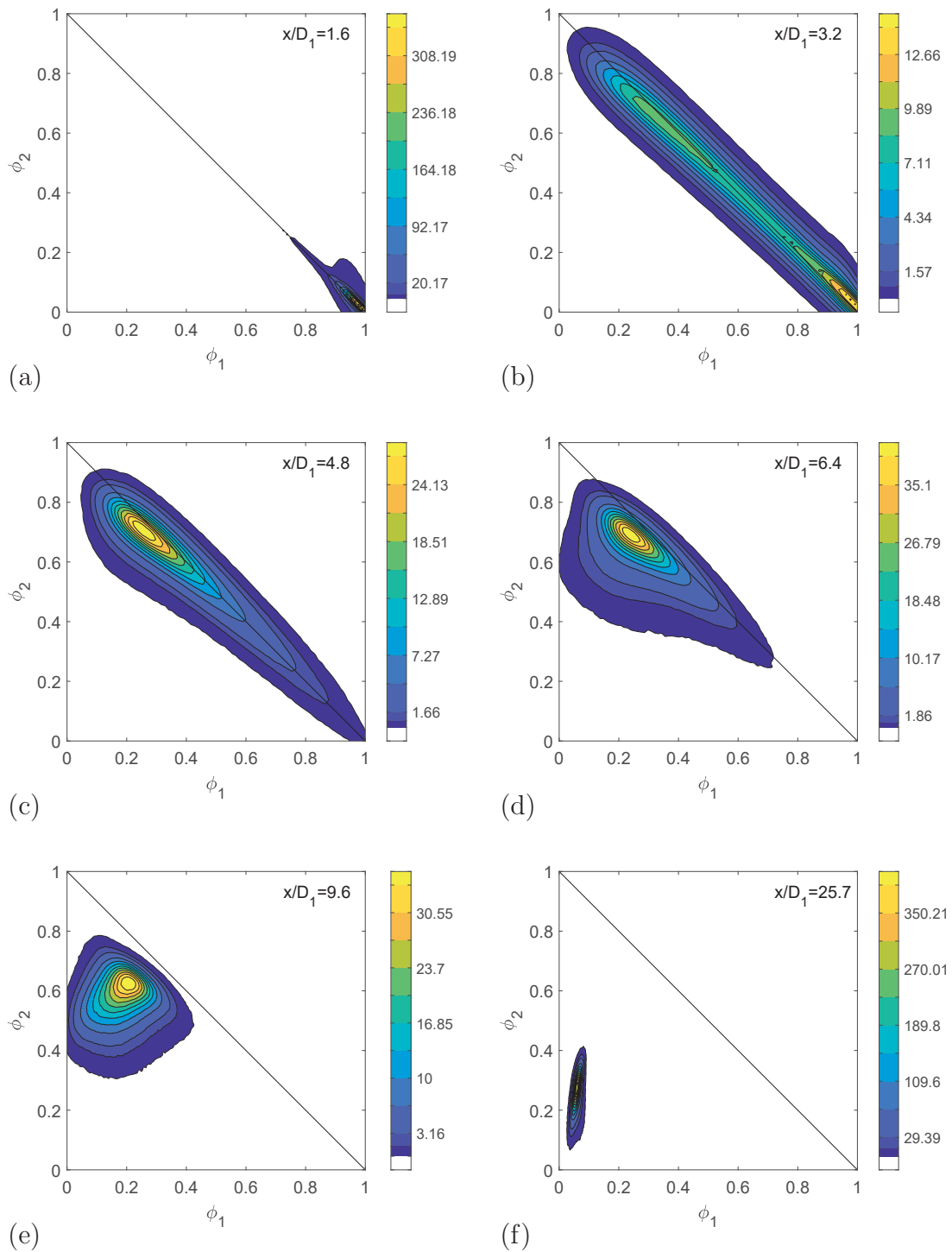


Figure 6.14: JPDFs of  $\phi_1$  and  $\phi_2$  for case III ( $M = 4.2$ ). The 3 last contours contain 99%, 95%, and 90% of the JPDF.

of  $\phi_3$  are affected by both noise (which was not filtered out since it was difficult to determine the noise spectrum/floor for this data) and temperature contamination of the annular jet. The former is particularly significant very close to the jet exit (where the SNR is low), and causes fluctuations of  $\phi_3$  to be overestimated. Accordingly, in the potential core of the center jet or the inner mixing region, where the flow should consist only of  $\phi_1$  or only of  $\phi_1$  and  $\phi_2$ , the JPDFs (which lie along the line defined by  $\phi_1 + \phi_2 = 1$ ) are thicker than expected, and extend into the unrealizable zone of scalar space. Although the effects of noise from the  $\phi_3$  measurements are most visible close to the jet exit (i.e. at  $x/D_1 = 1.6$  or  $x/D_1 = 3.2$ ), they do perpetuate farther downstream, and this should be kept in mind when interpreting the data. Despite this, the JPDFs reveal a significant amount of information about the flow, much of which is consistent with previously reported statistics from the present work.

As can be observed in figures 6.12 - 6.14,  $f_{\phi_1\phi_2}$  exhibits similar general trends for the three cases investigated herein ( $M = 0.77$ ,  $M = 2.1$ ,  $M = 4.2$ ). Close to the jet exit ( $x/D_1 = 1.6$ ), the JPDF is mainly concentrated in the lower-right corner of the  $\phi_1$ - $\phi_2$  scalar space, where  $\phi_1$  is large and  $\phi_2$  is small, as expected from the underlying physics of the flow, and which is also consistent with the mean profiles of  $\phi_1$  and  $\phi_2$ . Nevertheless, the first signs of mixing can be observed as the JPDFs begin to extend along the line defined by  $\phi_1 + \phi_2 = 1$ . This was briefly discussed in the previous subsection when analyzing the (marginal) PDFs of  $\phi_1$  and  $\phi_2$ , and it should be emphasized that this is not inconsistent with the idea of a potential core, which is generally quantified by measurements of mean quantities. Mixing between  $\phi_1$  and  $\phi_2$  becomes enhanced at  $x/D_1 = 3.2$ , as the JPDF extends much farther into  $\phi_1$ - $\phi_2$  scalar space. At this downstream location,  $\phi_1$  and  $\phi_2$  are still mostly distributed along the  $\phi_1 + \phi_2 = 1$  line, depicting the anti-correlated nature of  $\phi_1$  and  $\phi_2$ . Moreover, the

JPDF of cases I and II are bimodal, like the PDFs of  $\phi_1$  and  $\phi_2$  at this location. The JPDF remains anti-correlated at  $x/D = 4.8$ , but moves off the  $\phi_1 + \phi_2 = 1$  line, indicating that fluid from the coflow ( $\phi_3$ ) begins to reach the centerline. In cases II and III, the JPDF bends slightly towards lower values of  $\phi_1$  and  $\phi_2$ , and continues to do so at  $x/D = 6.4$ . By  $x/D = 9.6$ ,  $\phi_1$  and  $\phi_2$  are no longer anti-correlated and JPDFs have a rounder, but not Gaussian, shape. Finally, far downstream, the JPDF has moved to the corner defined by  $(\phi_1, \phi_2) = (0, 0)$ , and the scalars are positively correlated, as observed from the positive slope of the principal axis of the JPDF.

Close to the jet exit, the evolution of the JPDFs in the current work ( $A_2/A_1 = 1.8$ ) is similar to what Li *et al.* (2017) observed for coaxial jets with larger area ratios ( $A_2/A_1 = 2.6$ ), but differs from what they observed for coaxial jets with smaller area ratios ( $A_2/A_1 = 1.0$ ). In the former case,  $\phi_1$  and  $\phi_2$  are anti-correlated, and the JPDFs first evolve along the line defined by  $\phi_1 + \phi_2 = 1$ . In contrast, when the area ratio is smaller, the JPDF bends away from this line immediately beyond the end of the center jet's potential core, indicating the earlier presence of the coflow fluid (i.e.  $\phi_3$ ) along the axis. As the area ratio decreases, so too does the length of the outer potential core (see figure 6.15), which allows mixtures of  $\phi_2$  and  $\phi_3$  to reach the centerline much earlier. Farther downstream, the evolution and shapes of the JPDFs herein differ from both cases examined in Li *et al.* (2017) ( $A_2/A_1 = 1.0$ ,  $A_2/A_1 = 2.6$ ), which underlines the importance of other initial conditions, such as  $M$ , have on the mixing of  $\phi_1$  and  $\phi_2$ .

### **Effects of momentum ratio on the JPDFs of $\phi_1$ and $\phi_2$**

The effects of the momentum ratio ( $M$ ) on the evolution of  $f_{\phi_1\phi_2}$  is examined in more detail for the following select locations: (i)  $x/D_1 = 3.2$ , just beyond the end of the potential core, and where fluctuations of  $\phi_1$  and  $\phi_2$  are largest, (ii)  $x/D_1 = 6.4$ ,

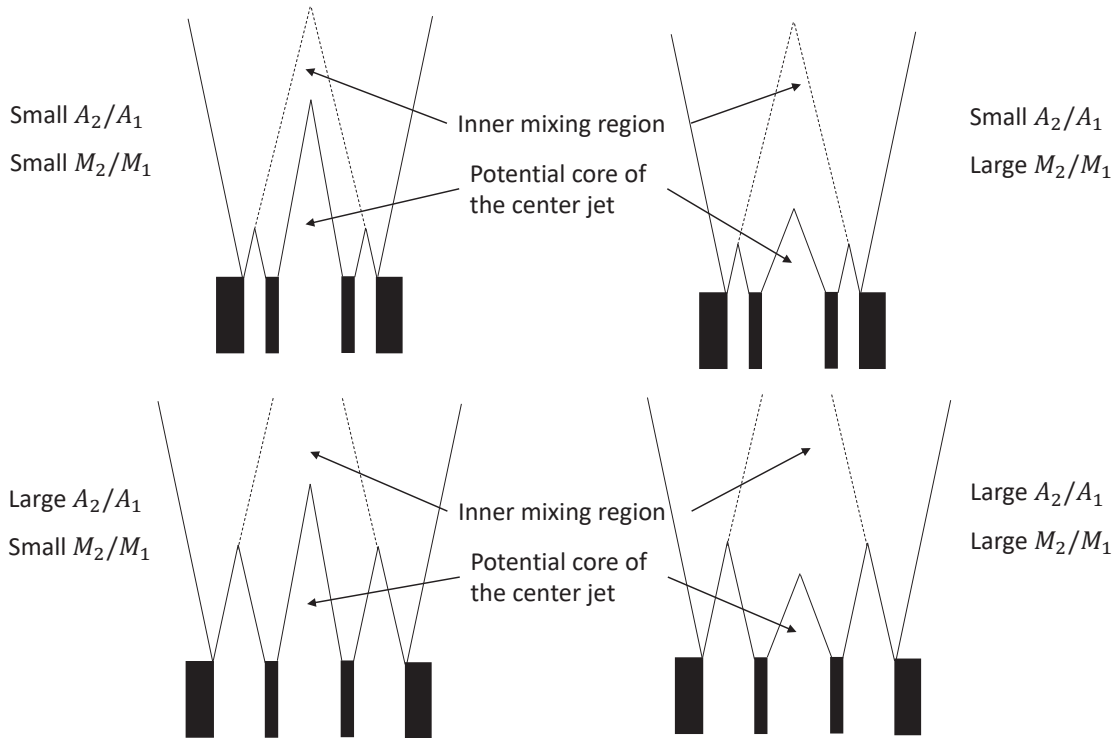


Figure 6.15: Schematic representation of the effects of the area ( $A_2/A_1$ ) and momentum ( $M = M_2/M_1$ ) ratios of the coaxial jets on the flow. As can be seen above, the former controls the length of the outer potential core, and the latter controls the length of the potential core of the center jet. Note that these sketches are based on data from previous studies of coaxial jets (e.g., Ko and Au 1985; Au and Ko 1987; Schumaker and Driscoll 2012).

which marks the end of the inner mixing region and the beginning of the fully merged region, and (iii)  $x/D_1 = 25.7$ , the farthest downstream location at which measurements were obtained. JPDFs at the previously mentioned downstream locations are replotted side-by-side in figure 6.16 to more effectively compare the effects of  $M$  on the mixing of  $\phi_1$  and  $\phi_2$ . It is worth pointing out that at  $x/D_1 = 3.2, 6.4,$  and  $25.7$ ,  $\rho_{\phi_1\phi_2}$  is approximately equal for each of the three cases (at  $x/D = 3.2$ ,  $-0.98 \leq \rho_{\phi_1\phi_2} \leq -0.97$ ; at  $x/D_1 = 6.4$ ,  $-0.82 \leq \rho_{\phi_1\phi_2} \leq -0.67$ ; at  $x/D_1 = 25.7$ ,  $0.55 \leq \rho_{\phi_1\phi_2} \leq 0.57$ ), yet the JPDFs at these locations are not identical. Consistent with previous work (Li *et al.* 2017), one can observe that correlation coefficients do not fully describe the state of mixing between scalars.

At  $x/D_1 = 3.2$ , the JPDFs of cases II and III extend much farther along the line defined by  $\phi_1 + \phi_2 = 1$  than for case I, such that the range of possible values for  $\phi_1$  and  $\phi_2$  (i.e. 0 to 1) is almost fully spanned for these two cases. Additionally, the location of the peaks of the JPDFs, which indicate the most likely values  $\phi_1$  and  $\phi_2$  in the flow, shift with increasing  $M$ . Examination of figures 6.16(a), (b), and (c) suggests that at  $x/D_1 = 3.2$ , mixing is progressing fastest for case II, where the flow is more likely to consist of low  $\phi_1$  and high  $\phi_2$  (i.e. fluid from the inner mixing region) followed by case III, where the flow is very likely to consist of either low  $\phi_1$  and high  $\phi_2$  (like in case II) *or* fluid from the center jet ( $\phi_1 = 1, \phi_2 = 0$ ), and finally case I, where the JPDF retains its bimodal nature, but is mostly composed of high  $\phi_1$  and low  $\phi_2$  scalars. The latter is expected, given that as  $M$  decreases, (i) the inner potential core increases, which delays mixing between  $\phi_1$  and  $\phi_2$ , and (ii) the proportion of  $\phi_1$  (compared to  $\phi_2$  and  $\phi_3$ ) in the flow increases. By  $x/D_1 = 6.4$ , one can observe that as  $M$  increases, the peaks of JPDFs move towards lower values of  $\phi_1$  and higher values of  $\phi_2$ , consistent with the mean profiles of these quantities. Furthermore, the

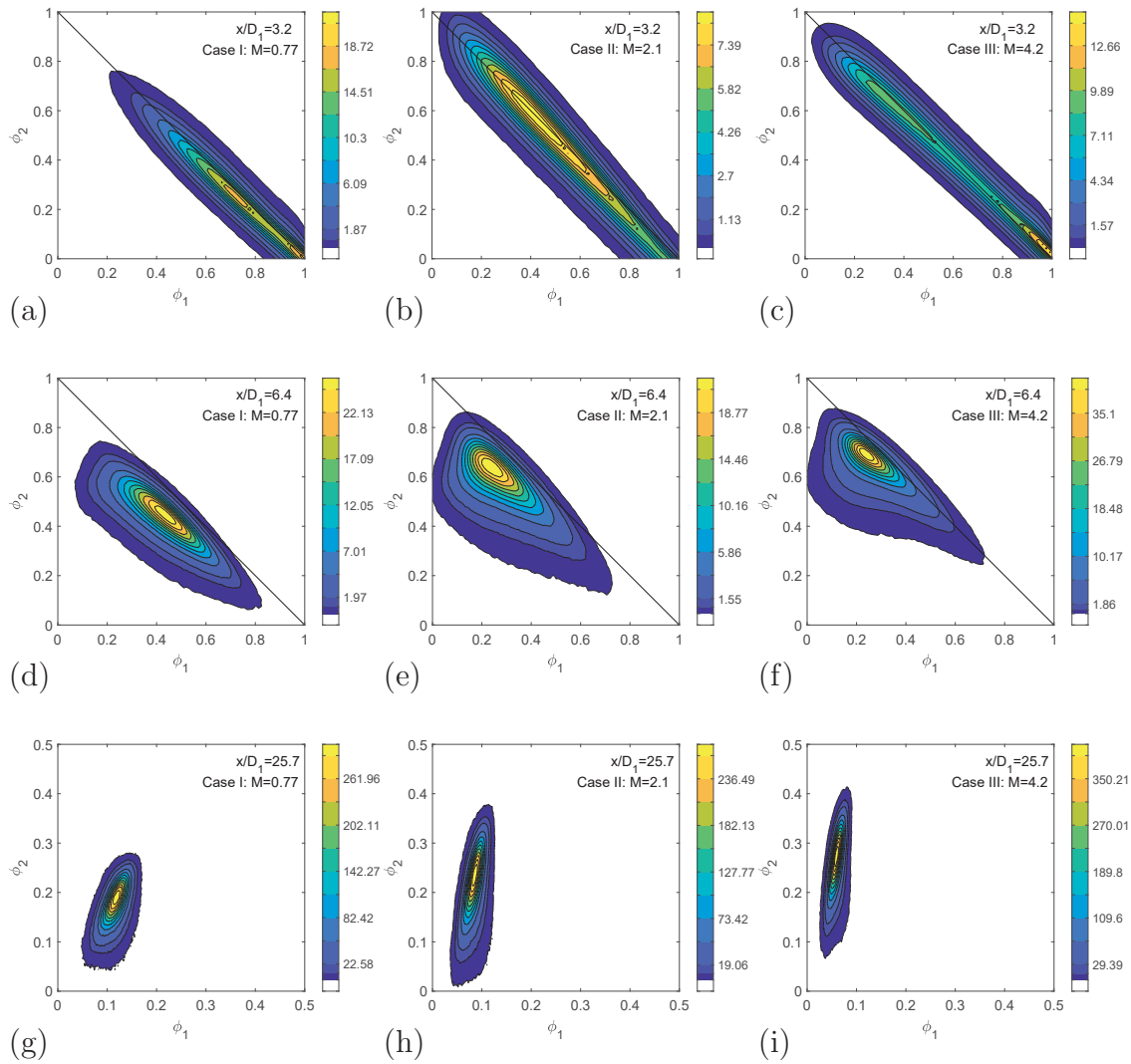


Figure 6.16: Effect of the momentum ratio ( $M$ ) on the JPDFs of  $\phi_1$  and  $\phi_2$  at  $x/D_1 = 3.2$ ,  $x/D_1 = 6.4$ , and  $x/D_1 = 25.7$ . Note that the data figures 6.12-6.14 is replotted here to more effectively compare the effects of  $M$ .

JPDFs bend progressively towards  $(\phi_1, \phi_2) = (0, 0)$ , their final (asymptotic) state, indicating an increased presence of large, but rare, fluctuations of  $\phi_3$  that mix  $\phi_1$  and  $\phi_2$  together. Finally, as depicted in figures 6.16(g), (h), and (i), at  $x/D_1 = 25.7$ , the JPDFs become thinner and longer as  $M$  gets larger, since fluctuations of  $\phi_1$  decrease and those of  $\phi_2$  increase. Given that the JPDF of case I is centered at  $(\phi_1, \phi_2) \approx (0.1, 0.2)$ , closest to  $(\phi_1, \phi_2) = (0, 0)$ , and has a shape which appears to approach a joint-normal distribution, it is suggested that the scalars may be more fully mixed for this case, when compared to the other two cases.

Consequently, one may infer that mixing between  $\phi_1$  and  $\phi_2$  initially progresses faster for cases II and III, where  $M$  is larger, but farther downstream, it appears to progress faster for case I. The former is consistent with what was observed when examining profiles of  $\rho_{\phi_1\phi_2}$ , which indicated that for  $4.8 < x/D_1 < 22.5$ ,  $\phi_1$  and  $\phi_2$  mix faster as  $M$  increases. The latter, however, agrees with the results of Li *et al.* (2017) for coaxial jets in which  $M < 1$ . Li *et al.* (2017) found that as  $M$  (or, alternatively, the velocity ratio, which is directly related to  $M$  since the density ratio is constant) increased, the JPDF moved farther into the  $\phi_1$ - $\phi_2$  scalar space, and towards smaller values of  $\phi_1$ . However, farther downstream their scalars were more fully mixed for the case with a lower value of  $M$ . From their results, they concluded that as  $M$  increased, so did turbulent transport (i.e. transport by the conditional mean of the fluctuating velocity), which initially caused the JPDFs to evolve faster. However, small-scale mixing was slower, and delayed the evolution of JPDFs far downstream.

#### 6.4.2 JPDFs of $\phi_1$ and $\phi_3$

Similarly to the PDFs of  $\phi_3$ , the JPDFs of  $\phi_1$  and  $\phi_3$  were only measured at  $x/D_1 = 6.4, 9.6$ , and  $25.7$  for each of the three cases. The results are presented in figure 6.17, and again, it should be noted that the JPDFs of  $\phi_1$  and  $\phi_3$  should be

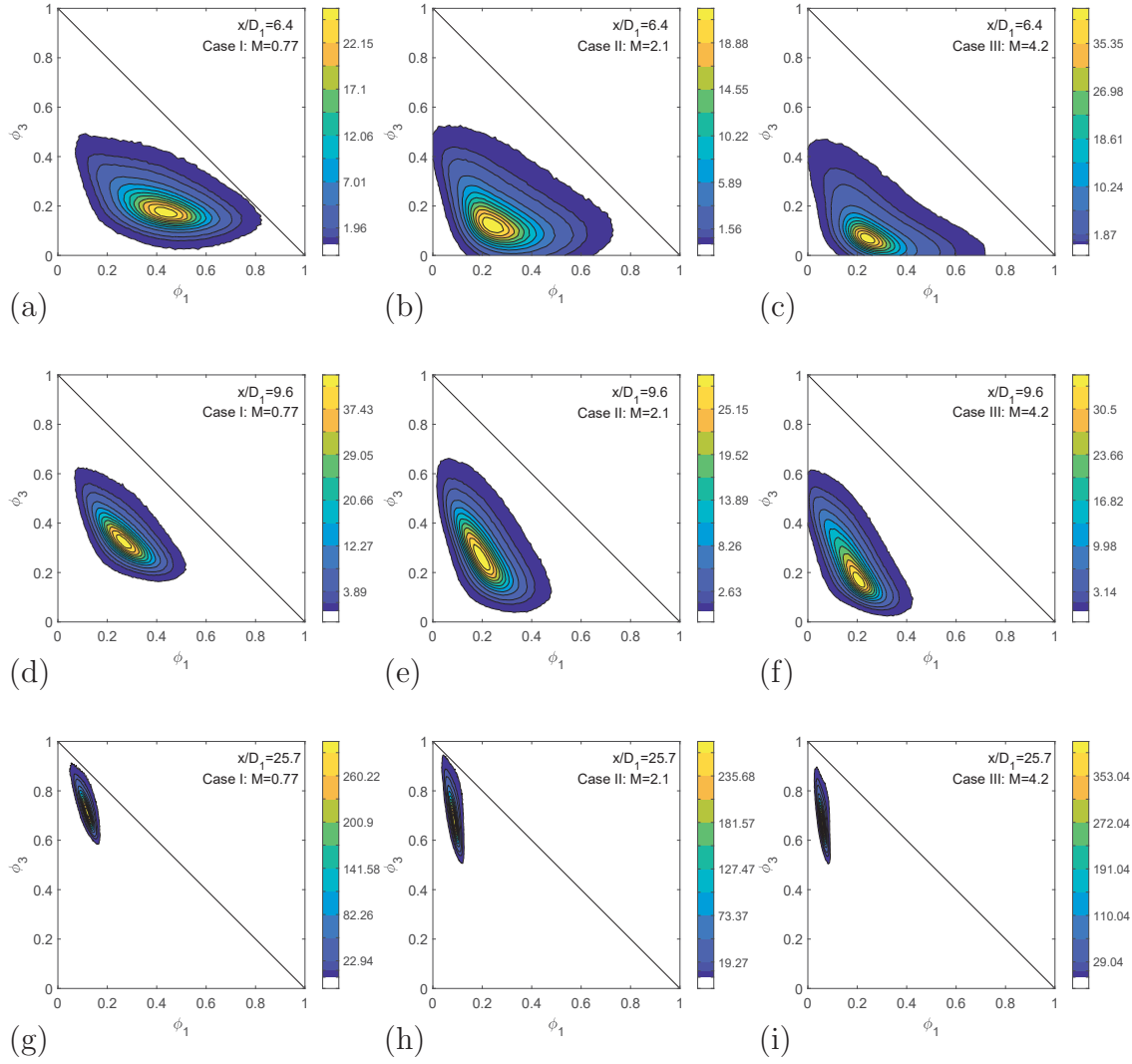


Figure 6.17: JPDFs of  $\phi_1$  and  $\phi_3$ . The 3 last contours contain 99%, 95%, and 90% of the JPDF

confined to the triangle in the lower-left corner of  $\phi_1$ - $\phi_3$  space, since  $\phi_1 + \phi_2 + \phi_3 = 1$ . As  $x/D_1$  increases,  $f_{\phi_1\phi_3}$  moves from the bottom of  $\phi_1$ - $\phi_3$  scalar space, where  $\phi_3$  is small, to the top-left corner of  $\phi_1$ - $\phi_3$  scalar-space, where  $\phi_1$  is small and  $\phi_3$  is large, in agreement with previous results presented herein. At  $x/D_1 = 6.4$ , fluctuations of  $\phi_1$  and  $\phi_3$  are generally large. Although fluctuations of  $\phi_3$  remain relatively large far downstream, fluctuations of  $\phi_1$  have significantly diminished, in accordance with the rms measurements depicted in figure 6.3. Like measurements of  $f_{\phi_1\phi_2}$  presented in the previous subsection, both the shape and evolution of  $f_{\phi_1\phi_3}$  depend on  $M$ . For example, at  $x/D_1 = 6.4$ , as  $M$  increases, the peak of the JPDF moves closer to  $(\phi_1, \phi_3) = (0, 0)$ , due to increasing amounts of  $\phi_2$  at this location (see figure 6.2(c)), and its shape approaches that of a right triangle, such that one may also observe instances where the flow consists only of  $\phi_1$ - $\phi_2$  mixtures or only of  $\phi_2$ - $\phi_3$  mixtures. There are no mixtures consisting of only of  $\phi_1$  and  $\phi_3$ , an indication that these two scalars must first mix with  $\phi_2$  before being able to mix with each other. The evolution of  $f_{\phi_1\phi_3}$  when  $M$  is large therefore bears some resemblance to the evolution of the scalar-scalar JPDFs observed in the work of Soltys and Crimaldi (2015), where two parallel jets mix in a slow-moving coflow. Soltys and Crimaldi (2015) found that the scalar-scalar JPDFs evolved along the axes of scalar space (i.e. lines defined by  $\phi_1 = 0$  and  $\phi_2 = 0$ ), and coalescence of the scalars only occurred after significant dilution with the ambient fluid. The situation herein is slightly different, given that  $\phi_2$  is not present in sufficient quantity to permit  $\phi_1$  and  $\phi_3$  to effectively mix, however, one can nevertheless, observe a tendency for  $f_{\phi_1\phi_3}$  to evolve along the axes of scalar space (at least for  $M > 1$ ).

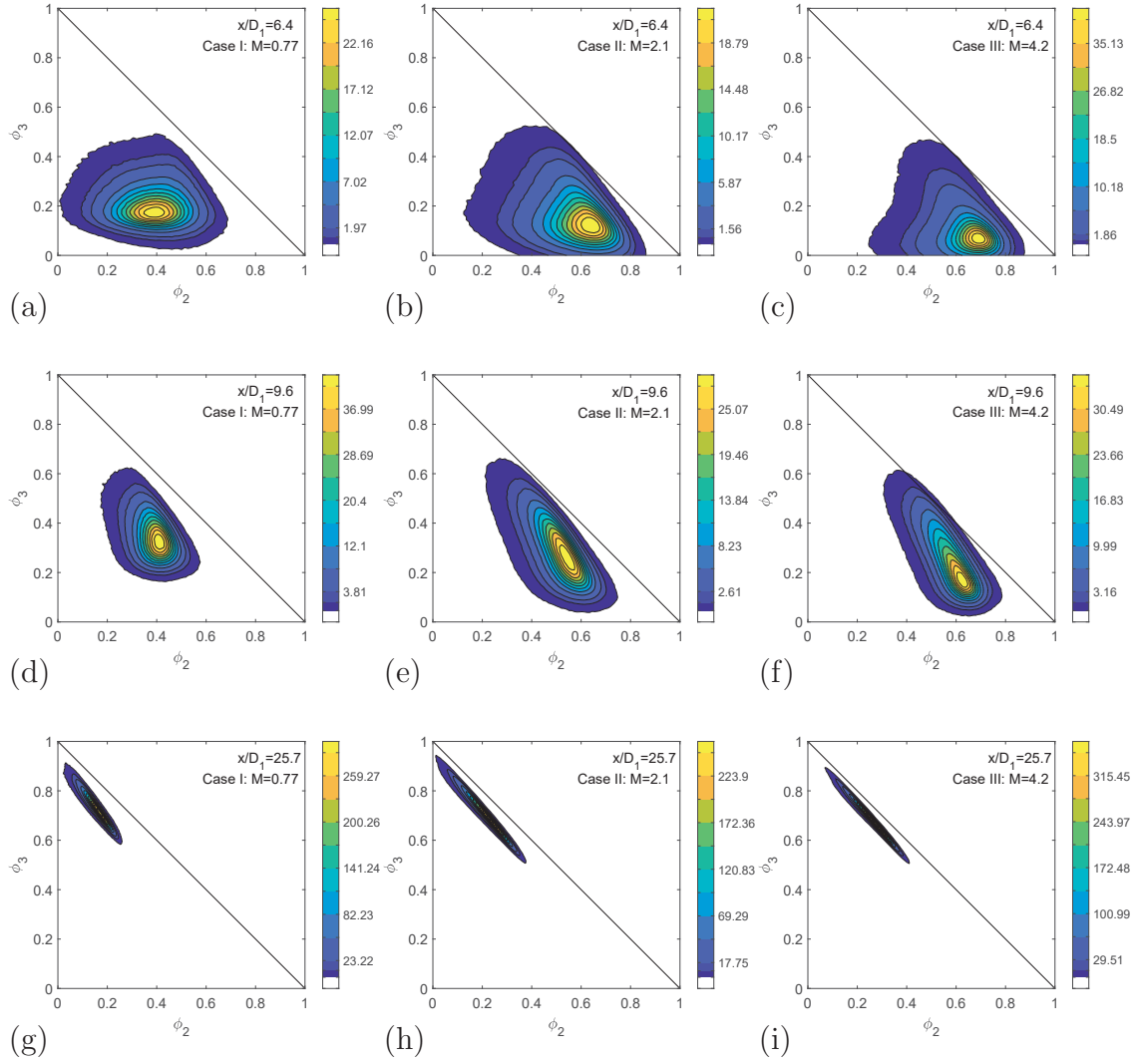


Figure 6.18: JPDFs of  $\phi_2$  and  $\phi_3$ . The 3 last contours contain 99%, 95%, and 90% of the JPDF.

### 6.4.3 JPDFs of $\phi_2$ and $\phi_3$

The JPDFs of  $\phi_2$  and  $\phi_3$  were also measured at  $x/D_1 = 6.4, 9.6,$  and  $25.7$  for the three cases investigated herein. As can be seen in figure 6.18, at  $x/D_1 = 6.4$ , which marks the location at which  $\langle \phi_2 \rangle$  reaches its maximum value,  $f_{\phi_2\phi_3}$  is accordingly located in the lower-right corner of  $\phi_2$ - $\phi_3$  space, where  $\phi_2$  is large and  $\phi_3$  is small. Again, quasi-triangular shapes are observed when  $M$  large. In this case, the JPDF is bounded on one side by  $\phi_3 = 0$ , indicating the presence of a mixture purely composed of  $\phi_1$  and  $\phi_2$ , and on the other by  $\phi_2 + \phi_3 = 1$ , indicating the presence of a mixture purely composed of  $\phi_2$  and  $\phi_3$ , consistent with what was discussed in the previous subsection. At  $x/D_1 = 9.6$ , the JPDFs move towards this line for cases in which  $M > 1$ , and by  $x/D_1 = 25.7$ , the JPDFs of all cases are nearly aligned with  $\phi_2 + \phi_3 = 1$ . Although the flow appears to mainly consist of anti-correlated  $\phi_2$  and  $\phi_3$ , it is important to note that  $\phi_1$  is still present, albeit in very small quantities.

These results, along with those for  $f_{\phi_1\phi_3}$  presented in the previous subsection, further confirm something that has been discussed sporadically throughout this chapter — there are often significant differences observed between coaxial jets in which  $M < 1$  and  $M > 1$ . Both the present and aforementioned subsection demonstrate that when  $M < 1$ , all three scalars are present and mix together in the fully merged region, as indicated by the fact that the JPDFs evolve through the center of scalar space. However when  $M > 1$ , even in what is considered the fully merged zone (where the coaxial jets are expected to behave as single jet mixing in a fluid of  $\phi_3$ ), there are instances in which either  $\phi_1$  or  $\phi_3$  are absent, which suggests that the jets are not as well mixed for these cases.

## 6.5 Velocity-Scalar Joint Probability Density Functions

In the previous subsection, the evolution of the scalar-scalar JPDFs along the centerline was discussed. The current section describes the evolution of the velocity-scalar JPDFs, which, as noted earlier, are also of interest when using PDF methods to model scalar flows.

The JPDFs of  $U$  and  $\phi_1$  ( $f_{U\phi_1}$ ) and  $U$  and  $\phi_2$  ( $f_{U\phi_2}$ ) are presented in figures 6.19 and 6.20, respectively. The evolutions of  $f_{U\phi_1}$  and  $f_{U\phi_2}$  are similar, although the former is initially centered in the upper-right region of  $U$ - $\phi_1$  sample-space, where both  $U$  and  $\phi_1$  are large, whereas the latter is initially centered in the lower-right region of the sample-space, where  $U$  is large and  $\phi_2$  is small. As may be inferred from the vertical shapes of  $f_{U\phi_1}$  and  $f_{U\phi_2}$  at  $x/D_1 = 3.2$ , both  $\phi_1$  and  $\phi_2$  are uncorrelated with  $U$  at this location. This is consistent with measurements of  $\rho_{u\phi_1}$  and  $\rho_{u\phi_2}$ , which as discussed in §6.2.2, are approximately zero in the inner mixing region. Moreover, in agreement with measurements of the scalar PDFs and JPDFs presented in previous sections, the velocity-scalar PDFs of case III are bimodal, and along with those for case II, spread much farther into scalar space than case I. Farther downstream, one may observe that  $U$  and  $\phi_1$  become positively correlated earlier (given the inclined orientation of  $f_{U\phi_1}$  at  $x/D_1 = 9.6$ , with  $0.32 \leq \rho_{U\phi_1} \leq 0.47$ ) than  $U$  and  $\phi_2$ , which are still effectively uncorrelated in the fully merged region (given the mostly vertical orientation of  $f_{U\phi_2}$  at  $x/D_1 = 9.6$ , with  $-0.12 \leq \rho_{u\phi_2} \leq -0.04$ ). In general, the velocity-scalar JPDFs still exhibit non-Gaussian shapes in the fully merged region, but as may be observed in figure 6.20(j)-(l), the shape of  $f_{U\phi_2}$  tends towards a joint-Gaussian one far downstream. (Although this is less clear in figures 6.19(j)-(l), due to the smaller variations of  $\phi_1$ , the shape of  $f_{U\phi_1}$  is also expected to tend towards a joint-Gaussian one.) Similarly, the shapes of the JPDFs of  $U$  and  $\phi_3$ , which are presented in figure

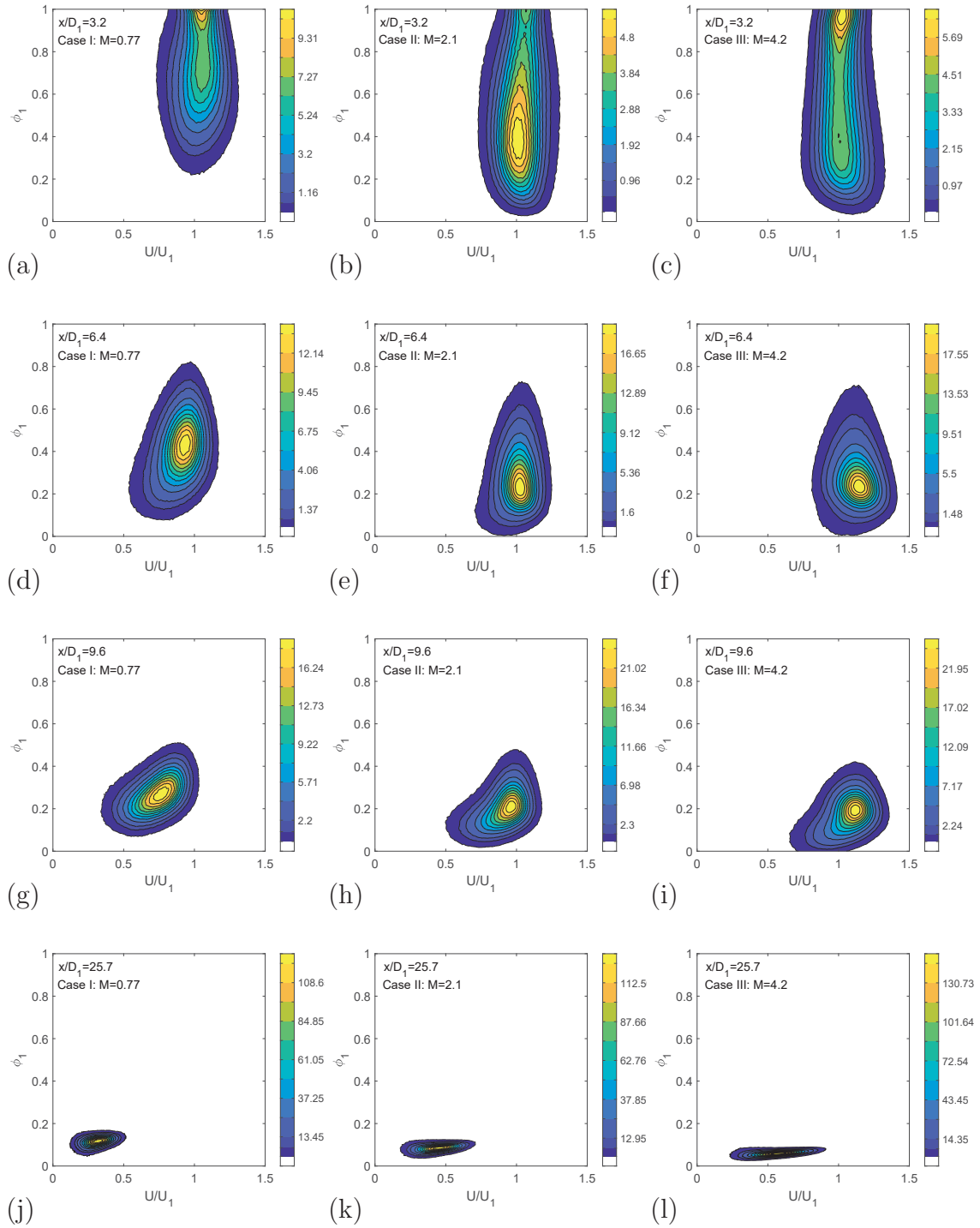


Figure 6.19: JPDFs of  $U$  and  $\phi_1$ . The 3 last contours contain 99%, 95%, and 90% of the JPDF.

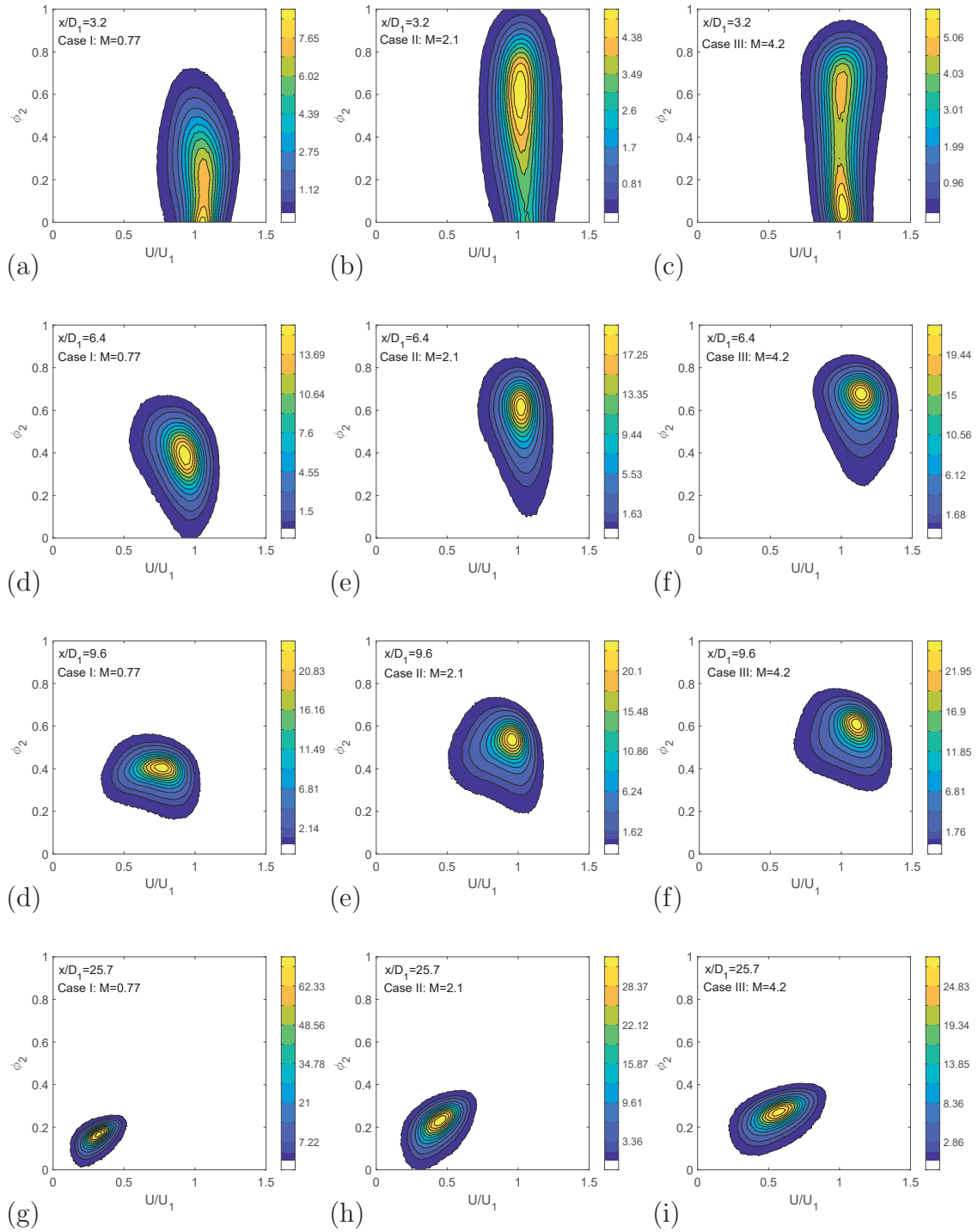


Figure 6.20: JPDFs of  $U$  and  $\phi_2$ . The 3 last contours contain 99%, 95%, and 90% of the JPDF.

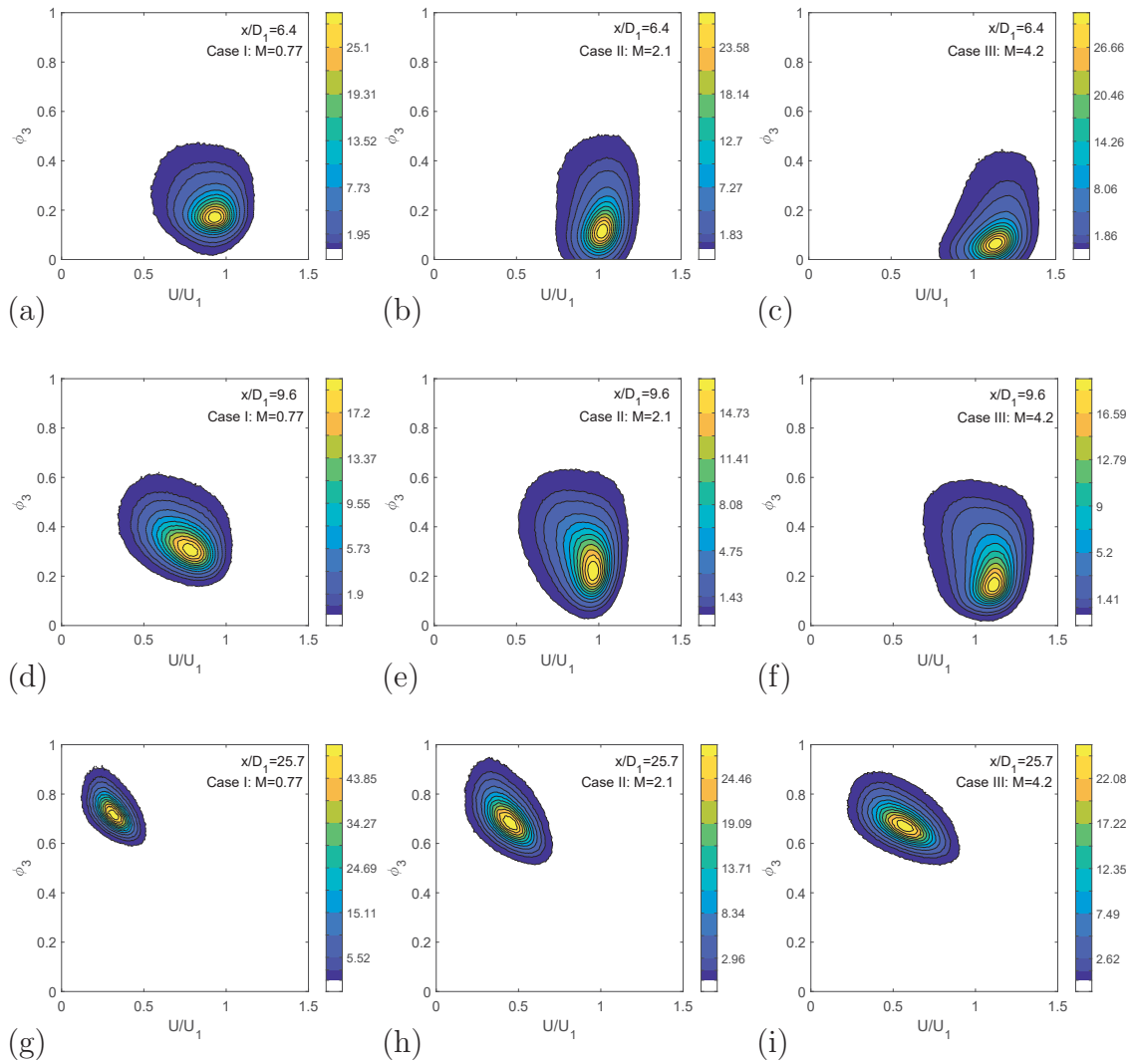


Figure 6.21: JPDFs of  $U$  and  $\phi_3$ . The 3 last contours contain 99%, 95%, and 90% of the JPDF. Note that similarly to data presented in §6.3 and §6.4, measurements of  $f_{U\phi_3}$ , which contain  $\phi_3$ , are limited to  $x/D_1 \geq 6.4$ .

6.21, are again non-Gaussian for  $6.4 \leq x/D_1 \leq 9.6$ , and only begin to approach a joint-Gaussian shape at  $x/D_1 = 25.7$ .

These results appear to be consistent with those of Venkataramani *et al.* (1975) and So *et al.* (1991), both of whom found that JPDFs of  $U$  (the axial velocity) and  $\phi$  (the scalar of interest) were generally non-Gaussian along the centerline of single jets, as well as conclusions put forth by Pope (2000), who, as previously stated, suggests that in the center of free shear flows, PDFs (or JPDFs) will be bell-shaped, but not perfectly Gaussian.

## 6.6 Conditional Expectations of the Fluctuating Velocity

To gain additional insight into interactions between the velocity and scalar fields, measurements of the conditional expectation of the fluctuating streamwise velocity  $\langle u | \phi_\alpha = \hat{\phi}_\alpha, \phi_\beta = \hat{\phi}_\beta \rangle$ , which is equal to the average value of  $u$  given that  $\phi_\alpha = \hat{\phi}_\alpha$  and  $\phi_\beta = \hat{\phi}_\beta$ , are also presented herein. The conditional expectation of the fluctuating velocity appears in the transport equation of the scalar-scalar JPDF as part of the term representing turbulent transport in physical space. Given that it is one of two unclosed terms in this equation, measurements of  $\langle u | \phi_\alpha, \phi_\beta \rangle$  (dropping the sample-space variable from the notation) are consequently of interest to those using PDF methods. Accordingly, the evolutions of  $\langle u | \phi_1, \phi_2 \rangle$ ,  $\langle u | \phi_1, \phi_3 \rangle$ ,  $\langle u | \phi_2, \phi_3 \rangle$  are examined in the current section. Measurements are presented for the locations at which  $f_{\phi_1\phi_2}$ ,  $f_{\phi_1\phi_3}$ ,  $f_{\phi_2\phi_3}$  were measured, and once again limited to the sample-space region containing 99% of the scalar-scalar JPDF.

As depicted in figures 6.22, 6.23, and 6.24, close to the jet exit  $\langle u | \phi_1, \phi_2 \rangle \approx 0$ , indicating that the velocity is independent of  $\phi_1$  and  $\phi_2$ , and, consequently, approximately equal to  $\langle U \rangle$  throughout the sample space. This is consistent with measurements of the velocity-scalar JPDFs ( $f_{U\phi_1}$  and  $f_{U\phi_2}$ ) and velocity-scalar correlation

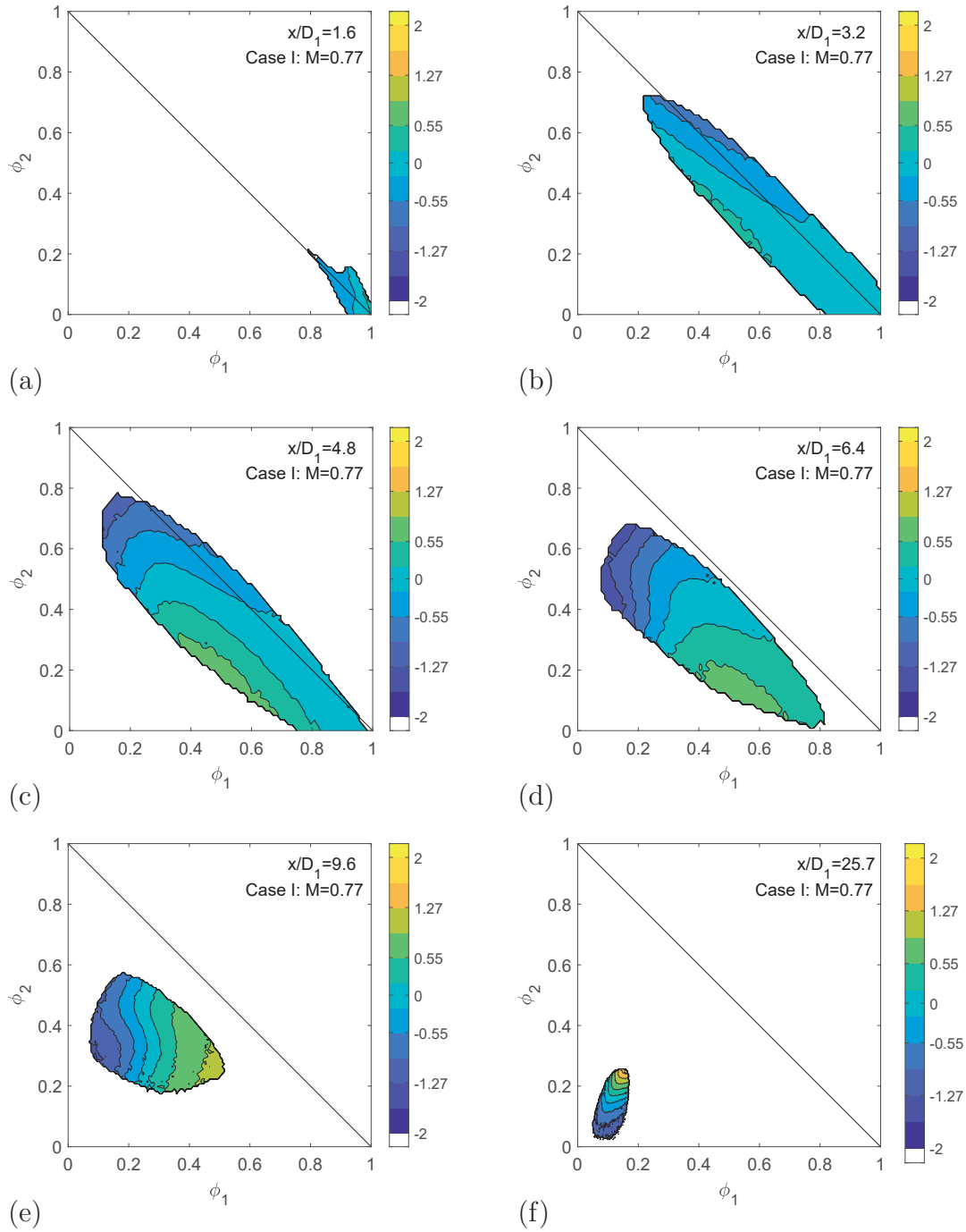


Figure 6.22: Downstream evolution of  $\langle u | \phi_1, \phi_2 \rangle / u_{rms}$  along the centerline for  $M = 0.77$ . The outer contour corresponds to the one containing 99% of the JPDF of  $\phi_1$  and  $\phi_2$ .

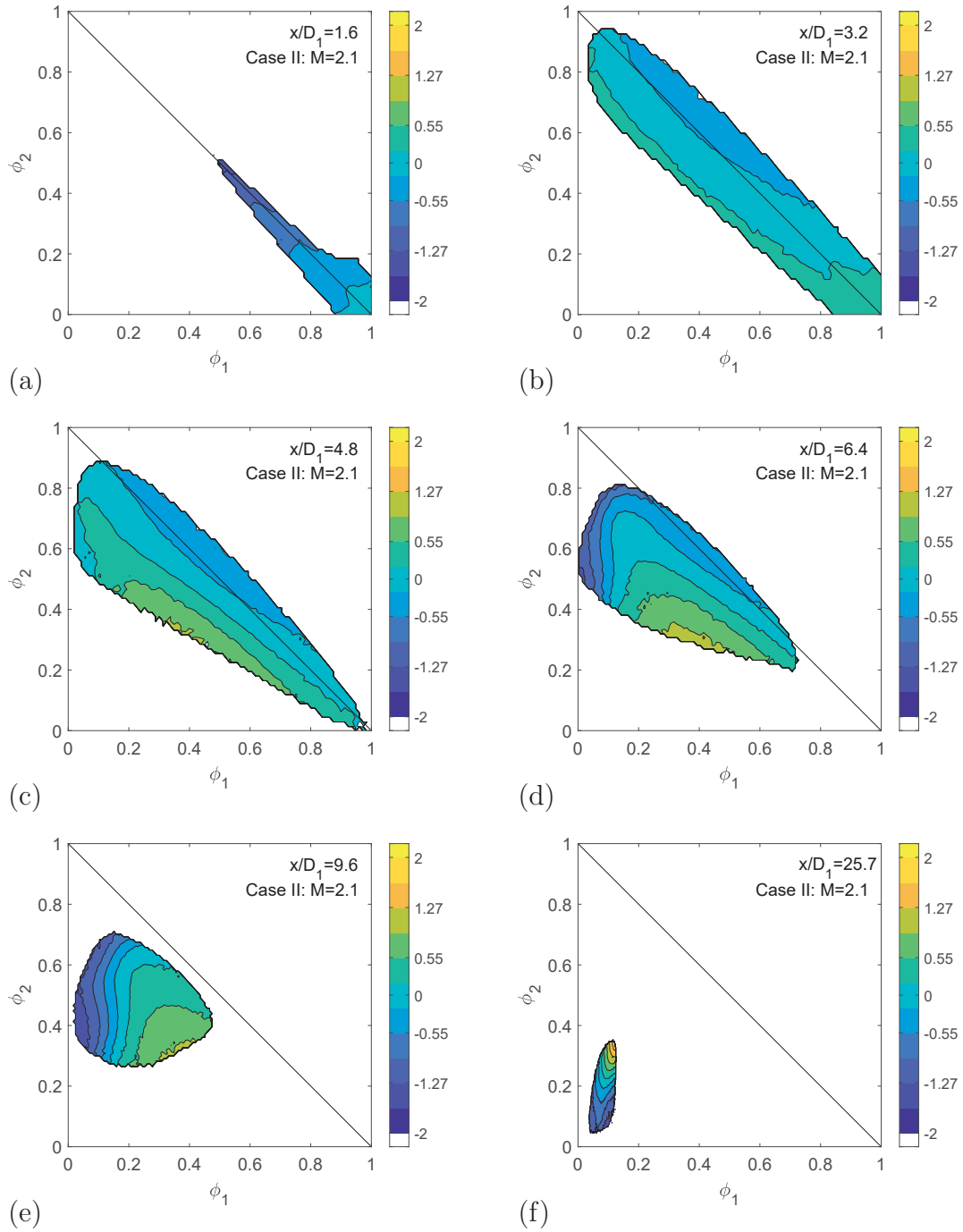


Figure 6.23: Downstream evolution of  $\langle u|\phi_1, \phi_2\rangle/u_{rms}$  along the centerline for  $M = 2.1$ . The outer contour corresponds to the one containing 99% of the JPDF of  $\phi_1$  and  $\phi_2$ .

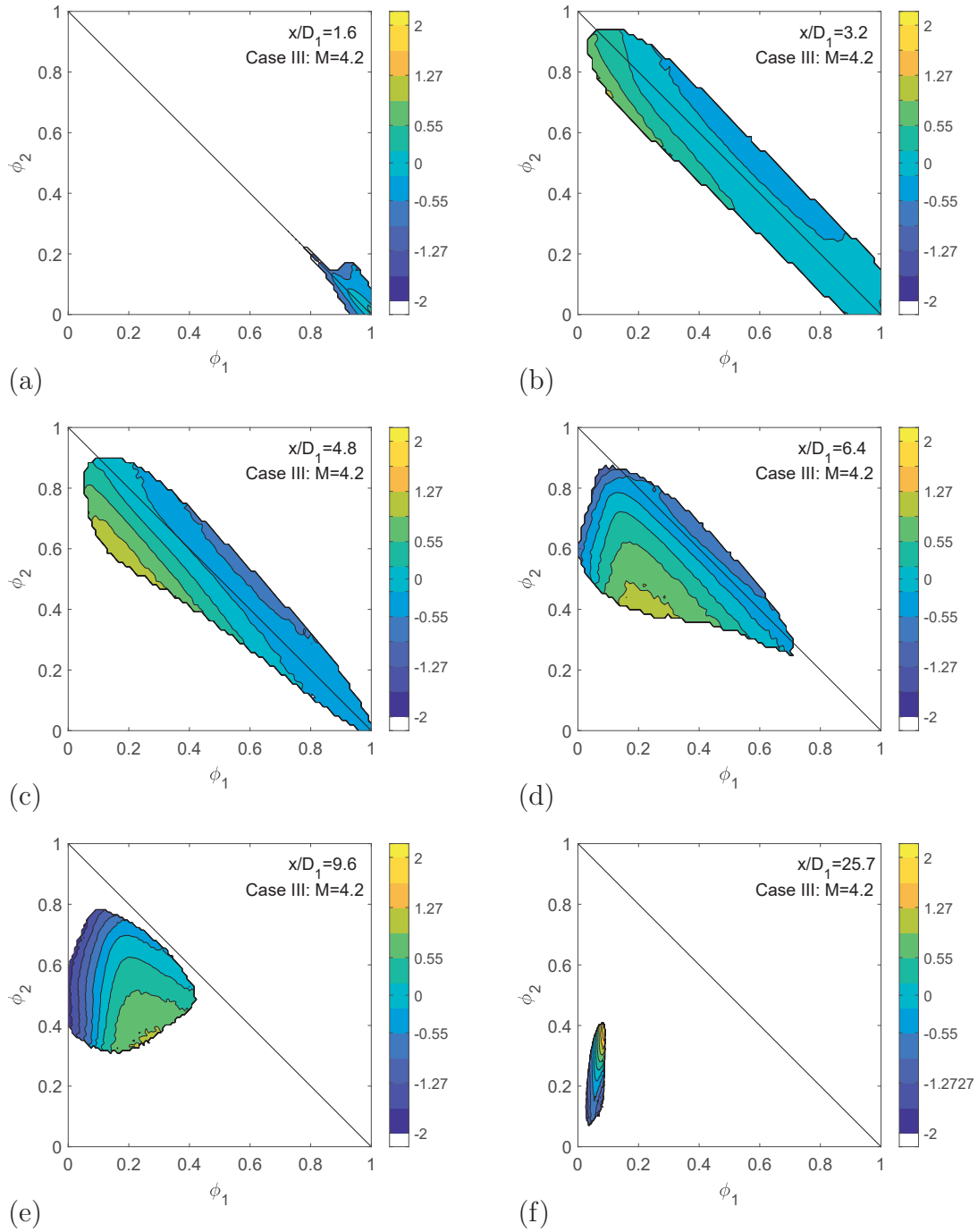


Figure 6.24: Downstream evolution of  $\langle u|\phi_1, \phi_2\rangle/u_{rms}$  along the centerline for  $M = 4.2$ . The outer contour corresponds to the one containing 99% of the JPDF of  $\phi_1$  and  $\phi_2$ .

coefficients ( $\rho_{u\phi_1}$  and  $\rho_{u\phi_2}$ ), none of which demonstrate a strong correlation between  $U$  and  $\phi_1$  or  $U$  and  $\phi_2$  until the fully merged region of the flow. Nevertheless, there exist small variations in  $\langle u|\phi_1, \phi_2 \rangle$  that lend some additional insight into the flow. For example, at  $x/D_1 = 1.6$ ,  $\langle u|\phi_1, \phi_2 \rangle$  decreases slightly along the line defined  $\phi_1 + \phi_2 = 1$ , an indication that  $\phi_1$ - $\phi_2$  mixtures are associated with slightly lower velocities than pure  $\phi_1$  emanating from the center jet. One can infer that, very close to the jet exit (where the flow is still affected by the presence of the jet walls, and, as depicted in figure 6.8, the cross-stream velocity profiles still retain their fully-developed nature), the shear layers, where  $\phi_1$ - $\phi_2$  first mix, move more slowly than pure fluid from either of the jets. By  $x/D_1 = 3.2$ , where the center and annular jets have begun to merge and mix, this effect diminishes (at least for cases II and III), and the  $\phi_1$ - $\phi_2$  mixing line is primarily defined by  $\langle u|\phi_1, \phi_2 \rangle = 0$ , suggesting that the velocities in the shear layers between the jets are not necessarily slower anymore. It is only at  $x/D_1 = 4.8$  that substantial variations in the values  $\langle u|\phi_1, \phi_2 \rangle$ , along with differences between the three cases ( $M = 0.77$ ,  $M = 2.1$ ,  $M = 4.2$ ), become apparent. For example, where  $\phi_1$  is small and  $\phi_2$  large,  $\langle u|\phi_1, \phi_2 \rangle < 0$  when  $M = 0.77$ , but  $\langle u|\phi_1, \phi_2 \rangle > 0$  when  $M = 4.2$ . As  $R$  increases beyond one, the highest velocities are no longer associated with the center jet (and thus  $\phi_1$ ), but the annular jet (which transports  $\phi_2$ ). Incursions of mixtures containing significant amounts of  $\phi_2$  onto the centerline will therefore be associated with these higher velocities. Moving farther downstream ( $4.8 \leq x/D_1 \leq 9.6$ ), one can observe a gradual change in the isovelocity lines. At  $x/D_1 = 4.8$  these lines are generally parallel to the line defined by  $\phi_1 + \phi_2 = 1$ , whereas by  $x/D = 9.6$ , they are either perpendicular to the  $\phi_1 + \phi_2 = 1$  line, or parallel to the line defined by  $\phi_1 = 0$ . As will subsequently be discussed when examining measurements of  $\langle u|\phi_1, \phi_3 \rangle$  and  $\langle u|\phi_2, \phi_3 \rangle$ , the evolution and orientation of these lines appears to depend on

$M$ , and more specifically whether  $M < 1$  or  $M > 1$ . Finally, far downstream (at  $x/D_1 = 25.7$ ), values of  $\langle u|\phi_1, \phi_2 \rangle$  tend to increase as both  $\phi_1$  and  $\phi_2$  get larger. The two are positively correlated by this point, and so similar trends are expected for both scalars. Variations in  $\langle u|\phi_1, \phi_2 \rangle$  are very large, which suggests a strong dependence of  $U$  on  $\phi_1$  and  $\phi_2$  (which is consistent with  $\rho_{u\phi_1} > 0$  and  $\rho_{u\phi_2} > 0$ ).

Measurements of  $\langle u|\phi_1, \phi_3 \rangle$  and  $\langle u|\phi_2, \phi_3 \rangle$  are depicted in figures 6.25 and 6.26. Consistent with the discussion on the evolution of  $\langle u|\phi_1, \phi_2 \rangle$ , at  $x/D_1 = 6.4$ , the isovelocity lines of  $\langle u|\phi_1, \phi_3 \rangle$  and  $\langle u|\phi_2, \phi_3 \rangle$  are parallel to the line defined by  $\phi_1 = 0$  and, when  $M > 1$ , the line defined by  $\phi_3 = 0$  (i.e.  $\phi_1 + \phi_2 = 1$ ). In particular, one can observe from figures 6.25(a)-(c) and 6.26(a)-(c), that the lowest values of  $\langle u|\phi_1, \phi_3 \rangle$  and  $\langle u|\phi_2, \phi_3 \rangle$  occur where  $\phi_1$  is small when  $M < 1$ , and where  $\phi_3 \approx 0$  (i.e. where the flow consists of  $\phi_1$ - $\phi_2$  mixtures) and  $\phi_1 \approx 0$  (i.e. where the flow consists of  $\phi_2$ - $\phi_3$  mixtures) when  $M > 1$ . The latter is consistent with the fact that when  $M > 1$ , fluid from the center jet (i.e.  $\phi_1$ ) and fluid from the coflow (i.e.  $\phi_3$ ) will be entrained into the faster annular jet, where all three scalars will mix. In such cases, one may assume the flow (at  $x/D_1 = 6.4$ ) consists of (i) slower moving mixtures of  $\phi_1$  and  $\phi_2$ , which were not entrained into the annular jet, (ii) faster-moving mixtures of all three scalars, resulting from entrainment of  $\phi_1$  and  $\phi_3$  into the annular jet, and (iii) slower moving mixtures of  $\phi_2$  and  $\phi_3$  from the outer regions on the jet. In contrast, when  $M < 1$ ,  $\phi_3$  is entrained into the annular jet, which is then entrained into the center jet. As a result, the conditional expectation of the fluctuating velocity tends to decrease with decreasing  $\phi_1$  (or alternatively, with increasing  $\phi_2$  and  $\phi_3$ ).

As a final note, it is worth pointing out that, in general, the behavior of  $\langle u|\phi_2, \phi_3 \rangle$ ,  $\langle u|\phi_1, \phi_3 \rangle$  and  $\langle u|\phi_2, \phi_3 \rangle$  is complex, and that the fluctuating velocity is often a non-linear function of the scalars ( $\phi_1, \phi_2, \phi_3$ ) upon which it is conditioned, which is

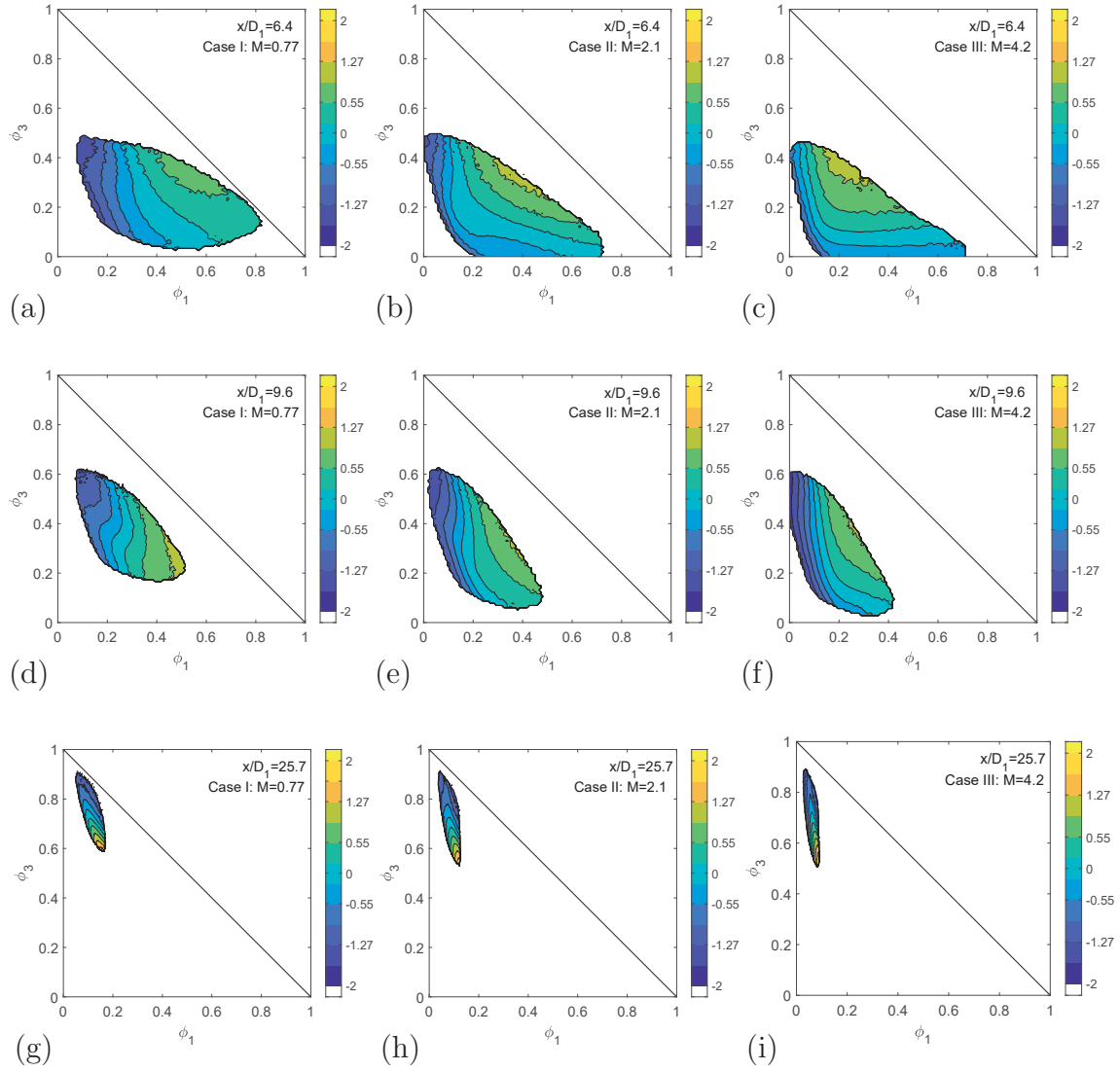


Figure 6.25: Downstream evolution of  $\langle u | \phi_1, \phi_3 \rangle / u_{rms}$  along the centerline. The outer contour corresponds to the one containing 99% of the JPDP of  $\phi_1$  and  $\phi_3$ .

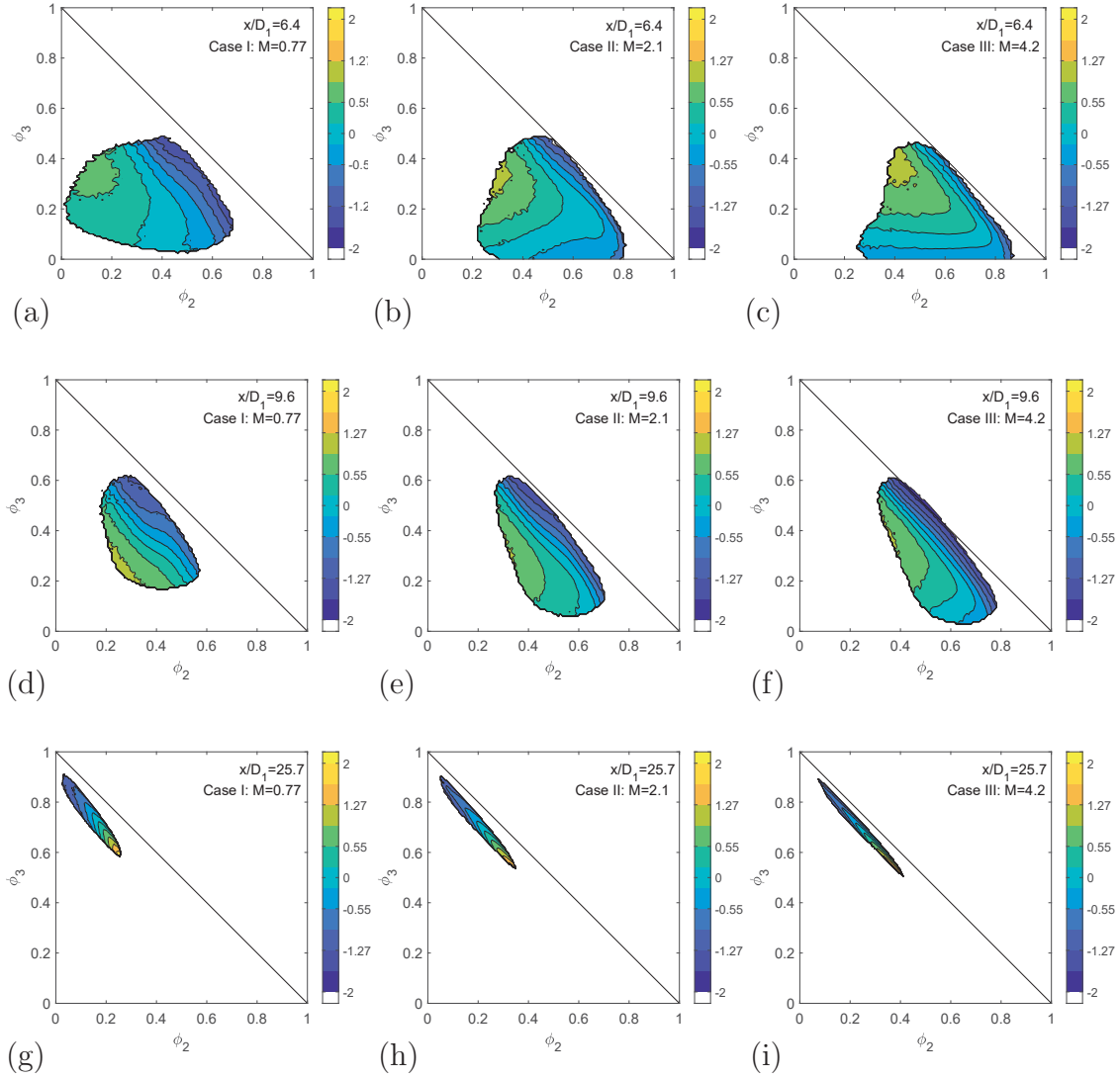


Figure 6.26: Downstream evolution of  $\langle u|\phi_2, \phi_3\rangle/u_{rms}$  along the centerline. The outer contour corresponds to the one containing 99% of the JPDF of  $\phi_2$  and  $\phi_3$ .

consistent with the generally non-Gaussian behavior of the velocity-scalar JPDFs depicted in the previous section.

## **CHAPTER 7**

### **Conclusions**

This final chapter summarizes pertinent conclusions drawn from the current work, which was motivated by the desire to study multi-scalar mixing by way of simultaneous two-scalar/velocity measurements. A novel 3-wire thermal anemometry-based probe was developed to this end, and used in a flow of turbulent coaxial jets transporting helium and temperature. Conclusions pertaining to both of these subjects are discussed in the remainder of this chapter. Furthermore, the novel contributions of this thesis are itemized, and possible extensions of the current research are described.

#### **7.1 Thermal-Anemometry-Based Measurement Techniques**

Despite the need for simultaneous velocity-scalar measurements to fully describe the mixing of scalars in turbulent flows, the vast majority of (experimentally-based) studies of multi-scalar mixing only measured the scalar fields of the flow. The first objective of the present work was therefore to rectify this situation, and develop an experimental technique capable of simultaneously measuring two scalars and velocity in turbulent flows. Ultimately, a novel 3-wire thermal-anemometry-based probe was created for this purpose. As previously discussed, thermal anemometry-based techniques have relatively high spatial and temporal resolutions, in addition to high signal-to-noise ratios, making them an excellent choice for studying turbulent flows. Moreover, these techniques can be adapted to measure velocity, temperature, or

gas concentration, and, as a result, are well suited to making multi-scalar mixing measurements.

The 3-wire probe developed in the present study consists of an interference probe (to simultaneously measure velocity and helium concentration), and a cold-wire thermometer (to measure temperature). The design of interference probes is complex, and not particularly well understood. Although there has been some discussion related to the design of such probes — for example, the theoretical analysis of Corrsin (1949), or the experimental studies of Way and Libby (1970), McQuaid and Wright (1974), and Harion *et al.* (1996) — there has been no comprehensive investigation of the necessary design parameters to construct interference probes (with the exception of preceding work by Hewes (2016)). Unlike what has previously been suggested in the literature, it is demonstrated herein that hot-wires of different diameters are *not* required to make simultaneous velocity and concentration measurements. This has significant practical implications for experimentalists, since interference probes can be constructed with two hot-wires of the same diameter. Moreover, by eliminating the requirement that the wires of the interference probe have different diameters, the probe can be designed to have a spatial and temporal resolution comparable to that of a single-normal hot-wire. Additional recommendations for the design of interference probes, including the separation distance between wires and the choice of overheat ratios, are also provided to aid future researchers seeking to build such probes.

To develop the 3-wire probe, (i) a temperature compensation technique was created to use interference probes in non-isothermal flows, and (ii) the use of cold-wire thermometers was extended to mixtures of air and helium. Theoretical arguments

were provided to demonstrate that the cold-wire is (for practical purposes) insensitive to the presence of helium, and measurements confirmed this. Accordingly, the cold-wire thermometer can be used to measure temperature independently of velocity or helium concentration. When combined with the interference probe, simultaneous measurement of velocity, helium concentration, and temperature is therefore possible.

## 7.2 Multi-Scalar Mixing in Coaxial Jets

The second objective of the current work involved using the novel 3-wire probe to study the evolution of multiple scalars in turbulent coaxial jets. The jets consist of (i) a center jet containing a mixture of helium and air, (ii) an annular jet containing cold, helium-free air, and (iii) a heated coflow that surrounds the two. Accordingly, the flow can be viewed as containing three scalars, where  $\phi_1$  is the normalized helium concentration,  $\phi_2$  is the cold, helium-free air from the annular jet, and  $\phi_3$  is the normalized temperature. Mean and rms quantities, correlation coefficients, velocity-scalar triple moments, PDFs, JPFDs, and conditional expectations of the fluctuating velocity were measured along the axis of jets of three different momentum ratios:  $M = 0.77$ ,  $M = 2.1$ , and  $M = 4.2$ . Based on the results presented herein, the centerline of the coaxial jets can be characterized by three distinct regions: the potential core of the center jet, the inner mixing region, and the fully merged region.

### Potential Core of the Center Jet:

The potential core of the center jets extends to the location where  $\phi_1 = 0.9$ , which corresponds to a downstream position of  $1.6 \leq x/D_1 \leq 3.2$  for the three cases investigated herein. Although the potential core consists primarily of  $\phi_1 = 1$ , small incursions of  $\phi_1$ - $\phi_2$  mixtures (originating from the shear layers between the jets) can nevertheless be observed as early as  $x/D_1 = 1.6$ .

### Inner Mixing Region:

The inner mixing region of the flow extends from approximately  $x/D_1 = 3.2$  to  $x/D_1 = 6.4$ . The flow in this region consists primarily of large fluctuations of anti-correlated  $\phi_1$  and  $\phi_2$ . At the beginning of the inner mixing region ( $x/D = 3.2$ ), fluid from the center jet ( $\phi_1 = 1$ ) is still very likely to be present, along with  $\phi_1$ - $\phi_2$  mixtures from the shear layers, such that the PDFs and JPDFs of  $\phi_1$  are (at least for cases I and III) bimodal. In the remainder of the inner mixing region,  $\langle\phi_2\rangle$  increases and, when  $R > 1$ ,  $\langle U\rangle$  also increases. Furthermore,  $U$  is, for the most part, uncorrelated with  $\phi_1$  and  $\phi_2$ , with the exception of case III ( $R = 1.75$ ), where one can observe that  $U$  and  $\phi_1$  are very slightly anti-correlated, and  $U$  and  $\phi_2$  are very slightly positively correlated.

### Fully Merged Region:

As the coflow increasingly penetrates the centerline,  $\langle\phi_2\rangle$  and  $\langle U\rangle$  decrease for all three cases, and the coaxial jets tend to behave similarly to a single jet of  $\phi_1$  and  $\phi_2$  mixing in a fluid composed of  $\phi_3$ . Accordingly, one can observe that  $\rho_{u\phi_1}$ ,  $\rho_{u\phi_2}$ , and  $\rho_{\phi_1\phi_2}$  all increase to positive values, whereas  $\rho_{u\phi_3}$ ,  $\rho_{\phi_1\phi_3}$ , and  $\rho_{\phi_2\phi_3}$  all decrease to negative values. Throughout most of the fully merged region, the PDFs and JPDFs are non-Gaussian, although they do tend to approach Gaussian distributions far downstream (i.e.  $x/D_1 = 25.7$ ). Furthermore,  $u_{rms}/\langle U\rangle$ ,  $\phi_{1,rms}/\langle\phi_1\rangle$ , and  $\phi_{2,rms}/\langle\phi_2\rangle$  all approach asymptotic values similar (but not identical) to those observed in single jets. It is likely that differences between the near-field of single jets and that of coaxial jets perpetuate far downstream, such that their asymptotic behaviors are not identical. Thus, the present work reinforces the arguments of George (2012), which are that the initial conditions of the flow do matter. Finally, unlike what may be expected from previous studies of multi-scalar mixing,  $\rho_{\phi_1\phi_2}$  was not observed

to asymptote to 1, and instead approached a value of 0.6. It is unclear if this is a reflection of the reduced signal-to-noise ratio of measurements far downstream, or the asymptotic tendency of  $\rho_{\phi_1\phi_2}$  to a non-uniform value (or both).

Although the description of the flow given above generally describes all three cases examined herein ( $M = 0.77$ ,  $M = 2.1$ ,  $M = 4.2$ ), it is important to note that distinct behavior is nevertheless observed for each of these cases. The momentum ratio can have significant effects on the evolution and mixing of scalars within coaxial jets, as discussed below:

- The length of the potential core is inversely related to  $M$ , and as a result  $\phi_1$  and  $\phi_2$  mix earlier with increasing  $M$ . Moreover, given that the end of the inner mixing region does not appear to depend significantly on  $M$  (based on both the current work and previous work, notably that of Ko and Au 1985), this region therefore increases with increasing  $M$  (see figure 6.15). Conversely, one can imagine that when  $M$  becomes very small, the inner mixing region may become negligibly small.
- As  $M$  increases, the coaxial jets appear to mix more slowly with the coflow, suggesting that entrainment of the coflow in the jets is retarded. For example,  $\langle\phi_3\rangle$ ,  $u_{rms}/\langle U\rangle$ ,  $\phi_{1,rms}/\langle\phi_1\rangle$ , and  $\phi_{3,rms}/\langle\phi_3\rangle$  all evolve more slowly along the centerline with increasing  $M$ . Additionally, examination of the PDFs and JPDFs of each of the quantities of interest ( $U$ ,  $\phi_1$ ,  $\phi_2$ ,  $\phi_3$ ) reveals that these approach Gaussian behavior more slowly as  $M$  increases. However, it should be noted that it is not clear if these effects are directly related to  $M$ , or if they only result from  $M_2$ , given that  $M_1$  was kept constant in the present work.
- Based on analyses of both  $\rho_{\phi_1\phi_2}$  and  $f_{\phi_1\phi_2}$  (the JPDF of  $\phi_1$  and  $\phi_2$ ), it is concluded that  $\phi_1$  and  $\phi_2$  initially mix more quickly with increasing  $M$ , but

may mix more slowly far downstream, in agreement with previous studies of multi-scalar mixing (i.e. Grandmaison *et al.* 1996; Li *et al.* 2017). The former is based on the observation that  $\rho_{\phi_1\phi_2}$  increases more quickly as  $M$  increases, at least in the range of  $4.8 \leq x/D_1 \leq 22.5$ , and the latter is inferred from the behavior of  $f_{\phi_1\phi_2}$  far downstream.

- In general, the behavior of the flow in case II ( $M = 2.1$ ) resembles that of case III ( $M = 4.2$ ) much more than it does case I ( $M = 0.77$ ). This appears to result from the fact when  $M < 1$ , the annular jet is entrained into the center jet, whereas when  $M > 1$ , the center jet is entrained into the annular jet. Consequently, when  $M < 1$ , one can observe that beyond the inner mixing region, the scalar-scalar JPDFs evolve through the center of scalar-space, indicating that all three scalars are always present in the flow. In contrast, when  $M > 1$ , just beyond the inner mixing region ( $6.4 \leq x/D_1 \leq 9.6$ ), the flow still contains instances in which either  $\phi_1$  or  $\phi_3$  are absent, and the scalar-scalar JPDFs tend to evolve along lines defined by  $\phi_1 = 0$  or  $\phi_3 = 0$  (i.e. the edge of the scalar-space).

As a final note, it is worth making two additional comments. First, it should be emphasized that simultaneous measurements are essential for studying multi-scalar mixing. Although correlation coefficients (which can be inferred from non-simultaneous measurements of scalar variances) may, to a certain extent, quantify the state mixing between two quantities, they do not provide a full description of the state of mixing. For example, in the current work it is demonstrated that even if the correlation coefficients of the three cases are equal, the shapes and distributions of the JPDFs of the same quantities will differ from case to case. Second, it bears noting that simultaneously measuring multiple scalars and velocity, especially with high spatial and temporal resolutions, is complex. The current work therefore only focused on

making measurements along the axis of the jets, where the turbulence intensity is sufficiently low ( $< 25\%$ ) that thermal-anemometry-based measurements are accurate. However, as will be discussed in §7.4, ultimately, a future objective is to also perform radial (cross-stream) measurements.

### 7.3 Novel Contributions of the the Present Study

The novel contributions of this thesis, including those pertaining to (i) the development of thermal-anemometry-based techniques, and (ii) multi-scalar mixing, are itemized below.

#### 7.3.1 Thermal-Anemometry-Based Measurement Techniques

1. The design of thermal-anemometry-based interference probes to simultaneously measure velocity and concentration was investigated in much greater detail than any other previous study, allowing optimal designs of these probes to be identified.
2. The use of interference probes was extended to non-isothermal flows by developing a technique to compensate for the effects of temperature. Although interference probes were previously used in non-isothermal flows by Sirivat and Warhaft (1982), no compensation technique was developed, and these probes, which were assumed to be insensitive to the effects of temperature, were limited to flows in which temperature fluctuations were very small ( $t_{rms} < 0.1^\circ\text{C}$ ).
3. The use of cold-wire thermometers, which have historically been limited to flows of pure air, was extended to mixtures of helium and air. Additionally, it was shown that the cold-wire is (mostly) insensitive to the presence of small helium fluctuations.
4. A novel 3-wire probe was designed to simultaneously measure velocity, helium concentration, and temperature in turbulent flows. Such measurements have

only been performed once before, in the work of Sirivat and Warhaft (1982). The probe developed herein is, however, distinct from the one developed by Sirivat and Warhaft (1982), as alluded to above.

### 7.3.2 Multi-Scalar Mixing in Coaxial Jets

1. The present work was the first to simultaneously measure two scalars and velocity in turbulent coaxial jets. Moreover, it should be noted that the only other record of simultaneous two-scalar and velocity measurements appears in the work of Sirivat and Warhaft (1982), performed nearly forty years ago in grid turbulence.
2. The evolution of multiple scalars ( $\phi_1, \phi_2, \phi_3$ ) and velocity ( $U$ ) along the axis of coaxial jets (in which  $0.77 \leq M \leq 4.2$ ) was examined by measuring mean and rms quantities, correlation coefficients, velocity-scalar triple moments, PDFs, JPDFs, and conditional expectations of the fluctuating velocity. In contrast to previous studies of multi-scalar mixing in coaxial jets (i.e. the work of Grandmaison *et al.* (1996), Cai *et al.* (2011), Rowinski and Pope (2013), and Li *et al.* (2017)), which focused only on the scalar fields of the flow, the present work also analysed the flow through the use of mixed velocity-scalar statistics — in particular, velocity-scalar correlation coefficients, velocity-scalar triple moments, velocity-scalar JPDFs, and conditional expectations of the fluctuating velocity.
3. A general description of the behavior of the flow, and the mixing of scalars within it, was presented for three distinct regions along the centerline of coaxial jets: the potential core of the center jet, the inner mixing region, and the fully merged region. The behavior of the flow in each of these regions was compared to previous studies of coaxial jets (e.g. Grandmaison *et al.* 1996;

Cai *et al.* 2011; Li *et al.* 2017), and although general trends in the evolution of the scalar statistics can be observed between the present work and that of previous studies, so too were many differences – in particular, the asymptotic values of  $\rho_{\phi_1\phi_2}$  and the shapes of some of the JPDFs of  $\phi_1$  and  $\phi_2$ . The present work therefore reinforces some of the comments made at the beginning of this thesis, which is that mixing of multiple scalars is *complex* and *highly dependent on initial conditions*, and as a result, worth investigating in greater detail.

4. Finally, the effects of the momentum ratio of the coaxial jets ( $M$ ) on multi-scalar mixing within the flow was clearly described. Although previous studies have focused either on coaxial jets in which  $M < 1$ , or in which  $M > 1$ , the current work examined both, and found significant differences in the flow between these two cases. For example, the composition of the flow at certain points depended on whether  $M < 1$  or  $M > 1$ , which may be of interest to those modelling or studying piloted flames. To the author’s knowledge, these differences relating to  $M$  have not been discussed previously, and merit additional research.

## 7.4 Future Work

Given the 3-wire probe developed herein, and the paucity of work on turbulent multi-scalar mixing, there are a number of possible extensions to the present work. A few of these are discussed in the current section.

### 7.4.1 Extension of Measurements Pertaining to the Current Experimental Conditions

As was briefly touched upon in §7.1, simultaneously measuring two scalars and velocity is not a trivial task. To ensure the turbulent velocity and scalar statistics could be measured accurately, the current work focused on making measurements

along the axis of the jets. The first extension to the present work therefore involves making measurements of radial (cross-stream) profiles in the jets. However, since the turbulence intensity along these profiles is much higher, a flying hot-wire anemometry system must first be developed.

Given the importance of PDF methods in modeling turbulent scalar mixing, the JPDFs and other large-scale quantities relevant to PDF transport equations were measured in the present work. However, small-scale quantities, like the conditional scalar diffusion  $\langle \gamma \nabla^2 \phi | \hat{\phi} \rangle$  or the conditional scalar dissipation  $\langle \gamma (\partial \phi / \partial x_i)^2 | \hat{\phi} \rangle$  are also needed to validate and/or develop mixing models for PDF methods. Moreover, since the former transports the scalar-scalar JPDF in scalar-space, it can also be used to gain insight into how the JPDF evolves through this space and/or to identify likely compositions towards which nearby mixtures tend to diffuse. Although subsequent work should focus on making these measurements, the size of the coaxial jets (i.e. the diameters) may need to be increased to improve the relative spatial resolution of the 3-wire probe to be able to more accurately measure small-scale statistics.

#### 7.4.2 Additional Multi-scalar Mixing Studies in Coaxial Jets

Due to the relative lack of multi-scalar mixing studies in coaxial jets (which is principally limited to the present work and that of Grandmaison *et al.* (1996), Cai *et al.* (2011), and Li *et al.* (2017)), there is significant room for additional experiments in such flows. A few possible questions to guide future work are suggested:

- In the current work, as well as that of Grandmaison *et al.* (1996) and Li *et al.* (2017), it was shown that differences in the momentum (or velocity) ratios of the jets affect the mixing process in coaxial jets. Thus, one may ask whether this is also true for differences in density ratios? Moreover are these effects accounted for by exclusively considering the momentum ratio ( $M$ )? In

other words, since  $M = R^2S$ , will coaxial jets with the same momentum ratio ( $M$ ), but different velocity ( $R$ ) and density ( $S$ ) ratios behave similarly, or do secondary density effects remain, as has been observed in previous studies of coaxial jets where  $M$  is small (see Favre-Marinet and Schettini (2001))?

- Similarly, the momentum flow rate of the center jet ( $M_1$ ) was held constant herein, while the momentum flow rate of the annular jet ( $M_2$ ), was varied. Do the current conclusions on the effects of  $M$  hold true if  $M_1$  is varied and  $M_2$  is held constant?
- Finally, how do differences in diffusivities affect the multi-scalar mixing process? Without comparing the present experiments to identical ones containing scalars with equal molecular diffusivities, it is difficult to comment on this question. Nevertheless, as can be observed when examining the budget for the scalar covariance:

$$\begin{aligned} \frac{\langle \phi'_\alpha \phi'_\beta \rangle}{\partial t} + \langle U_j \rangle \frac{\partial \langle \phi'_\alpha \phi'_\beta \rangle}{\partial x_j} + \langle u_j \phi'_\beta \rangle \frac{\partial \langle \phi_\alpha \rangle}{\partial x_j} + \langle u_j \phi'_\alpha \rangle \frac{\partial \langle \phi_\beta \rangle}{\partial x_j} + \frac{\partial \langle u_j \phi'_\alpha \phi'_\beta \rangle}{\partial x_j} \\ = \gamma_\alpha \frac{\partial^2 \langle \phi'_\alpha \phi'_\beta \rangle}{\partial x_j \partial x_j} - 2\gamma_\alpha \left\langle \frac{\partial \phi'_\alpha}{\partial x_j} \frac{\partial \phi'_\beta}{\partial x_j} \right\rangle + (\gamma_\beta - \gamma_\alpha) \left\langle \phi'_\alpha \frac{\partial^2 \phi'_\beta}{\partial x_j \partial x_j} \right\rangle, \end{aligned} \quad (7.1)$$

it is clear that differences in diffusivities can have an effect on the mixing process. Whether this effect is significant, or whether it is negligible, is however not clear. Future studies are therefore needed to better understand the role of differential diffusion in multi-scalar mixing.

### 7.4.3 Variable Viscosity and Variable Thermal Diffusivity

In §5.2.2, the temperature field measured by a cold-wire thermometer was shown to be affected by the presence of helium fluctuations. As previously discussed, differences between the temperature field of flows of pure air and that of flows containing helium fluctuations are most significant at the small scales, which suggests that these

are the result of the effects of either variable viscosity, variable thermal diffusivity, or both. Previous studies of variable viscosity flows have shown that differences in viscosity can have significant effects on the dynamics of turbulent flows, and in particular the dissipation rate of the turbulent kinetic energy ( $\epsilon$ ) of the flow (Talbot *et al.* 2013; Voivenel *et al.* 2016; Danaila *et al.* 2017). It is therefore reasonable that these effects could also be observed in a passive scalar transported by the flow. There does not appear to be any work on the effects of variable viscosity on the transport of scalars, or on the effects of variable thermal diffusivity. Both merit further research.

## REFERENCES

- AHMED, S. and SO, R. (1986). “Concentration distributions in a model combustor”. *Exp. Fluids* 4.2, pp. 107–113.
- AIHARA, Y., KASSOY, D. R., and LIBBY, P. A. (1967). “Heat transfer from circular cylinders at low Reynolds numbers. II. Experimental results and comparison with theory”. *Phys. Fluids* 10.5, pp. 947–952.
- AIHARA, Y., KOYAMA, H., and MORISHITA, E. (1974). “Effects of an air stream on turbulent diffusion of a helium jet from a small nozzle”. *Phys. Fluids* 17.4, pp. 665–673.
- AMIELH, M., DJERIDANE, T., ANSELMET, F., and FULACHIER, L. (1996). “Velocity near-field of variable density turbulent jets”. *Intl. J. Heat Mass Transfer* 39.10, pp. 2149–2164.
- ANDREWS, G., BRADLEY, D, and HUNDY, G. (1972). “Hot wire anemometer calibration for measurements of small gas velocities”. *Intl. J. Heat Mass Transfer* 15.10, pp. 1765–1786.
- AU, H. and KO, N. W. M. (1987). “Coaxial jets of different mean velocity ratios, part 2”. *J. Sound Vib.* 116.3, pp. 427–443.
- BANERJEE, A. and ANDREWS, M. (2007). “A convection heat transfer correlation for a binary air-helium mixture at low Reynolds number”. *J. Heat Transf.* 129.11, pp. 1494–1505.

- BOERSMA, B. J., BRETHER, G., and NIEUWSTADT, F. T. (1998). “A numerical investigation on the effect of the inflow conditions on the self-similar region of a round jet”. *Phys. Fluids* 10.4, pp. 899–909.
- BROWNE, L. and ANTONIA, R. (1987). “The effect of wire length on temperature statistics in a turbulent wake”. *Exp. Fluids* 5.6, pp. 426–428.
- BRUUN, H. (1995). *Hot-wire Anemometry: Principles and Signal Analysis*. Oxford University Press.
- CAI, J., DINGER, M., LI, W., CARTER, C., RYAN, M., and TONG, C. (2011). “Experimental study of three-scalar mixing in a turbulent coaxial jet”. *J. Fluid Mech.* 685, pp. 495–531.
- CHA, C., DE BRUYN KOPS, S., and MORTENSEN, M. (2006). “Direct numerical simulations of the double scalar mixing layer. Part I: Passive scalar mixing and dissipation”. *Phys. Fluids* 18.6, p. 067106.
- CHAMPAGNE, F. and WYGNANSKI, I. J. (1971). “An experimental investigation of coaxial turbulent jets”. *Intl J. Heat Mass Transfer* 14.9, pp. 1445–1464.
- CHEN, C. J. and RODI, W. (1980). “Vertical turbulent buoyant jets: a review of experimental data”. *NASA STI/Recon Technical Report A 80*.
- CHUNG, M. and KYONG, N. (1989). “Measurement of turbulent dispersion behind a fine cylindrical heat source in a weakly sheared flow”. *J. Fluid Mech.* 205, pp. 171–193.
- COLLIS, D. and WILLIAMS, M. (1959). “Two-dimensional convection from heated wires at low Reynolds numbers”. *J. Fluid Mech.* 6.03, pp. 357–384.
- CORRSIN, S. (1949). *Extended application of the hot-wire anemometer NACA Tech. Tech. rep. Note 1864*.

- CORRSIN, S. (1951). “On the spectrum of isotropic temperature fluctuations in an isotropic turbulence”. *J. Appl. Phys.* 22.4, pp. 469–473.
- COSTA-PATRY, E. and MYDLARSKI, L. (2008). “Mixing of two thermal fields emitted from line sources in turbulent channel flow”. *J. Fluid Mech.* 609, pp. 349–375.
- CURL, R. (1963). “Dispersed phase mixing: I. Theory and effects in simple reactors”. *AIChE J.* 9.2, pp. 175–181.
- DALLY, B. B., KARPETIS, A., and BARLOW, R. (2002). “Structure of turbulent non-premixed jet flames in a diluted hot coflow”. *Proceedings of the combustion institute* 29.1, pp. 1147–1154.
- DANAILA, L, VOIVENEL, L, and VAREA, E (2017). “Self-similarity criteria in anisotropic flows with viscosity stratification”. *Phys. Fluids* 29.2, p. 020716.
- DARISSE, A., LEMAY, J., and BENAÏSSA, A. (2013). “LDV measurements of well converged third order moments in the far field of a free turbulent round jet”. *Exp. Therm. Fluid Sci.* 44, pp. 825–833.
- DARISSE, A., LEMAY, J., and BENAÏSSA, A. (2014). “Extensive study of temperature dissipation measurements on the centerline of a turbulent round jet based on the  $\overline{\theta^2}/2$  budget”. *Exp. Fluids* 55.1, p. 1623.
- DARISSE, A., LEMAY, J., and BENAÏSSA, A. (2015). “Budgets of turbulent kinetic energy, Reynolds stresses, variance of temperature fluctuations and turbulent heat fluxes in a round jet”. *J. Fluid Mech.* 774, pp. 95–142.
- DAVIES, B., JONES, C., MANNING, A., and THOMSON, D. (2000). “Some field experiments on the interaction of plumes from two sources”. *Q. J. R. Meteorol. Soc.* 126.565, pp. 1343–1366.

- DIMOTAKIS, P. E. (2005). “Turbulent mixing”. *Annu. Rev. Fluid Mech.* 37, pp. 329–356.
- DJERIDANE, T., AMIELH, M., ANSELMET, F., and FULACHIER, L. (1996). “Velocity turbulence properties in the near-field region of axisymmetric variable density jets”. *Phys. Fluids* 8.6, pp. 1614–1630.
- DOPAZO, C. and O’BRIEN, E. (1974). “An approach to the autoignition of a turbulent mixture”. *Acta Astronaut.* 1.9-10, pp. 1239–1266.
- DOWLING, D. R. and DIMOTAKIS, P. E. (1990). “Similarity of the concentration field of gas-phase turbulent jets”. *J. Fluid Mech.* 218, pp. 109–141.
- DUNN, M. J., MASRI, A. R., and BILGER, R. W. (2007). “A new piloted premixed jet burner to study strong finite-rate chemistry effects”. *Combustion and Flame* 151.1-2, pp. 46–60.
- ESWARAN, V. and POPE, S. (1988). “Direct numerical simulations of the turbulent mixing of a passive scalar”. *Phys. Fluids* 31.3, pp. 506–520.
- FACKRELL, J. and ROBINS, A. (1982). “Concentration fluctuations and fluxes in plumes from point sources in a turbulent boundary layer”. *J. Fluid Mech.* 117, pp. 1–26.
- FAVRE-MARINET, M., CAMANO, E., and SARBOCH, J. (1999). “Near-field of coaxial jets with large density differences”. *Exp. Fluids* 26.1-2, pp. 97–106.
- FAVRE-MARINET, M and SCHETTINI, E. B. C. (2001). “The density field of coaxial jets with large velocity ratio and large density differences”. *Intl J. Heat Mass Transfer* 44.10, pp. 1913–1924.
- FERDMAN, E., OTUGEN, M. V., and KIM, S. (2000). “Effect of initial velocity profile on the development of round jets”. *J. Propul. Power* 16.4, pp. 676–686.

- FORNEY, L. and LEE, H. (1982). “Optimum dimensions for pipeline mixing at a T-junction”. *Aiche J* 28.6, pp. 980–987.
- FORNEY, L. and KWON, T. (1979). “Efficient single-jet mixing in turbulent tube flow”. *AICHE Journal* 25.4, pp. 623–630.
- FRANK, J., LYONS, K., and LONG, M. (1996). “Simultaneous scalar/velocity field measurements in turbulent gas-phase flows”. *Combust. Flame* 107.1-2, pp. 1–12.
- GEORGE, W. K. (2012). “Asymptotic effect of initial and upstream conditions on turbulence”. *J. Fluids Eng.* 134.6, p. 061203.
- GEORGE, W. K. and ARNDT, R. (1989). “The self-preservation of turbulent flows and its relation to initial conditions and coherent structures”. *Advances in turbulence* 3973, pp. 75–125.
- GER, A. M. and HOLLEY, E. R. (1974). “Turbulent jets in crossing pipe flow”. *Hydraulic Engineering Series, no. 30*.
- GRANDMAISON, E., POLLARD, A., and NG, S. (1991). “Scalar mixing in a free, turbulent rectangular jet”. *Intl. J. Heat Mass Transfer* 34.10, pp. 2653–2662.
- GRANDMAISON, E., BECKER, H., and ZETTLER, N. (1996). “Scalar mixing in turbulent concentric round jets”. *Can. J. Chem. Eng.* 74.4, pp. 433–447.
- GUIBERT, P. and DICOCCO, E. (2002). “Development of a local continuous sampling probe for the equivalence air-fuel ratio measurement. Application to spark ignition engine”. *Exp. Fluids* 32.4, pp. 494–505.
- HARION, J.-L., FAVRE-MARINET, M., and CAMANO, B. (1996). “An improved method for measuring velocity and concentration by thermo-anemometry in turbulent helium-air mixtures”. *Exp. Fluids* 22.2, pp. 174–182.
- HAWORTH, D. (2010). “Progress in probability density function methods for turbulent reacting flows”. *Prog. Energy Combust. Sci.* 36.2, pp. 168–259.

- HEWES, A., MEDVESCEK, J. I., MYDLARSKI, L., and BALIGA, B. R. (2020). “Drift compensation in thermal anemometry”. *Meas. Sci. Technol.* 31.4, p. 045302.
- HEWES, A. (2016). “Development of an interference probe for the simultaneous measurement of turbulent concentration and velocity fields”. M Eng thesis. McGill University.
- HU, H., SAGA, T., KOBAYASHI, T., and TANIGUCHI, N. (2004). “Analysis of a turbulent jet mixing flow by using a PIV-PLIF combined system”. *J. Visual.* 7.1, pp. 33–42.
- HUSSEIN, H. J., CAPP, S. P., and GEORGE, W. K. (1994). “Velocity measurements in a high-Reynolds-number, momentum-conserving, axisymmetric, turbulent jet”. *J. Fluid Mech.* 258, pp. 31–75.
- JANICKA, J., KOLBE, W., and KOLLMANN, W. (1979). “Closure of the transport equation for the probability density function of turbulent scalar fields”. *J. Non-Equilib. Thermodyn.* 4.1, pp. 47–66.
- JENSEN, K. D. (2004). “Flow measurements”. *J. Braz. Soc. Mech. Sci.* 26.4, pp. 400–419.
- JONÁŠ, P., MAZUR, O., ŠARBOCH, J., and URUBA, V. (2003). “Contribution to the simultaneous measurements of the gas–mixture velocity and concentration”. *Proc. Appl. Math. Mech.* 3.1, pp. 356–357.
- JUNEJA, A. and POPE, S. (1996). “A DNS study of turbulent mixing of two passive scalars”. *Phys. Fluids* 8.8, pp. 2161–2184.
- KARNIK, U. and TAVOULARIS, S. (1989). “Measurements of heat diffusion from a continuous line source in a uniformly sheared turbulent flow”. *J. Fluid Mech.* 202, pp. 233–261.

- KASSOY, D. R. (1967). “Heat transfer from circular cylinders at low Reynolds numbers. I. Theory for variable property flow”. *Phys. Fluids* 10.5, pp. 938–946.
- KENNARD, E. H. (1938). *Kinetic Theory of Gases*. McGraw-Hill.
- KERR, R. (1985). “Higher-order derivative correlations and the alignment of small-scale structures in isotropic numerical turbulence”. *J. Fluid Mech.* 153, p. 31.
- KHORSANDI, B., GASKIN, S, and MYDLARSKI, L (2013). “Effect of background turbulence on an axisymmetric turbulent jet”. *J. Fluid Mech.* 736, p. 250.
- KO, N. W. M. and AU, H. (1981). “Initial region of subsonic coaxial jets of high mean-velocity ratio”. *J. Fluid Eng.* 103.2, pp. 335–338.
- KO, N. W. M. and AU, H. (1982). “Spreading rate and reattachment of coaxial jets of high mean-velocity ratio”. *J. Fluid Eng.* 104, pp. 400–401.
- KO, N. W. M. and AU, H. (1985). “Coaxial jets of different mean velocity ratios”. *J. Sound Vib.* 100.2, pp. 211–232.
- KO, N. W. M. and KWAN, A. S. H. (1976). “The initial region of subsonic coaxial jets”. *J. Fluid Mech.* 73.2, pp. 305–332.
- KOLMOGOROV, A. (1941). “The local structure of turbulence in incompressible viscous fluid for very large Reynolds numbers”. *Dokl. Akad. Nauk SSSR* 30.4, pp. 301–305.
- KWAN, A. S. H. and KO, N. W. M. (1976). “Coherent structures in subsonic coaxial jets”. *J. Sound Vib.* 48.2, pp. 203–219.
- LAVERTU, R. and MYDLARSKI, L. (2005). “Scalar mixing from a concentrated source in turbulent channel flow”. *J. Fluid Mech.* 528, pp. 135–172.
- LAVERTU, T., MYDLARSKI, L., and GASKIN, S. (2008). “Differential diffusion of high-Schmidt-number passive scalars in a turbulent jet”. *J. Fluid Mech.* 612, pp. 439–475.

- LAVERTU, T. (2006). “Differential diffusion in a turbulent jet”. PhD thesis. McGill University.
- LAW, A. and WANG, H. (2000). “Measurement of mixing processes with combined digital particle image velocimetry and planar laser induced fluorescence”. *Exp. Therm. Fluid Sci.* 22.3, pp. 213–229.
- LEE, J. H. W. and CHU, V. (2003). *Turbulent jets and plumes: a Lagrangian approach*. Kluwer Academic Publishers.
- LEMAY, J. and BENAÏSSA, A. (2001). “Improvement of cold-wire response for measurement of temperature dissipation”. *Exp. Fluids* 31.3, pp. 347–356.
- LEMOINE, F., WOLFF, M., and LÉBOUCHE, M. (1996). “Simultaneous concentration and velocity measurements using combined laser-induced fluorescence and laser Doppler velocimetry: Application to turbulent transport”. *Exps. Fluids* 20.5, pp. 319–327.
- LEPORE, J. and MYDLARSKI, L. (2011). “Lateral dispersion from a concentrated line source in turbulent channel flow”. *J. Fluid Mech.* 678, pp. 417–450.
- LI, W, YUAN, M, CARTER, C., and TONG, C (2017). “Experimental investigation of the effects of mean shear and scalar initial length scale on three-scalar mixing in turbulent coaxial jets”. *J. Fluid Mech.* 817, pp. 183–216.
- LOCKWOOD, F. and MONEIB, H. (1980). “Fluctuating temperature measurements in a heated round free jet”. *Combust. Sci. Technol.* 22.1-2, pp. 63–81.
- LOMAS, C. (1986). *Fundamentals of hot wire anemometry*. Cambridge University Press.
- MASON, E. and SAXENA, S. (1958). “Approximate formula for the thermal conductivity of gas mixtures”. *Phys. Fluids* 1.5, pp. 361–369.

- MCQUAID, J. and WRIGHT, W. (1973). “The response of a hot-wire anemometer in flows of gas mixtures”. *Intl. J. Heat Mass Transfer* 16.4, pp. 819–828.
- MCQUAID, J. and WRIGHT, W. (1974). “Turbulence measurements with hot-wire anemometry in non-homogeneous jets”. *Intl. J. Heat Mass Transfer* 17.2, pp. 341–349.
- MEYER, D. (2010). “A new particle interaction mixing model for turbulent dispersion and turbulent reactive flows”. *Phys. Fluids* 22.3, p. 035103.
- MEYER, D. and DEB, R. (2012). “Modeling molecular mixing in a spatially inhomogeneous turbulent flow”. *Phys. Fluids* 24.2, p. 025103.
- MI, J., NOBES, D., and NATHAN, G. (2001). “Influence of jet exit conditions on the passive scalar field of an axisymmetric free jet”. *J. Fluid Mech.* 432, 91–125.
- MILLER, P. L. and DIMOTAKIS, P. E. (1991). “Reynolds number dependence of scalar fluctuations in a high Schmidt number turbulent jet”. *Phys. Fluids A* 3.5, pp. 1156–1163.
- MYDLARSKI, L. and WARHAFT, Z. (1998). “Passive scalar statistics in high-Péclet-number grid turbulence”. *J. Fluid Mech.* 358, pp. 135–175.
- NG, W. F. and EPSTEIN, A. H. (1983). “High-frequency temperature and pressure probe for unsteady compressible flows”. *Rev. Sci. Instrum.* 54.12, pp. 1678–1683.
- NINNEMANN, T. and NG, W. (1992). “A concentration probe for the study of mixing in supersonic shear flows”. *Exp. Fluids* 13.2-3, pp. 98–104.
- OBOUKHOV, A. (1949). “Structure of the temperature field in turbulent flows”. *Izv. Akad. Nauk. SSSR, Geogr. Geofiz.* 13, pp. 58–69.
- OSKOUIE, S. N., WANG, B., and YEE, E. (2015). “Study of the interference of plumes released from two near-ground point sources in an open channel”. *Intl. J. Heat Fluid Fl.* 55, pp. 9–25.

- OSKOUIE, S. N., WANG, B., and YEE, E. (2017). “Numerical study of dual-plume interference in a turbulent boundary layer”. *Bound.-Lay. Meteorol.* 164.3, pp. 419–447.
- PANCHAPAKESAN, N. and LUMLEY, J. L. (1993a). “Turbulence measurements in axisymmetric jets of air and helium. Part 1. Air jet”. *J. Fluid Mech.* 246, pp. 197–223.
- PANCHAPAKESAN, N. and LUMLEY, J. (1993b). “Turbulence measurements in axisymmetric jets of air and helium. Part 2. Helium jet”. *J. Fluid Mech.* 246, pp. 225–247.
- PARANTHOEN, P., FOUARI, A., DUPONT, A., and LECORDIER, J. (1988). “Dispersion measurements in turbulent flows (boundary layer and plane jet)”. *Intl. J. Heat Mass Transfer* 31.1, pp. 153–165.
- PERRY, A. (1982). *Hot-wire Anemometry*. Clarendon Press.
- PITTS, W. M. (1991a). “Effects of global density ratio on the centerline mixing behavior of axisymmetric turbulent jets”. *Exp. Fluids* 11.2-3, pp. 125–134.
- PITTS, W. M. (1991b). “Reynolds number effects on the mixing behavior of axisymmetric turbulent jets”. *Exp. Fluids* 11.2-3, pp. 135–141.
- PITTS, W. M. and MCCAFFREY, B. J. (1986). “Response behaviour of hot wires and films to flows of different gases”. *J. Fluid Mech.* 169, pp. 465–512.
- POPE, S. (1985). “PDF methods for turbulent reactive flows”. *Prog. Energy Combust. Sci.* 11.2, pp. 119–192.
- POPE, S. (1991). “Application of the velocity-dissipation probability density function model to inhomogeneous turbulent flows”. *Phys. Fluids A* 3.8, pp. 1947–1957.

- POPE, S. (1994a). “Lagrangian PDF methods for turbulent flows”. *Annu. Rev. Fluid Mech.* 26.1, pp. 23–63.
- POPE, S. (1994b). “On the relationship between stochastic Lagrangian models of turbulence and second-moment closures”. *Phys. Fluids* 6.2, pp. 973–985.
- POPE, S. (1998). “The vanishing effect of molecular diffusivity on turbulent dispersion: implications for turbulent mixing and the scalar flux”. *J. Fluid Mech.* 359, pp. 299–312.
- POPE, S. (2000). *Turbulent Flows*. Cambridge University Press.
- POPE, S. and CHEN, Y. (1990). “The velocity-dissipation probability density function model for turbulent flows”. *Phys. Fluids A* 2.8, pp. 1437–1449.
- PUMIR, A. (1994). “A numerical study of the mixing of a passive scalar in three dimensions in the presence of a mean gradient”. *Phys. Fluids* 6.6, pp. 2118–2132.
- REHAB, H., VILLERMAUX, E., and HOPFINGER, E. J. (1997). “Flow regimes of large-velocity-ratio coaxial jets”. *J. Fluid Mech.* 345, pp. 357–381.
- RICOU, F. P. and SPALDING, D. (1961). “Measurements of entrainment by axisymmetrical turbulent jets”. *J. Fluid Mech.* 11.1, pp. 21–32.
- RIVA, R., BINDER, G., FAVRE-MARINET, M., and HARION, J.-L. (1994). “Development of turbulent boundary layer with large density gradients”. *Exp. Therm. Fluid Sci.* 9.2, pp. 165–173.
- ROWINSKI, D. and POPE, S. (2013). “An investigation of mixing in a three-stream turbulent jet”. *Phys. Fluids* 25.10, p. 105105.
- SAKAI, Y., WATANABE, T., KAMOHARA, S., KUSHIDA, T., and NAKAMURA, I. (2001). “Simultaneous measurements of concentration and velocity in a CO<sub>2</sub> jet issuing into a grid turbulence by two-sensor hot-wire probe”. *Int. J. Heat Fluid Fl.* 22.3, pp. 227–236.

- SAWFORD, B. (2006). “Lagrangian modeling of scalar statistics in a double scalar mixing layer”. *Phys. Fluids* 18.8, p. 085108.
- SAWFORD, B. and DE BRUYN KOPS, S. (2008). “Direct numerical simulation and Lagrangian modeling of joint scalar statistics in ternary mixing”. *Phys. Fluids* 20.9, p. 095106.
- SAWFORD, B., FROST, C., and ALLAN, T. (1985). “Atmospheric boundary-layer measurements of concentration statistics from isolated and multiple sources”. *Bound.-Lay. Meteorol.* 31.3, pp. 249–268.
- SAYLOR, J. and SREENIVASAN, K. (1998). “Differential diffusion in low Reynolds number water jets”. *Phys. Fluids* 10.5, pp. 1135–1146.
- SCHUMAKER, S. A. and DRISCOLL, J. F. (2012). “Mixing properties of coaxial jets with large velocity ratios and large inverse density ratios”. *Phys. Fluids* 24.5, p. 055101.
- SHLIEN, D. and CORRSIN, S. (1976). “Dispersion measurements in a turbulent boundary layer”. *Intl. J. Heat Mass Transfer* 19.3, pp. 285–295.
- SHOAEI, F. and CRIMALDI, J. (2017). “Effect of instantaneous stirring process on mixing between initially distant scalars in turbulent obstacle wakes”. *Exp. Fluids* 58.4, p. 26.
- SHRAIMAN, B. and SIGGIA, E. (2000). “Scalar turbulence”. *Nature* 405.6787, pp. 639–646.
- SIRIVAT, A. and WARHAFT, Z. (1982). “The mixing of passive helium and temperature fluctuations in grid turbulence”. *J. Fluid Mech.* 120, p. 475.
- SIRIVAT, A. (1983). “Experimental Studies of Homogeneous Passive Scalars in Grid-generated Turbulence”. PhD thesis. Cornell University.

- SO, R., ZHU, J., ÖTÜGEN, M., and HWANG, B. (1990). “Some measurements in a binary gas jet”. *Exps. Fluids* 9.5, pp. 273–284.
- SO, R., ZHU, J., ÖTÜGEN, M., and HWANG, B. (1991). “Behavior of probability density functions in a binary gas jet”. *Exp. Fluids* 11.4, pp. 227–242.
- SOLTYS, M. and CRIMALDI, J. (2011). “Scalar interactions between parallel jets measured using a two-channel PLIF technique”. *Exps. Fluids* 50.6, pp. 1625–1632.
- SOLTYS, M. and CRIMALDI, J. (2015). “Joint probabilities and mixing of isolated scalars emitted from parallel jets”. *J. Fluid Mech.* 769, pp. 130–153.
- SREENIVASAN, K. (1991). “On local isotropy of passive scalars in turbulent shear flows”. *Proc. R. Soc. Lond.* Vol. 434. 1890. The Royal Society, pp. 165–182.
- SREENIVASAN, K., TAVOULARIS, S., HENRY, R., and CORRSIN, S. (1980). “Temperature fluctuations and scales in grid-generated turbulence”. *J. Fluid Mech.* 100.3, pp. 597–621.
- STANFORD, R. A. and LIBBY, P. A. (1974). “Further applications of hot-wire anemometry to turbulence measurements in helium-air mixtures”. *Phys. Fluids* 17.7, p. 1353.
- STAPOUNTZIS, H. and BRITTER, R. (1989). “Turbulent diffusion behind a heated line source in a nearly homogeneous turbulent shear flow”. *Turbulent Shear Flows 6*. Springer, pp. 97–108.
- STAPOUNTZIS, H., SAWFORD, B., HUNT, J., and BRITTER, R. (1986). “Structure of the temperature field downwind of a line source in grid turbulence”. *J. Fluid Mech.* 165, pp. 401–424.

- SUBRAMANIAM, S. and POPE, S. (1998). “A mixing model for turbulent reactive flows based on Euclidean minimum spanning trees”. *Combust. Flame* 115.4, pp. 487–514.
- TALBOT, B., DANAILA, L., and RENO, B. (2013). “Variable-viscosity mixing in the very near field of a round jet”. *Phys. Scr.* 2013.T155, p. 014006.
- TAVOULARIS, S. (2005). *Measurement in Fluid Mechanics*. Cambridge University Press.
- TAYLOR, G. (1935). “Statistical theory of turbulence. IV. Diffusion in a turbulent air stream”. *Proc. R. Soc. Lond.* Vol. 151. 873. The Royal Society, pp. 465–478.
- TENNEKES, H. and LUMLEY, J. L. (1972). *A First Course in Turbulence*. MIT Press.
- TONG, C. and WARHAFT, Z. (1995). “Passive scalar dispersion and mixing in a turbulent jet”. *J. Fluid Mech.* 292, pp. 1–38.
- TOWNSEND, A. A. (1954). “The diffusion behind a line source in homogeneous turbulence”. *Proc. R. Soc. Lond.* Vol. 224. 1159. The Royal Society, pp. 487–512.
- TOWNSEND, A. A. (1980). *The Structure of Turbulent Shear Flow*. Cambridge university press.
- TROPEA, C., YARIN, A., and FOSS, J. (2007). *Springer Handbook of Experimental Fluid Mechanics*. Springer.
- UBEROI, M. and CORRSIN, S. (1953). “Diffusion of heat from a line source in isotropic turbulence”. *NACA Rep.* 1142.
- VEERAVALLI, S. and WARHAFT, Z. (1990). “Thermal dispersion from a line source in the shearless turbulence mixing layer”. *J. Fluid Mech.* 216, pp. 35–70.

- VENKATARAMANI, K., TUTU, N., and CHEVRAY, R. (1975). “Probability distributions in a round heated jet”. *Phys. Fluids* 18.11, pp. 1413–1420.
- VILLERMAUX, E. and REHAB, H. (2000). “Mixing in coaxial jets”. *J. Fluid Mech.* 425, pp. 161–185.
- VILLERMAUX, J. and DEVILLON, J. (1972). “Représentation de la coalescence et de la redispersion des domaines de ségrégation dans un fluide par un modèle d’interaction phénoménologique”. *Second International Symposium on Chemical Reaction Engineering*, pp. 1–13.
- VISWANATHAN, S. and POPE, S. (2008). “Turbulent dispersion from line sources in grid turbulence”. *Phys. Fluids* 20.10, p. 101514.
- VOIVENEL, L., DANAILA, L., VAREA, E., RENOUE, B., and CAZALENS, M. (2016). “On the similarity of variable viscosity flows”. *Phys. Scr.* 91.8, p. 084007.
- VRIELING, A. and NIEUWSTADT, F. (2003). “Turbulent dispersion from nearby point sources? interference of the concentration statistics”. *Atmos. Environ.* 37.32, pp. 4493–4506.
- WANG, G. and FIEDLER, H. (2000). “On high spatial resolution scalar measurement with LIF Part 2: The noise characteristic”. *Exp. Fluids* 29.3, pp. 265–274.
- WARHAFT, Z. (1981). “The use of dual heat injection to infer scalar covariance decay in grid turbulence”. *J. Fluid Mech.* 104, pp. 93–109.
- WARHAFT, Z. (1984). “The interference of thermal fields from line sources in grid turbulence”. *J. Fluid Mech.* 144, p. 363.
- WARHAFT, Z. (2000). “Passive scalars in turbulent flows”. *Annu. Rev. Fluid Mech.* 32.1, pp. 203–240.

- WARHAFT, Z. and LUMLEY, J. L. (1978). “An experimental study of the decay of temperature fluctuations in grid-generated turbulence”. *J. Fluid Mech.* 88.4, pp. 659–684.
- WAY, J. and LIBBY, P. A. (1970). “Hot-wire probes for measuring velocity and concentration in helium-air mixtures”. *AIAA J.* 8.5, pp. 976–978.
- WAY, J. and LIBBY, P. (1971). “Application of hot-wire anemometry and digital techniques to measurements in a turbulent helium jet”. *AIAA J.* 9.8, pp. 1567–1573.
- WEBSTER, D., ROBERTS, P., and RA’AD, L. (2001). “Simultaneous DPTV/PLIF measurements of a turbulent jet”. *Exps. Fluids* 30.1, pp. 65–72.
- WHITE, B. (1987). “Wind tunnel wake measurements of heavier-than-air gas dispersion near a two-dimensional obstacle”. *Bound.-Lay. Meteorol.* 38, pp. 105–124.
- WILKE, C. (1950). “A Viscosity Equation for Gas Mixtures”. *J. Chem. Phys.* 18.4, p. 517.
- WILSON, R. A. M. and DANCKWERTS, P. V. (1964). “Studies in turbulent mixing—II: A hot-air jet”. *Chem. Eng. Sci.* 19.11, pp. 885–895.
- WU, P. and LIBBY, P. A. (1971). “Heat transfer to cylinders in helium and helium-air mixtures”. *Intl. J. Heat Mass Transfer* 14.8, pp. 1071–1077.
- WYGNANSKI, I. and FIEDLER, H. (1969). “Some measurements in the self-preserving jet”. *J. Fluid Mech.* 38.3, pp. 577–612.
- WYNGAARD, J. (1971). “The effect of velocity sensitivity on temperature derivative statistics in isotropic turbulence”. *J. Fluid Mech.* 48.4, pp. 763–769.
- XU, G. and ANTONIA, R. (2002). “Effect of different initial conditions on a turbulent round free jet”. *Exp. Fluids* 33.5, pp. 677–683.

ZHU, J., SO, R., and OTUGEN, M. (1988). “Turbulent mass flux measurements using a laser/hot-wire technique”. *Intl. J. Heat Mass Transfer* 31.4, pp. 819–829.

## Appendix A: Derivation of King's Law

The heat-rate balance equation for a wire element is as follows:

$$\dot{Q}_e = \dot{Q}_{fc} + \dot{Q}_c + \dot{Q}_r + \dot{Q}_s, \quad (\text{A.1})$$

where  $\dot{Q}_e$  is the electrical heat-generation rate,  $\dot{Q}_{fc}$  is the forced-convective heat-transfer rate,  $\dot{Q}_c$  is the conductive heat-transfer rate,  $\dot{Q}_r$  is the radiation heat-transfer rate, and  $\dot{Q}_s$  is the heat storage rate. Assuming that the wire element is at steady-state, that heat transfer by radiation is negligible, and that heat transfer by conduction can be neglected (reasonable for wires with large  $l/d$ ), the equation above reduces to:

$$\dot{Q}_e = \dot{Q}_{fc}. \quad (\text{A.2})$$

Moreover, given that,

$$\dot{Q}_e = I^2 R_w, \quad (\text{A.3})$$

where  $I$  is the current and  $R_w$  is the (operating) resistance of the wire, and,

$$\dot{Q}_{fc} = \pi h l d (T_w - T), \quad (\text{A.4})$$

where  $h$  is the heat transfer coefficient,  $T_w$  is temperature of the wire, and  $T$  is the temperature of the fluid, equation A.2 becomes:

$$I^2 R_w = \pi h l d (T_w - T). \quad (\text{A.5})$$

Since the temperature of the wire can be related to its resistance by:

$$R_w = R_{20}[1 + \alpha_{20}(T_w - T_{20})], \quad (\text{A.6})$$

where  $R_{20}$  and  $\alpha_{20}$  are the resistance and temperature coefficient of resistivity of the wire at 20°C, equation A.5 can then be expressed as:

$$I^2 R_w = \pi l h d \left( \frac{R_w - R_a}{\alpha_{20} R_{20}} \right) = \pi l k \text{Nu} \left( \frac{R_w - R_a}{\alpha_{20} R_{20}} \right). \quad (\text{A.7})$$

Note that  $k$  is the thermal conductivity of the fluid,  $\text{Nu} \equiv h d / k$  is the Nusselt number, and all fluid properties are evaluated at  $T_f$ . Using the Collis and Williams (1959) convective heat transfer correlation, the Nusselt number (Nu) can be expressed as a function of the Reynolds number (Re):

$$\text{Nu} \left( \frac{T_f}{T} \right)^{-0.17} = 0.24 + 0.56 \text{Re}^{0.45}. \quad (\text{A.8})$$

Thus, equation A.7 becomes:

$$I^2 R_w = \frac{E_w^2}{R_w} = \pi l k \left( \frac{R_w - R_a}{\alpha_{20} R_{20}} \right) \left( \frac{T_f}{T_a} \right)^{0.17} (0.24 + 0.56 \text{Re}^{0.45}). \quad (\text{A.9})$$

To account for assumptions in the derivation of equation A.9, such as, for example, end conduction effects, the Reynolds number exponent (0.45) is replaced by a variable, denoted as  $n$ . Additionally, given that experimentalists typically measure the bridge voltage ( $E$ ):

$$E_w = \frac{R_w}{R_T + R_L + R_w} E, \quad (\text{A.10})$$

where  $R_T$  is the top resistance of the anemometer's wheatstone bridge and  $R_L$  is the sum of the cable, support, and internal probe resistances, equation A.9 can be

rewritten in the following form:

$$E^2 = \pi l k \left( \frac{R_w - R_a}{\alpha_{20} R_{20}} \right) \frac{(R_T + R_L + R_w)^2}{R_w} \left( \frac{T_f}{T_a} \right)^{0.17} (0.24 + 0.56 \text{Re}^n). \quad (\text{A.11})$$

Finally, if the overheat ratio ( $OH$ ) is assumed to be constant,

$$\frac{R_w - R_a}{R_w} = \frac{OH - 1}{OH}, \quad (\text{A.12})$$

the measured (bridge) voltage can be expressed as:

$$E^2 = A + BU^n, \quad (\text{A.13})$$

where:

$$A = 0.24\pi \left( \frac{OH - 1}{OH} \right) \left( \frac{T_f}{T_a} \right)^{0.17} k \left( \frac{1}{\alpha_{20} R_{20}} \right) (R_T + R_L + R_w)^2 l, \quad (\text{A.14})$$

and,

$$B = 0.56\pi \left( \frac{OH - 1}{OH} \right) \left( \frac{T_f}{T_a} \right)^{0.17} k \left( \frac{\rho}{\mu} \right)^n \left( \frac{1}{\alpha_{20} R_{20}} \right) (R_T + R_L + R_w)^2 l d^n, \quad (\text{A.15})$$

yielding equations (2.1), (2.2), and (2.3), which were presented in §2.1.1.

## Appendix B: LabVIEW Program automating the He/Air Mixing System

The LabVIEW program described in §3.1.3 was written to automate the He/Air mixing system for calibrations and experiments. The user sets a desired helium mass fraction ( $C$ ) for the flow, which is immediately converted to a volumetric fraction ( $Y$ ) at standard conditions using the following equation:

$$Y = \frac{C\rho_{air}}{(1-C)\rho_{He} + C\rho_{air}}. \quad (\text{B.1})$$

Accordingly, the densities above ( $\rho_{air}$ ,  $\rho_{He}$ ) are evaluated at standard temperature and pressure, so that  $\rho_{air} = 1.18402 \text{ kg/m}^3$  and  $\rho_{He} = 0.16353 \text{ kg/m}^3$ . Given that the volumetric fraction of helium ( $Y$ ) can be defined as:

$$Y = \frac{Q_{He}}{Q_{He} + Q_{air}}, \quad (\text{B.2})$$

where  $Q_{air}$  and  $Q_{He}$  are respectively the flow rates of air and helium at standard conditions, the flow rate of helium required to maintain a volumetric fraction of helium ( $Y$ ) in the flow is calculated as follows:

$$Q_{He,MFC} = \frac{Y}{1-Y} Q_{air,MFM}. \quad (\text{B.3})$$

Thus,  $Q_{air,MFM}$ , which is measured by the mass flow meter, can be used to set  $Q_{He,MFC}$  on the mass flow controller. As data acquired from the mass flow meter are in the form of a 0-5 V analog signal ( $V_{MFM}$ ), they must first be converted to a flow rate. Per the specifications of the mass flow meter, the voltages and flow rates at standard conditions are linearly related with an offset of 0.01 V at zero flow rate.

The full scale of the device is 100 slpm, yielding the relationship below:

$$Q_{air,MFM} = \frac{V_{MFM} - 0.01}{4.99} 100. \quad (\text{B.4})$$

Similarly, the desired helium flow rate must be converted to a voltage signal ( $V_{MFC}$ ) so it can be sent to the mass flow controller. Given a linear relationship between the output voltage and flow rate, as well as a full scale value of 20 slpm for the mass flow controller,  $V_{MFC}$  is found to be:

$$V_{MFC} = 5 \frac{Q_{He,MFC}}{20}. \quad (\text{B.5})$$

## Appendix C: Uncertainty Analysis

This appendix presents an analysis of the uncertainty associated with the velocity, concentration, and temperature measurements performed herein. Using the approach of Tavoularis (2005), errors are classified either as (i) bias errors, which are systematic, and thus representative of the accuracy of the measurements, or (ii) precision errors, which are associated with the repeatability of the measurements. The latter may further be classified into two categories:

- Type 1 errors, which are estimated from a series of  $N$  measurements with mean  $\mu$  and standard deviation  $\sigma$ . According to Tavoularis (2005) the precision error ( $p$ ) for such measurements may be calculated as follows:

$$p = \frac{2\sigma}{\sqrt{N}}. \quad (\text{C.1})$$

- Type 2 errors, which are estimated from the precision of an instrument (denoted  $\sigma$ ). It is assumed that the error is uniformly distributed between  $\pm\sigma$ , such that the precision error ( $p$ ) is:

$$p = \frac{\sigma}{\sqrt{3}}. \quad (\text{C.2})$$

The total measurement uncertainty ( $u$ ) is estimated from the bias ( $b$ ) and precision ( $p$ ) errors in the following manner: (Tavoularis 2005):

$$u = \sqrt{\sum b_i^2 + \sum p_i^2}. \quad (\text{C.3})$$

Using this approach, uncertainties arising from (i) the calibration apparatus, (ii) instantaneous measurements of the velocity, concentration, and temperature, and (iii) finally the turbulent statistics of these quantities can be calculated.

## Calibration Apparatus

The uncertainty analysis presented herein begins by examining uncertainties associated with the calibration apparatus. As discussed in Chapter 3, velocities, concentrations, and temperatures in the calibration jet were calculated using a thermocouple, mass flow meter (MFM), mass flow controller (MFC), and mercury barometer. The uncertainties associated with each of these components are summarized in table C.1, and their total uncertainties are calculated using equation (C.3), such that:

- $u_{\text{thermocouple}} = \pm 1.701 \text{ K}$ ,
- $u_{\text{MFM}} = 0.687 \text{ slpm} = \pm 1.15 \cdot 10^{-5} \text{ m}^3/\text{s}$ ,
- $u_{\text{MFC}} = 0.201 \text{ slpm} = \pm 3.35 \cdot 10^{-6} \text{ m}^3/\text{s}$ ,
- $u_{\text{barometer}} = \pm 0.06 \text{ mmHg} = \pm 8.0 \text{ Pa}$ .

Since the temperature of the calibration jet ( $T_{\text{cal}}$ ) is measured only with the thermocouple, it has the following uncertainty.

$$u_{T,\text{cal}} = u_{\text{thermocouple}} = \pm 1.701 \text{ K}. \quad (\text{C.4})$$

Similarly, as the velocity of the calibration jet ( $U_{\text{cal}}$ , which is calculated from equations (3.2), (3.3), and (3.4)) is inferred from measurements of the thermocouple, mass flow meter, mass flow controller, and mercury barometer, its uncertainty is:

$$u_{U,\text{cal}} = \left[ \left( \frac{\partial U_{\text{cal}}}{\partial Q_{\text{air,MFM}}} u_{\text{MFM}} \right)^2 + \left( \frac{\partial U_{\text{cal}}}{\partial Q_{\text{He,MFC}}} u_{\text{MFC}} \right)^2 + \left( \frac{\partial U_{\text{cal}}}{\partial T} u_{\text{thermocouple}} \right)^2 + \left( \frac{\partial U_{\text{cal}}}{\partial P} u_{\text{barometer}} \right)^2 \right]^{1/2} = \pm 0.15 \text{ m/s}. \quad (\text{C.5})$$

Given that the concentration of the flow (i.e. the He mass fraction) is controlled by the LabVIEW program described in Appendix B, there is added uncertainty from

Table C.1: Summary of various sources of error in the calibration apparatus and the corresponding uncertainties.

Source of Error	Description	Type	$\sigma$	$b_i$ or $p_i$
Thermocouple	Accuracy of Type E thermocouple	Bias	N/A	$\pm 1.7$ K
	Precision of thermocouple display	Precision Type 2	0.1 K	$\pm 0.0577$ K
Mass Flow Meter	Accuracy of mass flow meter	Bias	N/A	$\pm 0.68$ slpm
	Repeatability of mass flow meter	Precision Type 2	0.14 slpm	$\pm 0.081$ slpm
	Precision of display	Precision Type 2	0.1 slpm	$\pm 0.0577$ slpm
Mass Flow Controller	Accuracy of mass flow controller	Bias	N/A	$\pm 0.2$ slpm
	Repeatability of mass flow controller	Precision Type 2	0.04 slpm	$\pm 0.023$ slpm
	Precision of display	Precision Type 2	0.01 slpm	$\pm 0.0058$ slpm
Mercury Barometer	Precision of pressure reading	Precision Type 2	0.1 mmHg	$\pm 0.06$ mmHg
A/D DAQ board	Accuracy of PCI-MIO-16E-4 board	Bias	N/A	$\pm 5.697$ mV
	Resolution of PCI-MIO-16E-4 board	Precision Type 2	2.4 mV	$\pm 1.39$ mV

the DAQ A/D board used in the calibration apparatus:

$$u_{\text{DAQ,cal}} = \sqrt{5.697^2 + 1.39^2} = \pm 5.86 \text{ mV}. \quad (\text{C.6})$$

Moreover, to maintain constant concentrations in the calibration jet, the LabVIEW program continuously re-calculates the flow rate of helium ( $Q_{\text{He,MFC}}$ ) in terms of the flow rate of air ( $Q_{\text{air,MFM}}$ ). Thus, when analyzing the accuracy of the concentration of the flow, uncertainties associated with the mass flow controller are re-expressed

as follows:

$$u_{\text{MFC,C}} = \sqrt{u_{\text{MFC}} + \left( \frac{\partial Q_{\text{He,MFC}}}{\partial E} u_{\text{DAQ,cal}} \right)^2} + u_{\text{MFC,set}}^2 = \pm 0.215 \text{ slpm}, \quad (\text{C.7})$$

where  $u_{\text{MFC,set}}$  denotes the uncertainty resulting from calculations used in the LabVIEW program to set the helium flow rate in terms of the air flow rate:

$$u_{\text{MFC,set}} = \frac{C_{\text{set}} \rho_{\text{air}}}{(1 - C_{\text{set}} \rho_{\text{He}})} \sqrt{u_{\text{MFM}} + \left( \frac{\partial Q_{\text{air,MFM}}}{\partial E} u_{\text{DAQ,cal}} \right)^2} = \pm 0.073 \text{ slpm}. \quad (\text{C.8})$$

The concentration of the flow ( $C_{\text{cal}}$ ) may be expressed as the ratio of the mass flow rate of helium to the total mass flow rate of the flow:

$$C_{\text{cal}} = \frac{\rho_{\text{air}} Q_{\text{air,MFM}}}{\rho_{\text{He}} Q_{\text{He,MFC}} + \rho_{\text{He}} Q_{\text{He,MFC}}}, \quad (\text{C.9})$$

such that it can be maintained with the following accuracy:

$$u_{C,\text{cal}} = \sqrt{\left( \frac{\partial C_{\text{cal}}}{\partial Q_{\text{air,MFM}}} u_{\text{MFM}} \right)^2 + \left( \frac{\partial C_{\text{cal}}}{\partial Q_{\text{He,MFC}}} u_{\text{MFC,C}} \right)^2} = \pm 9.3 \cdot 10^{-5}, \quad (\text{C.10})$$

at the lowest flow rates (at higher flow rates, the uncertainty decreases to  $\pm 2.5 \cdot 10^{-7}$ ).

## Uncertainty of Instantaneous Measurements

Errors associated with measurements of the instantaneous velocity, concentration, and temperature (using either single-normal hot-wire probes, cold-wire probes, or interference probes) generally fall into three categories: (i) errors arising from the DAQ board, (ii) errors arising from the calibration measurements, or (iii) errors arising from arising from curve-fits to the calibration data. The DAQ board used herein is a 16-bit PCI 6143 A/D DAQ board (with a maximum voltage span of  $\pm 5V$ ), which, as may be observed in table C.2, has an accuracy of 3.613 mV and precision of 0.00881 mV. Given that the DAQ board is used in both calibrations *and*

Table C.2: Summary of various sources of error for the PCI-6143 A/D DAQ board and the corresponding uncertainties.

Source and Description of Error	Type	$\sigma$	$b_i$ or $p_i$
Accuracy of PCI-6143 A/D DAQ board	Bias	N/A	$\pm 3.613$ mV
Resolution of PCI-6143 A/D DAQ board	Precision Type 2	0.153 mV	$\pm 0.0881$ mV

experiments, errors due to its accuracy may be omitted, and the total uncertainty of the board ( $u_{\text{DAQ}}$ ) is therefore  $\pm 0.0881$  mV. The propagation of the board's error to the instantaneous measurements may be calculated as follows:

- Single-normal hot-wire ( $U$ ):  $u_{U,\text{DAQ}} = \frac{\partial U}{\partial E} u_{\text{DAQ}} = \pm 0.065$  m/s,
- Cold-wire ( $T$ ):  $u_{T,\text{DAQ}} = \frac{\partial T}{\partial E} u_{\text{DAQ}} = \pm 8.4 \cdot 10^{-5}$  K,
- Interference Probe ( $C$ ):  $u_{C_i,\text{DAQ}} = \sqrt{\left(\frac{\partial C}{\partial E_{\text{up}}} u_{\text{DAQ}}\right)^2 + \left(\frac{\partial C}{\partial E_{\text{down}}} u_{\text{DAQ}}\right)^2} = \pm 1.6 \cdot 10^{-4}$ ,
- Interference Probe ( $U$ ):  $u_{U_i,\text{DAQ}} = \frac{\partial U}{\partial E_{\text{up}}} u_{\text{DAQ}} = \pm 0.013$  m/s.

The uncertainties arising from the DAQ board are all listed in table C.3, along with those arising from calibration measurements and curve-fits to the data. The former were calculated in the previous section, and the latter are calculated as follows:

- Single-Normal hot-wire ( $U$ ):  $u_{U,\text{fit}} = \sqrt{\frac{1}{N-3} \sum_{i=1}^N (U_{\text{meas}} - U_{\text{fit}})^2} = \pm 0.0346$  m/s,
- Cold-wire ( $T$ ):  $u_{T,\text{fit}} = \sqrt{\frac{1}{N-2} \sum_{i=1}^N (T_{\text{meas}} - T_{\text{fit}})^2} = \pm 0.0392$  K,
- Interference Probe ( $C$ ):  $u_{C_i,\text{fit}} = \sqrt{\frac{1}{N-10} \sum_{i=1}^N (C_{\text{meas}} - C_{\text{fit}})^2} = \pm 4.5 \cdot 10^{-4}$ ,
- Interference Probe ( $U$ ):  $u_{U_i,\text{fit}} = \sqrt{\frac{1}{N-10} \sum_{i=1}^N (U_{\text{meas}} - U_{\text{fit}})^2} = \pm 0.069$  m/s.

As may be inferred from table C.3, the total uncertainties of the instantaneous single-normal hot-wire and cold-wire thermometer measurements are respectively:

$$u_U = \sqrt{u_{U,\text{DAQ}}^2 + u_{U,\text{cal}}^2 + u_{U,\text{fit}}^2} = \pm 0.17 \text{ m/s} \quad (\text{C.11})$$

Table C.3: Summary of various sources of error for the instantaneous measurements and the corresponding uncertainties.

Probe	Source of Error	Type	$b_i$ pr $p_i$
Single-Normal Hot-Wire ( $U$ )	DAQ board	Precision	$u_{U,DAQ} = \pm 0.065$ m/s
	Calibration Velocity	Bias	$u_{U,cal} = \pm 0.15$ m/s
	Curve-Fit	Bias	$u_{U,fit} = \pm 0.0346$ m/s
Cold-Wire Thermometer ( $T$ )	DAQ board	Precision	$u_{T,DAQ} = \pm 8.4 \cdot 10^{-5}$ K
	Calibration Velocity	Bias	$u_{T,cal} = \pm 1.701$ K
	Curve-Fit	Bias	$u_{T,fit} = \pm 0.0392$ K
Interference Probe ( $C$ )	DAQ board	Precision	$u_{C_i,DAQ} = \pm 1.6 \cdot 10^{-4}$
	Calibration Velocity	Bias	$u_{C_i,cal} = \pm 9.3 \cdot 10^{-5}$
	Curve-Fit	Bias	$u_{C_i,fit} = \pm 4.5 \cdot 10^{-4}$
	$T$ measurements	Bias / Precision	$u_{C_i,T} = \pm 0.0016$
Interference Probe ( $U$ )	DAQ board	Precision	$u_{U_i,DAQ} = \pm 0.013$ m/s
	Calibration Velocity	Bias	$u_{U_i,cal} = \pm 0.15$ m/s
	Curve-Fit	Bias	$u_{U_i,fit} = \pm 0.069$ m/s
	$C$ measurements	Bias / Precision	$u_{U_i,C} = \pm 0.048$ m/s
	$T$ measurements	Bias / Precision	$u_{U_i,T} = \pm 0.11$ m/s

$$u_T = \sqrt{u_{T,DAQ}^2 + u_{T,cal}^2 + u_{T,fit}^2} = \pm 1.70 \text{ K.} \quad (\text{C.12})$$

Furthermore, the total uncertainty of instantaneous measurements of concentration (using the interference probe) in *isothermal* flows is:

$$u_{C_i} = \sqrt{u_{C_i,DAQ}^2 + u_{C_i,cal}^2 + u_{C_i,fit}^2} = \pm 4.9 \cdot 10^{-4}. \quad (\text{C.13})$$

When the velocity is measured with an interference probe, the uncertainty of the concentration measurements must be taken into account (see equation 4.17, used to infer the velocity with an interference probe), such that the total uncertainty of these measurements in *isothermal* flows is:

$$u_{U_i} = \sqrt{u_{U_i, \text{DAQ}}^2 + u_{U_i, \text{cal}}^2 + u_{U_i, \text{fit}}^2 + u_{U_i, C}^2} = \pm 0.17 \text{ m/s}, \quad (\text{C.14})$$

where

$$u_{U_i, C} = \frac{\partial U}{\partial C} u_C. \quad (\text{C.15})$$

Consequently, one may observe that (at least in non-isothermal flows) the interference probe and single-normal hot-wire measure the instantaneous flow velocity with a comparable uncertainty.

In *non-isothermal* flows, the interference probe is combined with a cold-wire to form the 3-wire probe, and, as described in §4.3.2, the effects of temperature on the interference probe are compensated using measurements from the cold-wire. The uncertainties of the interference probe measurements in such flows ( $u_{C_{3W}}, u_{U_{3W}}$ ) must therefore take into the account the uncertainties of the temperature measurements (denoted  $u_{T_{3W}}$ ), such that:

$$u_{C_{3W}} = \sqrt{u_{C_i, \text{DAQ}}^2 + u_{C_i, \text{cal}}^2 + u_{C_i, \text{fit}}^2 + u_{C_i, T}^2} = \pm 0.0018, \quad (\text{C.16})$$

where

$$u_{C_i, T} = \frac{\partial C}{\partial T} u_{T_{3W}} = \pm 0.0016, \quad (\text{C.17})$$

and

$$u_{U_{3W}} = \sqrt{u_{U_i, \text{DAQ}}^2 + u_{U_i, \text{cal}}^2 + u_{U_i, \text{fit}}^2 + u_{U_i, T}^2} = \pm 0.20 \text{ m/s}, \quad (\text{C.18})$$

where,

$$u_{U_i,T} = \sqrt{\left(\frac{\partial U}{\partial T} u_{T_{3W}}\right)^2 + \left(\frac{\partial U}{\partial C} u_{C_{3W}}\right)^2} = \pm 0.11 \text{m/s}. \quad (\text{C.19})$$

Two assumptions are made when estimating  $u_{T_{3W}}$ . First, it is assumed that helium fluctuations have no effect on this quantity (given that the cold-wire thermometer is effectively insensitive to helium concentration). Second, uncertainties associated with the thermocouple measurements ( $u_{\text{thermocouple}}$ ) are neglected. Given that the thermocouple is both used to measure the temperature ( $T$ ), and to calibrate the interference probe in non-isothermal flows, any errors arising from the thermocouple measurements are canceled out. As a result,  $u_{T_{3W}}$  is  $\pm 0.0392$  K.

It should be noted that the uncertainties calculated in the present section apply only to *instantaneous* measurements. As will be discussed in the following section, the fluctuating quantities can be measured with far less uncertainty. Moreover, the temperature and concentration measurements reported herein are actually calculated from temperature and concentration differences. In the case of the temperature measurements, a reference temperature is subtracted from  $T$ , whereas in the case of the concentration measurements, the mean concentration measured in flows of pure air  $\langle C_{air} \rangle$  is subtracted from  $C$ . According to Tavoularis (2005), when differences are measured with the same instrument, systematic errors (i.e. the bias errors), will be canceled out. Consequently, the total uncertainty of the temperature measurements is more accurately  $u_T = \pm 8.4 \cdot 10^{-5}$  K, and the total uncertainty of both the isothermal and non-isothermal concentration measurements is more accurately  $u_{C,i} = u_{C_{3W}} = \pm 1.6 \cdot 10^{-4}$ .

## Uncertainty of Turbulent Statistics

The fluctuating quantities ( $u \equiv U - \langle U \rangle$ ,  $t \equiv T - \langle T \rangle$  and  $c \equiv \langle C \rangle$ ) are by definition differences, and accordingly, bias errors can be neglected when calculating the uncertainties of these measurements. Moreover, fluctuations of velocity and concentration are amplified (often by a factor of 10 or more) to minimize discretization errors (the gain is sufficiently large on the CCA that the temperature fluctuations do not need to be amplified). The uncertainties associated with measurements of the fluctuations are therefore:

- Single-normal hot-wire ( $u$ ):  $u_u = \pm 0.0065$  m/s,
- Cold-wire ( $t$ ):  $u_t = \pm 1.6 \cdot 10^{-4}$  K,
- interference probe in isothermal flows ( $c$ ):  $u_{c_i} = \pm 1.6 \cdot 10^{-5}$ ,
- interference probe in isothermal flows ( $u$ ):  $u_{u_i} = \pm 0.0015$  m/s,
- interference probe in non-isothermal flows ( $c$ ):  $u_{c_{3W}} = \pm 1.6 \cdot 10^{-5}$ ,
- interference probe in non-isothermal flows ( $u$ ):  $u_{u_{3W}} = \pm 0.0016$  m/s,

and as stated before, measured with far less uncertainty than the instantaneous quantities.

## Appendix D: Confirmation of Statistical Convergence of the Measurements

To ensure the data acquired in the experiments described in Chapter 6 were sampled sufficiently long such that the statistics reported herein are converged, and thus accurately computed, 6<sup>th</sup>-order moments of the quantities of interest ( $U$ ,  $\phi_1$ ,  $\phi_2$ , and  $\phi_3$ ) were calculated using (i) the full data set, (ii) the first three quarters of the data set, (iii) the first half of the data set, and (iv) the first quarter of the data set. As may be observed in figures D.1, D.2, D.3, and D.4 moments calculated with the four data sets are nearly identical. Percent differences between the full data set and the 3/4 data set are on the order of 1%. Consequently, it is concluded that the full data set was sampled long enough to ensure convergence, given that lower-order moments, such as those studied in Chapter 6, converge more rapidly.

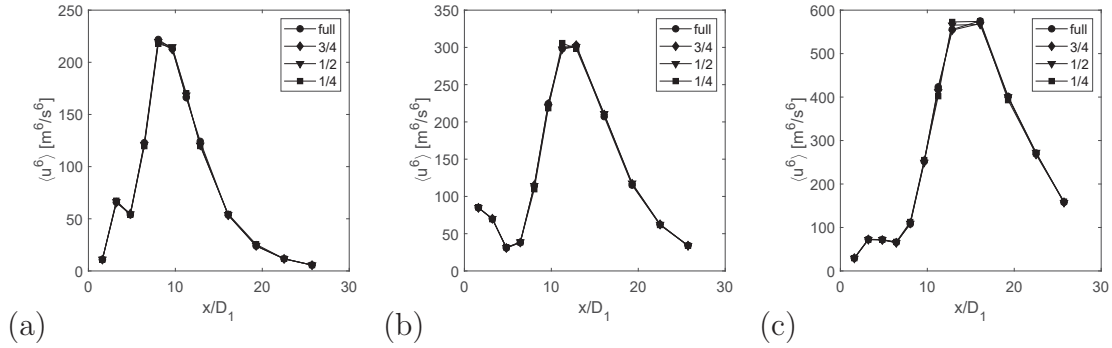


Figure D.1:  $\langle u^6 \rangle$  calculated from the full data set, 3/4 data set, 1/2 data set, and 1/4 data set for the three cases presented in chapter 6.

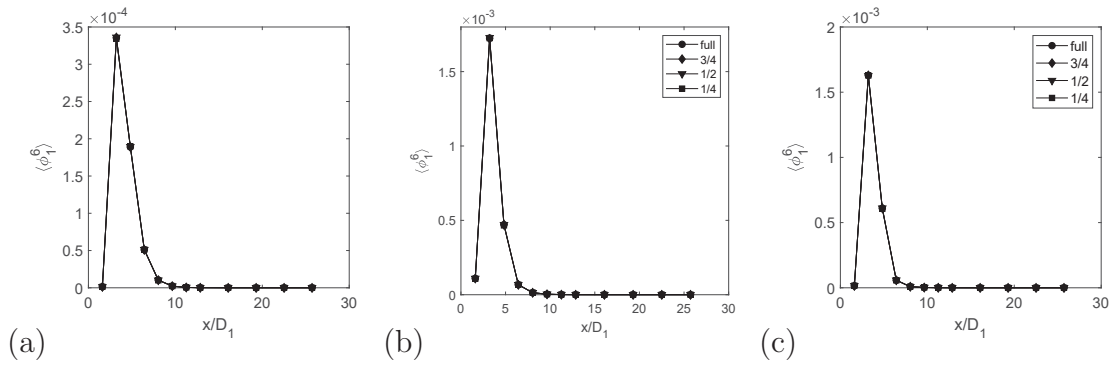


Figure D.2:  $\langle \phi_1^6 \rangle$  calculated from the full data set, 3/4 data set, 1/2 data set, and 1/4 data set for the three cases presented in chapter 6.

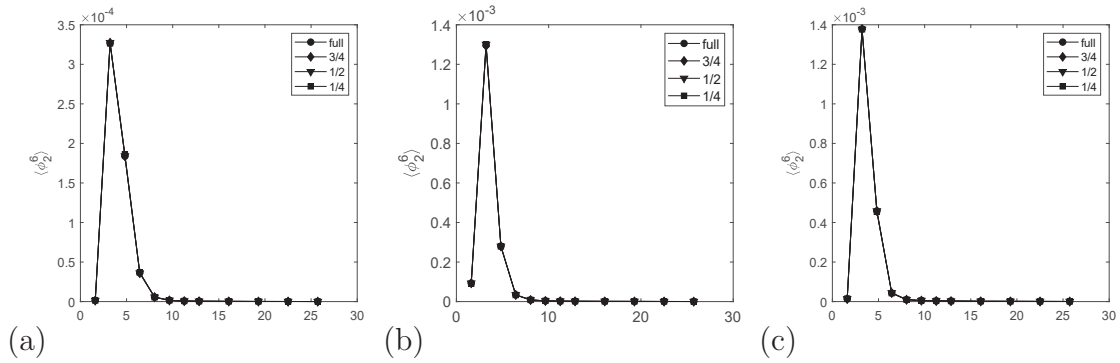


Figure D.3:  $\langle \phi_2^6 \rangle$  calculated from the full data set, 3/4 data set, 1/2 data set, and 1/4 data set for the three cases presented in chapter 6.

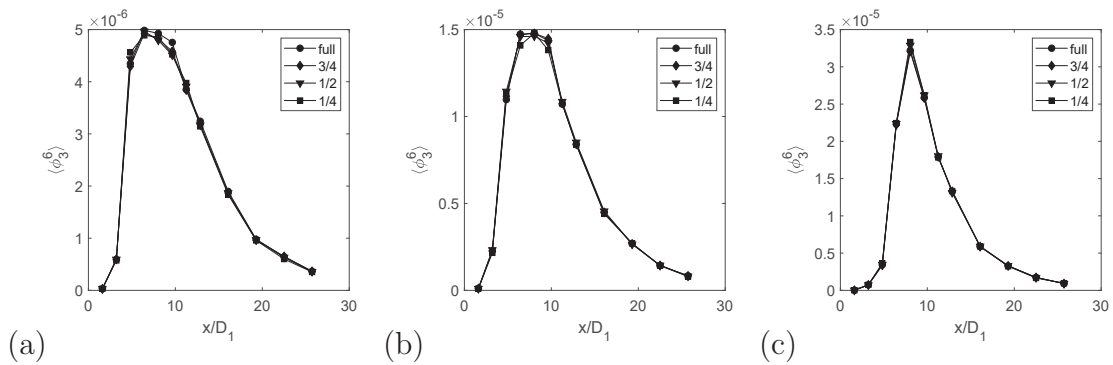


Figure D.4:  $\langle \phi_3^6 \rangle$  calculated from the full data set, 3/4 data set, 1/2 data set, and 1/4 data set for the three cases presented in chapter 6.

## Appendix E: Rarified Gas and Accommodation Effects

Hot-wires, which are typically used in flows of pure air, are generally assumed to operate in continuum flow. However, when extending the use of hot-wires to flows containing helium, this assumption may no longer be valid due to (i) rarified gas and (ii) accommodation effects. Given that most heat-transfer correlations that govern the behavior of hot-wires (such as that of Collis and Williams 1959) tend to only be accurate in the continuum flow regime, corrections must be developed for flows in which rarified gas and accommodation effects are significant. Following the analysis of Collis and Williams (1959) and Andrews *et al.* (1972), the current appendix presents such a correction, and applies it to the discussion presented in §4.2.2, in which a hot-wire's theoretical response in He/air mixtures must be predicted. However, rarified gas and accommodation effects are first briefly discussed.

The degree to which a flow can accurately be modeled as a continuum can be quantified by the Knudsen number (Kn) defined below:

$$\text{Kn} = \frac{\lambda}{d} = \left( \frac{\gamma_R \pi}{2} \right)^{1/2} \frac{M}{\text{Re}} = \frac{\nu}{d} \left( \frac{\pi M_{MM}}{2 R_{univ} T} \right)^{1/2}, \quad (\text{E.1})$$

where  $\lambda$  is the mean free path of gas molecules,  $\gamma_R$  is the ratio of specific heats,  $M$  is Mach number of the flow,  $M_{MM}$  is the molar mass of the gas, and  $R_{univ}$  is the universal gas constant. Using the Knudsen number, the flow is divided into three regimes (Bruun 1995):

- Continuum flow:  $\text{Kn} < 0.01$
- Slip flow:  $0.01 < \text{Kn} < 1$
- Free molecular flow:  $\text{Kn} > 1$

Table E.1: Typical Knudsen numbers of tungsten hot-wires with an overheat ratio of 1.8 ( $T_w = 515\text{K} = 242^\circ\text{C}$  and  $T_f = 404\text{K} = 131^\circ\text{C}$ ).

Flow	$d = 2.5 \mu\text{m}$	$d = 5 \mu\text{m}$
Air (He mass fraction = 0)	0.054	0.0164
He/Air mixture (He mass fraction = 0.06)	0.0664	0.0201
Helium (He mass fraction = 1)	0.1573	0.0474

As may be observed in table E.1, where the Knudsen numbers of typical hot-wires are presented, hot-wires operate in the lower end of the slip-flow regime. Although the continuum flow assumption is reasonably valid for larger hot-wires operated in flows of pure air, it becomes increasingly less valid as (i) the diameter decreases and (ii) the concentration of helium increases. Where the Knudsen number is large, and the flow has transitioned to slip flow, the temperature adjacent to the hot-wire is lower, and the velocity higher, than what is predicted for continuum flow (such that there is, essentially, a temperature and velocity discontinuity at the surface of the wire).

Thermal slip effects may also occur in what is normally considered the continuum regime ( $\text{Kn} < 0.01$ ) if the accommodation coefficient ( $\alpha$ ) for the gas on the wire is small. The accommodation coefficient is defined as:

$$\alpha = \frac{\varepsilon_I - \varepsilon_R}{\varepsilon_I - \varepsilon_S}, \quad (\text{E.2})$$

where  $\varepsilon_I$ ,  $\varepsilon_R$ , and  $\varepsilon_S$  represent the energy of a molecule incident on the wire, reflected by the wire, and in thermal equilibrium with the wire surface. As stated in §4.2.1, it is the ratio of the average increase in energy of the molecules after striking the wire surface to the increase in energy if the molecules were to have time to come into thermal equilibrium with the wire surface (Pitts and McCaffrey 1986). There is some disagreement in the literature regarding values of  $\alpha$  (which are bound between

0 and 1) for common hot-wire materials — but it appears that  $0.85 \leq \alpha \leq 1$  in flows of pure air and  $0.04 \leq \alpha \leq 0.48$  in flows of pure helium (Wu and Libby 1971; Andrews *et al.* 1972; Pitts and McCaffrey 1986). Consequently, accommodation effects are expected to be significant (such that thermal slip occurs) when using a hot-wire in flows of helium.

The remainder of this appendix presents a derivation of the correction used to account for rarified gas and accommodation effects in the heat-transfer relationship of a hot-wire. (The reader may skip ahead to equation E.17 to view the correction.) This derivation, which follows the approach described by Collis and Williams (1959) and Andrews *et al.* (1972) begins by examining the temperature discontinuity at the heated surface of a hot-wire undergoing thermal slip (Kennard 1938; Collis and Williams 1959; Andrews *et al.* 1972):

$$T_w - T_S = -\Delta \frac{\partial T}{\partial r}, \quad (\text{E.3})$$

where  $T_w$  is the temperature of the wire,  $T_S$  is what the fluid temperature would be if  $\partial T/\partial r$  remained unchanged up to the wire, and  $\Delta$  is the temperature jump distance:

$$\Delta = \left( \frac{2 - \alpha}{\alpha} \right) \left( \frac{2\gamma_R}{\gamma_R + 1} \right) \left( \frac{\lambda}{\text{Pr}} \right). \quad (\text{E.4})$$

The slip parameter ( $\beta$ ) is defined as:

$$\beta = \frac{\Delta}{d} = \theta \text{Kn}, \quad (\text{E.5})$$

where:

$$\theta = \left( \frac{2 - \alpha}{\alpha} \right) \left( \frac{2\gamma_R}{\gamma_R + 1} \right) \left( \frac{1}{\text{Pr}} \right). \quad (\text{E.6})$$

It is assumed that the actual rate of heat transfer from a hot-wire at temperature ( $T_w$ ) is the same as the rate of heat transfer that takes place from the same wire at temperature ( $T_S$ ) in a perfectly continuous gas, such that:

$$q = h_w(T_w - T) = h_S(T_S - T), \quad (\text{E.7})$$

where  $q$  is the heat flux. Accordingly,

$$h_S = h_w \left( 1 + \frac{T_w - T_S}{T_S - T} \right). \quad (\text{E.8})$$

Since the the flux ( $q$ ) is also equal to:

$$q = -k_{T_S} \left( \frac{\partial T}{\partial r} \right)_{T_S}, \quad (\text{E.9})$$

where  $k_{T_S}$  is the thermal conductivity of the gas at  $T_S$ , then:

$$\frac{T_w - T_S}{T_S - T} = \frac{\Delta_{T_S} h_S}{k_{T_S}}, \quad (\text{E.10})$$

so that equation (E.8) becomes:

$$h_S = h_w \left( 1 + \frac{h_S \Delta_{T_S}}{k_{T_S}} \right). \quad (\text{E.11})$$

The actual and continuum Nusselt numbers of the wire are respectively defined by  $\text{Nu} = h_w d / k_{T_f}$ , and  $\text{Nu}_c = h_S d / k_{T_f}$ , where  $k_{T_f}$  is the thermal conductivity of the gas at the film temperature ( $T_f$ ) (which in this derivation is assumed to be equal for the actual and continuum wires). Substituting the expressions for the Nusselt numbers into equation (E.11) yields:

$$\text{Nu}_c = \text{Nu} \left( 1 + \frac{\text{Nu}_c \Delta_{T_S} k_{T_f}}{k_{T_S} d} \right), \quad (\text{E.12})$$

which is re-arranged to give:

$$\begin{aligned} \text{Nu}_c &= \frac{\text{Nu}}{1 - (\text{Nu}\Delta_{T_s} k_{T_f}) / (k_{T_s} d)} \\ &= \frac{\text{Nu}}{1 - \text{Nu}\theta_{T_s} \text{Kn}_{T_s} (k_{T_f} / k_{T_s})} = \frac{\text{Nu}}{1 - \text{Nu}\Phi \text{Kn}}. \end{aligned} \quad (\text{E.13})$$

Since,  $k \sim T^y$ , then  $k_{T_f} / k_{T_s} = (T_s / T_f)^{-y}$ . Furthermore, since  $\mu \sim T^x$ , then from equation E.1,  $\text{Kn} \sim T^{-0.5+x+1} \sim T^{0.5+x}$ . Using these relations,  $\Phi$  in the equation above can be defined as:

$$\Phi = \theta_{T_s} \left( \frac{T_s}{T_f} \right)^{0.5+x-y}, \quad (\text{E.14})$$

and if  $T_s$  is approximately equal to  $T_w$ , then:

$$\Phi = \theta_{T_s} \left( \frac{2T_w / T}{1 + T_w / T} \right)^{0.5+x-y}. \quad (\text{E.15})$$

Equation (E.13) can therefore be combined with equation (E.15) to express  $\text{Nu}_c$  in terms of  $\text{Nu}$  for any gas of interest. Note that in flows of pure air,  $\Phi \approx 2$ , and the following (much simpler) equation derived by Collis and Williams (1959) can be used instead:

$$\frac{1}{\text{Nu}} - \frac{1}{\text{Nu}_c} = 2\text{Kn}. \quad (\text{E.16})$$

To predict the voltage across a hot-wire, while taking into account rarified gas effects and accommodation effects, one first calculates  $\text{Nu}_c$  from equation (A.8), and then calculates  $\text{Nu}$  from  $\text{Nu}_c$  using equations (E.13) and (E.15). The voltage measured across the hot-wire is consequently expressed as:

$$E^2 = \pi \left( \frac{OH - 1}{OH} \right) k \left( \frac{l}{\alpha_{20} R_{20}} \right) (R_T + R_L + R_w)^2 \frac{\text{Nu}_c}{1 + \text{Nu}_c \Phi \text{Kn}}. \quad (\text{E.17})$$

To obtain  $\Phi$ , the accommodation coefficient of the gas, which in the present work is a mixture of air and helium, must first be estimated. There is very little information on values of  $\alpha$  in gas mixtures, however Wu and Libby (1971) did measure the slip parameter ( $\beta$ ), which is defined in terms of  $\alpha$  (see equations (E.5) and (E.6)) in helium-air mixtures. Although they suggested that  $\beta = x_{He}\beta_{He}$ , where  $x_{He}$  is the mole fraction of helium, from inspection of their data, a linear relationship in terms of the helium mass fraction ( $C$ ) appears to be more appropriate<sup>1</sup> :

$$\beta = \beta_{He}C + \beta_{air}(1 - C). \quad (\text{E.18})$$

Both  $\beta_{air}$  and  $\beta_{He}$  are calculated from equations (E.5) and (E.6), assuming  $\alpha_{air} = 1$  and  $\alpha_{He} = 0.48$  (the values of  $\alpha$  given by Pitts and McCaffrey (1986)). Once the value of  $\beta$  in the helium-mixture has been estimated, equation (E.5) can then be used to obtain  $\theta_{Ts}$ , and thus  $\Phi$ . It should be emphasized that there is a large amount uncertainty surrounding values of  $\alpha$ , both in pure gases (i.e. air and helium) and gas mixtures (i.e. the helium/air mixtures). Accordingly, the techniques presented here only estimate the effects of accommodation effects on the hot-wire. Nevertheless, this is sufficient to lend some insight into the behavior of hot-wires in flows in which accommodation effects may be significant.

---

<sup>1</sup> It should be noted that the expression suggested by Wu and Libby (1971), predicts that  $\beta = 0$  in pure air, which yields an unrealistic value of  $\alpha$  ( $\alpha = 2$ , when it should be bound between 0 and 1).

## Appendix F: Calculations of Fluid Properties in He/Air Mixtures

To find the fluid properties of a gas mixture it is necessary to know the mole fractions of each of the individual gases. The helium-air mixtures used in the work herein are described in terms of the helium mass fraction ( $C$ ) and can be converted to mole fractions ( $x_{He}$ ,  $x_{air}$ ) by means of the following equations:

$$x_{He} = \frac{CM_{air}}{M_{He}(1-C) + M_{air}C} \quad (\text{F.1})$$

$$x_{air} = 1 - x_{He}, \quad (\text{F.2})$$

where  $M_{He}$  is the molecular weight of helium (4.00 kg/kmol) and  $M_{air}$  is the molecular weight of air (28.97 kg/kmol).

According to Banerjee and Andrews (2007), the density of a helium-air mixture ( $\rho_{mix}$ ) is a linear function of the densities of the pure gases:

$$\rho_{mix} = \rho_{air}x_{air} + \rho_{He}x_{He}. \quad (\text{F.3})$$

The dynamic viscosity of a helium-air mixture ( $\mu_{mix}$ ) is determined from the expression below, derived by Wilke (1950):

$$\mu_{mix} = \frac{\mu_{air}}{1 + \frac{x_{He}}{x_{air}} \left[ 1 + \left( \frac{\mu_{air}}{\mu_{He}} \right)^{1/2} \left( \frac{M_{He}}{M_{air}} \right)^{1/4} \right]^2 \left[ 8 \left( 1 + \frac{M_{air}}{M_{He}} \right) \right]^{-1/2}} + \frac{\mu_{He}}{1 + \frac{x_{air}}{x_{He}} \left[ 1 + \left( \frac{\mu_{He}}{\mu_{air}} \right)^{1/2} \left( \frac{M_{air}}{M_{He}} \right)^{1/4} \right]^2 \left[ 8 \left( 1 + \frac{M_{He}}{M_{air}} \right) \right]^{-1/2}}, \quad (\text{F.4})$$

where  $\mu_{air}$  and  $\mu_{He}$  refer to the dynamic viscosity of air and helium respectively.

The thermal conductivity of a gas mixture can be obtained using a kinetic-theory-based formula derived by Mason and Saxena (1958). For a mixture of helium and air, this is found to be:

$$k_{mix} = \frac{k_{air}}{1 + \frac{x_{He}}{x_{air}} 1.065 \left[ 1 + \left( \frac{k_{air}^\circ}{k_{He}^\circ} \right)^{1/2} \left( \frac{M_{He}}{M_{air}} \right)^{1/4} \right]^2 \left[ 8 \left( 1 + \frac{M_{air}}{M_{He}} \right) \right]^{-1/2}} + \frac{k_{He}}{1 + \frac{x_{air}}{x_{He}} \left[ 1 + \left( \frac{k_{He}^\circ}{k_{air}^\circ} \right)^{1/2} \left( \frac{M_{air}}{M_{He}} \right)^{1/4} \right]^2 \left[ 8 \left( 1 + \frac{M_{He}}{M_{air}} \right) \right]^{-1/2}}, \quad (\text{F.5})$$

where  $k^\circ$  is the “frozen” thermal conductivity, and can be related to the dynamic viscosity by the following equation:

$$k^\circ = \mu / M_{MM}. \quad (\text{F.6})$$